Mode III Fracture in Advanced Engineering Materials

This thesis is submitted in accordance with the requirements of the University of Liverpool for the Degree of Doctor in Philosophy by:

Dimitrios Christou Pennas

June 2007

THE UNIVERSITY *of* LIVERPOOL

Acknowledgements

First and foremost I would like to thank my supervisor, Professor Wesley J. Cantwell for his continual encouragement, excellent guidance and supervision during my PhD studies. This thesis and the work contained herein would not have been possible without his support.

I would like to thank the technical staff Dave Whitehurst and Chris Jackson for their invaluable help during the first stages of my studies, as well as Dr P. Compston from the Australian National University for the scanning electron micrographs included in this thesis.

I am also grateful to the Engineering and Physical Sciences Research Council (EPSRC), for financing part of my research.

A huge thanks to my parents and my sister, Vana, for providing me with unconditional love and support throughout my studies all these years.

Good wishes and appreciation also extend to Ken, Jackie and Warren for their friendship, continual support and encouragement.

Finally, my thanks to Biba, who provided me with sufficient love and patience to last anyone a lifetime.

List of Publications

- Pennas D., Cantwell W.J., The Influence of Loading Rate on the Mode III Interlaminar Fracture of Composite Materials, accepted for publication in Journal of Composite Materials.

- Pennas D., Cantwell W.J., The Influence of Loading Rate on the Mode III Fracture Properties of Composites and Adhesives, to be submitted to Composite Structures.

- Pennas D., Compston P., Cantwell W.J., The Influence of Loading Rate on the Mode III Fracture Properties of Composites and Adhesives, to be presented at the FOURTEENTH INTERNATIONAL CONFERENCE on COMPOSITE STRUCTURES, Melbourne, Australia, 2007.

Abstract

Delamination is a fundamental failure mode of laminated composites. When laminates are subjected to out-of-plane loading, the resin matrices between the plies often fail, resulting in ply separation or delamination failure. Such loading conditions occur in various ways and depend heavily on the load transfer modes in the composite structures. Delamination cracks can be visualised in the fracture mechanics sense to grow, and thus can be characterised in Mode I (opening), Mode II (shear) and Mode III (scissoring or anti-plane shear) and their combinations.

The test techniques for delamination in Mode I and Mode II, as well as mixed Mode I/II, have been well established. However, few workers have investigated the Mode III interlaminar fracture properties of composites, partly because of the experimental difficulties associated with the introduction of pure Mode III loading to the delamination crack.

The aim of this study was to investigate the Mode III interlaminar fracture properties of composite materials based on both thermoplastic and thermosetting matrices, adhesive joints and bi-material samples. For this reason, both numerical and experimental methods were used. The Edge Crack Torsion (ECT) test geometry was employed in order to evaluate the Mode III response of the samples studied, as it is commonly accepted that this is the most effective technique for characterising this mode of delamination. The Virtual Crack Closure Integral has also been extensively used to characterise the loading conditions at the crack tip in these samples. Once the quasi-static response of the composites were analysed, dynamic tests were undertaken to investigate the rate-sensitive behaviour of these high-performance materials. Finally, the Mode III geometry was modified to look at possible mixed-mode failure involving Mode II contributions.

Abbreviations

PMC	Polymer Matrix Composite
MMC	Metal Matrix Composite
PAN	Polyacrylonitrile
VCCT	Virtual Crack Closure Technique
DCB	Double Cantilever Beam
ENF	End Notch Flexure
MMB	Mixed Mode Bending
UD	Unidirectional
MD	Multidirectional
PEEK	Polyetheretherketone
WDD	Wedge Driven Delamination
SENB	Single End Notch Bend
CFRP	Carbon Fibre Reinforced Plastics
SENF	Stabilised End Notch Flexure
ELS	End Loaded Split
CCC	Coordinate Conversion Control
JIS	Japanese Industrial Standards
3D	3-Dimensional
DENF	Double Edge Notch Flexure
SCB	Split Cantilever Beam
CRS	Crack Rail Shear
ECT	Edge Crack Torsion
ASTM	American Society for Testing and Materials
EDT	Edge Delamination Tension
CAD	Computer Aided Design
SEM	Scanning Electron Microscopy

Symbols

σ	Applied stress
σ_b	Applied stress for onset of buckling
E	Young's modulus of elasticity
d	Fibre diameter
M	Moment required to bend fibre
k	Reciprocal of radius curvature
k_{max}	Maximum curvature before fracture occurs
G	Strain energy release rate
G_I	Mode I strain energy release rate
G_{II}	Mode II strain energy release rate
G_{III}	Mode III strain energy release rate
G_{Ic}	Mode I fracture toughness
G_{IIc}	Mode II fracture toughness
G_{IIIc}	Mode III fracture toughness
G_T	Total strain energy release rate
G_{Ta}	Average total strain energy release rate
P	Applied load
dC/da	Change in compliance as the crack grows
L	Distance between points of applied displacement
m	Constant in the specimen compliance expression
A	Constant in the specimen compliance expression
C	Compliance
ν	Poisson's ratio
P_{max}	Force at crack propagation
δ	Applied displacement
θ	Material angle

Contents

1. Introduction

2. Literature Review

3. Numerical Procedure

4. Experimental Procedure

5. Numerical Results and Discussion

6. Experimental Results and Discussion

7. Conclusions

1. Introduction

1.1. Background

Composite materials have found significant use through the ages from the incorporation of straw into mud bricks through to concrete and Kevlar reinforced polymeric systems. Naturally occurring composite materials such as wood, bamboo and bone were initially used by ancient civilisations. Gradually, materials such as copper, bronze and iron started being used on a small scale. During the industrial revolution, the importance of natural materials was reduced with the introduction of cast iron, steels and metallic alloys into mass production items. These newly-manufactured materials fulfilled the structural requirements of the time, but since the mid-twentieth century there has been a return to composites due to the improvements in specific properties they can offer. This has occurred through the development of artificially-produced composite materials such as glass fibre reinforced epoxies. More complex, composite systems have replaced conventional steels in the marine, aerospace, mechanical and civil engineering industries, resulting in the composites' increased use.

1.2. Definition of a Composite Material

Many materials in common day use are effectively composites. This is mainly the case with natural biological materials, which are generally made up of at least two constituents. In many cases, a strong and stiff component is present, often in elongated form, embedded in a softer constituent forming the matrix. For example, wood is made up of fibrous chains of cellulose molecules in a matrix of lignin, while bone and teeth are both essentially composed of hard inorganic crystals (hydroxyapatite or osteones) in a matrix of tough organic constituent called collagen. Commonly, such composite materials show marked anisotropy, meaning that their properties vary significantly when measured in different directions. This usually arises because the harder constituent is in fibrous form, with the fibre axes preferentially aligned in particular directions. Moreover, one or more of the constituents may exhibit inherent anisotropy as a result of their crystal structure. In natural materials, such anisotropy of mechanical properties is often exploited within the structure. For example, wood is much stronger in the direction of the fibre tracheids, which are usually aligned parallel to the axis of the trunk or branch, than it is in the transverse directions. High strength is required in the axial direction, since the branch becomes loaded like a cantilever beam by its own weight and the trunk is stressed in a similar way by the action of the wind. Such beam bending causes high stresses along its length, but not through the thickness.

When artificially making composite materials, considerable scope for integration between the processes of material specification and component design is offered by the potential for controlled anisotropy. This is the most important aspect about the use of composites, as it represents a departure from conventional engineering practice. Normally, an engineer designing a component commonly takes the material properties to be isotropic. In composite materials on the other hand, large anisotropy exists both in stiffness and strength and must be taken into account during the design phase. Factors such as the variation in strength with direction, as well as the effect of any stiffness anisotropy on the stresses set up in the component under a given external load, must be considered. A very important consideration when producing a composite material, is the way it will be loaded when it is made into a component. As

a consequence it is common that the processes of material production and component manufacture are integrated into a single operation. Similarly, this is exactly what happens when biological materials are produced.

1.3. Types of Composites

There are many different types of composite materials. Most of them in industrial use are based on polymeric matrices; thermosets and thermoplastics. By definition, a thermosetting polymer is a material that becomes permanently hard and rigid when heated or cured, whereas a thermoplastic is a material that softens when heated and hardens again when cooled. These are usually reinforced with short, stiff fibres, such as glass and carbon. Since the matrix is much weaker and less stiff than the fibres, the materials exhibit marked anisotropy. Furthermore, there has been considerable interest in metal matrix composites, such as aluminium reinforced with ceramic particles or short fibres, and titanium containing long, large-diameter fibres. The property enhancements being sought through the introduction of a reinforcement in a metal matrix, are often less pronounced than for polymer matrices, in which case, the improvements in high-temperature performance or tribological properties are often of interest. The commercial use of metal matrix composites is still limited compared to that of polymer composites, although various industrial applications have been developed or are being explored. Finally, composites based on ceramic matrices are also being studied. The main aim is to increase the toughness of the ceramic by introducing other constituents, since the stiffness and strength are unlikely to be much affected. Unfortunately, ceramic matrix composites still remain in the early stages of development, due to difficulties associated with the manufacture of such materials.

When considering the formulation of a composite material for a particular type of application, the properties exhibited by the potential constituents should be considered. The properties of particular interest are the stiffness (Young's modulus), strength and toughness. Density is also of great significance in numerous cases, since the mass of the component may be of critical importance. It is common that composites are subjected to temperature changes (during manufacture and/or in

service). As a result, the thermal properties such as the coefficient of thermal expansion and conductivity should be taken into account. A mismatch between the coefficient of thermal expansion of the constituents could lead to internal residual stresses, which could have a strong effect on the mechanical behaviour of the composite.

Table 1.1 contains representative data relating to the properties of a range of matrix materials, as well as some typical engineering materials and a few representative composites. It can be seen that some attractive property combinations (high stiffness/strength and low density) can be achieved with composites.

Type of material (example)	**Density ρ ($Mg\ m^{-3}$)**	**Young's modulus E (GPa)**	**Tensile strength σ (MPa)**	**Fracture toughness K_c (MPa $\sqrt{m}$)**	**Thermal conductivity K ($W\ m^{-1}\ K^{-1}$)**	**Thermal expansivity α ($10^{-6}\ K^{-1}$)**
Thermosetting resin (epoxy)	1.25	3.5	50	0.5	0.3	60
Engineering thermoplastic (nylon)	1.1	2.5	80	4	0.2	80
Rubber (polyurethane)	1.2	0.01	20	0.1	0.2	200
Metal (mild steel)	7.8	208	400	140	60	17
Construction ceramic (concrete)	2.4	40	20	0.2	2	12
Engineering ceramic (alumina)	3.9	380	500	4	25	8
General PMC (in-plane) (chopped strand mat)	1.8	20	300	40	8	20
MMC Al – 20% SiCp	2.8	90	500	15	140	18

Table 1.1: Overview of properties exhibited by different classes of material [1].

1.4. Materials used in Composites

The material consists of two contrasting phases, the resin and the fibres. The fibres possess excellent mechanical properties along their length, but cannot transmit forces to each other by shear, and have very small resistance to bending or buckling under compression. Advanced fibres such as Kevlar or Spectra are in fact used on their own for high performance tension cables, usually enclosed within a braided nylon or polypropylene sleeve.

The main function of the resin is to connect the fibres together so that the whole cross section of the composite can resist bending and shear loads. Moreover, the resin stabilises the fibres against individual buckling in compression. The fibres also inhibit the growth of cracks in the otherwise brittle resin. The resulting composite material is of much more practical use than either of its constituents.

Small fibres offer a structural advantage compared to the bulk material and this is because the strength of the material is governed partly by its purity and freedom from flaws. One way of improving these properties on a micro-scale is to produce the material as very fine fibres. Griffith was one of the first to discover that if the fibres were fine enough, then the tip energy of cracks started by the flaws was too low to enable the crack to propagate and hence enable the material to fail under load. In other words, the fibres' rapture strength decreases as their diameter increases and very small fibre diameters allow for effective radius of curvature in fibre bending to be on the order of half a millimetre. On a macro scale, in a laminated composite panel, crack propagation tends to be arrested by the fibres, so in general the fatigue properties of fibre composites are excellent.

However, the fibre properties are good only along their length. Transverse to the fibres, the properties of the material are dominated by the strength of the resin holding the fibres together. The transverse strength can be less than 10% of the aligned strength for carbon fibre reinforced composites. In order to improve these transverse properties, plies or fibres can be applied at 90° to the original basic lamina, but this of course degrades specific properties in the original direction. This composite is still

dependent on the resin for transmitting any in-plane shear forces applied to it. +-45° plies can be added, until the combination of all these plies leads to a 'quasi-isotropic' lay-up which has similar properties in all in-plane directions. The main disadvantage of this lay-up is that it will only have one third of the strength and stiffness in any direction compared to the equivalent unidirectional composite.

Many reinforcements are now available, some of which are designed for particular matrix systems. A selection of them is listed in Table 1.2. Typical properties of fibres are given in Table 1.3. All have high stiffness and relatively low density. Carbon, glass and aramid fibres are now used extensively in polymer matrix composites. Carbon fibres are also important for carbon/carbon composites. Ceramic fibres, whiskers and particles can be used to reinforce metal and ceramic matrices.

Form	Size (μm)		Fabrication route	Examples
	d	L		
Monofilaments (large-diameter single fibres)	100-150	∞	CVD onto core fibres (e.g. of C or W)	SiC (SCS-6™) Boron
Multifilaments (tows or woven rovings with up to 14000 fibres per strand)	7-30	∞	Precursor stretching; pyrolysing; melt spinning	Carbon (HS & HM) Glass Kevlar™ 49 Nicalon™
Short fibres (staple fibres aggregated into blankets, tapes, wool, etc.)	1-10	50-50000	Spinning of slurries or solutions, heat treatment	Saffil™ Kaowool Fiberfrax™
Whiskers (fine single crystals in loose aggregates)	0.1-1	5-100	Vapour phase growth/reaction	SiC Al_2O_3
Particulate (loose powder)	5-20	5-20	Steelmaking byproduct; refined ore; sol-gel processing, etc.	SiC Al_2O_3 B_4C TiB_2

Table 1.2: Some common types of reinforcement [1].

Fibre	Density ρ ($Mg\ m^{-3}$)	Young's modulus E (GPa)	Poisson's ratio ν	Tensile strength σ_* (GPa)	Failure strain ε_* (%)	Thermal expansivity α ($10^{-6}\ K^{-1}$)	Thermal conductivity K ($W\ m^{-1}\ K^{-1}$)
SiC monofilament	3.0	400	0.20	2.4	0.6	4.0	10
Boron monofilament	2.6	400	0.20	4.0	1.0	5.0	38
HM[a] carbon	1.95	Axial 380 Radial 12	0.20	2.4	0.6	Axial -0.7 Radial 10	Axial 105
HS[b] carbon	1.75	Axial 230 Radial 20	0.20	3.4	1.1	Axial -0.4 Radial 10	Axial 24
E glass	2.56	76	0.22	2.0	2.6	4.9	13
Nicalon™	2.6	190	0.20	2.0	1.0	6.5	10
Kevlar™ 49	1.45	Axial 130 Radial 10	0.35	3.0	2.3	Axial -6 Radial 54	Axial 0.04
FP™ fibre	3.9	380	0.26	2.0	0.5	8.5	8
Saffil™	3.4	300	0.26	2.0	0.7	7.0	5
SiC whisker	3.2	450	0.17	5.5	1.2	4.0	100
Cellulose (flax)	1.0	80	0.30	2.0	3.0	-	-

[a] High modulus

[b] High strength

Table 1.3: Typical properties for fibres used in composites [1].

1.4.1. Fibres

1.4.1.1. Carbon Fibres

Carbon fibres are generally produced by the oxidation and thermal pyrolysis of polyacrylonitrile (PAN), a polymer used in the creation of many synthetic materials. Like all polymers, polyacrylonitrile molecules are long chains, which are aligned in the process of drawing continuous filaments. When heated in the correct conditions, these chains bond side-to-side (letter polymers), resulting in the formation of narrow graphene sheets which eventually merge to form a single, jelly roll-shaped or round filament. The result is usually 93-95% carbon. Lower-quality fibre can be manufactured using pitch or rayon as the precursor instead of PAN. The carbon can become further enhanced, as high modulus, or high strength carbon, by heat treatment processes. Carbon heated in the range of 1500-2000 °C (carbonization) exhibits the highest tensile strength (5,650 MPa), while carbon fibre heated from 2500 to 3000 °C (graphitizing) exhibits a higher modulus of elasticity (531 GPa).

There are several categories of carbon fibres: standard modulus (240 GPa), intermediate modulus (300 GPa) and high modulus (>300 GPa). The tensile strength of different yarn types varies between 2000 and 7000 MPa. The density of carbon fibres is 1750 kg/m^3.

Precursors for carbon fibres are PAN, rayon and pitch. In the past, rayon was used more as a precursor and still is for certain specialized applications (rockets). Carbon fibre filament yarns are used in several processing techniques: the direct uses are for prepregging, pultrusion, braiding, weaving, filament winding.

These filaments are stranded into a yarn. Carbon fibre yarn is rated by the linear density (weight per unit length = 1g/1000 m = tex) or by number of filaments per yarn count, in thousands. For example 200 tex for 3K (3000 filaments) carbon fibre is 3 times as strong as 1K carbon fibre, but is also 3 times as heavy. This thread can then be used to weave carbon filament fabric or cloth. The appearance of this fabric generally depends on the linear density of the yarn and the weave chosen. Carbon

fibre is naturally a glossy black but recently coloured carbon fibre has become available.

1.4.1.2. Glass Fibres

Most glass fibres are based on silica (SiO_2), with additions of oxides of calcium, boron, sodium, iron and aluminium. These glasses are usually amorphous, although some crystallisation may occur after prolonged heating at high temperatures, leading to a reduction in strength. Typical compositions of three types of glass popular for composites are given in Table 1.4. The most widely used is E-glass (E for electrical). Its main advantages are that it draws well and has good strength, stiffness, electrical and weathering properties. In some other cases, C-glass (C for corrosion) is preferred, because of its better resistance to corrosion compared to E-glass. On the other hand its strength is lower. Finally, S-glass (S for strength) is more expensive than E-glass, but has a higher strength, Young's modulus and temperature resistance.

Glass fibres are produced by melting the raw materials (silicon and sodium carbonate and calcium carbonate; T>1000°C) in a reservoir and feeding them into a series of platinum bushings, each of which has several hundred holes in its base. Forced by gravity, the glass flows and fine filaments are drawn mechanically downwards as the glass extrudes from the holes. The fibres are wound onto a drum at speeds of several thousand metres per minute. The fibre diameter can be controlled by adjusting the head of the glass in the tank, the diameter of the holes, the viscosity of the glass (depending on composition and temperature) and the winding speed. The diameters of E-glass fibres range between 8 and 15 μm.

The atomic structure is used to determine important mechanical properties such as the strength and modulus. Silica-based glasses consist primarily of covalently bonded tetrahedral, with silicon at the centre and oxygen at the corners. The oxygen atoms are shared between tetrahedral, leading to a rigid three-dimensional network. The presence of elements with low valency, such as Ca, Na and K, tends to break up this network by forming ionic bonds with oxygen atoms, which then no longer bond the

tetrahedral together. As a result, the addition of such elements tends to lower the stiffness and strength. On the other hand, formability is improved. Compared to carbon fibres, the properties of glass fibres are isotropic. Thus, the axial and transverse Young's moduli are the same. The strength depends on processing conditions and test environment. Freshly drawn E-glass fibres have a strength of 3.5 GPa, provided they are handled very carefully to avoid surface damage. In addition, the variability in strength is small. Environmental conditions such as humid air lead to a reduction in strength. This is due to the absorption of water on the surface. A sharper decrease in strength can occur if the surface is exposed to mineral acids.

	E-glass	**C-glass**	**S-glass**
Composition (weight %)			
SiO_2	52.4	64.4	64.4
$Al_2O_3 + Fe_2O_3$	14.4	4.1	25.0
CaO	17.2	13.4	-
MgO	4.6	3.3	10.3
$Na_2O + K_2O$	0.8	9.6	0.3
B_2O_3	10.6	4.7	-
BaO	-	0.9	-
Properties			
ρ (Mg m^{-3})	2.60	2.49	2.48
K (W m^{-1} K^{-1})	13	13	13
α (10^{-6} K^{-1})	4.9	7.2	5.6
σ_* (GPa)	3.45	3.30	4.60
E (GPa)	76.0	69.0	85.5
T_{max} °C	550	600	650

Table 1.4: Glass fibre compositions and properties [1].

1.4.1.3. Organic Fibres

The most important high modulus polymer fibres have been developed from aromatic polyamides and are called aramid fibres. These were first developed by Du Pont de Nemours (USA) with the trade name Kevlar. The principles involved are best understood by considering fibres based on a simple polymer, polyethylene. Chain-extended polyethylene single crystals consist of straight zig-zag backbone chains, fully aligned and closely packed. These have a Young's modulus of about 220 GPa parallel to the chain axis. By drawing and stretching, fairly good chain alignment can be achieved and a modulus of 70 GPa has been achieved. Comparatively, in the case of carbon fibres, the modulus normal to the fibre axis is much less than that along the fibre axis.

There is a wide range of natural organic fibres which are potentially useful as reinforcements. The most common natural fibre is cellulose which is formed by the polymerisation of glucose molecules. The most common natural composite is timber and this is essentially composed of crystalline cellulose fibres in a matrix of amorphous or partially crystalline hemi-cellulose and lignin. The properties of cellulose fibres compare fairly well with those of many artificial fibres, especially when density is important. The current production of composites based on such fibres is very limited but may increase in the future.

1.4.2. The Strength of Reinforcements

Information on the tensile strengths of fibres is given in Tables 1.3 and 1.4. A number of factors should be taken into consideration when quoting tensile strength figures.

1.4.2.1. Thermal Stability

In the absence of air and other oxidising environments, carbon fibres possess exceptionally good high-temperature properties. Carbon fibres retain their superior properties to well above 2000 °C. This property is of no use for applications involving polymer matrices since most of them cannot withstand temperatures more than 200 °C. Moreover, carbon fibres have not been excessively employed for metal matrix composites, since they tend to react chemically during fabrication. On the other hand, in carbon/carbon composites, the high-temperature capability is fully exploited, provided the composite is isolated from oxidising environments. In the presence of oxygen, carbon fibres rapidly degenerate at elevated temperatures.

Bulk silica-based glasses have softening temperatures around 850 °C, although the strength and modulus of E-glass decrease rapidly above 250 °C. This is not usually a problem for polymer composites, but it eliminates glass fibres from use in any inorganic composites. Although the thermal stability of aramid fibres is inferior to both glass and carbon, it is again adequate in most cases where polymer matrix systems are used. It is essential that apart from retaining the properties during service at elevated temperatures, they don't deteriorate during manufacturing operations. In the case of glass, the properties are reversible with temperature. On the other hand, aramid fibres suffer irreversible deterioration which is due to changes in internal structure. Care must be taken that the heating during curing of thermosetting resins and in melt processing of thermoplastics does not degrade the properties of fibres such as Kevlar.

Oxide, nitride and carbide ceramics have very high melting points. Such fibres retain their properties to high temperatures, providing there are no adverse reactions with the matrix material, either during processing or in service. A lot of research on the need to protect fibres under these conditions is taking place and a variety of coating treatments have been developed. In addition to temperature and oxidation effects, aramid fibres are prone to photo-degradation on exposure to sunlight. Both visible and ultraviolet light have an effect to discoloration and reduction of mechanical

properties. In order to avoid the degradation, coating the surface of the composite material with a light-absorbing layer is essential.

1.4.2.2. Compressive Strength

As can be seen from Table 1.3, no reference is made regarding the axial compressive strength of fibres. This is because of the difficulty in measuring this property and is best inferred from the behaviour of composites fabricated with the fibres. The axial compressive strength of unidirectional composites is controlled by the buckling modes of the fibres. This is in contrast to the tensile strength, which is dependent primarily on the tensile strength of the fibres. Under compressive loads, failure may occur in several different modes. These include crushing or shearing, one of the most likely modes being Euler buckling of individual fibres. This type of buckling occurs when a rod under compression becomes stable against lateral movement of the central region. The applied stress for the onset of buckling, in the case of a cylindrical rod is given by the following equation:

$$\sigma^*_b = \frac{\pi^2 E}{16}\left(\frac{d}{L}\right)^2$$

where E is the Young's modulus, d is the diameter and L is the length of the rod. Buckling will be favoured when the rod has a high aspect ratio (L/d). The buckling of fibres in a composite is more difficult to predict since some lateral stabilisation is provided by the matrix, even when it has a relatively low stiffness. It should be stressed that, for compressive loading of a composite specimen, large-diameter fibres will tend to exhibit greater resistance to local buckling and this is will often increase the resistance to macroscopic failure.

Apart from the fibre diameter, the compressive strength is influenced by the fibre structure. For example, the axial compressive strength of a unidirectional lamina made from Kevlar fibres is only 20% of its tensile strength, whereas for carbon and

glass (which have similar diameters), the strengths are approximately equal in tension and compression. And this is attributed to the structure of the aramid fibre. In compression, elastic deformation (of the strong covalent bonds) only occurs to a limited degree before the weak van der Waals forces between the adjacent molecules are overcome and local fibrillation and damage occur. This leads to buckling and kink formation at low applied loads.

1.4.2.3. Fibre Fracture and Flexibility

In tension, most fibres tend to fracture in a brittle manner, without any yield or flow. Carbon, glass and ceramic fibres are almost completely brittle and fracture without any reduction in cross-sectional area. In contrast, aramid fibres fracture in a ductile manner, although the overall strain to failure is still small.

The diameter of the fibres has a large effect on the ease with which they can be deformed and bent. This is important in operations where fibres are fed through eyes and over bobbins, as in weaving, knitting and filament winding. The same is true of moulding and mixing operations where fibres are intimately mixed and subsequently extruded or injection moulded using screw-fed machines. The flexibility of a fibre can be expressed in terms of the moment, M, required to bend a fibre with a circular cross-section to a given curvature, κ, (the reciprocal of the radius curvature)

$$M = \frac{\pi E \kappa d^4}{64}$$

where E is the Young's modulus and d is the fibre diameter. The flexibility, defined as κ/M, is dominated by d but also depends on E. A comparison of the flexibilities of carbon, glass, aramid and ceramic fibres is given in Table 1.5.

Bending of fibres results in high surface tensile stresses, which can lead to fibre fracture. Assuming elastic deformation, the surface tensile stress is given by:

$$\sigma = \frac{E\kappa d}{2}$$

For a fibre with a given fracture strength, σ^*, there will be a maximum curvature which the fibres can sustain before fracture occurs, given by:

$$\kappa_{max} = \frac{2\sigma^*}{Ed}$$

Values of κ_{max} are given in Table 1.5, neglecting any statistical variation in fracture strength along the fibre. Glass fibres are much more tolerant of bending than carbon or ceramic fibres. Large-diameter monofilaments are very difficult to weave or form in any way, since they tend to break at a radius of curvature around 10 mm. Staple fibres and whiskers on the other hand, are very unlikely to be broken by normal handling operations. As far as aramid fibres are concerned, bending produces high surface compressive and tensile stresses. As a result, the compressive region of the fibre undergoes yielding by the development of deformation bands, resulting in a permanent deformation. This happens long before the bending curvature is sufficient to cause tensile failure.

Fibre	Diameter d (μm)	Young's modulus E (GPa)	Flexibility k/M (GPa^{-1} mm^{-4})	Fracture strength σ_* (GPa)	Maximum curvature K_{max} (mm^{-1})
SiC monofilament	150	400	1×10^2	2.4	0.08
Nicalon™	15	190	2.1×10^6	2.0	1.4
Kevlar™ 49	12	130	7.6×10^6	3.0	3.8
E-glass	11	76	1.8×10^7	2.0	4.8
HM carbon	8	390	1.3×10^7	2.2	1.4
HS carbon	8	250	2.0×10^7	2.7	2.7
Saffil™	3	300	8.4×10^8	2.5	5.5
SiC whisker	1	450	4.5×10^{10}	5.0	22.2

Table 1.5: Mechanical properties for various types of fibres [1].

1.4.3. Matrices

The properties exhibited by various types of matrix are represented in Table 1.6. By combining this information with other data for reinforcements, the potential systems can be immediately selected. For example, it is evident that glass wouldn't be appropriate for the reinforcement of metals if improved stiffness is what we are after. At this point, it should be noted that one of the most important factors during the selection process is the ease of manufacture.

Matrix	Density ρ ($Mg\ m^{-3}$)	Young's modulus E (GPa)	Tensile strength σ_* (GPa)	Failure strain ε_* (%)
Thermosets				
Epoxy resins	1.1-1.4	3-6	0.035-0.1	1-6
Polyesters	1.2-1.5	2.0-4.5	0.04-0.09	2
Thermoplastics				
Nylon 6,6	1.14	1.4-2.8	0.06-0.07	40-80
Polypropylene	0.90	1.0-1.4	0.02-0.04	300
PEEK	1.26-1.32	3.6	0.17	50
Metals				
Al	2.70	70	0.2-0.6	6-20
Mg	1.80	45	0.1-0.3	3-10
Ti	4.5	110	0.3-1.0	4-12
Ceramics				
Borosilicate glass	2.3	64	0.10	0.2
SiC	3.4	400	0.40	0.1
Al_2O_3	3.8	380	0.50	0.1

Table 1.6: Selected properties for different types of matrix [1].

1.4.3.1. Polymer Matrices

i. Thermosetting Resins

The most commonly used resins are epoxy, unsaturated polyester and vinyl ester. These cover a very broad class of chemicals and a wide range of physical and mechanical properties can be obtained. In thermosetting polymers, the liquid resin is converted into a hard rigid solid and infusible state by chemical cross-linking, which

leads to the formation of a tightly bound three-dimensional network. This is usually done while the composite is being formed. The mechanical properties depend on the molecular units making up the network, as well as the length and density of the cross-links. Initial chemicals used affect the first factor, whereas the latter depends on the control of the cross-linking processes in the cure. A cure schedule is commonly used, involving heating at one or more temperatures for predetermined times to achieve optimum cross-linking and hence optimum properties. However, curing can also be achieved at room temperature. Final post-cure treatment is often given at relatively high temperature in order to minimise any further cure and change in properties during service. It is important to avoid shrinkage during cure and thermal contraction on cooling after cure, which can lead to residual stresses in the composite.

Thermosets offer different properties than thermoplastics, such as much lower strains to failure. Thermosets are essentially brittle materials, while thermoplastics can undergo appreciable plastic deformation. However, there are also significant differences between different types of thermosets. For example, epoxies are in general tougher than unsaturated polyesters or vinyl esters, particularly in the case of recent advanced epoxy formulations. Additionally, epoxies frequently offer a high resistance to distortion and also exhibit less shrinkage than polyesters. Another significant advantage of epoxies is the fact that they can be partially cured, so that they can be supplied in the form of pre-pregs. Epoxies are generally superior in most respects to other thermosetting systems, although the latter are frequently preferred due to their lower cost.

ii. Thermoplastics

A thermoplastic is a material that is plastic (the material can undergo a non-reversible change of shape in response to an applied force) or deformable, melts to a liquid when heated and freezes to a brittle, glassy state when cooled sufficiently. Most thermoplastics are high molecular weight polymers whose chains associate through weak van der Waals forces (polyethylene); stronger dipole-dipole interactions and hydrogen bonding (nylon); or even stacking of aromatic rings (polystyrene).

Thermoplastics differ from thermosetting polymers such as Bakelite and vulcanized rubber, which once formed and cured can never be re-melted and re-molded.

The main advantages of advanced thermoplastics developed fairly recently for use in composites are the ability to withstand high failure strains, as well as the good resistance to attack by chemicals. Moreover, they generally exhibit good thermal stability. Another important characteristic of thermoplastics is that they yield and undergo large deformations before finally fracturing and their mechanical properties are strongly dependent on the temperature and applied strain rate. Furthermore, under constant load conditions the strain tends to increase with time, leading to a redistribution of the load between matrix and fibres during deformation and under in-service loading conditions.

One of the significant features of thermoplastic composites is that processing tends to be more difficult than with thermosets. This is mainly because they are already polymeric, and hence highly viscous even when liquid, before the composite is fabricated. Although their transition and melting temperatures, T_g and T_m, are in many cases quite low, the melts they produce have high viscosities and cannot easily be impregnated into fine arrays of fibres. As a result, it is vital to ensure that flow distances are short, for example by interleaving thin polymer sheets with fibre performs, and to apply substantial pressures for appreciable times. Once fibre and matrix have been brought together in some way, then various shaping operations, such as injection moulding can be carried out.

1.4.3.2. Metal Matrices

Three metals are mainly used for the development of metal matrix composites, these being aluminium, magnesium and titanium. Metals are normally alloyed with other elements to improve their physical and mechanical properties and a wide range of alloy compositions is available. Final properties are depend greatly on the thermal and mechanical treatments which determine the microstructure. Some typical properties of common metal matrices are given in Table 1.6. Usually, the main characteristics of

the metals used for composites are ductility and isotropy. Unlike polymers, the increases in stiffness achieved by incorporating the reinforcement are often relatively small. However, important improvements are often achieved in properties such as wear characteristics, creep performance and resistance to thermal distortion. All three metals are very reactive, with strong affinity for oxygen. This has implications for the production of composites, particularly regarding to chemical reactions at the interface between the matrix and the reinforcement, which has proved especially troublesome for titanium.

1.4.3.3. Ceramic Matrices

There are four main classes of ceramic that have been in use in ceramic matrix composites. Glass ceramics are complex glass-forming oxides, such as borosilicates and aluminosilicates which have been heat-treated so that a crystalline phase precipicates to form a fine dispersion in the glassy phase. Glass ceramics have lower softening temperatures than crystalline ceramics and are easier to fabricate, which is an especially important consideration for ceramic composites. Conventional ceramics, such as SiC, Si_3N_4, Al_2O_3 and ZrO_2 are fully crystalline and have the normal structure of crystalline grains randomly oriented relative to each other.

By adding ceramic fibres to ceramics (or generating interfaces in some other way), improved toughness can be achieved. Ceramics are very brittle and as a result, a small increase in toughness may be advantageous. Usually the toughness increase derives from repeated crack deflection at interfaces and the nature of the interface assumes overriding importance.

1.4.4. Nanocomposites

Mineral fillers, metals, and fibres have been added to thermoplastics and thermosets for decades to form composites. Compared to neat resins, these composites have a

number of improved properties including tensile strength, heat distortion temperature, and modulus. As a result, for structural applications, composites have become very popular and are sold in billion pound quantities. These filled thermoplastics are sold in even larger volumes than neat thermoplastics. Additionally, the volume of fillers sold is roughly equal to the volume of thermoplastic resin sold. Clearly, the idea of adding fillers to thermoplastic and thermosetting matrices to improve properties, and in some cases decrease costs, has been very successful for many years.

Lately, with advances in synthetic techniques and the ability to readily characterize materials on an atomic scale has lead to interest in nanometer-size materials. Since nanometer-size grains, fibres and plates have dramatically increased surface area compared to their conventional-size materials, the chemistry of these nanosized materials is altered compared to conventional materials.

Polymer nanocomposites combine these two concepts, composites and nanometer-size materials. In principle, nanocomposites are an extreme case of composites in which interface interactions between two phases are maximised. Because the remarkable properties of conventional composites are mainly due to interface interactions, the modified materials can lead to interesting results. Many exciting new materials with novel properties can be obtained by combining the parent properties into one single material. If a suitable combination is made, it is even possible for new properties to be discovered that are unknown in the parent constituent materials. Thermoplastics filled with nanometer-size materials have different properties than thermoplastics filled with conventional materials. Some of the properties of nanocomposites, such as increased tensile strength, may be achieved by using higher conventional filler loading at the expense of increased weight and decreased gloss. Other properties of nanocomposites such as clarity or improved barrier properties cannot be duplicated by filled resins at any loading.

Polymer nanocomposites were developed in the late 1980s in both commercial research organizations and academic laboratories. The first company to commercialize these nanocomposites was Toyota, which used nanocomposite parts in one of its popular car models for several years. Following Toyota's lead, a number of other companies also began investigating nanocomposites.

Most commercial interest in nanocomposites has focused on thermoplastics. Thermoplastics can be broken into two groups: less expensive commodity resins and more expensive (and higher performance) engineering resins. One of the goals of nanocomposites was to allow substitution of more expensive engineering resins with a less expensive commodity resin nanocomposite. Substituting a nanocomposite commodity resin with equivalent performance as a more expensive engineering resin should yield overall cost savings. It should be said that there has been less commercial interest in thermoset nanocomposites compared to thermoplastics. This situation is expected to change as thermoset nanocomposites have some distinct advantages over neat thermoset resins.

1.5. Design of Composite Materials

The choice of the composition and structure of a composite material for a particular application is not a simple matter, since the introduction of reinforcement into a matrix alters all the properties of the resulting material. Possible changes in the microstructure of the matrix resulting from the presence of the reinforcement should also be taken into consideration. The generation of residual stresses from differential thermal contraction during manufacture may also be significant. Property maps provide a broad view of the property combinations obtainable from different composite systems. An example can be viewed in Figure 1.1, showing a plot of Young's modulus, E, against density, ρ. A particular material (or type of material) is associated with a point or a region. This is a convenient method of comparing the property combinations offered by potential matrices and comparing the property combinations offered by potential matrices and reinforcements with those of alternative conventional materials.

Attractive matrix/reinforcement combinations can be identified by deriving a 'merit index' for the performance required, in the form of a specified combination of properties. Once this has been done, appropriate models can be used to place upper

and lower bounds on the composite properties involved in the merit index, for a given volume fraction of reinforcement.

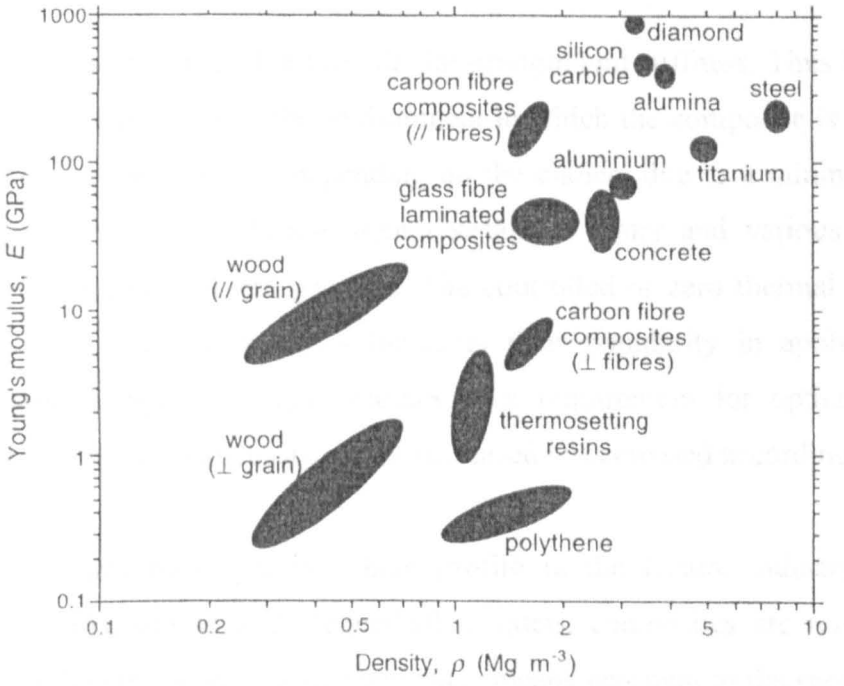

Figure 1.1: Data for some engineering materials in the form of areas on a map of Young's modulus E against density ρ [1].

1.6. Advantages of Composite Materials

The advantages of composites have seen a substantial increase in their use since their development in the 1960s. More applications are being utilised as composites are being tailored for different uses.

It should be pointed that the main advantage of composite materials and the fundamental reason why composites are gaining increasing use in structural applications is their high specific strength. In transport applications, a substantial reduction in weight gives a corresponding increase in performance. This property leads to boat, automobile, aircraft design enhancement. An advantage relevant to structural load bearing applications inherent in directional composites is that the

material can be tailored so the dominant strength or stiffness is in the load direction. Composite materials can also have good impact resistance although this form of dynamic loading is still a serious problem for many composites.

The matrix protects the fibres that provide the strength and stiffness. Thus the matrix can be chosen to be resistant to the environment in which the composite is operating. This can lead to longer part life depending on the choice, due to a minimisation of corrosion. Composite materials are often resistant to water and various industrial chemicals such as crude oil and gasoline. The controlled or zero thermal expansion characteristics of certain composites increases their popularity in applications in spacecrafts where high positional accuracy is a requirement for optical sensors. Thermal and electrical conductivity can be increased or decreased accordingly.

Composite materials have gained a high profile in the leisure industry. In high performance tennis, squash and racquetball racquets, composites are now the sole materials used. Inherent damping in composites means less pain to the sportsman and less fatigue. The tailorability of bending and twisting response and lightweight nature allows effective fabrication of golf shafts and fishing rods. The high specific stiffness of composites can be beneficial to applications such as skis, hockey sticks, surfboards, canoes, and diving boards.

1.6.1. Advantages of Fibrous Composites in the Aerospace Industry

The reasons for using fibrous composites (carbon, boron, aramid, or glass in organic matrices) in preference to metal alloys include the following:

- A lower density, which saves weight, particularly for minimum-gauge structures.

- Higher specific strengths, which sometimes but not always lead to lighter structures. (Large weight savings are easy to achieve in unrepairable structures or those which are used only once). The challenge is to overcome the inherent

brittleness of composite materials and achieve respectable weight savings for long-life structures, without giving up damage tolerance and repairability).

- The ability to tailor laminate patterns to achieve desired stiffness. (This feature is greatly overrated because of unstated limitations on the validity of customary laminate theories).

- Lower manufacturing costs in some cases, particularly with the use of integral stiffening, although such a policy can be detrimental to in-service maintenance and repair. It can also lead to much weaker structures with hidden internal wrinkles, so it must be used with discretion. Lower costs can also be obtained by replacing lightly loaded riveted metal structures with adhesively bonded composite ones.

- The virtual elimination of corrosion, a vital concern to naval aircraft, and/or crack growth due to mechanical fatigue.

- The ability to manufacture dimensionally stable components having the zero coefficient of expansion which is needed for many space structures and antennae.

- Improved surface finish and the ability to make lower drag shapes more easily than with metal.

- Lower equipment cost when establishing a new manufacturing facility.

- The opportunity to improve an original design during the process of changing the material under circumstances in which no permission would be granted to improve the design in conventional metal alloys. (Conversely, there have been cases where good metal designs have been replaced by inferior composite ones).

- The very significant enhancement of sales appeal by claiming that the product is 'high-tech'.

- Increased sales of the product via offset manufacture of components, or financial assistance to launch new programs in exchange for the right to manufacture components.

A typical example of the use of composites is the case of the vertical stabilizer in the Airbus A-310-300. The distribution of mass of composites is as follows:

- Facings in carbon/epoxy: 30% of total mass
- Honeycombs, adhesives: 35% of total mass
- Attachments: 25% of total mass
- Connections between carbon/epoxy components and attachments: overlayers of carbon/epoxy
- Allowance for the aging of the carbon/epoxy: overdimensions of the facings (the stresses are magnified about 10% more for subsonic aircraft and 13% for supersonic aircraft

In consequence, the overall gain of mass in comparison with a classical metallic construction for the vertical stabilizer is about 15-20%. An Airbus A-310 has a total mass of 180 tons, of which 6.2 tons is composites. By using 1.1 tons of high performance composites, the designers were able to reduce the mass of the structure by 1.4 tons. Figure 1.2 shows the composite components in the aforementioned aircraft:

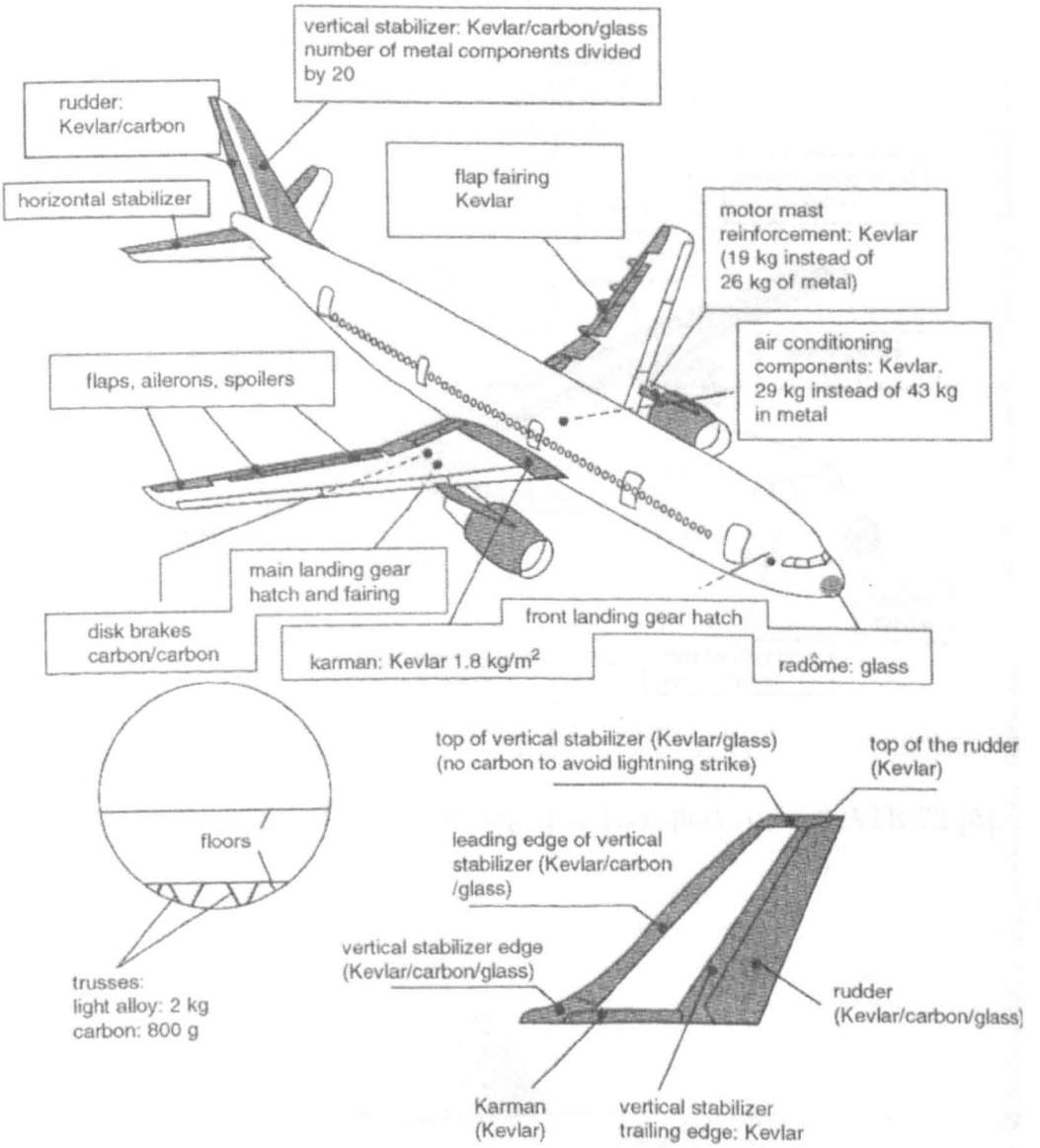

Figure 1.2: Composite components in an Airbus A-310 [4].

In regional jets such as the ATR 72, composites represent more than the 25% of the mass of the structure (total mass: 20 tons), as shown in Figure 1.3. In the business aircraft Falcon 10, long sections of the main structure like the wing box are made of composites, Figure 1.4.

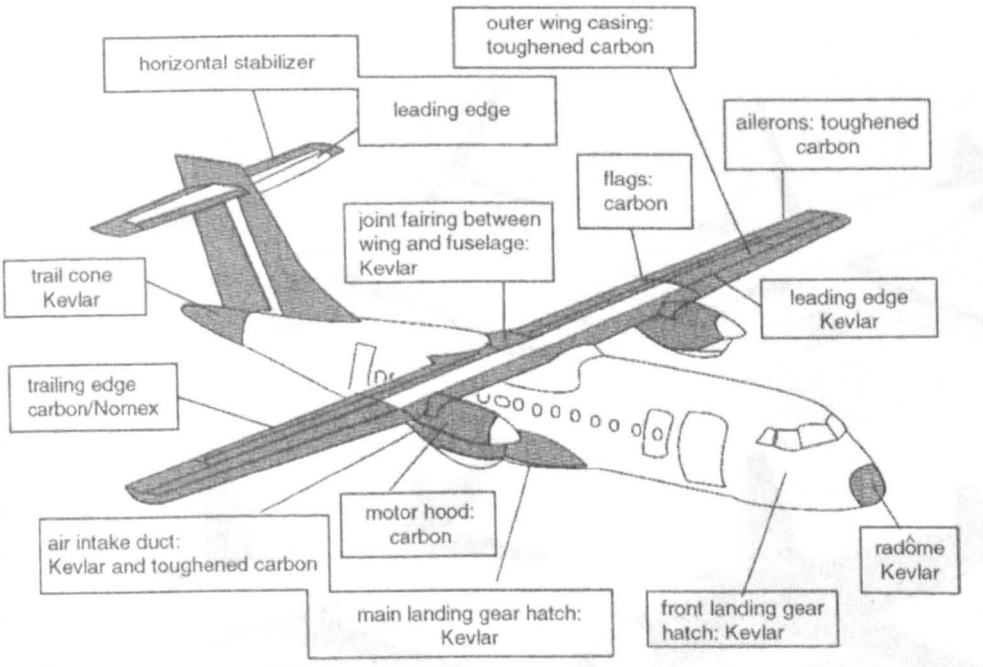

Figure 1.3: Composite components in the Regional Transport Aircraft ATR 72 [4].

Figure 1.4: The Business Aircraft Falcon 10 [4].

Such are the advantages from the use of composites in the aerospace industry, that the trend nowadays is moving towards these materials in large transport aircraft, as can be seen in Figure 1.5.

Figure 1.5: The Progressive Use of Composites on Commercial Transport Aircraft – each sketch represents roughly 10 years of development [11].

A typical example of this new generation of aircraft where high performance composites are the main type of material used in the structure, is the Beech Starship aircraft. Whole sections such as the wings and fuselage are made of composites and the engineers were able to achieve a total reduction of 35-40% in mass compared to

the metallic counterpart. 70% of the mass of the structure is composite. In conclusion, it is easily understood that composites are the future of the aerospace industry.

1.7. Forming of Composite Structures

It would be very wasteful in most circumstances to produce blocks of composite and then machine it to shape, as machining would interrupt the load carrying fibres. Sometimes this is done but only for small parts such as tufnol gears and cams, now largely superseded by injection mouldings. The most versatile method of producing composite structures is always some kind of moulding process. This 'mouldability' of the material is one of its greatest assets. Injecting the whole composite material into a closed mould is only practicable for very short fibres making up to 5% of the volume. For longer fibres and higher volume fractions, the fibres first have to be aligned in the mould in desired orientations and consolidated with resin. The moulding of the fibres along the contours of the mould confers strength in the plane of the mould surface where it is usually needed. As a result, it is always very important to orientate the fibres in the direction of loading.

It is often advantageous to use composites for structures where weight, stiffness or fatigue are of critical importance and have one primary axis of loading. These applications are somewhat limited, but probably the classic example of this is in helicopter rotor blades, where composite blades last four to five times the life of aluminium ones, are lighter and aerodynamically smoother. Other examples are in vehicle leaf springs, glider spars, fishing rods and skis.

Applications which demand multi-axial in-plane stiffness can only show a weight advantage over aluminium in advanced materials such as carbon, Kevlar or Spectra fibre composites. However, the consequences of the composites mouldability make them much more attractive than by simple material property comparisons.

When significantly three-dimensional stress fields exist in a component, especially with multiple load cases, composites cannot usually compete with isotropic materials

such as metals. This is the reason why local pickups in composite structures are often metal fittings. Sometimes, short-form fibre reinforcements can be used to improve the properties of injection-moulded thermoplastic components; glass-filled nylon is one example. This short-fibre usage is one possible way of recycling expensive composite materials.

The mouldability of the materials is fundamental and far reaching. The structure can be moulded to shapes impossible or uneconomic to produce any other way. Smooth, compound curved aero or hydrodynamic form can be readily created. Composite structures can also be co-moulded together to form co-cured structures, so that assembly costs can be greatly reduced. Other materials, such as sandwich honeycomb cores, can be incorporated into the moulding. Varying thicknesses and ply orientations can be incorporated to optimise the structural properties.

1.8. Disadvantages of Composite Materials

Composites are now used more and more, but have not yet realized what was expected of them. Some of this is due to failure to appreciate that enhanced properties along the length of the fibres are associated with greatly degraded properties transverse to that direction. And, even though cross-plying can alleviate that loss in the plane of the composite laminate, interlaminar weaknesses remain. It is therefore important to evaluate potential applications of advanced composites in the way they are to be used and not in terms of the relative merits of test coupons alone.

A major barrier to the more widespread use of advanced composite structures results from a general misunderstanding about the laminate strength prediction theories in regard to the stresses in the matrix. Far from becoming more efficient as the laminate patterns become more orthotropic and less isotropic, as most theories would suggest, the more highly orthotropic components have been found to suffer from widespread splitting and delaminations, with an associated loss of strength. Thus, a supposed major advantage of composites, the ability to tailor the fibre orientations instead of

having to accept isotropic properties, is often more of a liability than an improvement over what Mother Nature could do.

However, the greatest obstacles to using composites wisely are not technical at all. One is a widespread unshakeable belief that destiny requires composites to replace all metal structures. Another is the belief that composites must be superior to metal because they are newer.

But the greatest consideration in the manufacture of most structures is whether it is economically viable to use composites, as the costs of raw materials and fabrication are high. Re-use and disposal of composite materials can also be difficult, as they can't be simply melted down and recycled, especially when thermosetting matrices have been used. Re-use involving separating the matrix from the reinforcement can be difficult and is usually achieved by solvent extraction or thermal degradation. Some new techniques enable the recovery of the matrix using heat cleaning, re-polymerisation and reversible crosslinking. Other applications include mechanical granulation and milling to produce fillers and incineration and pyrolysis can enable the material to be used as fuel.

1.9. Applications of Composites

Composite materials are used in a very wide range of industrial applications, including the aerospace, marine, automotive, insulation and civil engineering sectors, as well as the sport equipment industry. Some examples are given, covering a range of composite type, engineering complexity, manufacturing route, market size and competitive position relative to conventional materials. A list of the requirements of each application is given to justify the use of composites [1].

Sheet processing rolls

- High beam stiffness (Young's modulus)
- High torsional stiffness (shear modulus)
- Low density
- Good thermal stability
- Good surface finish

Helicopter rotor blade

- High beam stiffness (Young's modulus)
- High torsional stiffness (shear modulus)
- Low density
- Good fatigue resistance

Golf driving club

- High beam stiffness (Young's modulus)
- High torsional stiffness (shear modulus)
- Low density
- High strength

Racing bicycle

- High stiffness
- Good fatigue resistance
- Low density

Diesel engine piston

- Good wear resistance
- High thermal stability
- High temperature strength
- Good thermal stability

Microelectronics housing

- Thermal expansion matched
- Low density
- High thermal conductivity
- Electrically conducting

Gas turbine combustor can

- High-temperature strength
- Good thermal shock resistance
- Low density
- Good oxidation resistance
- Stable up to 1450 °C

Aircraft brakes

- Good thermal stability and thermal shock resistance
- Low density
- Good strength at high temperature
- High thermal capacity
- High thermal conductivity
- Good frictional characteristics
- Good wear resistance

1.10. Project Objectives

Fibre reinforced composite materials are susceptible to delamination due to out of plane and shear loads, resulting in a reduction in structural integrity and reduced service lifetime. Extensive research has been carried out regarding Mode I (interlaminar tension) and Mode II (interlaminar sliding shear) types of loading in cracked structural laminates. In the light of the limited research carried out on Mode III (interlaminar scissoring shear), the principal objective of this study is to investigate

the Mode III fracture properties of high performance composites based on both thermoplastic and thermosetting matrices, adhesive joints and bi-material samples, similar to those used in the aerospace industry.

The project involves a detailed finite element analysis of the current ECT geometry in order to characterise the response of the ECT geometry for evaluating the Mode III response of composites. The Mode III geometry will then be modified to look at mixed-mode failure involving Mode III contributions. The project uses the Virtual Crack Closure Integral to characterise the loading conditions at the crack tip in these samples. Once the quasi-static response of the composites has been analysed, dynamic tests will undertaken using a newly-developed modified ECT test geometry in order to investigate the rate-sensitive behaviour of these high-performance materials. It is expected that the results of this research programme will lead to a greater understanding of the behaviour of composites under in-service conditions.

1.11. References

[1]. Hull D. and Clyne T.W., An Introduction to Composite Materials, Cambridge University Press, 1996.

[2]. Marshall A., Handbook of Composites, Ed. Lubin G., Von Nostrand Reinhold, 1982.

[3]. Jansson J., Olsson K.A. and Sorelius S.E., Fibre Reinforced Plastics 1, Swedish Tech Books, 1979.

[4]. Callister W.D., Materials Science and Engineering an Introduction, Seventh Edition, Wiley, 2007.

[5]. Richardson M.O.W., Polymer Engineering Composites, Applied Science Publishers LTD, London, 1977.

[6]. Richardson M.O.W., Ferreira J.A.M., Costa J.D.M., Reis P.N.B., Analysis of fatigue and damage in glass fibre reinforced polypropylene composite materials, Composites Science and Technology, Vol.59, 1999, p.1461.

[7]. Gay D., Hoa V. S., Tsai W., Composite Materials, Design and Applications, CRC Press, 2002.

[8]. Evans P.C., Holliday L., Composite Materials, Elsevier Publishing Company, 1966.

[9]. Tsai H., Introduction to Composite Materials, CRC Press, 1980.

[10]. Chawla K.K., Composite Materials: Science and Engineering, Springer, 2004.

[11]. Golam M., Advances in Thermoplastic Matrix Composite Materials, Newaz 1989.

[12]. Cole J.M., Bertholet J.M., Composite Materials: Mechanical Behavior and Structural Analysis, Technology Press 1999.

[13]. Eckold G., Design and Manufacture of Composite Structures, Woodhead Publishing Limited, 1988.

[14]. Michele M., Aerospace Vehicle Design, Fibre Reinforced Plastics, Cranfield University, 2004.

2. Literature Review

2.1. Introduction

High performance composite materials are finding widespread use in a variety of load-bearing aerospace applications. Fibre reinforced composites offer many distinct advantages over their metallic counterparts, including their excellent fatigue resistance combined with very high values of specific strength and stiffness.

Many composite components in aerospace structures are made of flat or curved panels with co-cured or adhesively-bonded frames and stiffeners. One of the most common failure modes is delamination. The remote loading applied to composite components is typically resolved into interlaminar tension and shear stress at discontinuities that create mixed Mode I, II and III delaminations. As a result, delamination in fibre-reinforced composites has been a subject of intensive research for many years. This mode of failure is especially insidious as it may easily escape detection since the delaminations are frequently embedded within the composite structure. They may arise out of low-velocity impact damage, manufacturing defects, lightning and even bird strikes. However, the effect they have on the structure may include a dramatic reduction of compressive residual strength of up to 60%. The behaviour of delaminations is influenced by specific issues such as crack jumping, matrix cracking, laminate lay-up sequence, friction and contact, thermal residual stresses, dynamic events and multiple delaminations. There is a connection between many of these effects and therefore, research is still needed in order to resolve some outstanding issues. These issues are particularly relevant to the analysis and modelling of

delaminations in more realistic composite structures. As a result, the analysis of delaminations has depended heavily on computational methods and particularly the finite element method. Additionally, recent efficient formulations that more accurately capture the mechanics near the delamination front are now available. These numerical tools, combined with well-designed experiments, should greatly enhance our understanding of delamination behaviour in composites.

This chapter discusses the various studies that have been conducted to investigate the Mode I, II and III delamination behaviour of composites. Initially, the test techniques that have been developed to simulate the three different types of delamination and to assess their suitability for determining the Mode I, II and III strain energy release rates, are discussed. The effects of lay-up, loading rate and crack length, as well as the presence of adhesive around the crack area on the Mode I, II and III fracture toughness are reviewed.

Finally, the virtual crack closure technique (VCCT), a method used to compute the strain energy release rate, is presented. The history and development of the technique are reviewed in this chapter

2.2. Overview of Delamination Fracture in Composites

Although delamination fracture has been one of the main reasons for developing standard interlaminar fracture test methods, it is not the only one. A second reason is that damage tolerance has been a major concern in the aerospace industry. The allowable damage which a composite structure can incur is a key parameter in determining the safety of the aircraft. A third reason has been the perceived need for determining values of G_c, the critical strain energy release rate, for structural calculations. Given that delamination is a common failure mode in these materials, it seems reasonable to expect that if mixed-mode failure envelopes were available, they could be usefully included in design procedures. While there have been some cases where such an approach has been used, in general, designers do not apply fracture mechanics criteria in the design of structures.

Interlaminar fracture mechanics have proven useful for characterizing the onset and growth of delaminations. The total strain energy release rate, G_T, the Mode I component due to interlaminar tension, G_I, the Mode II component due to interlaminar sliding shear, G_{II}, and the Mode III component, G_{III}, due to interlaminar scissoring shear, as shown in Figure 2.1, need to be calculated.

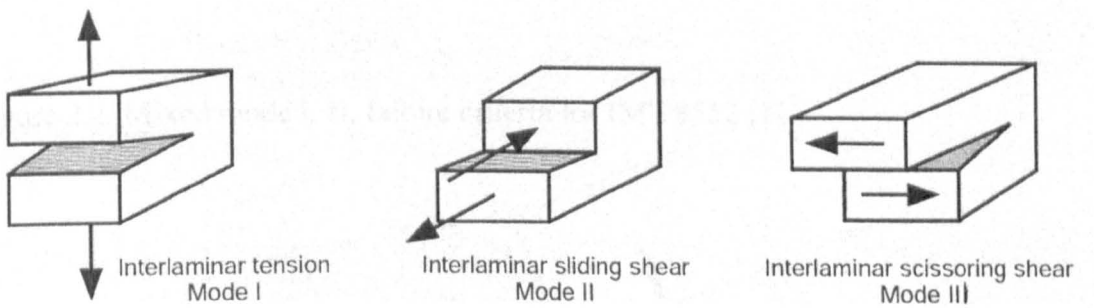

Figure 2.1: Fracture Modes (Mode I, II and III) [1].

In order to predict delamination onset or growth in two-dimensional problems, these calculated G components are compared to interlaminar fracture toughness properties measured over a range of mode-mixities from pure Mode I loading to pure Mode II loading. A quasi-static mixed-mode fracture criterion is determined by plotting the interlaminar fracture toughness G_C, versus the mixed-mode ratio, G_{II} / G_T, determined from data generated using the pure Mode I Double Cantilever Beam (DCB) ($G_{II} / G_T = 0$), the pure Mode II End Notched Flexure (4ENF) ($G_{II} / G_T = 1$) and Mixed Mode Bending (MMB) tests of varying ratios [1], as shown in Figure 2.2.

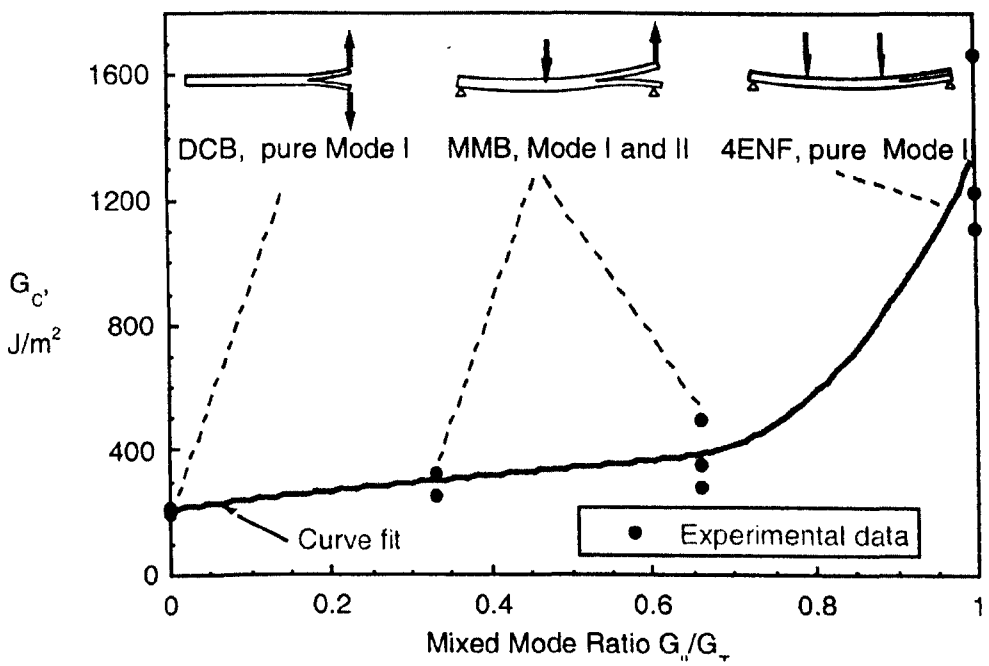

Figure 2.2: Mixed mode I, II, failure criteria for IM7/8552 [1].

A curve fit of these data is performed to determine a mathematical relationship between G_C and G_{II} / G_T [1,2]. Failure is expected when, for a given mixed-mode ratio G_{II} / G_T, the calculated total energy release rate, G_T, exceeds the interlaminar fracture toughness, G_C. In order to predict delamination onset or growth for three-

dimensional problems, the entire failure surface $G_C = G_C (G_I , G_{II} , G_{III})$,as shown in Figure 2.3 is required.

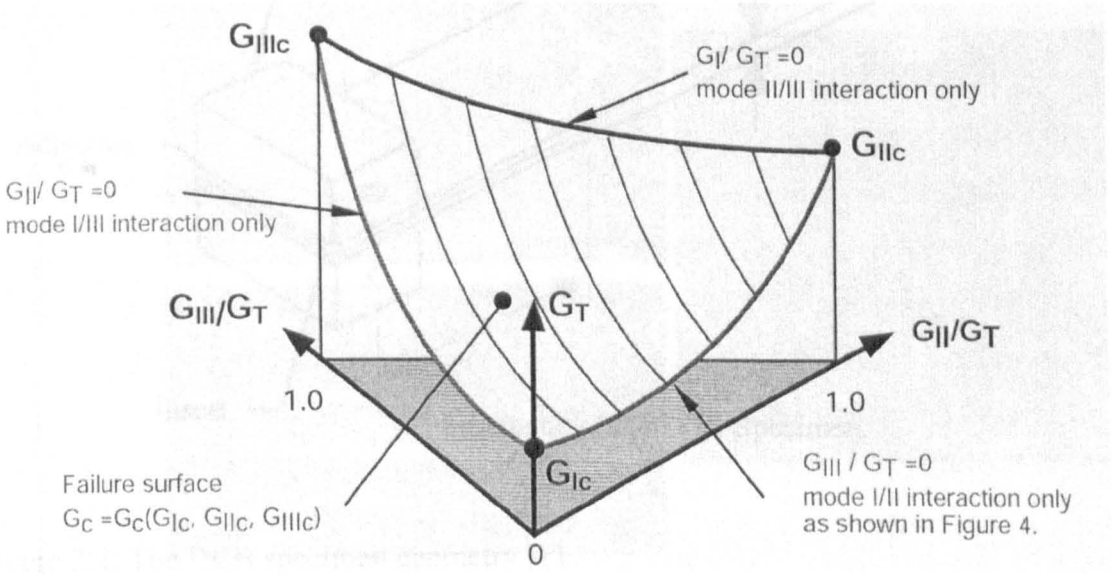

Figure 2.3: Mixed mode failure criteria for Modes I, II and III [1].

2.3. Mode I

2.3.1. Specimen Geometry

The Double Cantilever Beam Specimen (DCB) specimen shown in Figure 2.4 is the commonly accepted test geometry for Mode I (tensile opening) testing.

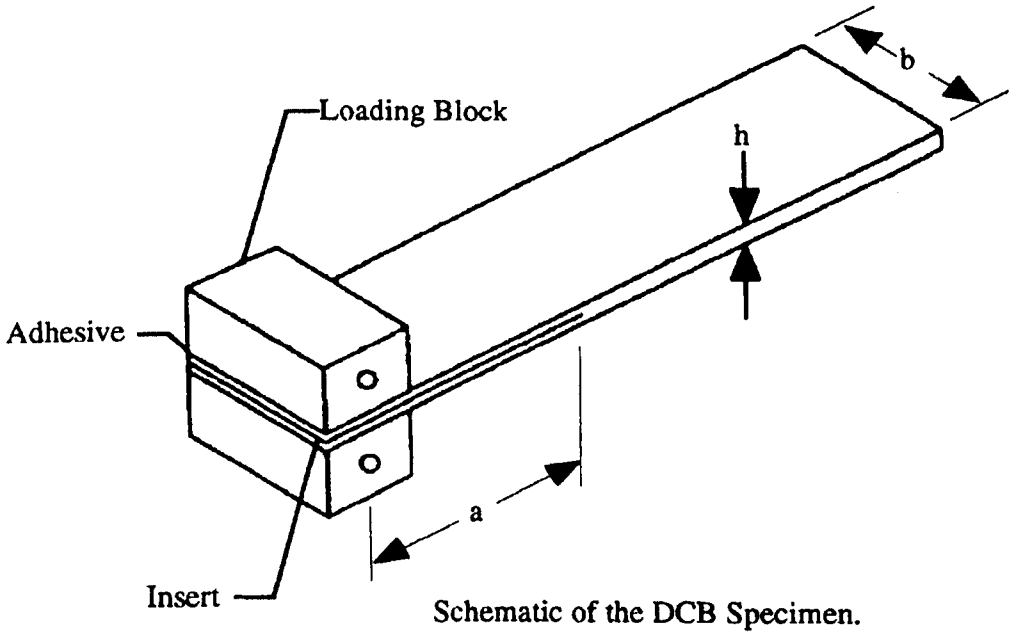

Figure 2.4: The DCB specimen geometry [1].

This configuration, which is a natural extension of monolithic or adhesive-cleavage specimens, has also been used by other researchers in tests of woven and non-woven laminates [3, 4].

2.3.2. Mode I Interlaminar Fracture

Mode I fracture has received the greatest attention and various standards have been developed for the Double Cantilever Beam (DCB) test [5, 6]. The current standards cover the measurement of the critical strain energy release rate, G_{Ic}, of unidirectional (UD) $[0°]_n$ laminates. In fact, UD specimens are generally used for DCB tests due to the high flexural stiffness and ability to maintain self-similar crack propagation.

Jimenez and Miravete [7] characterized experimentally the material interlaminar fracture in pure Mode I (DCB test) and presented a basic methodology for the application of the finite element simulation and linear elastic fracture mechanics to

predict the onset of delamination growth. An innovative aspect introduced was the analysis being carried out as a non-linear geometric problem (taking large displacements into account) and applying different elastic material properties depending on whether the material is under tension or compression.

When simulating DCB, ENF and MMB tests, differences due to using linear or non-linear geometric analysis (consideration of large displacements) are negligible in terms of the load-displacement response of the sample, as well as in terms of the calculated distribution of total G. However, important differences (larger than 10%) are found between the linear and non-linear analysis regarding the G partition into G_I in the MMB simulations. The origin of these differences is the influence of the small load rotation that occurs associated with rotation of the movable part of the test rig. For this reason, it is recommended to use a non-linear FEA for calculating the G_I distributions, meaning that large displacements are taken into account in such calculations although the global load-displacement response is linear.

The material used in the study by Jimenez and Miravete [7] was unidirectional prepeg carbon-epoxy with a nominal thickness of 0.125 mm per cured lamina. The samples consisted of 28 layers and had an initial delamination in the laminate central plane. The tests showed that G_I was almost constant along the whole delamination length apart from the free edge area. The value of G_I was considered to be constant for about 80% of the total length of the delamination front, resulting in the finding that simultaneous fracture of this large central portion of delamination front is the associated phenomenon to the maximum load in the load/displacement curve of the test. Moreover, a Mode III component of strain energy release rate, G_{III}, was found near the free edge of the sample, reducing quickly to zero along most of the delamination front. This was due to geometry or material anisotropy, but even in the free edge areas, the values were negligible. As a result, G_{III} was not considered when establishing an interlaminar fracture criterion.

The findings of previous research studies were successfully applied when used on unidirectional carbon-epoxy laminates. However, most applications in composite structures involve multidirectional (MD) laminates and delaminations tend to occur between layers of different orientations. Chai H. [3] conducted a series of DCB tests

in order to characterize Mode I delamination failure in fibre-reinforced epoxy laminates. Different stacking sequences were used, as well as two matrices, differing greatly in their mechanical behaviour, one being a brittle resin and the other one a highly ductile one. The initial cracks were introduced at the beam mid-plane or slightly (a few plies) away from it, so that the growth histories of delaminations initiated from various interfaces could be studied.

A general finding of this research work [3] was that the crack did not stay in its initial plane, but shifted interfaces as it grew, the particular manner of which depended on the lay-up. Moreover, the brittle resin enhanced the difference in the strengths of the fibres and matrix, leading to matrix-dominated failure. The ductile and tough matrix homogenized the two composite phases, thereby causing matrix as well as fibre rapture. Another important factor in the tests was the fibre alignment. It was found that 0° layers acted to preserve the delamination profile and to contain the damage, whereas 90° layers were easily penetrated. At intermediate angles, i.e. 45°, cracks shifted in a process initiated at the specimen edge. The interlaminar fracture surface was shown to consist of various matrix microstructural failure processes. These details varied for different types of interface and sometimes varied across a given interface. In both the brittle and ductile matrix based laminates these effects integrated out, leaving the Mode I interlaminar fracture energy to be independent of test specimen geometry (crack length or beam width) and the orientation of plies on both sides of the delamination interface. The Mode I interlaminar fracture energy is also associated with the lowest amount of energy dissipation during crack growth and is largely dependant only on the matrix properties.

Similar results were obtained by Jordan et al [8]. In this work, five resin systems were examined, having two main variables, the crosslink density and percentage of rubber additions. The interest work focused on determining how variations in resin chemistry and morphology affects fracture toughness through their effects on the constitutive behaviour of the matrix. One of the main findings was that when both the crosslink density is lowered and rubber particles are added, the increase in toughness is much greater than one would predict based on a simple addition of these two effects independently. Moreover, three different resin/fibre concentrations were tested, showing that the smaller the fibre volume fraction (or the larger the resin content), the

greater the delamination toughness of the composite. Microscopic examination of the specimens indicated that the composite with a lower fibre density had a resin rich region between plies that was approximately twice as thick as the composite with the highest fibre content. Therefore, it was concluded that a large resin rich region between plies results in a greater resistance to delamination, at least in composites with a ductile resin. The reverse may be true for composites based on brittle resins, as shown by Bradley et al [9].

Pereira at al [4] conducted some Mode I DCB tests on woven glass/epoxy multidirectional laminates. The study concerned specimens with θ°/-θ° and 0°/θ° ply interfaces, with θ being 15°, 22.5°, 30°, 45°, 67.5° and 90°. During the tests, most specimens suffered intraply damage and crack branching to a neighbouring interface. It was noted that initiation took place under a rising load. This indicated the presence of large plastic zones ahead of the crack tip, in which the nature of the reinforcement (glass fibre woven fabric) played an important role. As expected, 0°/0° specimens exhibited pure interlaminar crack propagation, although the interface was quite irregular. This was attributed to the migration and 'fitting in' of interfacial 0° plies. Obviously, weft fibres prevented the fibre bridging phenomenon usually observed in unidirectional laminates. The maximum values of G_{Ic} were similar, suggesting plastic deformation ahead of the crack tip is the toughening mechanism characteristic of this material. It was also noted that θ°/-θ° specimens offered higher G_{Ic} values from the starter film than 0°/0° samples, suggesting a consistent increase in G_{Ic} with θ°.

2.3.3. Mode I Studies on Adhesively Bonded Composites

Chai [10] investigated the effect of matrix properties on the Mode I interlaminar fracture of laminated composites, by comparing results obtained from composites and adhesively-bonded specimens fabricated from identical matrices. Resins offering diverse mechanical properties were employed, including brittle thermosets and thermoplastic (PEEK) resins. The fracture energy of the composites displayed an R-curve behaviour attributed to an increase in crack-tip damage with crack extension. The size of the damage zone strongly depended on the specimen geometry, leading to

a reduction of the value of the calculated G_{Ic}. Only during the initial phase of crack growth was G_{Ic} independent of specimen geometry, ply orientation and fibre surface treatment (adhesion failure excluded). The size of the damage zone decreased with increasing matrix toughness and specimen compliance, making it difficult to determine accurately the initial value of G_{Ic} in the ductile matrix composites that were examined. This difficulty was overcome through the use of the more rigid SDCB specimen, as can be seen in Figure 2.5.

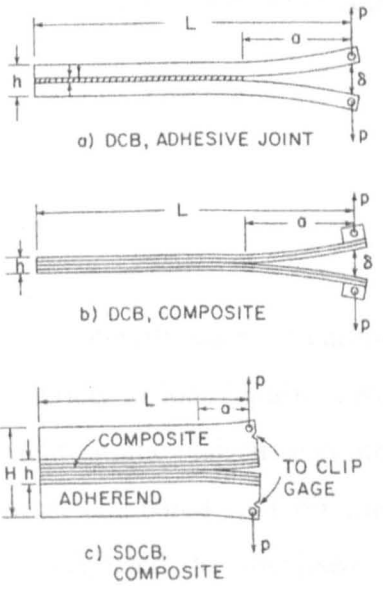

Figure 2.5: Schematic of Mode I fracture specimens for composite materials [10].

Chai [10] showed the fracture toughness of brittle adhesives varies only slightly with bond thickness, but ductile PEEK exhibited a pronounced bond thickness effect. Over the bond thicknesses investigated, two different characteristic regimes were identified. In the first, $t<35$ μm (thin-bond regime), G_{Ic} decreased with t, and failure occurred near the contact surface by means of shear yielding. This behaviour was attributed to the development of 'hydrostatic' tension at the bond centre. In the second regime where $t>35$ μm, G_{Ic} increased with t, and failure occupied a relatively large region near the contact surface. These changes were attributed to a relaxation in the stress

triaxiality at the crack tip with increasing bond thickness. Moreover, it was found that the adhesive fracture work depends heavily on adhesive ductility.

Blackman et al [11] performed experiments on three different substrate materials, a unidirectional carbon-fibre reinforced plastic, an aluminium alloy and mild steel. These substrates were all bonded using the same general-purpose structural epoxy-paste adhesive. The values of G_{Ic} were shown to be independent of test geometry but dependant on the substrate material used to make the joints. Additional studies have shown that this substrate dependence was due to the cured adhesive in the different joints exhibiting different values of glass transition temperature.

2.3.4. Effect of Loading Rate

High performance composite materials such as carbon fibre reinforced plastic are finding widespread use in a variety of load-bearing aerospace applications. The main reason for this is their excellent fatigue resistance combined with very high values of specific strength and stiffness, compared to their metallic counterparts. However, when these materials are subjected to localised impact loading, cracks and delaminations frequently initiate and propagate rapidly along the interfaces between the individual plies or layers within the material. The presence of these delaminations can result in localised buckling instabilities within the laminate leading to significant reductions in the residual compressive strength of the impacted component [12-14]. The impact event is a complex phenomenon which involves a material-dependent fracture process.

The influence of loading rate on the Mode I interlaminar fracture properties of continuous fibre composites has been investigated by a number of workers [15-22]. Much of this work has been undertaken using the double cantilever beam (DCB) specimen geometry. One of the inconveniences of the DCB specimen geometry for high rate testing is that, for a given crosshead velocity, the strain rate at the crack tip decreases rapidly with increasing crack length. It is therefore difficult to relate the

crosshead displacement rate to the loading conditions at the tip of the rapidly propagating crack.

Much work has been published on the effect of loading rate on the Mode I interlaminar fracture properties of brittle-matrix composites. Gillespie et al [17] conducted Mode I interlaminar fracture tests on AS4 carbon fibre/3501-6 epoxy resin composites over a range of crosshead displacement rates ranging from 0.25 to 250 mm/min, observing a linear elastic response and stable crack propagation at all rates. The value of the Mode I interlaminar fracture toughness, G_{Ic} , remained roughly constant at 190 J/m^2 over the range of loading rates examined. Smiley and Pipes [18] also conducted tests on the same material but at a much greater range of crosshead loading rates. According to their findings, this brittle-matrix composite exhibited a brittle stable mode of fracture under all conditions. At the highest rates of loading (2.5 x 10^{-2} to 2.1 x 10^{-1} m/s) the load-displacement curves exhibited an unusual trend with the load continuing to increase with increasing crack length. Moreover, their data showed that the Mode I interlaminar fracture toughness of the composite remained roughly constant at about 170 J/m^2 up to a crack tip opening rate of 2 x 10^{-8} m/s, as can be seen in Figure 2.6. At higher opening rates, the toughness decreased rapidly reaching a value of approximately 40 J/m^2 at 1 x 10^{-6} m/s. This decrease in the value of G_{Ic} was attributed to the rate sensitivity of the epoxy matrix.

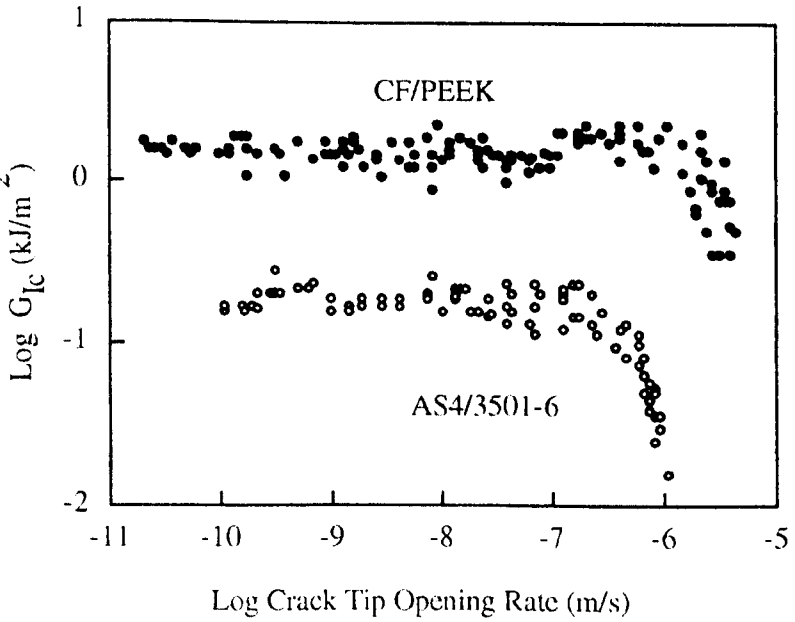

Figure 2.6: The variation of Mode I interlaminar fracture toughness, G_{Ic}, with crack tip opening rate of the carbon fibre reinforced epoxy AS4/3501-6 and AS4/PEEK (APC-2) [18].

Daniel et al [23] used the width-tapered DCB specimen geometry to study rate effects in AS4/3501-6. Their test programme spanned a similar range of loading rates to those of Smiley and Pipes. However, their experimental observations were significantly different, with crack propagation becoming unstable at higher rates. Furthermore, no unusual trends in the load-displacement curves at the highest rates were observed. The value of G_{Ic} was found to increase by approximately forty-six percent up to a crack velocity of 1 m/s and thereafter decreased slightly to a value that was still greater than the quasi-static value. As a result, the authors did not observe the dramatic drop in G_{Ic} at high rates of loading reported by Smiley and Pipes. Blackman et al [24] tested a unidirectional carbon fibre reinforced plastic and showed that the values of G_{Ic} remained insensitive to the rate of specimen displacement over a wide range of test rates.

Matsumoto et al [25] used the wedge-driven delamination test (WDD) to characterise the rate-dependency of a unidirectional glass/epoxy. The outcome of the tests was that

the value of G_{Ic} increased by approximately fifty per cent over less than three decades of rate. It should be noted that the main advantage of the WDD test is that, providing that the crack propagates in a stable manner, the rate of crack growth is constant throughout the test and equal to the speed of the crosshead.

The effect of varying loading rate on the Mode I interlaminar fracture toughness of a toughened epoxy has been investigated by Daniel and co-workers [23, 26]. A carbon fibre/elastomer-modified epoxy was tested at constant crosshead rates ranging from 7.5×10^{-3} mm/s to 460 mm/s. It was found that the strain energy release rate decreased by approximately thirty-five percent over five decades of crack velocity, as can be seen in Figure 2.7.

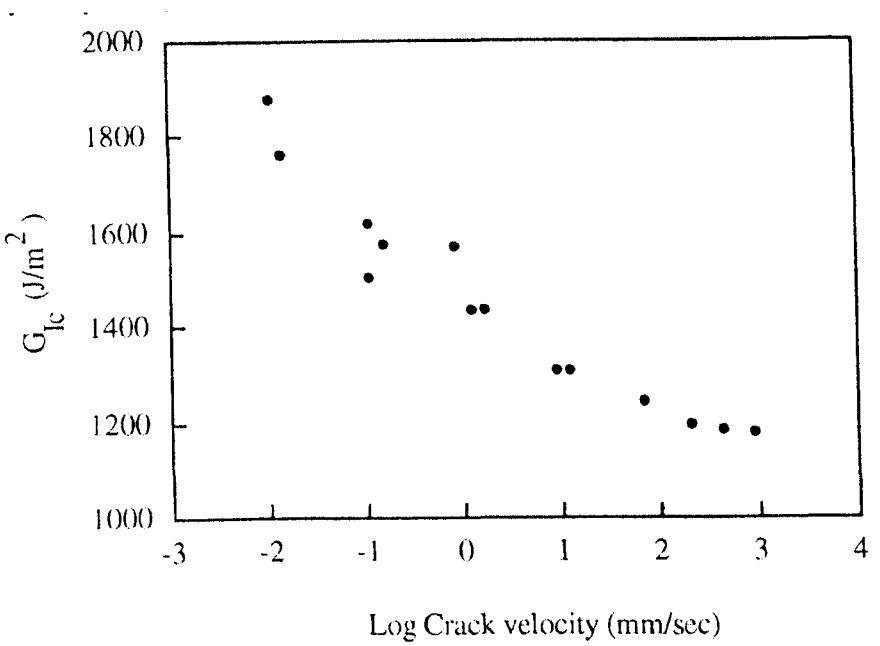

Figure 2.7: The variation of G_{Ic} with crack velocity for a T300 carbon fibre rubber-toughened epoxy composite [20].

Single edge notch bend (SENB) tests by Cantwell et al [27] highlighted a progressive decrease in toughness with increasing rate. A detailed study of thin sections removed from the crack-tip region indicated that extensive plastic deformation occurred around

the particles at low rates of loading, whereas at higher rates, little or no plastic deformation was in evidence. As a result, it seems reasonable to expect that the Mode I interlaminar fracture toughness of a rubber-toughened epoxy system will be adversely affected by loading rate.

A large amount of work has been published on the Mode I delamination behaviour of composites with thermoplastic matrices [15-22]. Gillespie et al [17] conducted tests on AS4 carbon fibre/PEEK at crosshead rates between 0.25 and 250 mm/min and characterised the Mode I toughness by determining a value of G for subcritical growth (G_{Isc}) and one for critical crack growth (G_{Ic}). The authors found that G_{Isc} remained constant whereas G_{Ic} first increased and then decreased. The initial increase in G_{Ic} was attributed to an increase in the matrix yield stress within the plastic zone and the reduction to a ductile/brittle transition of the polymer in the process zone. Using the WDD test, Glessner et al [20] varied both the temperature and loading rate and did not observe any distinct loading rate effects between -25°C and 120°C. Smiley and Pipes [18] considered a much larger range of loading rates (4.2×10^{-6} to 6.7×10^{-1} m/s) and again observed a dramatic reduction in G_{Ic} at very high crack tip opening rates and unusual load-displacement curves at high rates of loading. The great loss in interlaminar fracture properties was qualitatively explained in terms of the effect of the strain rate on the interaction of the crack-tip plastic zone and the carbon fibres. At low and intermediate rates of loading, the plastic zone size was constrained by the presence of the neighbouring carbon fibres limiting its size to that of the inter-fibre distance. As a result, any change in loading rate will not have any perceivable effect on the interlaminar properties of the composite. At some critical crack tip opening rate, the yield stress of the polymer is such that the size of the plastic zone just equals the distance between fibres. Any further increase in rate above this critical value will decrease the size of the plastic zone and, as a result, G_{Ic}.

Beguelin et al [21] conducted DCB tests on IM6 carbon fibre/PEEK at crosshead displacement rates between 1 mm/min and 1.1 m/s. According to the findings of this research work, a small reduction of G_{Ic} took place at very high rates of loading, as can be seen in Figure 2.8. It should be noted that their load-displacement curves at 1m/s were similar in form to those obtained at much lower speed rates and that the rising load-displacement curves obtained by Smiley and Pipes were not observed.

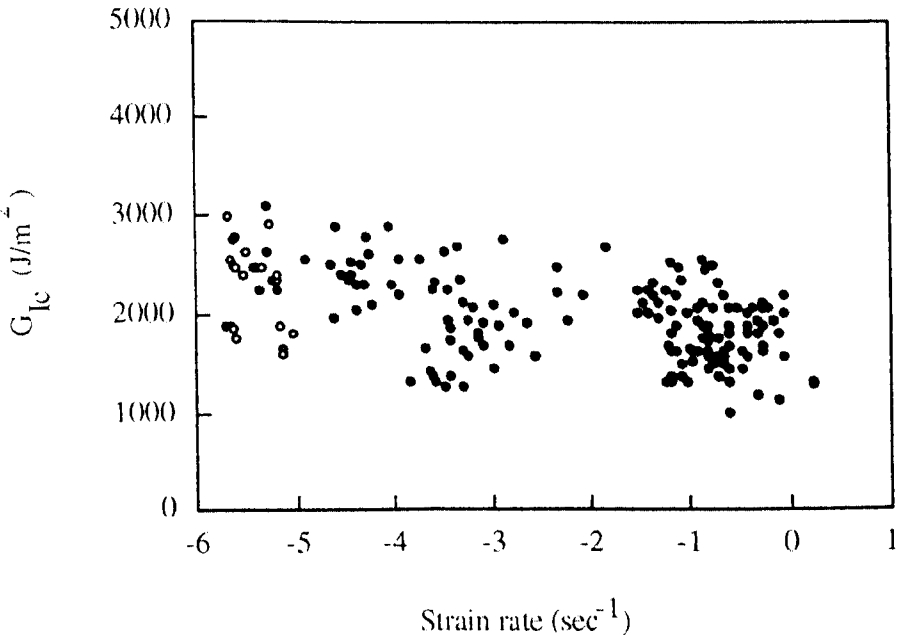

Figure 2.8: The variation of G_{Ic} with log strain rate for unidirectional IM6 carbon fibre/PEEK. Open circles correspond to stable propagation and filled circles to unstable propagation [21].

Much of the interlaminar fracture data reported in the literature has been conducted on unidirectional specimens made from axially aligned pre-impregnated tape. A disadvantage of using unidirectional samples is that considerable fibre bridging may occur during testing, which will influence the tape of the crack propagation (stable/unstable), as well as the measured values of G_{Ic}. Moreover, composite structures used in engineering applications are rarely based on unidirectional stacking configurations. Instead they contain well-defined interfaces between individual ply orientations. Johnson and Mangalgiri [28] showed that fibre bridging could be dramatically reduced by offsetting the centre plies by a few degrees to each other. Cantwell and Kausch [29] conducted tests on IM6/PEEK, showing that offsetting the centre plies by a few degrees not only resulted in a change from stable to unstable crack propagation but resulted in a material exhibiting a much greater degree of rate-sensitivity. Mall et al [30, 31] investigated loading rate effects in a woven fabric/PEEK composite, trying to reduce fibre bridging. Testing took place over a

range of crosshead speeds between 0.5 mm/min and 1000 mm/min. At the lowest crosshead speed, the interlaminar fracture toughness of the composite was approximately 5000 J/m^2. The value of G_{Ic} dropped steadily as the rate increased, reaching a value of approximately 1600 J/m^2 at the highest rate, as can be seen in Figure 2.9. For all crosshead speeds, crack growth occurred in an unstable manner.

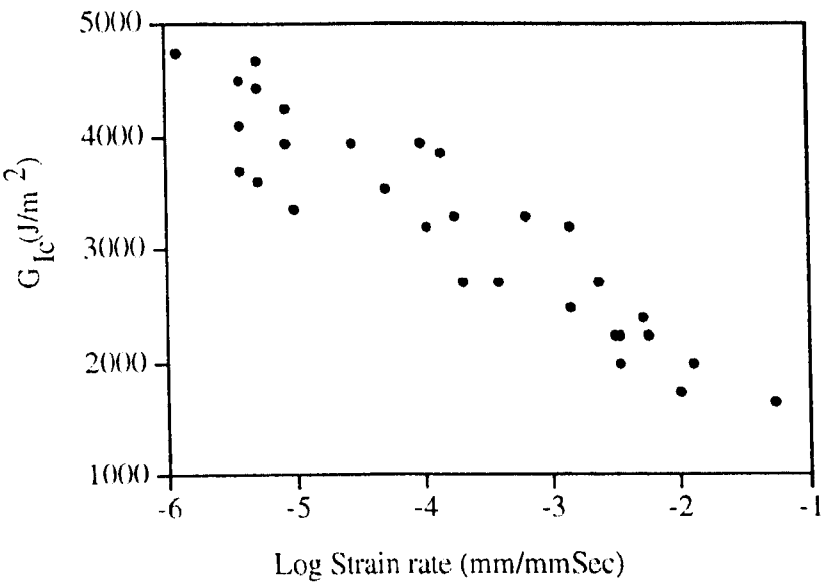

Figure 2.9: The variation of G_{Ic} with log strain rate for woven carbon fibre/PEEK [16].

Generally, it is believed that rate effects do exist in both thermosetting and thermoplastic-matrix composites. In unidirectional CFRP, however, much of this rate-sensitivity is concealed by the presence of rate-insensitive carbon fibre bridging in the vicinity of the crack tip. Rate effects in materials with offset plies or woven fabric composites exhibit much greater rate-dependency characteristics and it is believed that these materials reflect more closely the response of more representative multidirectional laminates.

It appears that the fracture response of the composites is largely determined by that of the neat polymer. In brittle thermosets, G_{Ic} appears to drop with increasing loading rate again as a result of the rate-dependent response of the neat resin.

2.4. Mode II

The End-Notched Flexure (ENF) specimen has been widely used for Mode II testing, mainly because of its simple set-up, it has also been adopted by Japanese Industrial Standards [32, 33]. This was originally developed for wood [34] and adapted to fibre reinforced polymer composites by Russell and Street [35].

2.4.1. Mode II Interlaminar Fracture

The Mode II test remains controversial, first for practical reasons (unstable propagation in the ENF specimen, friction effects, difficulty in defining a starter defect). Another fundamental objection that has been raised is the opinion that it is impossible to design a true Mode II test, as the failure will always be dominated by Mode I (tension). However, it is clear that no test is performed on materials as heterogeneous on a microscopic scale as fibre reinforced composites can ever involve pure loading at that microscopic scale. This is obvious when looking at fracture surfaces and a simple example is the Mode I test in which different areas of the fibre – matrix interface around a fibre will see other modes of loading. However, this does not prevent the DCB geometry from providing useful information and valid linear elastic fracture mechanics data on a macroscopic scale [36]. The initiation of cracks in the Mode II specimen is produced by relative horizontal sliding of the two faces of the specimen, which corresponds to a Mode II load and the subsequent rotation and opening of these cracks (which produce the fracture surfaces) are not considered in the data analysis.

As well as the ENF specimen geometry, there are another three geometries that are used for Mode II testing, the SENF (stabilised ENF), the ELS (end loaded split) and the 4ENF (4 point ENF), as can be seen in Figure 2.10.

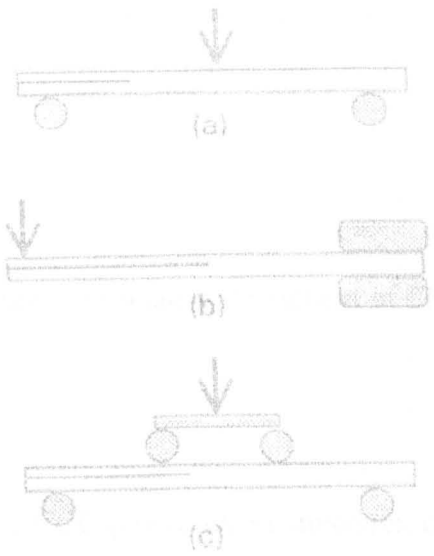

Figure 2.10: Mode II test configurations: (a) ENF (and SENF), (b) ELS, (c) 4-point ENF [36].

One of the main disadvantages of the ENF specimen is the associated unstable propagation (except for very long crack lengths) [36]. Work has been carried out in Japan, leading to a number of procedures for stabilising the test by feedback control of the test machine. Two methods were applied in the VAMAS round robin. The first is referred to as CSD control, in which crack shear displacement is measured as shown in Figure 2.11, and this is then used as the input parameter in a feedback loop whilst the CSD rate is held constant.

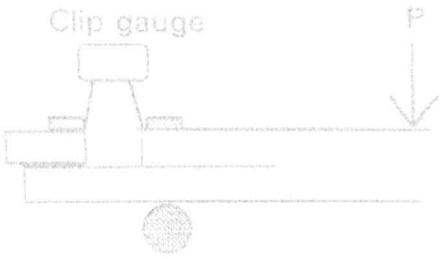

Figure 2.11: CSD measurement of relative movement of ENF arms [36].

An alternative is to use the CCC (coordinate conversion control) method [37, 38]. In this case, the load P and crosshead displacement d are input to a circuit which gives an output $C = d - \alpha P$. When C is controlled to increase monotonically, crack propagation is stabilised.

For both these test methods, a servo-controlled test machine is required. Two test procedures based on the SENF specimen were proposed by the JIS group for the VAMAS exercise [36].

The ELS specimen was used in early work at Texas A&M University [39] and later by Russell [40], and crack propagation along this specimen is intrinsically stable provided crack length to free length ratio exceeds 0.55. ESIS has run several round robins using this specimen and preferred it to the ENF on account of the stability of crack propagation.

Finally, a modified version of the ENF specimen using a four point flexure (4ENF) rather than three point bending was introduced by Martin and Davidson [41] and appears to show some advantages.

It is clear, from the fact that four specimen configurations are being considered that there are practical difficulties in measuring G_{IIc} for composites. The problems concern:

- Type of starter defect
- Definition of initiation
- Stability
- Friction
- Data Analysis

2.4.2. Effect of Ply Orientation

Owing to their high stiffness and ability to sustain self-similar crack growth conditions, unidirectional specimens are particularly suited for interlaminar fracture testing. However, most applications involve multidirectional laminates where delaminations generally occur between plies of different orientation.

Zile and Tamuzs [42] conducted an experimental study on the delamination of a unidirectional carbon fibre/epoxy composite using the four-point bend end-notched flexure (4ENF) test. A unidirectional Sica CarboDur S512 carbon fibre/epoxy composite was examined, with the fibres oriented along the specimen length. A symmetric test configuration was used, with a crosshead displacement rate of 0.5 mm/min. According to the experimental results, G_{II} was found to increase as the crack advanced. This fact can be explained by the presence of fibre bridging, which was found during inspection of the specimens after testing.

Various studies have been reported on the Mode II fracture of multidirectional laminates. Chai [43] performed ENF tests on carbon/epoxy and carbon/PEEK specimens with 0°/0° and +30°/-30° delaminating interfaces. Higher G_{IIc} values were obtained for the latter specimens. Chou et al [44] studied the Mode II fracture of carbon/epoxy specimens with delaminations at θ/-θ interfaces where θ = 0°, 30°, 60°.

The results of ENF tests showed that the G_{IIc} values increased with the ply angle θ. However, it was found that the starter delamination in +60°/-60° specimens jumped to a neighbouring 0°/60° interface via transverse cracks in the +60° and -60° plies.

Polaha et al [45] tested carbon/epoxy specimens with θ°/-θ° delaminating the interfaces where θ = 0°, 15° and 30°. In this case, G_{IIc} was largely unaffected by θ, but in the +15°/-15° and +30°/-30° specimens the starter delamination jumped to a neighbour interface through a transverse crack. Choi et al [46] performed ELS tests on specimens with 45°/-45° interfaces and obtained G_{IIc} values forty-five to eighty-four percent higher than those of unidirectional specimens. This difference was attributed to intraply damage in +45°/-45° specimens. Ozdil et al [47] tested glass/epoxy specimens with θ°/-θ° delaminating interfaces and reported that G_{IIc} increased almost 3 times when θ varied from 0° to 45°. However the specimens presented considerable permanent deformation after unloading, thus raising doubts about the validity of the results. Tao and Sun [48] conducted ENF tests on specimens with 0°/θ° delaminating interfaces, where θ = 0° to 90°. In order to avoid intraply cracking, the specimens were positioned so that the θ oriented ply would be under compression. In these circumstances, G_{IIc} values decreased with θ. Moreover, Hwang et al [49] obtained identical trends in G_{IIc} values for carbon/epoxy specimens with 0°/θ and θ°/-θ° delaminating interfaces, but they were attributed to the effect of transverse cracks.

Pereira and co-workers [50] conducted tests on Mode II fracture tests on carbon/epoxy multidirectional laminates. A 3D finite element analysis was first performed to define appropriate stacking sequences for end-notched flexure (ENF) specimens with starter delaminations at θ°/-θ° and 0°/θ° interfaces. This was chosen with the practical relevance and the results available in the literature, in mind. Moreover, the selection of specimen stacking sequences should avoid excessive elastic couplings that affect G_{IIc} measurements. For example, anticlastic deformation resulting from bending-bending coupling may generate highly curved delamination fronts and a considerable Mode III component at the specimen edges. On the other hand, bending-twisting and membrane-bending couplings are generally present in 0°/θ° and θ°/-θ° specimens. The former may lead to highly unsymmetrical delamination fronts, while the latter could induce significant effects of residual stresses on G_{IIc} measurements. In addition, multidirectional laminates are more

flexible than unidirectional ones, as well as considerably tougher. As a result, thick specimens should be used in order to avoid large displacements, plastic deformation and intraply damage. The stacking sequences used by Pereira and co-workers in their research, were the following [50]:

- $[(0°_2 / 90°)_6 / 0°_2 // (0°_2 / 90°)_6 / 0°_2]$
- $[(0°_2 / 90°)_6 / 0°_2 // \theta / (0°_2 / 90°)_6 / 0°_2]$, with $\theta = 22.5°$, $45°$, $67.5°$ and $90°$
- $[(0°_2 / 90°)_6 / 0°_2 / \theta // -\theta / (0°_2 / 90°)_6 / 0°_2]$, with $\theta = 15°$, $30°$ and $45°$

where // denotes the position of the starter delamination.

After performing the tests, the G_{II} distributions were found to be reasonably uniform along the specimen width. Moreover, G_{IIc} values increased with the ply angle θ, although premature transverse cracking prevented valid measurements in the 30°/-30° and 45°/-45° specimens [50].

Continuing the work on Mode I, Jordan and co-workers [51] examined five main resin systems in Mode II loading conditions, having two main variables, the crosslink density and the percentage of rubber additions. The work focused on determining how variations in resin chemistry and morphology effects fracture toughness through their effects on the constitutive behaviour of the matrix.

One of the main findings was that when the crosslink density has been lowered and rubber particles have been added, the increase in toughness is much greater than one would predict based on a simple addition of these two effects independently. Moreover, three different resin/fibre concentrations were tested, showing that the smaller the fibre volume fraction (or the larger the resin content), the greater the delamination toughness of the composite (for either Mode I or Mode II). Microscopic examination of the specimens indicated that the composite with a lower fibre density had a resin-rich region between plies that was approximately twice as thick as the composite with the highest fibre content. Therefore, it appeared that a large resin-rich region between plies results in a greater resistance to delamination, at least in

composites with a ductile resin. The reverse may be true for composites based on brittle resins.

The Mode II delamination fracture toughness, as was the case in Mode I, showed a monotonic increase in the delamination fracture toughness with increasing resin toughness. In all cases, the Mode II fracture toughness was larger than the Mode I fracture toughness.

2.4.3. Adhesively-bonded Specimens

Chai [52] examined the material aspects of Mode II fracture in adhesively-bonded joints, for a range of adhesives, using scanning electron microscopy. The adhesive thickness was varied from low volumes to very high values to investigate the bulk fracture behaviour.

The fracture process started with the initiation of tensile microcracks ahead of the crack tip and continued with the spreading of this damage away and towards the tip in a process accompanied by interfacial linkage of microcracks and intralaminar plastic yielding. Crack growth occurred when the damage zone became fully developed, the extent which exceeded the adhesive thickness by several orders of magnitude.

The fracture toughness exhibited a plateau followed by a monotonic decrease as t was decreased from t_p, a transition that is believed to be due to the interaction of the crack tip damage zone with adherends. For all the adhesive systems, the main source for energy consumption in thin bondline joints appeared to be homogeneous shear yielding or distortion. This, together with stable and coplanar cracking, allows for a useful engineering interpretation of shear fracture. At lower bond thicknesses, the shearing and opening fracture energies displayed opposite trends, which highlights the interdependance of joint toughness on both the dimensions of the plastic zone (shear) as well as the complex state of stresses within this zone (opening). In the limit where t approaches zero, however, all three fracture works were associated with shear yielding, and they converged to a single value, G_c, that may serve as a material

characterization parameter. The thin-bond results should be directly applicable to interlaminar fracture of composites [52].

Ducept and co-workers [53] conducted Mode II tests on adhesively-bonded unidirectional glass/epoxy laminates. The crack was initiated by an 8 μm thick polypropylene film that was placed at the mid-thickness of the laminate during moulding. The cracks in the bonded joints were stabilised, as the presence of a very long plastic zone in front of the crack tip enabled considerable energy dissipation. As a result, the use of a tough adhesive to bond less tough matrix composites appears very attractive as the assembly is less sensitive to bonding defects. It should also be noted, that this is similar to the inclusion of tough interleaf layers which have been used in the past to improve the Mode II delamination resistance and damage resistance of composites.

Further work by Chai [54] on the stress-strain behaviour in simple shear of a structural adhesive undergoing large-scale yielding was performed as a function of bond thickness (2μm to 600μm), strain rate and temperature (-60°C to Tg) using the Napkin Ring test specimen. Moreover, ENF tests were carried on adhesively bonded specimens, showing that the Mode II fracture energy per unit bond thickness in steady state agrees well with the area under the stress-strain curve of the nominally unflawed adhesive provided that bond thickness is sufficiently small. Accordingly, the fracture energy becomes negligibly small at both the absolute and the glass transition temperatures, reaching a maximum between these two extremes. Moreover, the result showed that thinner bonds lead to superior strength, but in order to achieve higher toughness values, thicker bonds are necessary. In this case, a multilayer design approach would be beneficial since this would reduce the size of the critical flaw in the bond.

2.4.4. Effect of Crosshead Displacement Rate

Very little work has been published in the literature concerning the effect of loading rate on the Mode II interlaminar fracture properties of composite materials. Smiley

and Pipes [18] reported a seventy-nine and an eighty-six percent reduction in the G_{IIc} of AS4/3501-6 and AS4/PEEK respectively at relatively modest crosshead speeds (less than 0.1 m/sec). The dramatic drop in interlaminar fracture toughness of AS4/PEEK was attributed to a ductile/brittle transition in the thermoplastic matrix. It should be pointed out, however, that at the higher rates, the response of load instrumentation was too slow to measure the force signal accurately. The critical load was therefore computed from the measured critical displacement and the specimen compliance. It is not clear, however, how the critical displacement was measured.

Blackman et al [55] used the end-loaded split geometry to investigate the Mode II properties of carbon fibre/PEEK and a carbon fibre/toughened epoxy. At high rates of loading, their data highlights a slight decrease in the value of G_{IIc} for the thermoplastic matrix composite and a slight increase in the corresponding values for the epoxy-based composite.

Cantwell [27] conducted ENF tests on a number of epoxy-based and thermoplastic based composites over a range of crosshead speeds between 0.01 mm/min and 3 m/sec. Figure 2.12 shows the variation of G_{IIc} with crosshead speed for unidirectional AS4/PEEK.

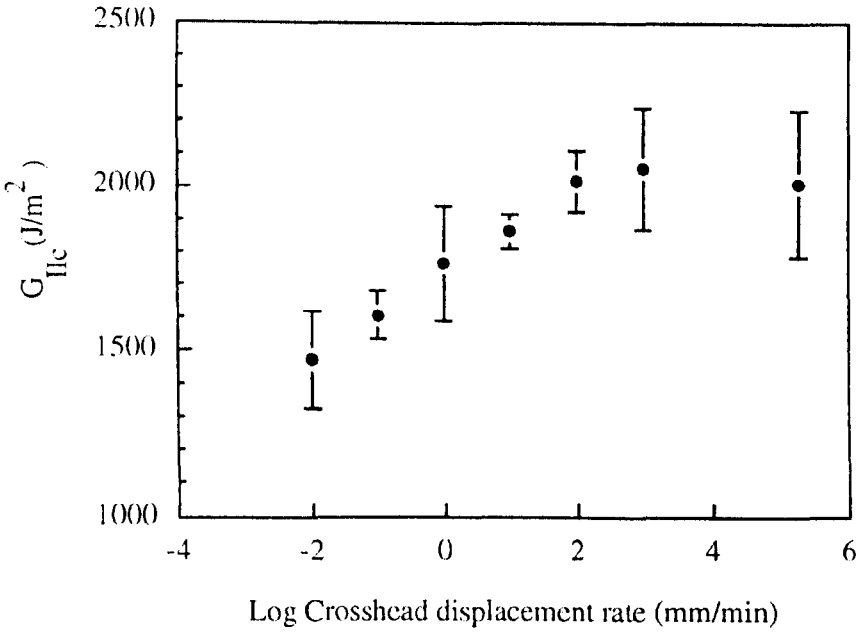

Figure 2.12: The variation of G_{IIc} (measured from a Mode II pre-crack) with loading rate for IM6 carbon fibre/PEEK with offset centre plies [27].

This tough thermoplastic-based composite exhibits a distinct rate sensitive behaviour with G_{IIc} increasing with rate. Tests on ENF samples with offset centre plies further highlighted the rate-dependent behaviour of G_{IIc} in tough thermoplastic-matrix composites, as can be seen in Figure 2.13. In this case, a sixty percent increase in G_{IIc} over just two decades in loading rate is apparent. At higher loading rates, the interlaminar fracture toughness data appear to plateau at a value of apparently 2000 J/m^2.

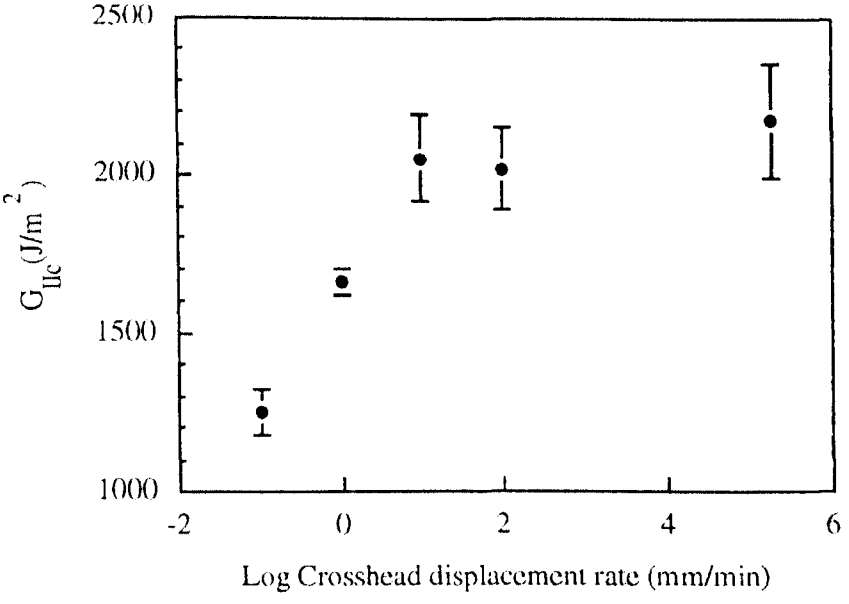

Figure 2.13: The variation of G_{IIc} (measured from a Mode II pre-crack) with loading rate for IM6 carbon fibre/PEEK with offset centre plies [27].

By conducting Mode II in-situ fracture tests in a scanning electron microscope, Corleto and Bradley [56] showed that a damage zone up to 1000 microns in length formed at the tip of a Mode II crack in a toughened epoxy composite. A detailed study of this zone indicated that the polymer had undergone extensive deformation leading the authors to conclude that the resin failed due to yielding.

Cantwell and Zulfkifli [57] used the Double Edge Notch Flexure (DENF) specimen geometry, as shown in Figure 2.14, to study crack tip failure mechanisms in carbon fibre PEEK. Prior to testing, the edges of the specimens were ground, polished and gold-coated in preparation for examination in the scanning electron microscope. The specimens were then loaded in three point bending until a crack propagated from one of the defects. The crack tip region around the other defect was then examined, enabling the failure mechanisms immediately prior to fracture to be illucidated. A detailed study of this region indicated that at low rates of loading, damage developed on planes well above and below that of the starter defect. At very high rates of

loading, damage was confined to the resin-rich region immediately ahead of the aluminium defect. The authors argued that the presence of a large damage zone in specimens tested at low strain rates lead to a reduced Mode II fracture resistance.

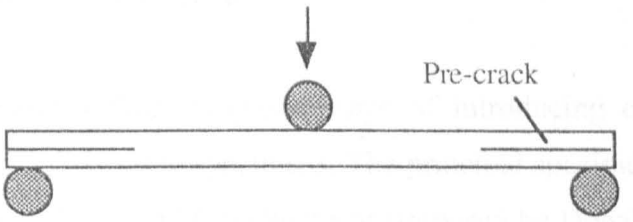

Figure 2.14: Schematic representation of the Double Edge Notch Flexure specimen [27].

Further work by Cantwell on the DENF geometry studied the failure mechanisms in a woven carbon fibre reinforced plastic. At the crack tip region at low loading rates, large inclined cracks were apparent around fibres oriented at 90° to the longitudinal axis of the specimen, no such cracks were apparent under impact loading conditions. The large shear cracks within the crack tip region were associated with a low Mode II fracture toughness. The rate-dependent properties of polymer matrices were further investigated by conducting Mode II tests on adhesively-bonded CFRP samples. In this case, it was shown that the Mode II fracture energy of the bonded samples increased significantly with loading rate, leading the authors to suggest that rate effects observed in fibre reinforced composites reflect the rate-sensitive behaviour of the polymeric matrix.

In conclusion, the available experimental data suggest that the Mode II interlaminar fracture properties of many composite materials are rate sensitive with the value of G_{IIc} increasing with strain rate. It is important that at low loading rates (especially for laminates in which bridging is not significant), the Mode II interlaminar fracture

toughness of many toughened matrix composites is significantly lower than the Mode I suggesting that the forward shear can, under certain conditions, be the more critical loading condition.

2.5. Mode III Interlaminar Fracture

In the late 80's several authors proposed ways of introducing out-of-plane shear (Mode III loading) into composite specimens. The principal specimens that were used were a Split Cantilever Beam (SCB) method was proposed by Donaldson [58, 59] and a Crack Rail Shear (CRS) by Becht and Gillespie [60]. Although both methods have been demonstrated to be feasible for Mode III fracture toughness G_{IIIc} measurements, certain experimental details need to be further addressed. For example, the crack tip strain energy release rate in the SCB specimen was found to have a significant Mode II component. The CRS specimen with double cracks may have difficulties in growing both cracks simultaneously, although a modified single crack CRS could solve this problem. However, both CRS configurations have relatively low compliance which makes it difficult to obtain fracture toughness values using the compliance calibration method.

The Edge Crack Torsion (ECT) test method developed by Lee [61] is widely used for characterizing the Mode III delamination behaviour of composites. The method is based on the torsion of a rectangular laminate plate specimen with an edge crack in its midplane. A pure Mode III loading was deduced to exist theoretically in such a specimen configuration under the given loading condition. The ECT specimen also has compliance sufficiently sensitive to crack length to allow fracture toughness to be determined by the compliance calibration principle.

2.5.1. Mode III Compliance Calibration Method

When the critical strain energy release rate is established experimentally from measuring the change in compliance of the cracked body as a function of crack length, the data reduction method is usually referred to as the compliance calibration method [62]. The strain energy release rate can be calculated from the change of compliance with crack length of the delaminated specimen as:

$$G = \frac{P^2}{2L}\frac{dC}{d\alpha} \tag{2.1}$$

where $\frac{dC}{d\alpha}$ is the rate of change in compliance as the crack grows, P is the applied load, L the distance between the points of applied displacement.

Two procedures are often adopted experimentally to approximate the derivative of C with respect to a [62]. In the first procedure, the delamination is extended by a small increment Δa and the change in compliance ΔC is measured. Then the ratio ($\Delta C/ \Delta a$) is used to approximate the derivative in Equation 2.1. In the second procedure, the compliance C is measured by varying the initial crack length a by moving the specimen in the test fixture and applying a small load to establish the specimen compliance without growing the crack. A plot of C versus a is thus generated. A least squares curve fit is applied to determine C as a function of crack length. The derivative of compliance as a function of α is then substituted into Equation 2.1.

Unfortunately, it is not possible to generate a compliance curve from a single ECT specimen using either method because of the unstable delamination growth [62]. Another reason is the fact that it is not possible to shift the specimen in the fixture and change the initial delamination length. As a result, a set of specimens with different insert lengths have to be tested to obtain a plot of compliance as a function of delamination length. First, the 1/C (inverse of compliance) values are plotted as a function of normalised delamination length a/b and then a least square straight line fit

to the data is determined. The linear relationship between (1/C) and (a/b) represented by a straight line can be expressed as:

$$\frac{1}{C} = A\,[1 - m(\frac{a}{b})] \tag{2.2}$$

where m and A are constants and b the width of the specimen. The Mode III fracture toughness G_{IIIc} can be obtained by differentiating equation 2.2 with respect to delamination length a and substituting the derivative of C with respect to a in equation 2.1, yielding

$$G_{IIIc} = \frac{mCP_c^{\,2}}{2Lb[1 - m(\frac{a}{b})]} \tag{2.3}$$

where P_c is the critical load for delamination propagation [62].

Crack propagation in the ECT test is non-uniform along the length of the specimen insert, peaking at the mid-span. This non-uniform crack propagation would only affect the toughness through the measurement of dC/da, not the critical load P_c. Since the crack propagation is unstable, separate specimens are used to measure dC/da, and the shape of the insert defines the initial crack front. While the absolute value of compliance C, cannot be accurately determined given the non-uniform crack growth, it is the change in C with a that is used in this method.

2.5.2. Validity of the ECT test

Previous analytical investigations of the ECT test indicate that the failure mode is Mode III determined in the portion of the specimen away from both ends where the loading point and supports contact the specimen [63]. However, experimental evidence on Mode III delamination growth from the insert is needed to justify the validity of the ECT test. Moreover, a three-dimensional finite element analysis is

required in order to understand boundary effects. This was the objective of the work by Li and co-workers [62]. G40-800/R6376 carbon/epoxy laminates were manufactured and tested monotonically to failure in the ECT fixture. The original stacking sequence was $[90/(+45/-45)_n/(-45/+45)_n/90]_s$, with n = 3 or 4 depending on the composite material used to manufacture the specimens. A three-dimensional finite element analysis of a typical ECT specimen was also performed. To compare the magnitude of Mode II fracture toughness to the Mode I fracture toughness, Mode II tests were performed using end-notched flexure (ENF) specimens. In addition, Mode I double cantilever beam (DCB) tests were also performed for a more complete comparison.

A typical load-displacement (P-δ) curve is shown in Figure 2.15. The curve is quite linear up to point A. After this point, the delamination grew from the insert and the stiffness decreased until a load drop was observed at P_c. A tangent to the initial linear portion of the loading curve was drawn to determine the initial compliance, $C = \delta/P$. Initial deviation from linearity due to seating of the loading fixture was ignored. The critical load P_c along with the initial delamination length was used to calculate the critical total strain energy release rate G_c.

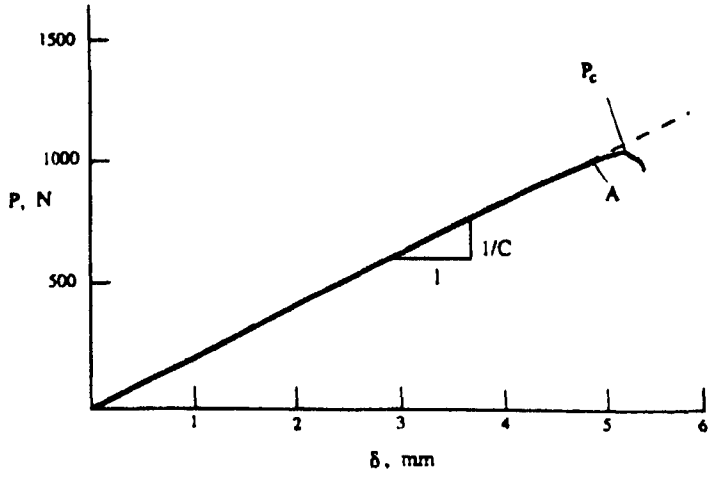

Figure 2.15: Compliance C and critical load P_c for the delamination onset determined from the ECT P – δ curve [62].

One of the main findings of the work by Li and co-workers [62] is that the delamination grew from the centre of the effective specimen length. An examination of the edge of the specimen indicated that delaminations grew at the 90°/45° and the 45°/-45° interfaces. No delamination growth was evident between the two mid-plane 90° plies where the insert was placed. As a result, Mode III type delamination growth was not achieved, which can be attributed to the fact that the insert length was too small. This leads to the conclusion that specimens with small insert lengths did not provide a big enough Mode III delamination.

A three-dimensional finite element analysis indicated that a state of pure Mode III loading exists at the middle of the specimen length away from both ends. A Mode II component was also found to exist near the ends where the loading and support points are located [62]. However, the magnitude of the Mode II strain energy release rate at the loading point is much smaller than that of Mode III component in the mid-section of the specimen. As a result, Mode III delamination is the anticipated failure mode. There was also good agreement between the total strain energy release rate calculated from the finite element model and the fracture toughness evaluated from the compliance calibration method for the ECT specimens. After performing Mode I DCB and Mode II ENF tests on the same composite material, it was found that the mean Mode II fracture toughness from five specimens was seventy-five percent of the Mode III fracture toughness. The average Mode I fracture toughness from five DCB specimens was about thirty percent of the Mode II fracture toughness and twenty-three percent of the Mode III fracture toughness.

It should be noted at this point that the original ECT test fixture consisted of a loading frame whereby the specimen was positioned between three support pins, and load was applied via a fourth pin, as can be seen in Figure 2.16.

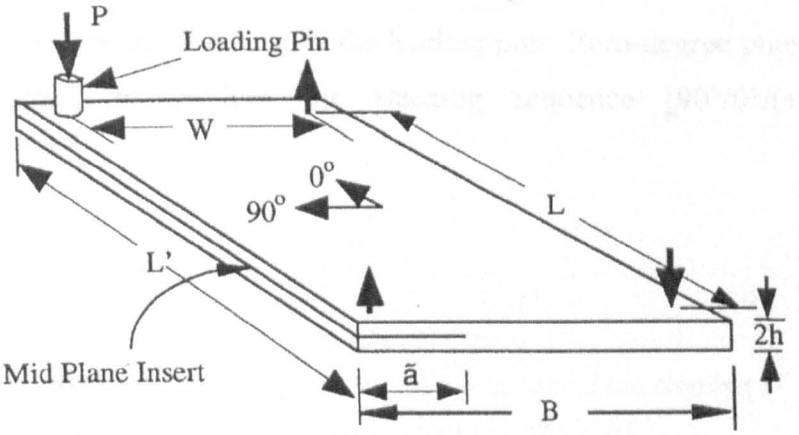

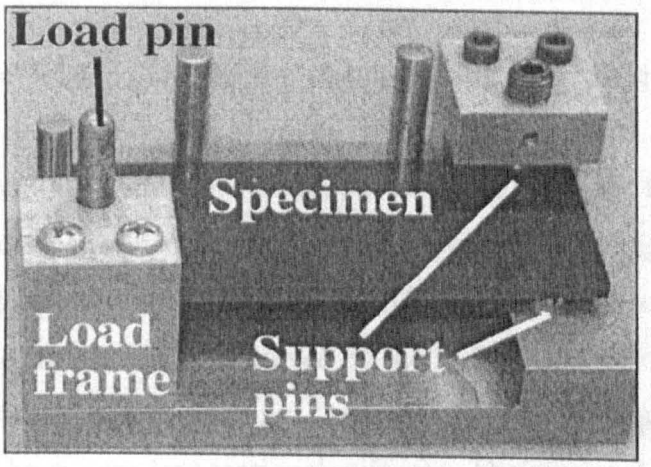

Figure 2.16: Original ECT test fixture [62].

A number of studies concluded that this specimen produced Mode III-dominated loading at the delamination front in the centre of the specimen, away from the loading points. A round-robin exercise was organised by the ASTM D30 committee to characterise the test method [64]. The ECT tests were undertaken in five independent laboratories on specimens manufactured from the toughened carbon/epoxy, HTA/6376. Large scatter in the calculated fracture toughness values were reported, and some laboratories reported significant non-linearity in the load-displacement

response of the specimens. Consequently, the test frame was modified, resulting in a symmetrical load application via two pins. A loading beam was used to allow uniform load transfer from the test machine to the loading pins. Zero-degree plies were added to the specimen, to produce the stacking sequence $[90°/0°/(+45°/-45°)_n/(-45°/+45°)_n/0°/90°]_s$.

2.5.3. Lay-up Effects

Li and Wang [65] examined favourable lay-ups for the Mode III interlaminar fracture toughness characterization and identified the Mode II influence due to bending-twist coupling in general symmetric laminates.

The success of the ECT specimen for characterizing the Mode III interlaminar fracture toughness depends on the selection of specimen lay-ups. The presence of bending-twisting coupling will induce a Mode II contribution to the total strain energy release rate. For lay-ups with negligible bending-twisting coupling, the total strain energy release rate approximately equals the Mode III strain energy release rate. Hence, a pure Mode III test can be achieved by the ECT specimen only for those lay-ups with small bending-twisting coupling. Cross-ply (0°/90°) laminates have no Mode II contribution but have very low torsional stiffness. The torsional stiffness must be high enough to initiate crack growth at a small twist angle. Adding (+45°/-45°) layers will increase the torsional stiffness but these layers create a Mode II contribution. However, as the number of (+45°/-45°) layers increases, the Mode II contribution decreases. Several lay-ups were selected by Li to rank their torsional stiffnesses and bending-twisting coupling effects against $[90°/(+45°/-45°)_3/(-45°/+45°)_3/90°]_s$ laminate. The results of their research showed that two repeat (+45°/-45°) layers in the half laminate were enough to eliminate the Mode II interference. However, more (+45°/-45°) layers may be needed to increase the torsional stiffness. Moreover, making the (+45°/-45°) layers in each half of the laminate symmetric has little effect on either the torsional stiffness or the energy release rate parameter. Taking away the outside 90° layer and putting a 0° inside, or changing the outer 90° layer to 45° or -45°, will increase the torsional stiffness considerably [65].

Another interesting finding by Li and O'Brien [63] regarding the layup of the ECT specimens, is that the sublaminates above and below the delamination plane should be symmetric about their own midplanes to eliminate any residual thermal stress contributions to strain energy release rate for delamination growth.

2.5.4. Crack Length Effects

Li and Wang [65] also investigated the effect of crack length on carbon/epoxy and glass/epoxy composite ECT specimens. The induced bending curvature was found to decrease as the crack length increased and reached a minimum as the crack ran across the entire width of the laminate. The magnitudes of the induced bending curvatures in both cases were very small compared to the twist (less than 5%). In all of the lay-ups examined, the torsional stiffness decreased as the crack length increased and reached a minimum as the crack propagated across the laminate width. Moreover, the total strain energy release rate, G_T, was found to increase as the crack length increased and reached a plateau. As the crack length continued to increase, the total strain energy release rate dropped reaching zero as the crack ran through the entire laminate width.

Ratcliffe et al [66] conducted edge crack torsion tests on specimens manufactured from IM7/8552 and S2/8552 laminates, using the modified ECT geometry. Specimens with different normalised insert lengths, ranging from 0.2 to 0.6 were tested at a rate of 1.3 mm/min. In addition, three-dimensional finite element models were constructed from both types of material, with different normalised insert lengths. The same displacement was prescribed to each model, therefore simulating displacement control used during actual ECT tests. The displacement values were chosen to ensure an elastic response from the specimens, this being 2 mm in all cases.

Figure 2.17 contains plots of G_{II} and G_{III} versus distance along the delamination front computed from analyses of the IM7/8552 ECT specimens. The plots correspond to specimens with the smallest and largest normalised insert lengths, a/b = 0.2 and a/b = 0.6 respectively.

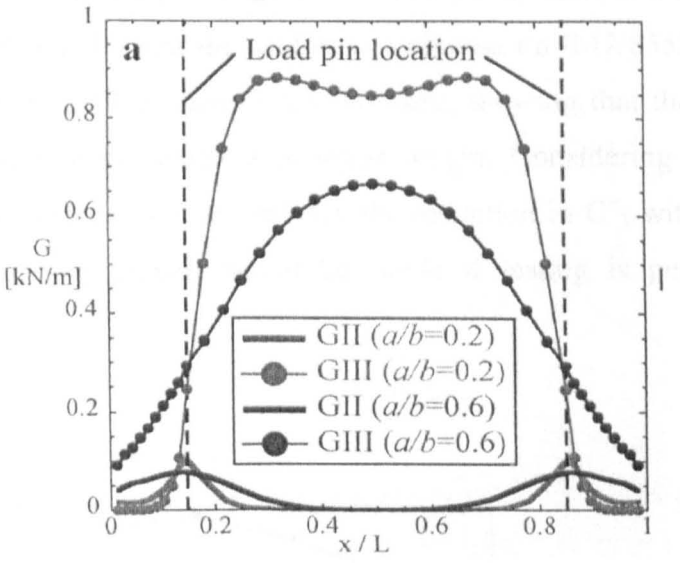

Figure 2.17: Computed strain energy release rate distribution across delamination front for IM7/8552 specimens [66].

The Mode I strain energy release rate was found to be negligible in comparison to G_{II} and G_{III} for all specimens modelled, and was therefore not included in the plot. The findings of Ratcliffe's work suggest that, for a given location along the delamination front, G_{II} and G_{III} decrease with increasing insert length. Furthermore, the strain energy release rate distributions were found to be symmetrical about the specimen mid-length. The parameter G_{II} , peaks at the locations of the load and support pins and G_{III} peaks along the centre of the specimen. The load and support pins produce a moment arm that causes relative sliding of the delaminated sections of the specimen, parallel to the intended direction of delamination growth. Consequently, G_{II} is expected to peak at the location of the load pins. The contact pressure was negligible across most of the delamination region, except at positions local to the load and support pins. Relative opening of the contact faces was also negligible, supporting the finding that G_I is negligible. In the analysis, it was assumed that sliding friction of the delaminated surfaces would not influence the strain energy release rate distributions along the delamination front, and was therefore not considered.

Ratcliffe [66] also calculated the average total strain energy release rate, $\bar{G}_T$, versus the normalised insert length from the analyses conducted on IM7/8552 and S2/8552 ECT specimens. Figure 2.18 contains a plot of these, showing that the average total strain energy release rate decreases with insert length. Considering that the same displacement was prescribed in each analysis, the reduction in $\bar{G}_T$ with insert length implies that delamination growth would be stable if testing is performed under displacement control.

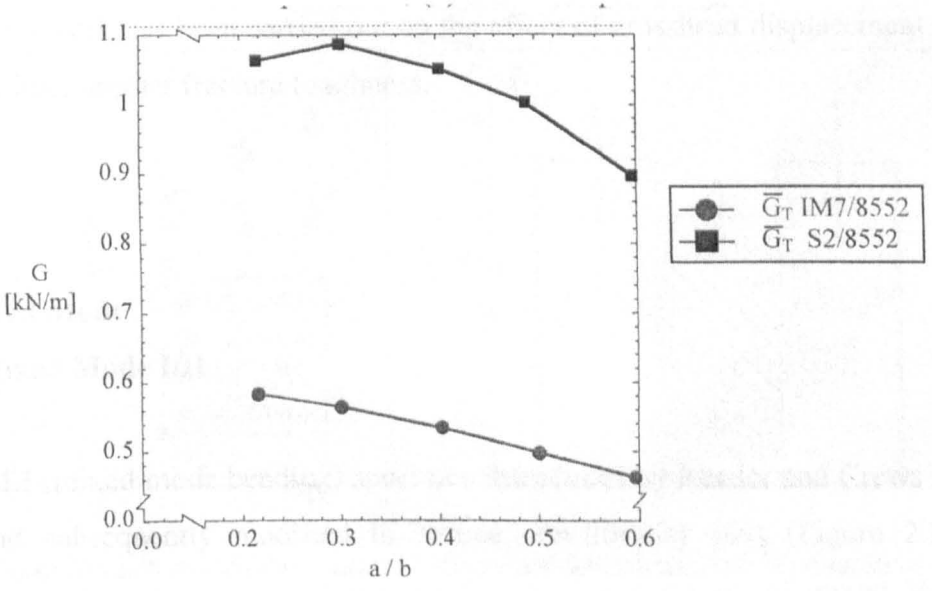

Figure 2.18: Computed average total strain energy release rate versus a/b [66].

2.5.5. Influence of Fibre Volume Fraction on Mode III Interlaminar Fracture Toughness

Li and co-workers [67] conducted ECT tests on E-glass/epoxy composite specimens with two widely differing fibre volume fractions. A large increase in the Mode III toughness was observed with decreasing fibre volume fraction. The fracture surfaces of broken specimens were inspected in optical and scanning electron microscopes. The higher initiation fracture toughness for the low fibre volume fraction composite was attributed to the increased matrix volume allowing for increased plastic

deformation energy dissipation in the matrix resin prior to macroscopic crack propagation. In addition, the fracture surfaces revealed interlaminar matrix cracks in the 90° plies adjacent to the crack plane, and such cracks were particularly numerous in the low fibre volume fraction specimens.

2.5.6. Effect of Crosshead Displacement Rate

To date, no work has been carried out on the effect of crosshead displacement rate on Mode III interlaminar fracture toughness.

2.6. Mixed Mode

2.6.1. Mixed Mode I/II

The MMB (mixed mode bending) specimen introduced by Reeder and Crews in 1988 [68], and subsequently modified to reduce non-linearity [69] (Figure 2.19) has become the most widely used specimen for the determination of mixed Mode I/II envelopes. The MMB test is the superposition of the DCB and ENF tests, and it allows any combination of Mode I and Mode II loadings to be obtained. It consists of a three-point bending test, in which the load P is applied by means of a lever with a central fulcrum, at a distance c from this fulcrum. The loading arm bends the MMB specimen at the fulcrum and pulls the delamination open at the same time, which gives a combination of Mode II (bending) and Mode I (crack opening) loadings. The mixed mode ratio I/II can be modified by changing the lever arm length c.

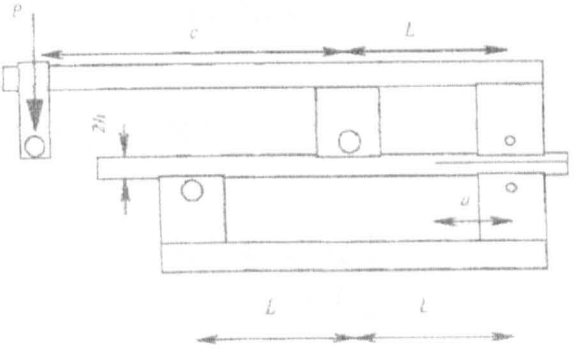

Figure 2.19: The MMB specimen geometry [68].

Furthermore, several authors have developed MMB mixed-mode envelopes using a number of different specimens. For example, the CLS (cracked lap shear) specimen was examined but then abandoned by ASTM [70, 71]. Mixed-mode loading induced by tensile tests on coupons with special stacking sequences such as the EDT (edge delamination tension) geometry [72, 73] were proposed at Texas A&M [39]. Several other mixed mode specimens have been proposed, but, compared to all these potential competitors, the advantages of the MMB configuration are the following:

- The specimen geometry is similar to that used in Mode I tests.
- It provides a simple means to vary the mixed-mode ratio over the whole range from pure Mode I to pure Mode II.

The data analysis initially proposed by Reeder and Crews [68] was based on the beam theory, and the Mode I and II components are given by:

$$G_I = \frac{3a^2P^2}{4B^2h^3E}(3c\text{-}L)^2 \qquad (2.4)$$

$$G_{II} = \frac{9a^2P^2}{16B^2h^3E}(c+L)^2 \tag{2.5}$$

Therefore the mode ratio is given by:

$$\frac{G_I}{G_{II}} = \frac{4}{3}\left[\frac{3c-L}{c+L}\right]^2 \tag{2.6}$$

with c the lever arm length and 2L the distance between the supports.

As significant Mode II components of loading can be induced with the MMB set-up it has been suggested that it might be possible to avoid the problems associated with trying to obtain a pure Mode II loading by extrapolating from a predominantly Mode II MMB test. Plotting the total G_c as a function of the G_{II} component makes the results easy to model and hence extrapolate:

$$G_{Tc} = G_{Ic} + (G_{IIc} - G_{Ic})\left(\frac{G_{II}}{G_T}\right)^m \tag{2.7}$$

Ducept and co-workers [74] conducted an experimental study on mixed-mode I/II loading of unidirectional glass/epoxy composites with variable thicknesses of the MMB specimen geometry. Crack initiation was carefully monitored and different criteria for the definition of initiation were applied. Data analysis of the MMB test was performed using both beam theory and also an experimental method based on direct displacement measurements. Fracture toughness values and mixed-mode partitioning given by both methods were shown to give similar results. The loading rate was 1 mm/min and four mixed mode ratios were selected, such that G_I/G_{II}=3, 1, 1/3 and 1/8. The components of initiation fracture toughness were calculated using the two methods mentioned above, giving similar results for the ratios and criteria.

However, it should be noted that the experimental method became less effective as the proportion of Mode II grew because the test became unstable.

The research also examined the independence of the MMB test results on specimen geometry. This was done for 16 and 24 ply composites and it was found that the results from the MMB tests were independent of specimen geometry when either onset of non-linearity or acoustic emission are used to define initiation. The experimental displacement measurement in the MMB tests yielded similar results to beam theory, in terms of mode separation and G_c values.

Further work by Ducept and co-workers [75] was carried on adhesively bonded composites, under Mode I (DCB), Mode II (ENF) and mixed mode I/II (MMB) loading. The specimens were obtained by bonding together two 8 ply glass epoxy laminates with a two-part epoxy adhesive. The starter defect film was placed in the adhesive layer. The test resulted in a typical failure behaviour concerning crack stability. In addition, very high fracture energies were measured. However, if one supposes that such stability can be attributed to the size of the crack tip plastic zone, the application of a linear elastic fracture mechanics approach beyond initiation should be used carefully when studying bonded joints. Based on a comparison of the mixed-mode envelopes the tough adhesive employed in this experimental work should provide a very damage tolerant assembly.

2.7. Other Mixed Mode Tests

In addition to mixed-mode I/II loading it is also possible to develop specimens for obtaining I/III and II/III combinations, however no standard test methods have been developed.

2.8. Virtual Crack Closure Technique

2.8.1. Introduction

A variety of methods are used to compute the strain energy release rate based on results obtained from finite element analyses. For delamination in laminated composite materials where the failure criterion is highly dependent on the mixed-mode ratio and propagation occurs in the laminate plane, the virtual crack closure technique (VCCT) has been the most widely used for computing energy release rates because fracture mode separation is determined explicitly. Krueger [1] gave a comprehensive overview of the virtual crack closure technique with equations for applying the technique using two-dimensional quadrilateral and three-dimensional solid elements, as well as plate/shell elements.

2.8.2. Crack Closure Method using Two Analysis Steps

Before referring to the VCCT, it would be appropriate to include the crack closure method because the crack is physically extended or closed, during two complete finite element analyses, as shown in Figure 2.20. This is based on Irwin's crack closure integral [76, 77]. The method is based on the assumption that the energy ΔE released when the crack is extended by $\Delta\alpha$ from α to $\alpha + \Delta\alpha$ is identical to the energy required to close the crack between location 1 and i. For a crack modelled with two-dimensional four-noded elements as shown in Figure 2.20, the work ΔE required to close the crack along one element side can be calculated as:

$$\Delta E = \frac{1}{2}\left[X_{1l}\,\Delta u_{2l} + Z_{1l}\,\Delta w_{2l}\right] \tag{2.8}$$

where X_{1l} and Z_{1l} are the shear and opening forces at the nodal point 1 to be closed and Δu_{2l} and Δw_{2l} are the differences in shear and opening nodal displacements at node l. The crack closure method establishes the original condition before the crack

was extended. Therefore the forces required to close the crack are identical to the forces acting on the upper and lower surfaces of the closed crack. The forces X_{II} and Z_{II} can be obtained from a first finite element analysis where the crack is closed, by summing the forces at common nodes from elements belonging either to the upper or the lower surface.

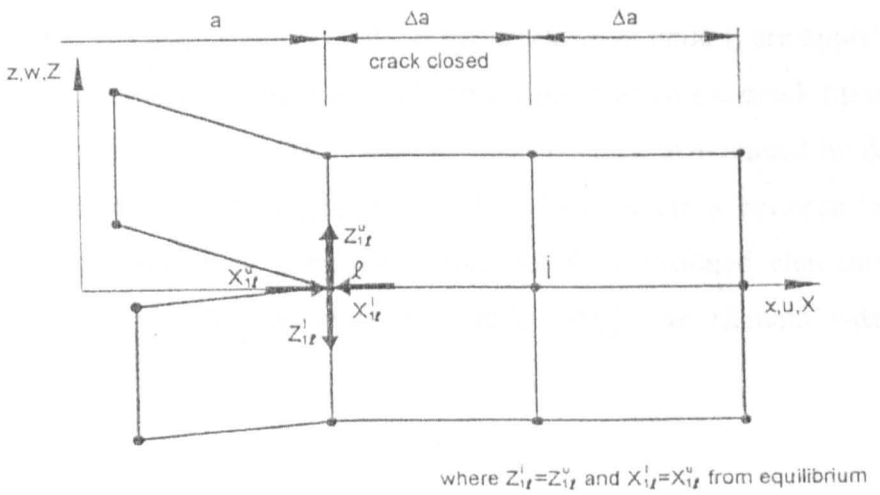

(a) First Step: Crack Closed [1].

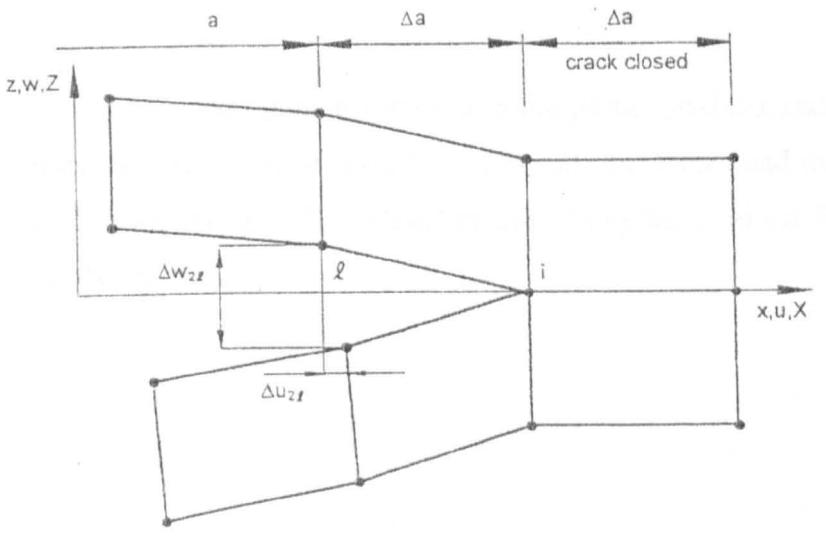

(b) Second Step: Crack Extended [1].

Figure 2.20: Crack closure method (two-step method)
(a) First Step-crack closed and (b) Second Step-crack extended

2.8.3. The Virtual Crack Closure Method (VCCT)

The virtual crack closure method (VCCT) is based on the same assumptions as the crack closure method, which has already been described. In addition, the assumption is made, that a crack extension of Δa from $a + \Delta a$ to $a + 2\Delta a$ (node k) does not significantly alter the stress state at the crack tip. As a result, when the crack tip is located at node k, the displacements behind the crack tip at node I, are approximately equal to the displacements behind the crack tip at node l when the crack tip is located at node i. Moreover, the energy ΔE released when the crack is extended by Δa from $a + \Delta a$ to $a + 2\Delta a$ is equal to the energy required to close the crack between locations i and k. For a crack modelled using two-dimensional, four-noded elements, Figure 2.21, the work ΔE required to close the crack along one element side can be calculated as:

$$\Delta E = \frac{1}{2}[X_i \, \Delta u_l + Z_i \, \Delta w_l] \tag{2.9}$$

where X_i and Z_i are the shear opening forces at nodal point I and Δu_l and Δw_l are the shear and opening displacements at node l. As a result, the forces and displacements required to calculate the energy ΔE to close the crack may be obtained from a single finite element analysis.

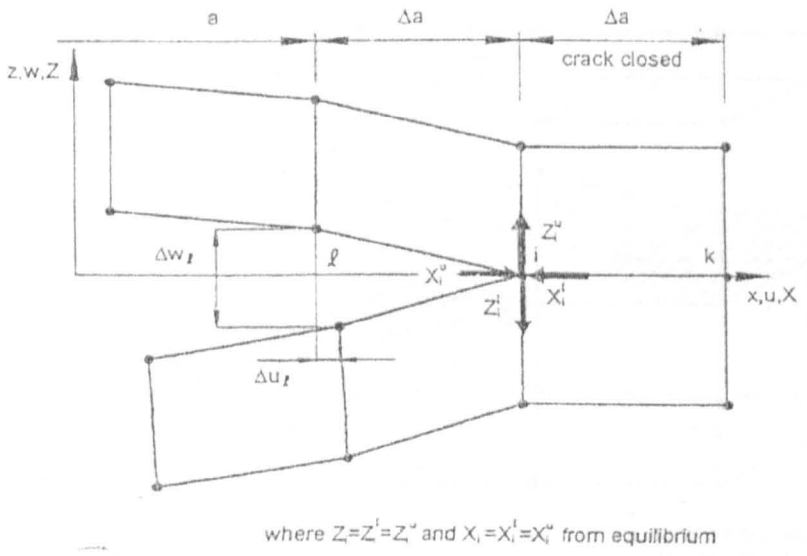

Figure 2.21: One-step VCC [1].

2.8.4. Formulas for Three-Dimensional Solid Elements

In a finite element model made of three-dimensional solid elements, the delamination of length α is represented as a two-dimensional discontinuity at two surfaces. The third dimension allows the calculation of the distribution of the energy release rates along the delamination front and makes it possible to obtain G_{III}, which is identical to zero for two-dimensional models. Nodes at the top and bottom surfaces are not connected to each other. The delamination front is represented by either a row of single nodes or two rows with identical coordinates, coupled through multipoint constraints. The undamaged section where the delamination is closed and the structure is intact, is modelled using single nodes or two nodes with identical coordinates coupled through multipoint constraints if a delamination propagation analysis is required.

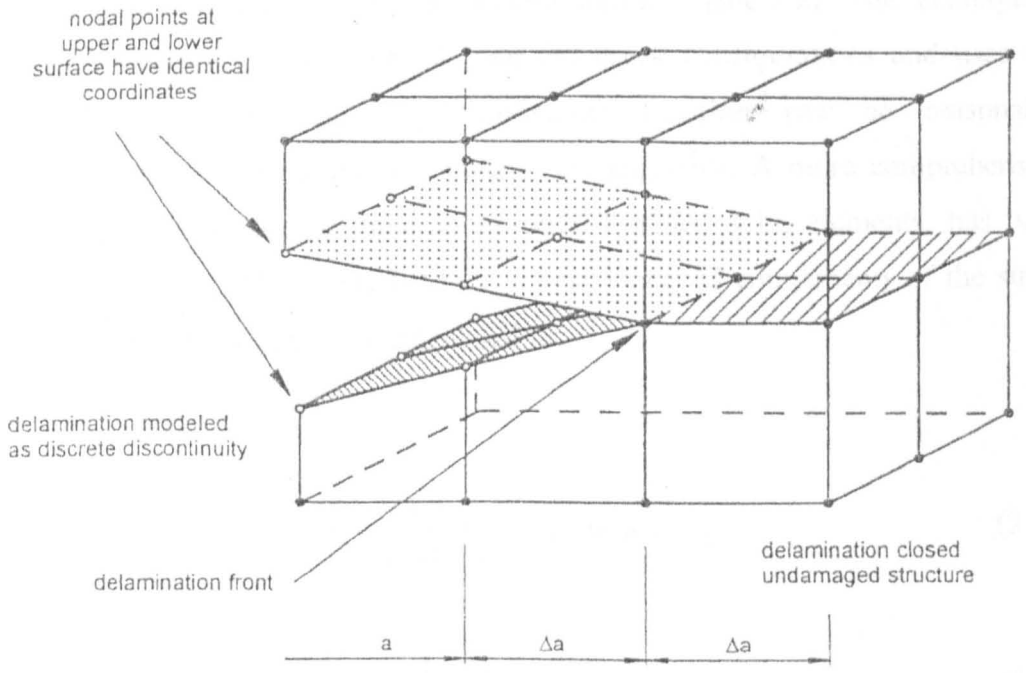

(a) Delamination modelled with bilinear three-dimensional solid elements [1].

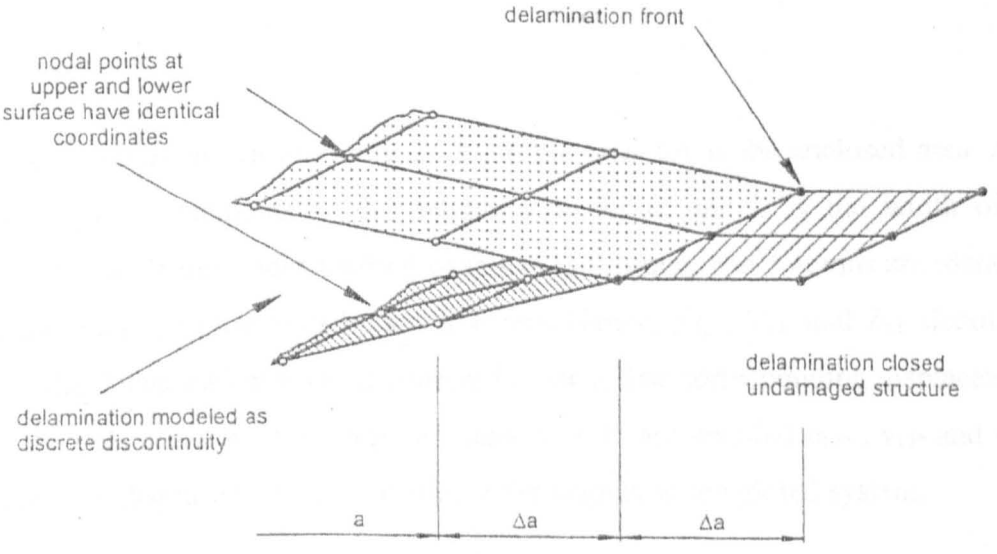

(b) Delamination modelled with bilinear plate/shell elements [1].

Figure 2.22: Delaminations modelled as two-dimensional discontinuity.

(a) Delamination modelled with bilinear 3D solid elements

(b) Delamination modelled with bilinear plate/shell elements

For convenience, only a section of the delaminated area that was modelled with eight-noded three-dimensional solid elements is illustrated in Figure 2.22. The technique is an extension of Rybicki-Kanninen [78] for 2D crack configurations and uses the fundamental assumption that any continuous function can be reasonably approximated by a finite number of straight line segments. A more comprehensive reference to the formulae for three-dimensional 8-noded solid elements, has been given by Krueger [1]. The Mode I, Mode II and Mode III components of the strain energy release rate G_I, G_{II}, G_{III} are calculated as:

$$G_I = \frac{1}{2\Delta A} Z_{Li} (w_{LI} - w_{LI^*}) \tag{2.10}$$

$$G_{II} = \frac{1}{2\Delta A} X_{Li} (u_{LI} - u_{LI^*}) \tag{2.11}$$

$$G_{III} = \frac{1}{2\Delta A} Y_{Li} (v_{LI} - v_{LI^*}) \tag{2.12}$$

With $\Delta A = \Delta a b$ as shown in Figure 2.23. In this case ΔA is the enclosed area, Δa is the length of the elements at the delamination front, and b is the width of the elements. For a clearer understanding of this in the figures, the columns are identified by capital letters and the rows by small letters. Hence, X_{Li}, Y_{Li} and Z_{Li} denote the forces at the delamination front in column L, row i. The corresponding displacements behind the delamination at the top face node row 1* are denoted u_{LI^*}, v_{LI^*} and w_{LI^*}. All forces and displacements are obtained with respect to the global system.

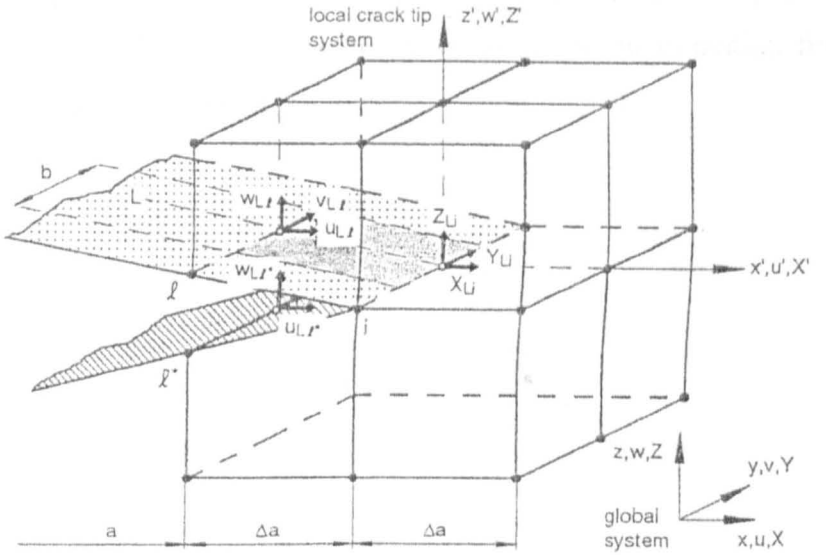

(a) 3D View (lower surface forces are omitted for clarity) [1].

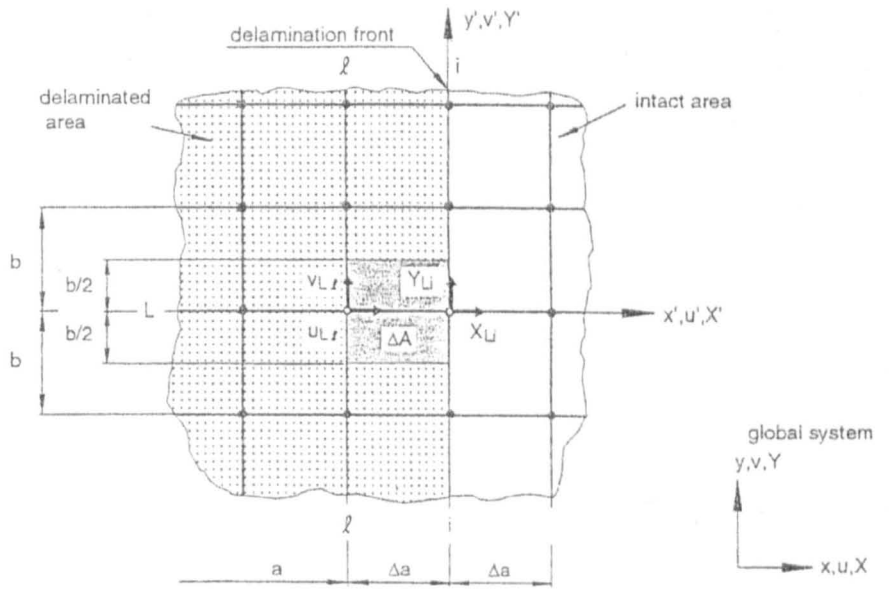

(b) Top view of upper surface (lower surface terms are omitted for clarity) [1].

Figure 2.23. Virtual Crack Closure Technique for four-noded plate/shell and eight-noded solid elements.

(a) 3D view (lower surface forces are omitted for clarity)

(b) Top view of upper surface (lower surface terms are omitted for clarity)

The virtual crack closure technique is a tool that has been extensively used in this research programme to calculate the Mode II and Mode III components of strain energy release rate (G_{II} and G_{III} respectively) along the delamination front the ECT finite element models examined.

2.9. References

1. Krueger R., Virtual crack closure technique: history, approach and applications, Applied Mechanics Review Vol.57, 2004, p.109.

2. Krueger R., Minguet P.J., O'Brien T.K., International Conference on Composite Materials, July 12-14, 2003.

3. Chai H., The characterization of Mode I delamination failure in non-woven multidirectional laminates, Composites, Vol.15, 1984, p.277.

4. Pereira A.B., de Morais A.B., de Moura M.F.S.F., Magalhaes A.G, Mode I interlaminar fracture of woven glass/epoxy multidirectional laminates, Composites Applied Science and Manufacturing, Part A 36, 2005, p.1119.

5. ASTM D5528-94a, Protocols for interlaminar fracture testing, American Society for Testing and Materials, Philadelphia, Pennsylvania, Vol. 4, 1994.

6. JIS 7086, Protocol for interlaminar testing of composites, Japanese Industrial Standards Group, Tokyo, Japan, 1993.

7. Jiménez M.A., Miravete A., Application of the finite element method to predict the onset of delamination growth, Journal of Composite Materials, Vol.38, 2004, p.1309.

8. Jordan W.M., Bradley W.L., Moulton R.J., Relating resin mechanical properties to composite delamination fracture toughness, Journal of Composite Materials, Vol.23, 1989, p.923.

9. Bradley W.L., Matrix deformation and fracture in graphite-reinforced epoxies, delamination and debonding of materials, A.S.T.M. STP 876, American Society for Testing and Materials, Philadelphia, Pennsylvania, 1986, p.389.

10. Chai H., On the correlation between the Mode I failure of adhesive joints and laminated composites, Engineering Fracture Mechanics, Vol.24, 1986, p.413.

11. Blackman B.R.K., Kinloch A.J., Paraschi M., Teo W.S., Measuring the Mode I adhesive fracture energy, GIc, of structural adhesive joints: the results of an international round-robin, International Journal of Adhesion & Adhesives, Vol.23, 2003, p.293.

12. Dorey G., Impact and crashworthiness of composite structures, New York, Elsevier Applied Science Publications, Vol.1, 1984.

13. Morton J. and Godwin E.W., Impact response of tough carbon-fibre composites, Composite Structures Vol.13, 1989, p.1.

14. Cantwell W.J., Curtis P.T., Morton J., An assessment of the impact performance of cfrp reinforced with high-strain carbon fibres, Composites Science and Technology, Vol.25, 1986, p.133.

15. Mall S., Law G.E., Katouzian M., Proceedings SEM Spring Conference on Experimental Mechanics, 1986, p.412.

16. Mall S., Law G.E., Katouzian M., Loading rate effect on interlaminar fracture toughness of a thermoplastic composite, Journal of Composite Materials, Vol.21, 1987, p.569.

17. Gillespie J.W., Carlsson L.A., Smiley A.J., Rate-dependent Mode I interlaminar crack growth mechanisms in graphite-epoxy and graphite-PEEK, Composite Science and Technology, Vol.28, 1987, p.1.

18. Smiley A.J., Pipes R.B., Rate effects on Mode I interlaminar fracture toughness in composite materials, Journal of Composite Materials, Vol.21, 1987, p.670.

19. Friedrich K., Walter R., Carlsson L.A., Smiley A.J., Gillespie J.W., Mechanisms for rate effects on interlaminar fracture toughness of carbon epoxy and carbon PEEK composites, Journal of Materials Science, Vol.24, 1989, p.3387.

20. Glessner A.L., Takemori M.T., Vallance M.A., Gifford S.K., Composite Materials, Fatigue and Fracture, The influence of loading rate on the mixed-mode interlaminar fracture properties of carbon fibre reinforced PEEK, Vol. 2, 1989, p.181.

21. Beguelin P., Barbezat M., Kausch H.H., Mechanical characterization of polymers and composites with a servohydraulic high-speed tensile tester, Journal of Physics III, Vol.1, 1991, p.1867.

22. Hashemi S., Kinloch A.J., Williams J.G., The effects of geometry, rate and temperature on the Mode I, Mode II and mixed-Mode I/II interlaminar fracture of carbon fibre/PEEK composites, Journal of Composite Materials, Vol.24, 1990, p.918.

23. Daniel I.M., Yaniv G., Auser J.W., Rate effects on delamination fracture toughness of graphite epoxy composites, Proceedings 4th International Conference on Composite Structures, 1987, p.2258.

24. Blackman B.R.K., Dear J.P., Kinloch A.J., MacGillivray H., Wang Y., Williams J.G., Yayla P., The failure of fibre composites and adhesively bonded fibre composites under high rates of test-Mode I loading, experimental studies, Journal of Materials Science, Vol.30, 1995, p.5885.

25. Matsumoto D.S., McKinley B.J., Todt M.L., Gifford S.K., General Electric Research Report No.89CRD104, 1989.

26. Daniel I.M., Shareef I., Aliyu A.A., Johnston N.J., Rate effects on delamination fracture toughness of a toughened composite, ASTM STP937, 1987.

27. Cantwell W.J., The influence of loading rate on the interlaminar fracture properties of a toughened carbon fibre reinforced plastic, Advanced Composite Letters, Vol.4, 1995, p.41.

28. Johnson W.S., Mangalgiri P.D., Investigation of fibre bridging in double cantilever beam specimens, NASA Technical Memorandum 87716, 1986.

29. Cantwell W.J., Kausch H.H., An evaluation of the interlaminar fracture toughness of a thermoplastic composite with offset center plies, Mechanics of Composite Materials, Vol.28, 1992, p.328.

30. Mall S., Law G.E., Katouzian M., Fracture toughness in random chopped fibre-reinforced composites and their strain rate dependence, Proceedings SEM Spring Conference on Experimental Mechanics, 1986, p.412.

31. Mall S., Law G.E., Katouzian M., Loading rate effect on interlaminar fracture toughness of a thermoplastic composite, Journal of Composite Materials, Vol.21, 1987, p.569.

32. Tanaka K., Kageyama K., Hojo M., Prestandardization study on Mode I interlaminar fracture toughness test for CFRP in Japan, Composites, Vol.26, 1995, p.243.

33. JIS K 7086:1993: Testing methods for interlaminar fracture toughness of carbon fibre reinforced plastics, Japanese Industrial Standards Group, Tokyo, Japan.

34. Barrett J.D., Foschi R.O., Mode II stress intensity factors for cracked wood beams, Engineering Fracture Mechanics, Vol.9, 1977, p.371.

35. Russell A.J., Street K.N., Influence des propriétés de la matrice sur l comportement mécanique de matériaux composites verre/polyester utilisés en construction navale de plaisance - Cas des résines polyester limitant les émissions de styrene, Proceedings ICCM4 Tokyo, 1982, p.279.

36. Davies P., Blackman B.R.K., Brunner A.J., Standard test methods for delamination resistance of composite materials: current status, Applied Composite Materials, Vol.5, 1998, p.345.

37. Hojo M., Kageyama K., Tanaka K., Prestandardization study on Mode I interlaminar fracture toughness test for CFRP in Japan, Composites, Vol. 26, 1995, p.243.

38. Tanaka K., Proceedings Meeting, Japan Society for Composite Materials, 1991, p.31.

39. Vanderkley P.S., M.S. Thesis, Texas A&M University, 1981.

40. Russell A.J., Street K.N., The effect of matrix toughness on fiber composites, ASTM STP 937, 1987.

41. Martin R., Davidson B.S., Proceedings 4th International Conference on Deformation & Fracture of Composites, 1997, p.243.

42. Zile E., Tamuzs V., Mode II delamination of a unidirectional carbon fibre/epoxy composite in four point bend end notched flexure tests, Mechanics of Composite Materials, Vol.41, 2005, p.383.

43. Chai H., Interlaminar shear fracture of laminated composites, International Journal of Fracture, Vol.43, 1990, p.117.

44. Chou I., Kimpara I., Kageyama K., Ohsawa I., Mode I and Mode II fracture in composites, Composite Materials, Fatigue and Fracture, Vol.5, ASTM STP 1230,1995.

45. Polaha J.J., Davidson B.D., Hudson R.C., Pieracci A., Effects of mode ratio, ply orientation and precracking on the delamination toughness of a laminated composite, Journal of Reinforced Plastics and Composites, Vol.15, 1996, p.141.

46. Choi N.S., Kinloch A.J., Williams J.G., Delamination fracture of multidirectional carbon-fiber/epoxy composites under Mode I, Mode II and mixed Mode I/II loading, Journal of Composite Materials, Vol.33, 1999, p.73.

47. Ozdil F., Carlsson L.A., Davies P., Beam analysis of angle-ply laminate end notched flexure specimens, Composite Science and Technology, Vol.58, 1998, p.1929.

48. Tao J.X., Sun C.T., Influence of ply orientation on delamination in composite laminates, Journal of Composite Materials, Vol.32, 1998, p. 1933.

49. Hwang J.H., Kwon O., Lee C.S., Hwang W., Interlaminar fracture and low velocity impact on carbon/epoxy composite materials, Mechanics of Composite Materials, Vol.36, 2000, p.117.

50. Pereira A.B., de Morais A.T., Marques A.T., de Castro P.T., Mode II interlaminar fracture of carbon/epoxy multidirectional laminates, Composite Science and Technology, Vol.64, 2004, p.1653.

51. Jordan W.M., Bradley W.L., Moulton R.J., Relating resin mechanical properties to composite delamination facture toughness, Journal of Composite Materials, Vol.23, 1989, p.923.

52. Chai H., Shear fracture, International Journal of Fracture, Vol.37, 1988, p.137.

53. Ducept F., Davies P., Gamby D., Mixed Mode failure criteria for a glass/epoxy composite and an adhesively-bonded composite/composite joint, International Journal of Adhesions &Adhesives, Vol.20, 2000, p.233.

54. Chai H., The effects of bond thickness, rate and temperature on the deformation and fracture of structural adhesives under shear loading, International Journal of Fracture, Vol.134, 2004, p.497.

55. Blackman B.R.K., Dear J.R., Kinloch A.J., MacGillivray H., Wang Y., Williams J.G., Yayla P., The failure of fibre composites and adhesively-bonded fibre composites under high rates of test. Mixed-Mode I/II and Mode II loadings, Journal of Materials Science, Vol.31, 1996, p.4467.

56. Corleto C.R., Bradley W.L., Mode II delamination fracture toughness of unidirectional graphite/epoxy composites, Composite Materials:Fatigue and Fracture, ASTM STP 1012, 1989.

57. Cantwell W.J., Zulfkifli R., The interlaminar fracture properties of composite materials under high rates of strain, Journal of Materials Science, 1998, p.509.

58. Donaldson S.L., Proceedings of the 6th International Conference on Composite Materials (ICCM-V1) held at Imperial College of Science and Technology, London, UK, Vol. 3, July 20-24, 1987, Vol. 3, p.274.

59. Donaldson S.L., Mode III interlaminar fracture characterization of composite materials, Composite Science and Technology, Vol.32, 1988, p.225.

60. Becht G., Gillespie J.W., Design and analysis of the crack rail shear specimen for Mode III interlaminar fracture, Composite Science and Technology, Vol.31, 1988, p.143.

61. Lee S.M., An edge crack torsion method for Mode III delamination fracture testing, Journal of Composites Technology and Research, Vol. 15, 1993, p.193.

62. Li J., Lee S.M., Lee E.W., O'Brien T., Evaluation of the edge crack torsion (ECT) test for Mode III interlaminar fracture toughness of laminated composites, Journal of Composites Technology and Research, Vol.19, 1997, p.174.

63. Li J., O'Brien T.K., Simplified data reduction methods for the ECT test for Mode III interlaminar fracture toughness, Journal of Composites Technology and Research, Vol.18, 1996, p.96.

64. Minutes of Sub-Committee D30.06 on Interlaminar Properties, Report from the First Round-Robin on the Edge Crack Torsion Test, May 1999.

65. Li J., Wang Y., Analysis of Mode III delamination fracture testing using the ECT specimen geometry, Composite Materials: Testing and Design, ASTM STP 1274, 1996.

66. Ratcliffe J.G., Characterization of the edge crack torsion (ECT) test for Mode III fracture toughness measurement of laminated composites, National Research Council, NASA Langley Research Centre, Hampton, Virginia, September 2004.

67. Li X., Carlsson L.A., Davies P., Influence of fibre volume fraction on Mode III interlaminar fracture toughness of glass/epoxy composites, Composites Science and Technology, Vol.64, 2004, p.1279.

68. Crews J.H., Reeder J.R., NASA TM100662, 1988.

69. Reeder J.R., Crews J.H., NASA TM102777, 1991.

70. Johnson W.S., NASA Tech. Memo 89006, 1986.

71. Gustafson C.G., Hojo M., Holm D.J., A nonlinear analysis of the CLS specimen, Composite Materials, Vol.23, 1989, p.146.

72. Johannesson T., Blikstad M., Proceedings ISCMS, Beijing, June 1986, p.495.

73. O'Brien T.K., ASTM STP 836, 1984.

74. Ducept F., Davies P., Gamby D., An experimental study to validate tests used to determine mixed mode failure criteria of glass/epoxy composites, Journal of Composites Vol. 29, 1997, p.719.

75. Ducept F., Davies P., Gamby D., Mixed-mode failure criteria for a glass/epoxy composite and an adhesively bonded composite/composite joint, International Journal of Adhesion and Adhesives, Vol.20, 2000, p.233.

76. Irwin G.R., Fracture I, Handbuch der Physik VI, Springer Verlag, Berlin, Germany, 1958.

77. Broek D., Elementary Engineering Fracture Mechanics, 4th Revised Edition, Kluwer Academic Publishers, Dordrecht, Netherlands, 1991.

78. Rybicki E.F., Kanninen M.F., Finite element calculation of stress intensity factors by a modified crack closure integral, Engineering Fracture Mechanics, Vol.9, 1977, p.931.

3. Numerical Procedure

3.1. Introduction

The Mode III interlaminar fracture properties, G_{IIIc}, of composite materials based on both thermoplastic and thermosetting-matrices have been investigated using the Edge Crack Torsion (ECT) test geometry. Information concerning the crack-tip loading conditions is obtained by undertaking a finite element analysis of the ECT specimen geometry.

The combinations of materials examined in this research programme were a glass fibre reinforced polypropylene, a woven glass fibre reinforced epoxy, an adhesively-bonded glass fibre reinforced epoxy and a bi-material system, consisting of spring steel bonded to a woven glass fibre reinforced epoxy. Three-dimensional finite element models of specimens manufactured using an isotropic material, as well those mentioned above, were constructed using the ANSYS finite element analysis software package.

Verification of the analyses was undertaken by comparing the predicted elastic responses of the ECT specimens with those determined experimentally during the ECT tests. The finite element analyses focused on determining the distribution of the Mode II and Mode III strain energy release rates along the crack front and investigating the influence of a number of factors, such as the crack length, the applied displacement and the specimen thickness on the crack-tip loading conditions in these specimens. The ECT specimen geometry and positions of applied loads were further modified to investigate their effect on the Mode III strain energy release rate.

3.2. Finite Element Analysis

Finite Element Analysis (FEA) is a computer-based numerical technique for calculating the strength and behaviour of engineering structures. It can be used to calculate deflection, stress, vibration, buckling behaviour and many other phenomena. Furthermore, it can be used to analyse either small or large-scale deflection under loading or applied displacement. It can also analyse elastic deformation, or "permanently bent out of shape" plastic deformation. The computer is required because of the astronomical number of calculations needed to analyse a large structure. The power and low cost of modern computers has made Finite Element Analysis available to many disciplines and companies.

In the finite element method, a structure is broken down into many small simple blocks or elements. The behaviour of an individual element can be described with a relatively simple set of equations. Just as the set of elements would be joined together to build the whole structure, the equations describing the behaviour of the individual elements are introduced into an extremely large set of equations that describe the behaviour of the whole structure. The computer can solve this large set of simultaneous equations. From the solution, the computer extracts the behaviour of the individual elements, yielding the stress and deflection of all the parts of the structure. The stresses will be compared to allowed values of stress for the materials to be used, to determine if the structure is sufficiently strong.

The term "finite element" distinguishes the technique from the use of infinitesimal "differential elements" used in calculus, differential equations, and partial differential equations. The method is also distinguished from finite difference equations, for which although the steps into which space is divided are finite in size, there is little freedom in the shapes that the discreet steps can take. The finite element analysis technique is a way to deal with structures that are more complex than can be dealt with analytically using partial differential equations. FEA deals with complex boundaries better than finite difference equations will, and gives answers to "real world" structural problems. It has been substantially extended in scope during the roughly 40 years of its use.

3.3. Model Steps

The ultimate purpose of a finite element analysis is to recreate mathematically the behaviour of an actual engineering system. In other words, the analysis must be an accurate mathematical model of the physical prototype. In the broadest sense, this model should comprise all the nodes, elements, material properties, real constants, boundary conditions and other features that are used to represent the physical system. In ANSYS terminology, the term "model generation" usually takes on the narrower meaning of generating the nodes and elements that represent the spatial volume and connectivity of the actual system. Thus "model generation" means the process of defining the geometric configuration of the model's nodes and elements.

The following steps were used as a guideline in preparing the isotropic ECT models using the ANSYS FE package:

- Define the Analysis Type
- Input Geometry
- Define Element Type, Material Model Properties
- Generate Mesh
- Apply Loads
- Obtain Solution
- Review Results

In the following pages, a brief description of these steps will be given.

3.4. Element Types

The element type used in a finite element analysis is of great importance; over 100 element types are available in ANSYS. Therefore, it has to be chosen correctly in order to characterise the degree of freedom set (displacements and/or rotations,

temperatures etc.), the characteristic shape of the element (line, quadrilateral, brick etc.), whether the element lies in 2-D or 3-D space, the response of the system and the accuracy level we are interested in. An overview of the elements used to create and analyze the FEA models ran in this research programme will be given.

3.4.1. SOLID45

SOLID45 was the element type used to model the isotropic materials used in this research programme. These involved the isotropic ECT specimens, the epoxy adhesive in the adhesively-bonded glass fibre reinforced epoxy specimens, as well as the spring steel used in the bi-material ECT specimens. This element is used for the 3-D modelling of solid structures. The element is defined by eight nodes having three degrees of freedom at each node: translations are permitted in the nodal x, y, and z directions. The element has plasticity, creep, swelling, stress stiffening, large deflection, and large strain capabilities [1]. A reduced integration option with hourglass control is also available. The geometry, node locations, and the coordinate system for this element are shown in Figure 3.1:

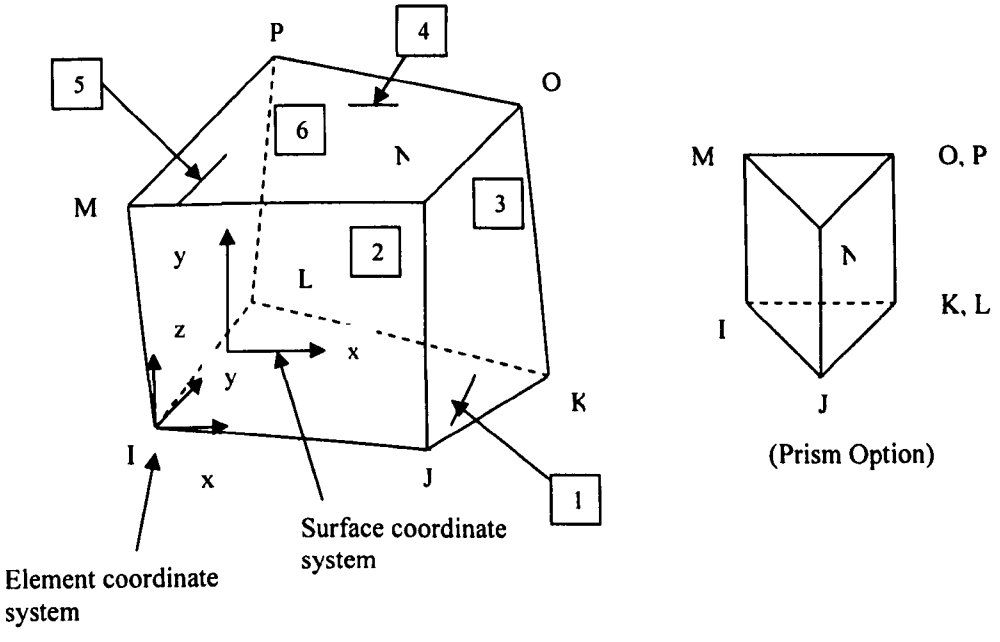

Figure 3.1: SOLID45 geometry [1].

3.4.2.SOLID46

SOLID46 is a layered version of the 8-node structural solid (SOLID45) designed to model layered thick shells or solids [1]. The element allows up to 250 different material layers and was used to model the two different orthotropic materials investigated in this research programme, these being the glass fibre reinforced polypropylene and woven glass fibre reinforced epoxy. If more than 250 layers are required, a user-input constitutive matrix option is available. The element may also be stacked as an alternative approach. The element has three degrees of freedom at each node: translations in the nodal x, y, and z directions. The geometry, node locations, and the coordinate system for this element are shown in Figure 3.2. The element is defined by eight nodes, the layer thicknesses, the layer material direction angles, and the orthotropic material properties. Shear moduli G_{XZ} and G_{YZ} must be within a factor of 10,000 of each other. The element z-axis is defined to be normal to a flat reference plane. If the nodes imply a warped surface, an averaged flat plane is used. The default element x-axis is the projection of side I-J, side M-N, or their average onto the reference plane. The input may be either in matrix form or layer form. For matrix form, the matrices must be computed outside of ANSYS. For layer (non-matrix) input, the layer thicknesses used are computed by scaling the input real constant thicknesses to be consistent with the thicknesses between the nodes. The node locations may imply that the layers are tilted or warped. However, the local coordinate system for each layer is effectively reoriented parallel to the reference plane. The layer number can range from 1 to 250. In this local right-handed system, the x'-axis is rotated an angle theta (in degrees) from the element x-axis toward the element y-axis. The material properties of each layer may be orthotropic in the plane of the element. A real constant is used to define the layer material number instead of the element material number. It should also be noted that the material x direction corresponds to the local layer x' direction.

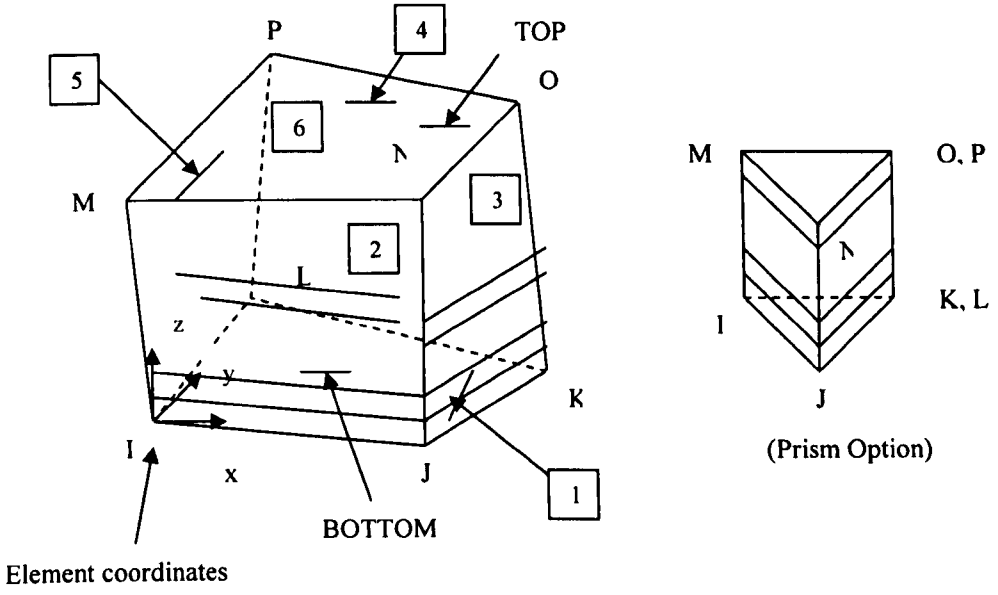

Figure 3.2: SOLID46 geometry [1].

3.4.3. CONTA175

CONTA175 may be used to represent contact and sliding between two surfaces (or between a node and a surface, or between a line and a surface) in 2-D or 3-D models [1]. The element is applicable to 2-D or 3-D structural contact analyses. This element can be located on the surfaces of solid, beam, and shell elements. 3-D solid elements with midside nodes are not supported. Contact occurs when the element surface penetrates one of the target segment elements (TARGE170) on a specified target surface. Coulomb and shear stress friction is allowed. The geometry of CONTA175 is shown in Figure 3.3:

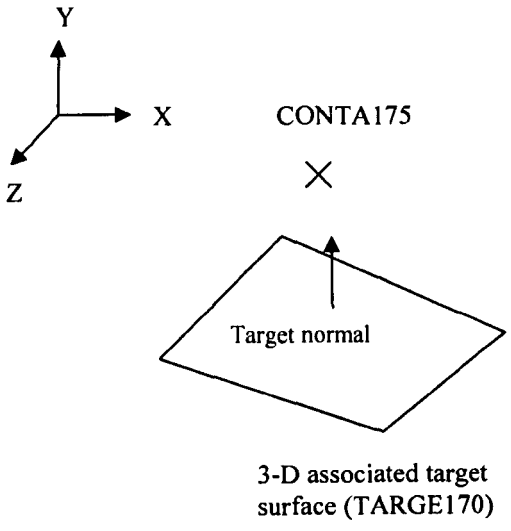

Figure 3.3: CONTA175 geometry [1].

The element is defined by one node. The underlying elements can be 2-D or 3-D solid, shell, or beam elements. The 3-D underlying elements must have no midside nodes. CONTA175 represents 2-D or 3-D contact depending on whether the associated 2-D (TARGE169) or 3-D (TARGE170) segments are used. Contact can occur only when the outward normal direction of the target surface points to contact surface.

3.4.4. TARGE170

TARGE170 is used to represent various 3-D "target" surfaces for the associated contact elements (CONTA173, CONTA174 and CONTA175) [1]. The contact elements themselves overlay the solid elements describing the boundary of a deformable body and are potentially in contact with the target surface, defined by TARGE170. This target surface is discretised by a set of target segment elements

(TARGE170) and is paired with its associated contact surface via a shared real constant set. Any translational or rotational displacement, temperature, voltage, and magnetic potential can be imposed on the target segment element. Forces and moments can be imposed on target elements too. In the following figure, the geometry of TARGE170 element is shown:

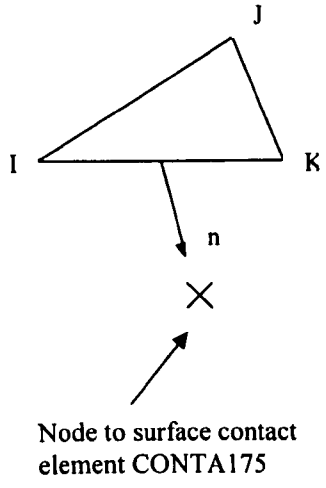

Figure 3.4: TARGE170 geometry [1].

3.5. ECT Specimen Models

3.5.1. Isotropic Models

Three-dimensional finite element models of isotropic ECT specimens were constructed and analysed using ANSYS. The specimens had normalised insert lengths ranging between 0.3 and 0.7. A linear isotropic model was used in the simulation and the material was assumed to have a Young's Modulus E_X of 73 GPa and a Poisson's ratio ν_{XY} of 0.3. The specimens had a length L of 108 mm, a width b of 38 mm and a thickness of 7 mm, as shown in Figure 3.5. It should be noted that the distance l is equal to 76 mm and the displacement is applied in the y direction at a distance of 3 mm from the edge.

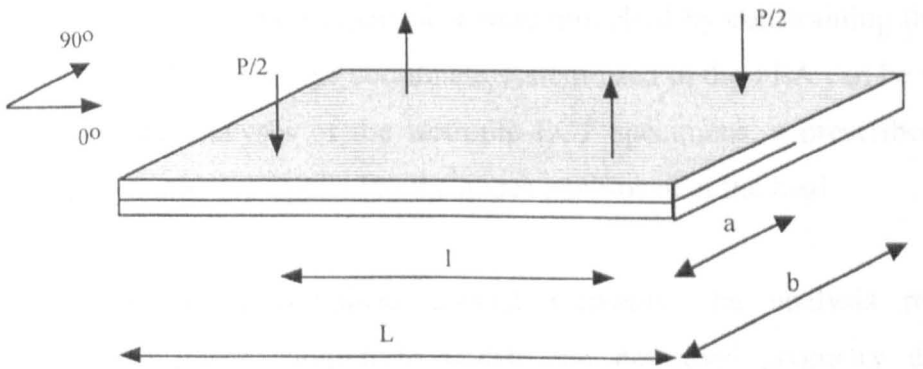

Figure 3.5: Schematic of the ECT specimen.

The main element used was SOLID45. The edge delamination was modelled by including elements with coincident nodes along the plane of delamination. A fine mesh was used in the vicinity of the delamination front to accommodate for the rapid change in strain field. The crack tip was modelled using focusing elements for greater accuracy. Contact elements CONTA175 and TARGE170 were used at the edge of the delamination plane to prevent interpenetration during the analysis. More specifically, the target surface was meshed using the TARGE170 element, whereas the contact surface was meshed using the CONTA175 element. Before meshing the target surface, one needs to identify the nodes attached to the surface that are expected to come into contact with the upper surface (contact surface). To do so, the select logic is used by selecting the target area and then the nodes attached to this area. In contact problems, the target surface is generally modelled through a set of target segments or elements. Several target elements comprise one target surface. These target elements will define the lower surface of the crack that is expected to come to contact with the upper crack surface. It should also be noted that relative sliding between points in the delamination zone was assumed to be frictionless. Zhao and Wang [4] ran a series of Mode III analyses, the result of which was that friction between crack faces has a negligible effect on the interlaminar properties.

The nodes positioned at the location of the guide pins were constrained from moving in the horizontal axes, thereby maintaining contact between the specimen and the pins throughout the analysis. The support pins were modelled by constraining the contact nodes in the vertical, z-axis. The coordinate system used in the FEA can be viewed in Figure 3.6. For the analyses of the isotropic ECT specimens, a prescribed vertical displacement of 2 mm was applied to the nodes positioned at the load.

Since the ECT model contained contact elements, the analysis required a geometrically non-linear solution to update the deformed geometry during the solution process. The reaction loads at the nodes to which displacements were prescribed were calculated and the specimen compliance was determined by dividing the prescribed displacement by the applied load.

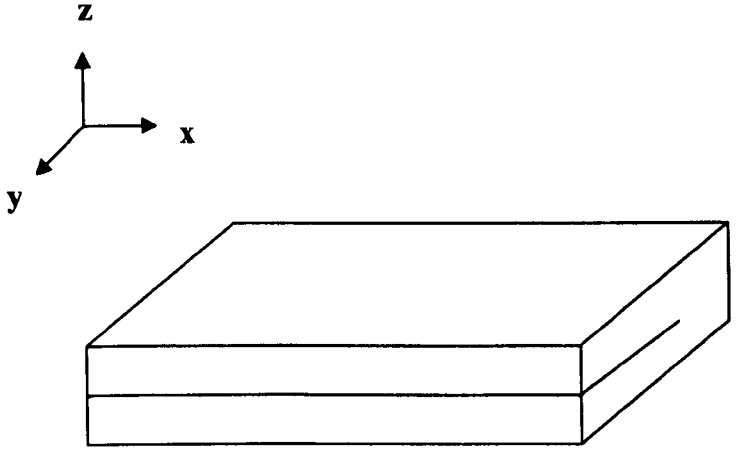

Figure 3.6. Coordinate system used in the finite element analyses.

Details of the mesh around the crack area can be viewed in Figures 3.7a and b:

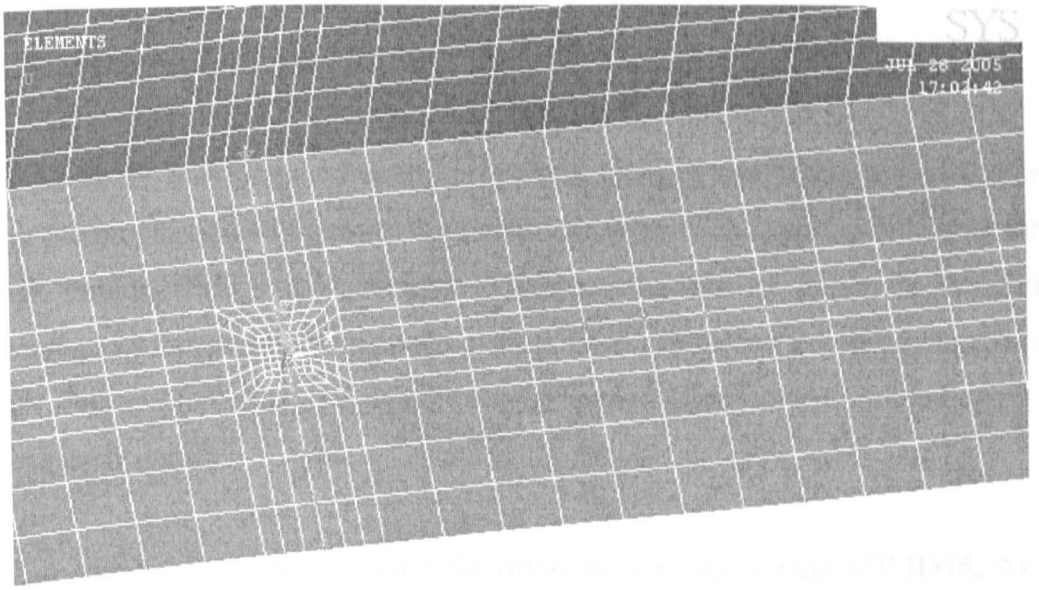

Figure 3.7a: Details of the mesh around the crack front in the isotropic ECT specimen.

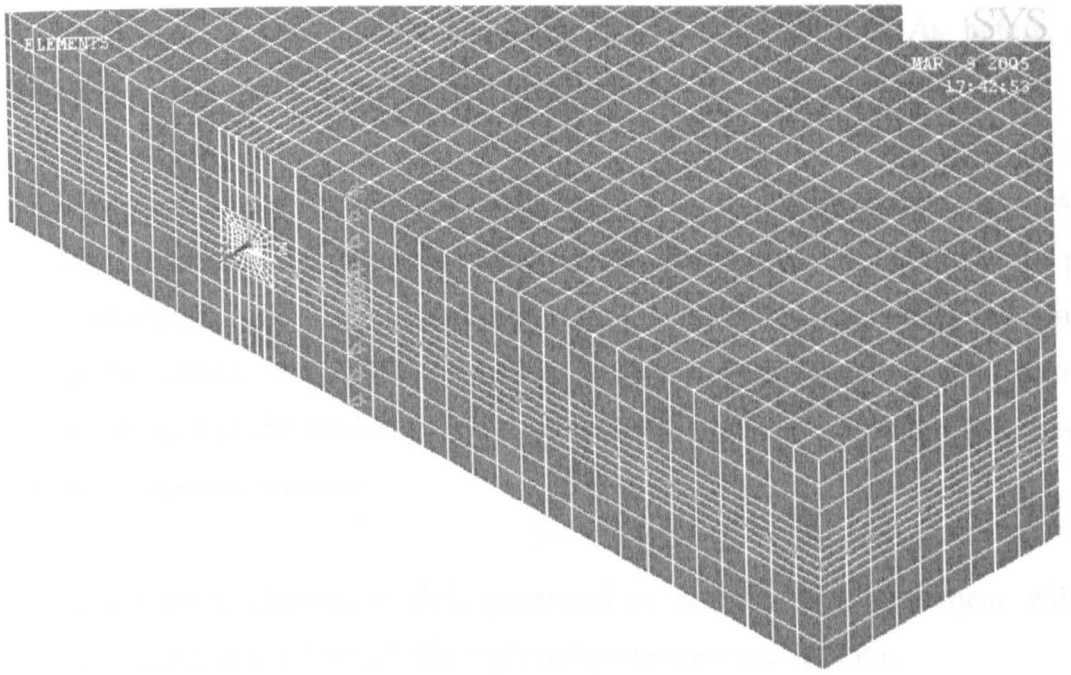

Figure 3.7b: Details of finer mesh near a corner of the isotropic ECT specimen.

3.5.2. Orthotropic Models

The Mode III interlaminar fracture properties, G_{IIIc}, of composite materials based on both thermoplastic and thermosetting–matrices have been investigated using the edge crack torsion (ECT) test geometry. The combinations of materials examined, as presented in the introduction, were a glass fibre reinforced polypropylene, a woven glass fibre reinforced epoxy, an adhesively-bonded glass fibre reinforced epoxy and a bi-material system.

The main element used to model the orthotropic material was SOLID46. As in the case of the isotropic specimens, the edge delamination was modelled by including elements with coincident nodes along the plane of delamination. A fine mesh was used in the vicinity of the delamination front to accommodate for the rapid change in strain field. Contact elements CONTA175 and TARGE170 were used at the edge of the delamination plane to prevent interpenetration during the analysis. More specifically, the target surface was meshed using the TARGE170 element, whereas the contact surface was meshed using the CONTA175 element. As before, the delamination zone was assumed to be frictionless.

The nodes positioned at the location of the guide pins were constrained from moving in the horizontal axes, thereby maintaining contact between the specimen and the pins throughout the analysis. The support pins were modelled by constraining the contact nodes in the vertical, z-axis. The prescribed vertical displacement was applied to the nodes positioned at the load pins and a geometrical non-linear solution was used to model the specimen response.

The various finite element models generated to analyse these specimens will be presented with details relating to the material properties and meshing.

3.5.2.1. Glass Fibre Reinforced Polypropylene

Three-dimensional finite element models of the glass fibre reinforced polypropylene were constructed using ANSYS. Specimens with 16, 24 and 32 plies, having the stacking sequences:

$$[90° / 0° (+45° / -45°) / (-45° / +45°) 0° / 90°]_s$$

$$[90° / 0° (+45°/-45°)_2 / (-45°/+45°)_2 / 0° / 90°]_s$$

$$[90° / 0° (+45°/-45°)_3 / (-45°/+45°)_3 / 0° / 90°]_s$$

respectively, were simulated. The nominal elastic properties used to model the specimens are given in Table 3.1:

	Glass Fibre/Polypropylene
E_1	28 GPa
E_2	3.72 GPa
E_3	3.72 GPa
ν_{12}	0.31
ν_{13}	0.31
ν_{23}	0.39
G_{12}	0.644 GPa
G_{13}	0.644 GPa
G_{23}	0.622 GPa

Table 3.1: Mechanical properties of glass fibre reinforced polypropylene.

The nominal ply thickness was 0.29 mm, as in the actual experiments, giving overall thicknesses of 4.7, 7.05 and 9.4 mm for the 16, 24 and 32-ply specimens respectively. Sixteen-ply ECT specimens with normalised insert lengths ranging from 0.2 to 0.7 were simulated using ANSYS. For the cases of the 24 and 32-ply glass fibre reinforced polypropylene specimens, insert lengths of 0.5 were examined in order to determine the effect of thickness on the Mode III strain energy release rate distribution. The element thickness at the delamination front (in the through-thickness direction) was set equal to one ply thickness, Figure 3.8. The element length in the y direction was 0.5 mm and the width in the x direction, 1 mm. For purposes of symmetry, the top and bottom plies of the ECT specimen were modelled using a finer mesh with an element size equal to one ply thickness, this being similar to that used in the vicinity of the crack, Figure 3.8. Contact elements were used along the delamination plane to prevent mesh interpenetration during the analysis. Relative sliding between points within the delamination region was assumed to be frictionless. The nodes positioned at the location of the guide pins were constrained from moving in the horizontal axes, thereby maintaining contact between the specimen and the pins throughout the analysis. The support pins were modelled by constraining the contact nodes in the vertical, z-axis.

For most analyses, a prescribed vertical displacement of 2 mm was applied to the nodes positioned at the load pins and a geometrical non-linear solution was used to model the specimen response. Additionally, the effect of applied displacement to the Mode III strain energy release rate was investigated by running a series of analyses on 16 ply glass fibre reinforced polypropylene ECT specimens with a normalised insert length of 0.5 and applied displacements ranging from 1 to 7 mm.

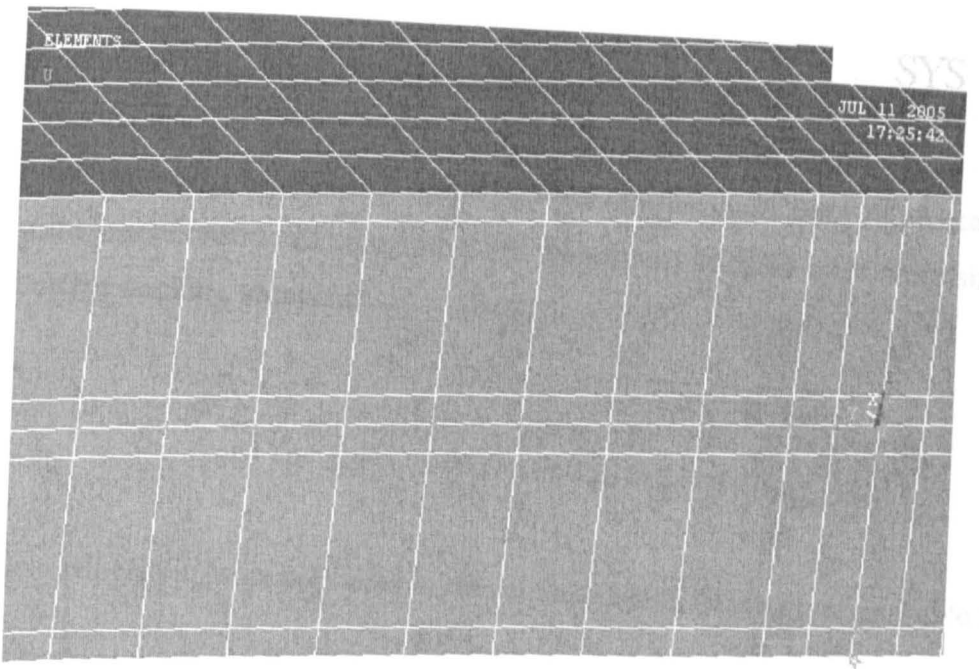

Figure 3.8a: Details of the finite element model near the crack front in the ECT composite specimen.

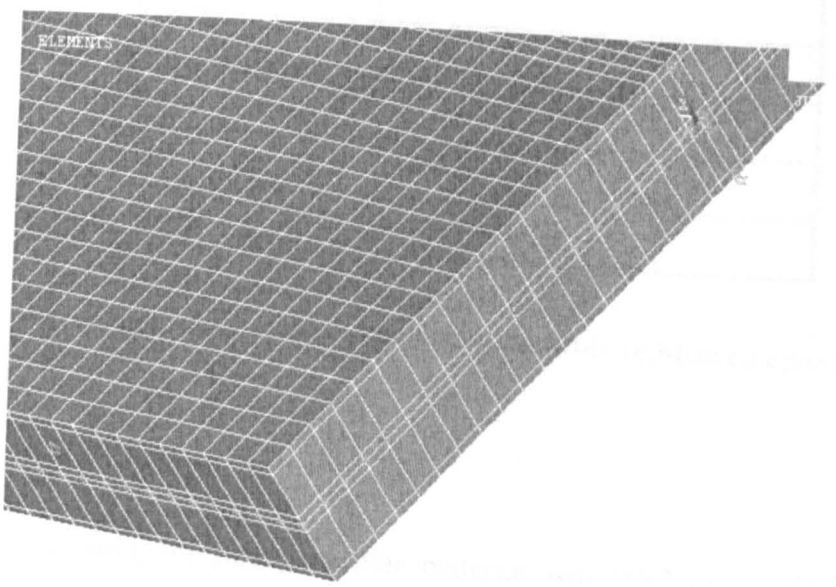

Figure 3.8b: Details of the mesh near a corner of the ECT composite specimen.

3.5.2.2. Woven Glass Fibre Reinforced Epoxy

Three-dimensional finite element models of the woven glass fibre reinforced epoxy specimens were constructed using ANSYS. Specimens with 24 plies were simulated, based on the stacking sequence:

$$[90° / 0° (+45°/-45°)_2 / (-45°/+45°)_2 / 0° / 90°]_s$$

The nominal elastic properties used to model the specimens are given in Table 3.2:

	Woven Glass Fibre/Epoxy
E_1	25 GPa
E_2	25 GPa
E_3	1.75 GPa
ν_{12}	0.3
ν_{13}	0.3
ν_{23}	0.38
G_{12}	3.5 GPa
G_{13}	3.5 GPa
G_{23}	3.25 GPa

Table 3.2: Mechanical properties of woven glass fibre reinforced epoxy.

The ply thickness for this particular material was 0.27 mm, calculated from the nominal overall thickness of the manufactured ECT specimens. Models of these specimens with normalised insert lengths ranging from 0.2 to 0.7 were examined.

The woven glass fibre reinforced epoxy specimens were modelled following the same principles to those used for the glass fibre reinforced polypropylene. The element thickness at the delamination front (in the through-thickness direction) was set equal to one ply thickness. The element length in the y direction was 0.5 mm and the width in the x direction, 1 mm. Finally, the applied displacement for all the models examined was 2 mm.

The effect of a variable crack across the thickness of the specimen on the Mode III strain energy release rate distribution was investigated by running a series of finite element models on 24-ply woven glass fibre reinforced epoxy ECT specimens. These tests were done in order to get mixed mode fracture (Mode II/III) and to do so, the crack was positioned at 4, 8, 16 and 20 plies from the top surface, in addition to the specimen mid-thickness. The normalised insert length for the models with the crack positioned at 8, 12 and 20 plies from the top surface was 0.5. For models which the delamination was simulated at 4 plies from the top surface, a range of insert lengths from 0.2 to 0.7 was examined. It should be noted that for all cases, the applied displacement was set to 2 mm to ensure an elastic response in the specimens.

Figure 3.9 shows the FEA models in which the crack was positioned at 4, 8, 16 and 20 plies from the top surface:

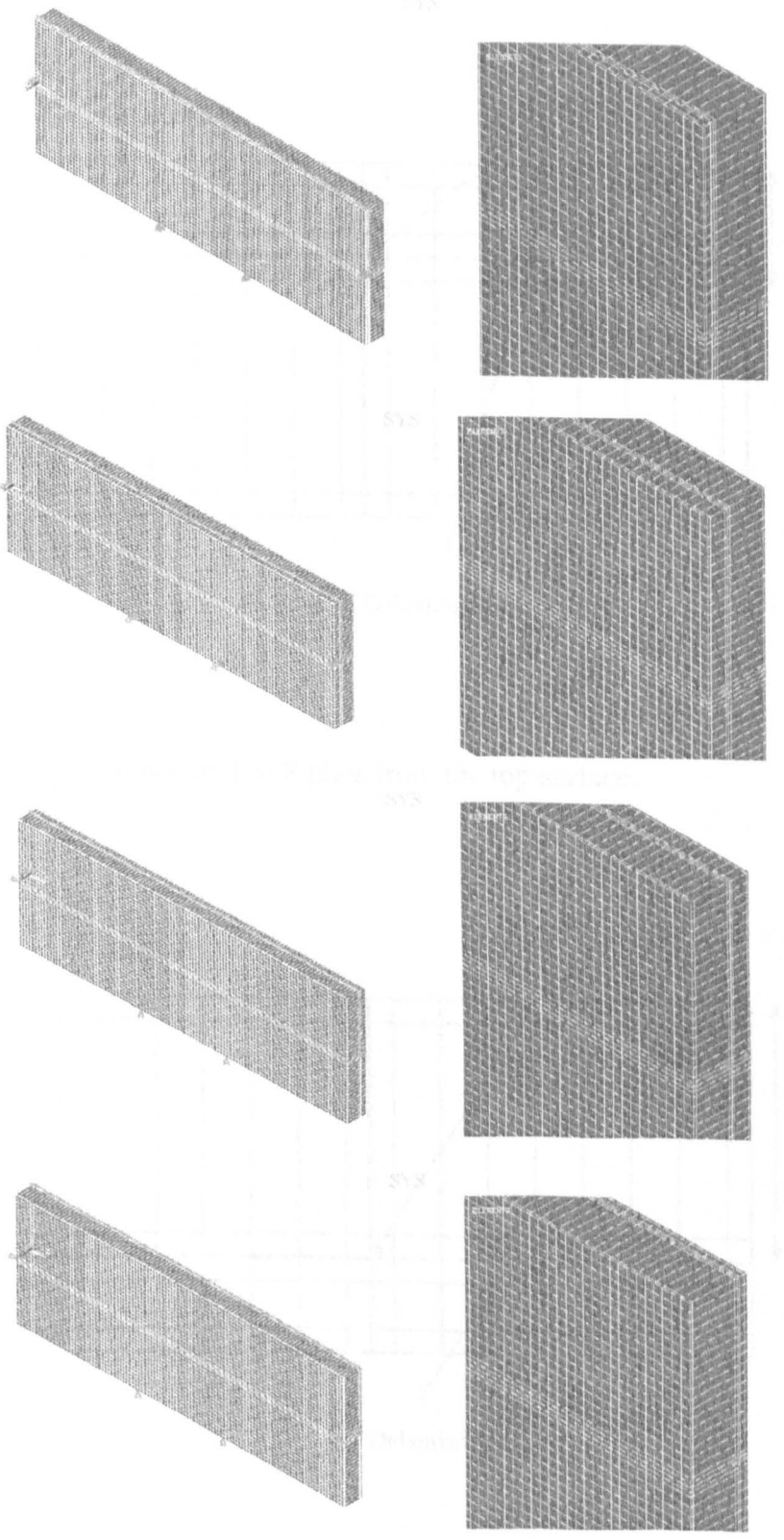

Figure 3.9: FE models and expanded views of the crack fronts in the ECT specimens in which the crack was positioned at 4, 8, 16 and 20 plies from the top surface respectively.

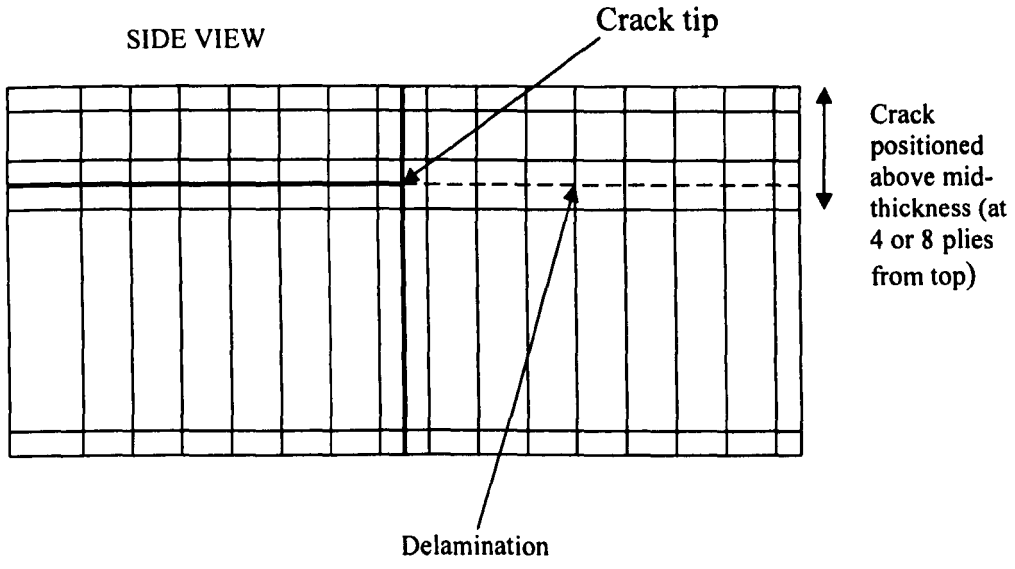

(a). Crack positioned at 4 or 8 plies from the top surface.

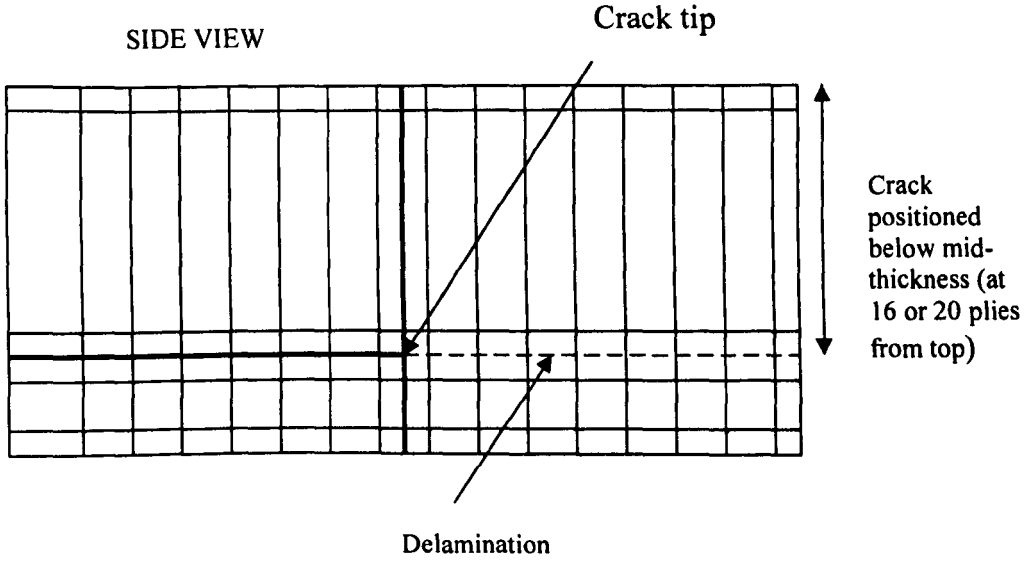

(b). Crack positioned at 16 or 20 plies from the top surface.

Figure 3.10: Variable positioning of the delamination through the specimen thickness. (a) at 4 or 8 plies from the top, (b) at 16 or 20 plies from the top.

In another series of FEA models of the woven glass fibre reinforced epoxy material, specimens with normalised insert lengths of 0.2 to 0.7, with the crack positioned at mid-thickness, were subjected to displacements equal to the critical values for delamination extension, as measured during the actual tests. The experimental data was introduced into the FEA models in order to determine the G_{III} distributions along the crack front. As the critical displacement was used, the Mode III strain energy release rate corresponds to the G_{IIIc}. These maximum values were then compared to those obtained during the experiments.

3.5.2.2.1. Modified ECT Geometry

Three additional models of modified ECT geometries were constructed and analysed in ANSYS, based on the woven glass fibre reinforced epoxy material properties. The aim of this work was to investigate the effect of varying the position of the applied loads on the Mode III strain energy release rate across the delamination front and create a mixed-mode II/III test specimen geometry, if possible.

In the original ECT geometry, the specimen had an overall length of 108 mm and a width of 38 mm. Each load and support pin was located from each edge at a distance of 16 mm in the x-direction and 3 mm in the y-direction from each edge. In modifying the ECT geometry, the dimensions of the specimen remained unchanged. The specimens consisted of 24 plies and were modelled in the same way as the previously examined woven glass fibre reinforced epoxy ECT specimens. The displacement applied in these modified geometries was 2 mm in all cases.

In the first specimen, the load and support pins were positioned at a distance of 1 mm from each edge. In the second model, the specimen was loaded (and supported) at a distance of 1 mm in the x direction and 3 mm in the y direction from the corner. In the third model examined, the load and support pins were positioned at mid-points relative to the plain ECT specimen, i.e. 8 mm in the x direction and 2 mm in the y direction, from each edge.

A geometrically non-linear solution was required in order to update the deformed geometry during the solution process. The Mode III strain energy release rate distributions were plotted as a function of position along the crack front and compared to that obtained from the original ECT geometry. Figure 3.11 shows the three modified geometries investigated:

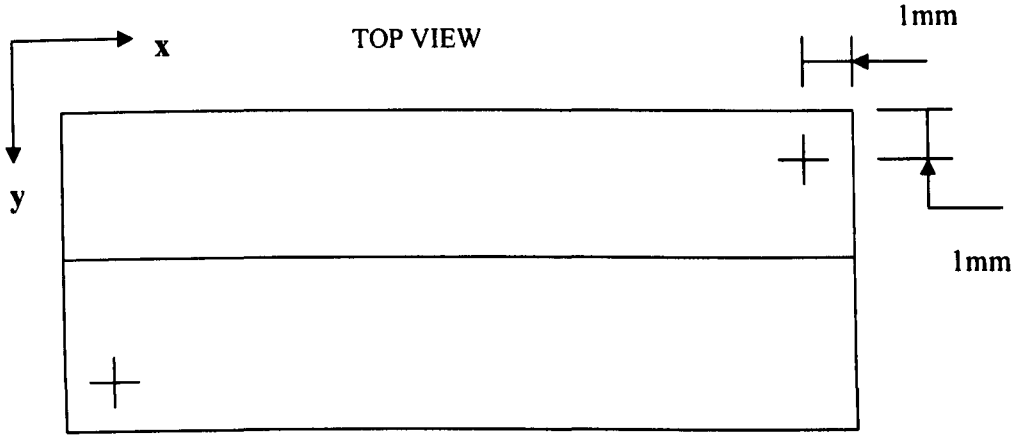

(a). Support and displacement applied at 1 mm from each edge.

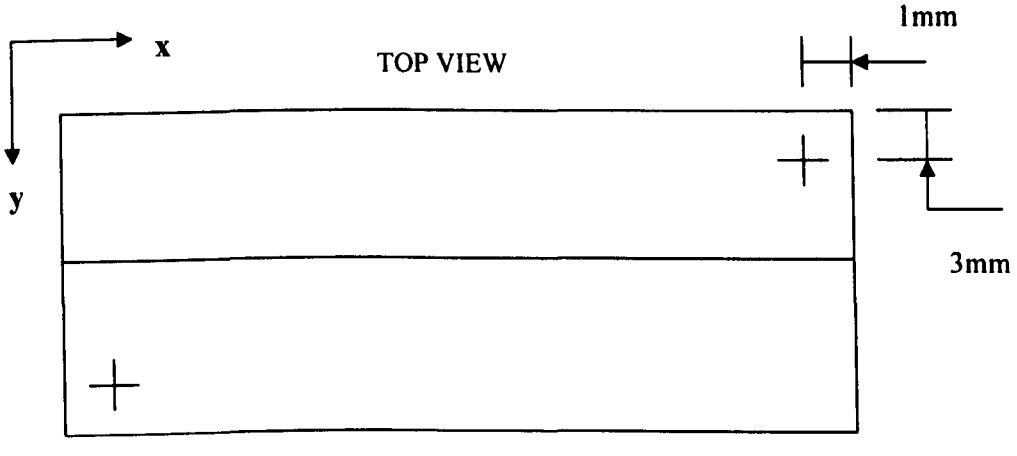

(b). Support and displacement applied at 1 mm in the x direction and 3 mm in the y direction from each edge.

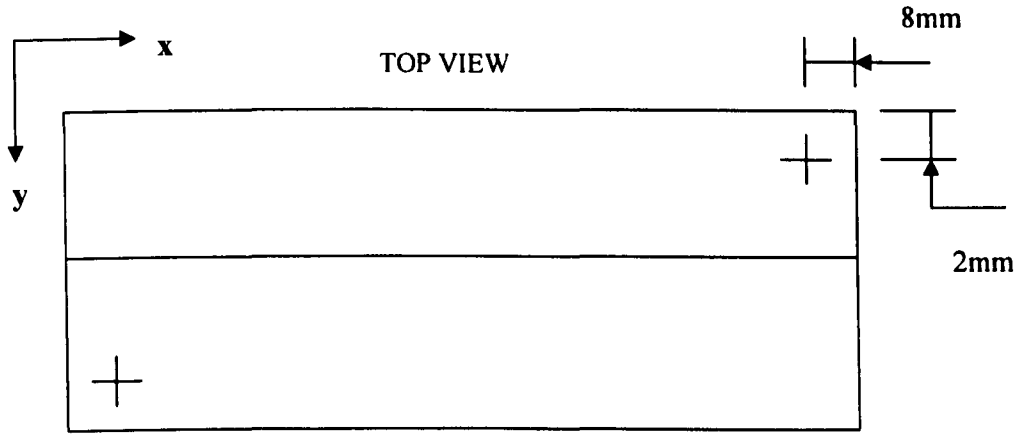

(c). Support and displacement applied at middle distances compared to original ECT test geometry.

Figure 3.11a, b, c: Modified woven glass fibre reinforced epoxy ECT specimens examined.

3.5.2.3. Adhesively-bonded Glass-Fibre Reinforced Epoxy

Three-dimensional adhesively-bonded composite specimens based on the same woven glass-fibre reinforced epoxy were analysed using FEA in order to investigate the Mode III interlaminar fracture properties.

The epoxy adhesive was modelled as a linear isotropic material with a Young's Modulus E_X of 3 GPa and a Poisson's ratio ν_{XY} of 0.3. As in the case of the pure isotropic ECT specimens, SOLID45 was used to model the adhesive. The element thickness at the delamination front (in the z axis) was equal to half the thickness of the epoxy adhesive, since the crack was assumed to be located at the mid-thickness of the adhesive. The element length in the y direction at the delamination front was 0.5 mm and the width in the x direction was 1 mm.

The 24 plies of the orthotropic material were modelled using SOLID46 brick elements as outlined in the previously-presented models. To ensure that the finite element models were symmetrical, the top and bottom plies of the ECT specimen were modelled using a finer mesh with an element size equal to one ply thickness (0.27 mm). Contact elements CONTA175 and TARGE170 were used along the delamination plane to prevent mesh interpenetration during the analysis. Relative sliding between points within the delamination region was assumed to be frictionless in nature. The locations of guide, support and load pins remained the same as in the original ECT test geometry and the prescribed displacement was set to 2 mm to ensure an elastic response during the analysis.

Two different thicknesses of adhesive were considered in the analysis of the specimens, these being 100 μm and 1.42 mm. These values were selected in order to investigate the effect of the adhesive thickness on the Mode III strain energy release rate distribution, the latter being the nominal thickness measured prior to the experiments. As a result, the total thickness for the first set of finite element ECT models was 6.5 mm and 7.42 mm for the second. In both cases, normalised insert lengths of 0.2 to 0.7 were examined.

Figures 3.12 and 3.13 show details of the mesh near a corner, as well as a side view of the adhesively-bonded composite ECT specimen:

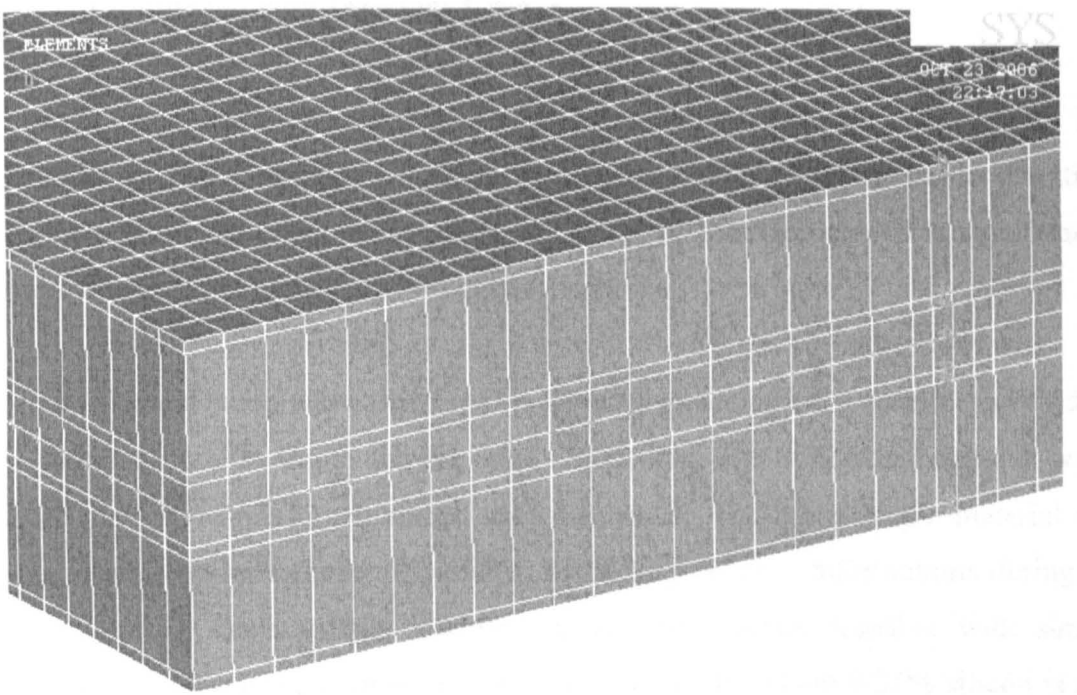

Figure 3.12. Details of the mesh near the corner of the adhesively-bonded ECT specimen.

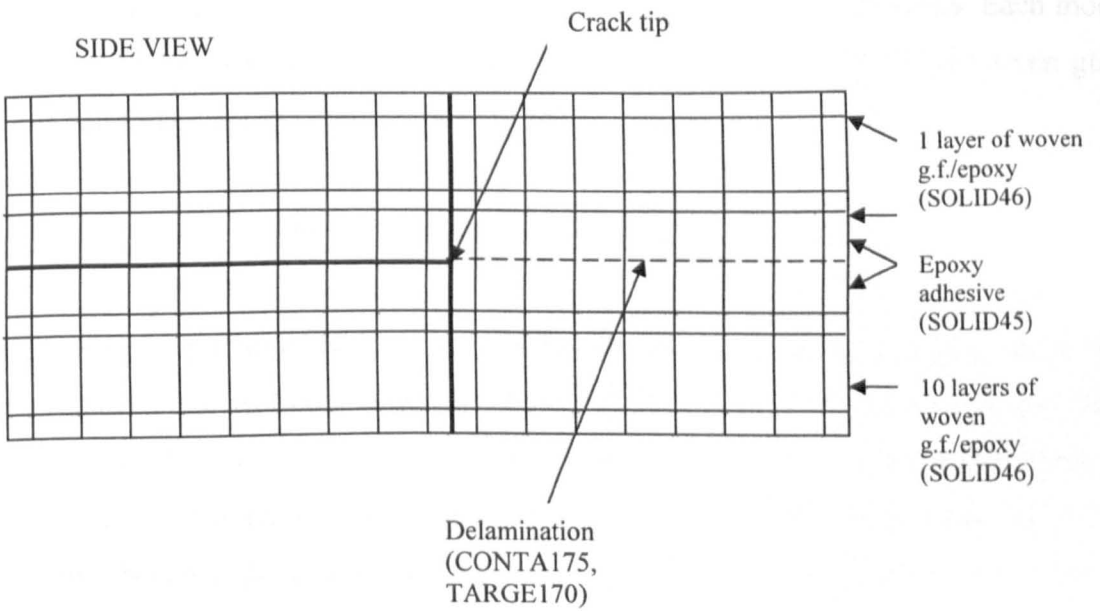

Figure 3.13: Side view of the adhesively-bonded glass fibre epoxy ECT model.

3.5.2.4. Bi-material with Interface Cracks

In many cases, cracks occur at interfaces between two different constituents. The study of fracture behaviour of these cracks has attracted considerable attention, mainly because the phenomenological behaviour of interface cracks is significantly different from that of cracks in homogeneous media.

A finite element study was carried out on three-dimensional ECT specimens based on two materials, one isotropic and the other orthotropic. The orthotropic material was a woven glass fibre reinforced epoxy, used previously, and the isotropic material was spring steel. This was chosen in order to avoid large plastic deformations during the testing. Spring steels usually contain 0.6 to 0.9% carbon together with similar quantities of manganese to provide appropriate hardness. About 0.35% silicon is also included to resist 'sag'. About 1% vanadium is also included in some specifications, as well as chromium and/or molybdenum.

A series of models with normalised insert lengths of 0.2 to 0.7 were constructed in ANSYS. The dimensions of the two different materials used in the analysis were the same as the nominal dimensions measured on the actual ECT specimens. Each model consisted of a 2.05 mm thick spring steel sheet bonded to 8 layers of woven glass fibre reinforced epoxy material with the stacking sequence:

$$[90° / 0° (+45°/-45°) / (-45°/+45°) / 0° / 90°]_s$$

Following a previous analysis by Dattaguru and co-workers [5], the crack was positioned in an isotropic resin rich layer which was assumed to be 0.02 mm thick (20% of a ply thickness). The crack was positioned in a resin-rich layer because the individual components of the strain energy release rate calculated using the VCCT method become dependent on the crack tip element length when the crack is positioned at a bi-material interface or within an orthotropic material, as shown by previous researchers [6, 7]

The resin rich area and the spring steel were modelled as linear isotropic materials and their nominal properties are given in Table 3.3. SOLID45 was used to model both materials. Since the crack was assumed to be located at the mid-thickness of the resin rich area, the element length in the y direction at the delamination front was 0.5 mm, the width in the x direction was 1 mm and the thickness was equal to 10% of a ply thickness. In order for the finite elements to be symmetrical, the spring steel was meshed using three elements across the thickness, the top and bottom having a thickness equal to 0.27 mm, equal to the ply thickness of the orthotropic material.

	Spring Steel	**Resin Rich Layer**
E_X	200 GPa	3 GPa
ν_{XY}	0.28	0.3

Table 3.3: Mechanical properties of the spring steel and resin rich layer used in the analysis.

The eight plies of the woven glass fibre reinforced epoxy material were modelled using SOLID46 elements. The top and bottom plies of the orthotropic constituent were modelled with a finer mesh across the thickness, equal to one ply.

CONTA175 and TARGE170 elements were employed along the delamination plane inside the resin rich area in order to define the contact of the two delaminated surfaces and prevent mesh interpenetration. Relative sliding between points within the delamination region was ignored. The locations of guide, support and load pins remained the same as in the original ECT test geometry and the prescribed displacement was set to 2 mm in all the models examined.

Figures 3.14 and 3.15 show details of the mesh near a corner and a side view of the ECT specimen:

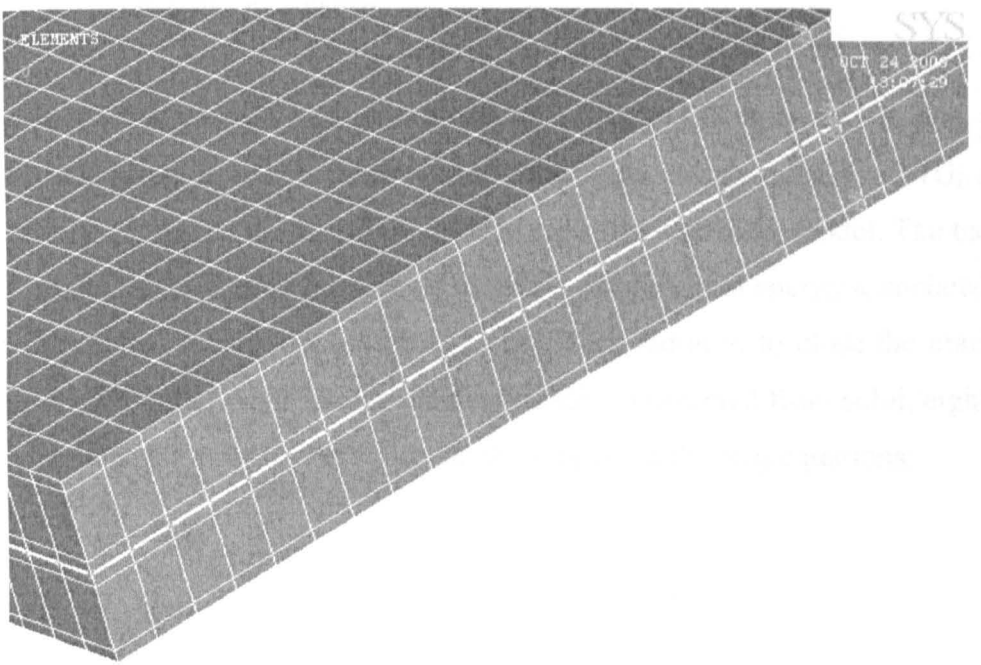

Figure 3.14: Detail of the very fine mesh surrounding the delaminated area in the bi-material ECT specimen.

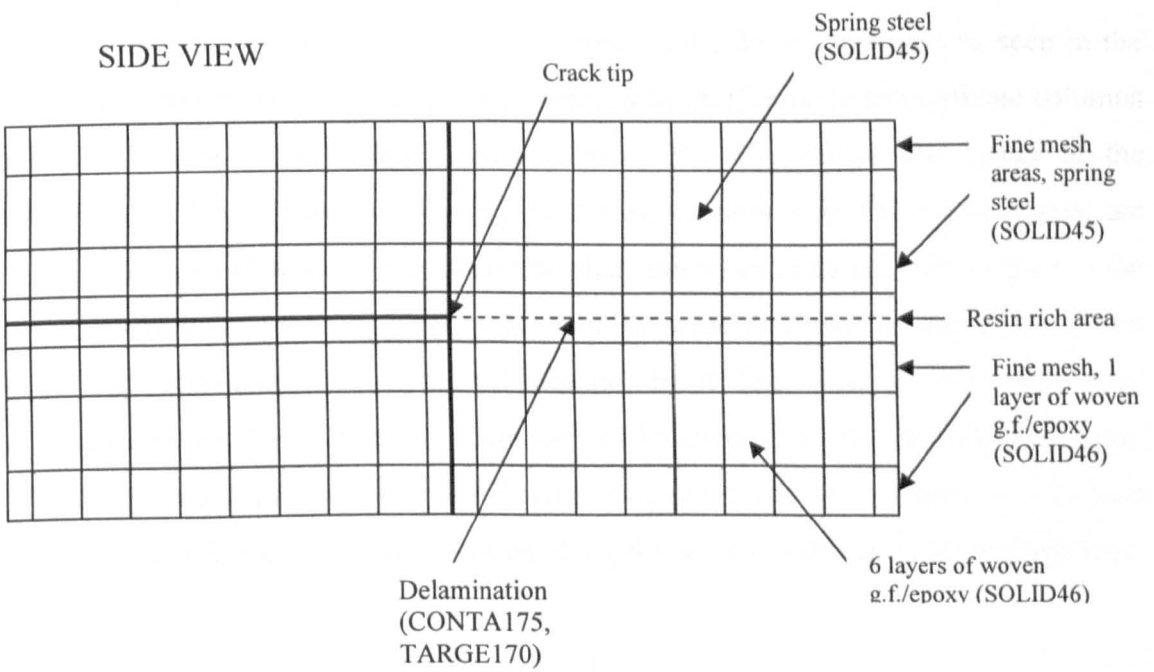

Figure 3.15: Side view of the finite element bi-material model.

3.5.3. Post-processing of Results

The virtual crack closure technique (VCCT), presented in Section 2.8, was used to calculate the Mode II and III components of the strain energy release rate (G_{II} and G_{III} respectively) along the delamination front in each finite element model. The technique works on the principle that the change in stored elastic strain energy associated with a small extension of crack area is equal to the work required to close the crack to its original length. In terms of a finite element model constructed from solid, eight-noded brick elements, G_{II} and G_{III} were calculated using the following equations:

$$G_{II} = \frac{1}{2\Delta A} X_{Li}(u_{Li} - u_{Li^*}) \tag{3.1}$$

$$G_{III} = \frac{1}{2\Delta A} Z_{Li}(w_{Li} - w_{Li^*}) \tag{3.2}$$

In these two equations, $\Delta A = \Delta a^* B$ is the virtual area enclosed by the element, where Δa is the length of the elements at the delamination front (y direction) and B is their width (x direction). The subscripts denote rows and columns of nodes as seen in the top view of the elements along the delamination front. Capital letters indicate columns and lower case letters indicate rows. Hence, X_{Li}, Z_{Li} denote the forces at the delamination front at the top face of node row, column L in the x and z axes are denoted by u_{L^*} and w_{L^*}. All forces and displacements are obtained with respect to the global coordinate system. Equations 3.1 and 3.2 were then used to calculate G_{II} and G_{III} at each node located along the delamination front. The values of the strain energy release rate were then plotted as a function of location along the delamination front, x/L. By summing all of the individual strain energy release rate components, the total strain energy release rate at any location along the delamination front was determined.

$$G_T = G_I + G_{II} + G_{III} \tag{3.3}$$

The compliance C_{spc}, was also determined from the finite element models and plotted as a function of normalised insert length.

3.5.4. Finite Element Model Verification

The accuracy of the finite element models was evaluated by comparing the predicted elastic responses of the ECT specimens with those determined experimentally during the ECT tests. The variation of the inverse of specimen compliance with normalised insert length, a/b, calculated from the FEA models was plotted against the experimental results for each material examined.

3.5.5. Summary of Finite Element Analysis

Table 3.4 summarises the analyses conducted during the course of this research programme:

Material	Crack location	Normalised insert length	Adhesive Thickness	Δα (mm)	No. of plies	Applied displacement (mm)	Parameter varied	No. of models examined
Isotropic	Specimen mid-thickness	0.3 – 0.7	-	1	-	2	Insert length	5
G.F.-Polypropylene	Specimen mid-thickness	0.2, 0.3, 0.4, 0.6, 0.7	-	0.5	16	2	Insert length	5
G.F.-Polypropylene	Specimen mid-thickness	0.5	-	0.5	16	1-7	Applied displacement	7
G.F.-Polypropylene	Specimen mid-thickness	0.5	-	0.5	24, 32	2	Total number of plies	2
Woven G.F.-Epoxy	Specimen mid-thickness	0.2, 0.3, 0.4, 0.6, 0.7	-	0.5	24	2	Insert length	5
Woven G.F.-Epoxy	4, 8, 12, 16, 20 plies from top surface	0.5	-	0.5	24	2	Crack positioning through thickness	5
Woven G.F.-Epoxy – Modified ECT geometry	Specimen mid-thickness	0.5	-	0.5	24	2	Locations of applied displacements	3
Adhesively-bonded G.F.-Epoxy	Adhesive mid-thickness	0.2 - 0.7	100 μm	0.5	24	2	Insert length	6
Adhesively-bonded G.F.-Epoxy	Adhesive mid-thickness	0.2 - 0.7	1.42 mm	0.5	24	2	Insert length	6
Bi-material (Woven G.F.-Epoxy bonded to Spring Steel)	Resin-rich area mid-thickness	0.2 - 0.7	-	0.5	8	2	Insert length	6

Table 3.4: Summary of finite element analyses conducted in the duration of the research programme.

3.6 References

1. ANSYS User's Guide.

2. Moaveni S., Finite Element Analysis, Theory and Application with ANSYS.

3. ANSYS Tutorial Release 6.1, Kent Lawrence, Mechanical and Aerospace Engineering University of Texas at Arlington.

4. Zhao D., Wang, Y., Mode III fracture behaviour of laminated composite with edge crack in torsion, Theoretical and Applied Fracture Mechanics, Vol.29, 1998, p.109.

5. Dattaguru B, Venkatesha K.S., Ramamurthy T.S., Buchholz F.G., Finite element estimates of strain energy release rate components at the tip of an interface crack under Mode I loading, Engineering Fracture Mechanics, Vol.49, 1994, p.451.

6. Raju I.S., Crews J.H., Aminpour M.A., Convergence of strain energy release rate components for edge-delaminated composite laminates, Engineering Fracture Mechanics, Vol.30, 1998, p.383.

7. Krueger R., Virtual crack closure technique: history, approach and applications, Applied Mechanics Revision, Vol.57, March 2004, p.109.

4. Experimental Procedure

4.1. Introduction

This chapter provides an overview of the experimental procedures used in this research programme to investigate the Mode III interlaminar fracture properties, G_{IIIc}, of composite materials based on both thermoplastic and thermosetting-matrices. The test method used in this research programme is the Edge Crack Torsion test, which is commonly used for Mode III testing.

Tests have been conducted on a glass fibre reinforced polypropylene, a woven glass fibre reinforced epoxy, an adhesively-bonded glass fibre reinforced epoxy and a bi-material system, consisting of spring steel bonded to a woven glass fibre reinforced epoxy.

Initial tests focused on establishing the influence of crack length on the interlaminar fracture properties of the composite materials. Following this, the ECT test method was modified to characterise the rate sensitivity of the Mode III interlaminar fracture toughness of the materials by performing tests over a range of crosshead displacement rates and under impact loading.

Initially, an overview of the materials and the manufacturing procedures used in this research programme is given. The ECT tests performed are presented and analysed, as well as the modifications to the original method, the latter being necessary to perform the dynamic tests.

4.2. Specimen and Materials

An ECT specimen is a rectangular laminate of tape composite material with a length of 108 mm and a width of 38 mm. Tests were conducted on ECT specimens manufactured from a glass fibre reinforced polypropylene with a fibre volume fraction of 35% (Plytron from Gurit Composite Technologies) and a thickness of 0.29 mm, a woven glass fibre/epoxy with a fibre volume fraction of 45% (Stesapreg EP127-C15-45 from Stesalit AG) and a thickness of 0.27 mm, an adhesively-bonded and a bi-material system consisting of spring steel bonded to a woven glass fibre reinforced epoxy, based on the aforementioned woven glass fibre reinforced epoxy composite.

During lamination, a layer of folded aluminium foil (0.02 mm thick) was introduced at the laminate mid-thickness to act as a starter defect. Panels with dimensions 200 mm x 240 mm were then manufactured in a picture-frame mould using a hot press according to the manufacturer's recommended processing cycle. An overview of the stacking sequences adopted in the manufacture of the composite specimens and the normalised insert lengths examined, will be given.

4.2.1. Glass Fibre Reinforced Polypropylene

Specimens with normalised insert lengths ranging from 0.2 to 0.7 were manufactured from a glass fibre reinforced polypropylene pre-preg material. The specimens manufactured from this material had the following stacking sequence:

$$[90° / 0° (+45° / -45°) / (-45° / +45°) 0° / 90°]_s$$

The prepreg sheets were placed in a 200 mm x 240 mm picture-frame mould and heated in a hot press at a temperature of 185 °C and 6 bar pressure. The temperature was constantly monitored by thermocouples that were placed in the prepreg layers. The starter defect was made by introducing a layer of folded aluminium foil (0.02 mm

thick) at the laminate mid-thickness during the lamination process. Figure 4.1 shows the Meyer press used for the manufacture of the specimens.

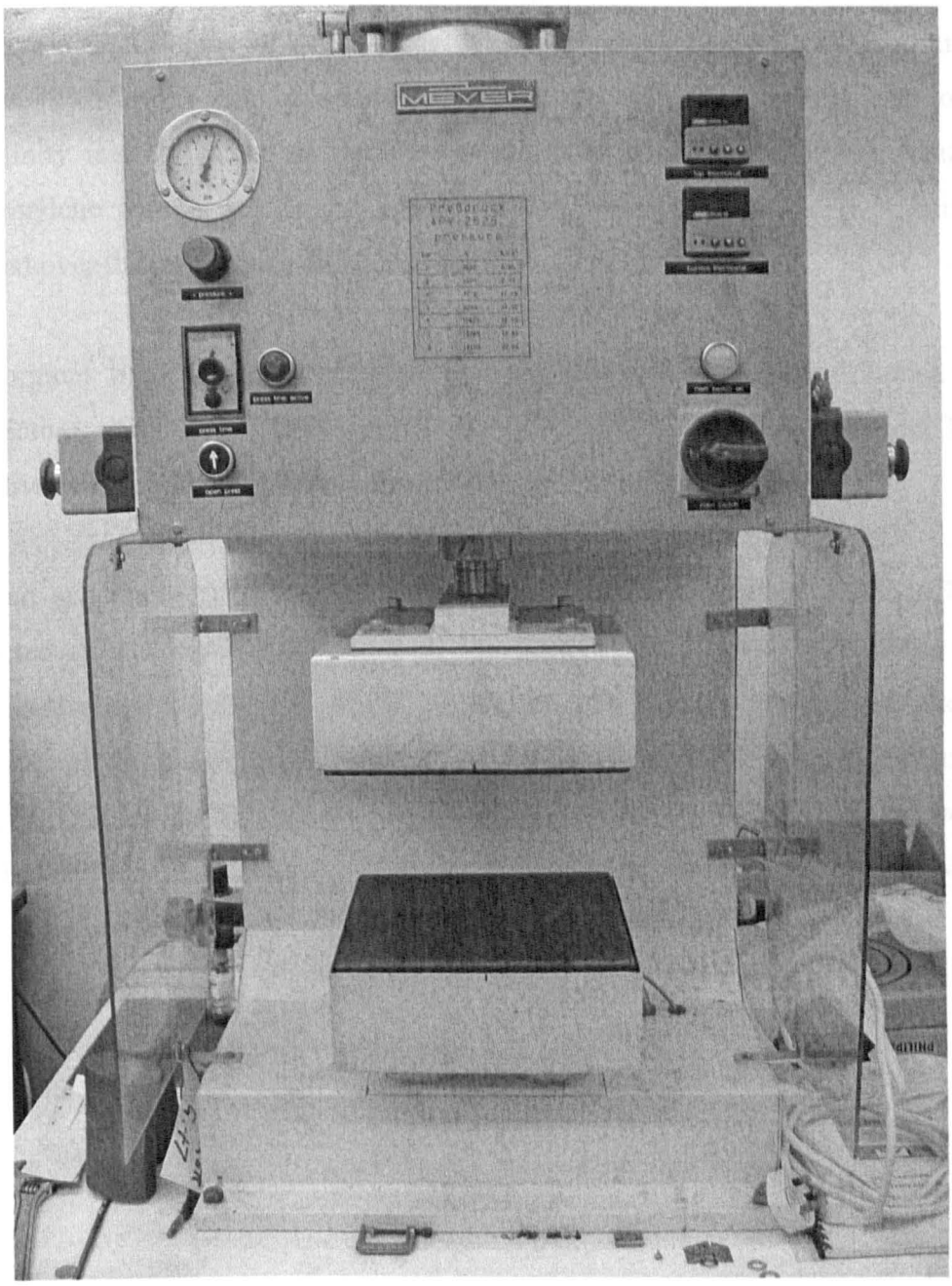

Figure 4.1: Photograph of the Meyer hot press.

The use of the thermocouples also enabled the monitoring and recording of the temperature during cooling. Davies and Cantwell [1] found that the cooling rate affects the matrix structure and strongly influences fracture properties of glass fibre reinforced polypropylene laminates. According to their research work, low cooling rates give a high degree of crystallinity. The research work by Richardson and co-workers [2] showed similar results regarding the effect of cooling rate on the crystallinity and its effect on the mechanical properties of glass fibre reinforced polypropylene composites. In the present study, a cooling rate of 2.6 °C/min was achieved over the range from 185 °C to 60 °C.

The nominal final thickness of the glass fibre/PP laminates was 4.7 mm. After manufacture, specimens with length 'L' and width 'b' dimensions of 108 and 38 mm respectively were removed from the laminates.

Tests on specimens with normalised insert lengths ranging from 0.2 to 0.7 were conducted on an Instron 4505 universal test machine. In addition, specimens with a normalised crack length, a/b, of 0.5, were tested in order to investigate the rate-sensitivity of the Mode III interlaminar fracture properties. Crosshead displacement rates of 0.2, 2, 20 and 200 mm/min were used. Furthermore, impact tests on the ECT glass fibre/PP samples were undertaken using an instrumented drop-weight impact tower, at an impact speed of 3 m/sec, illustrated in Figure 4.2.

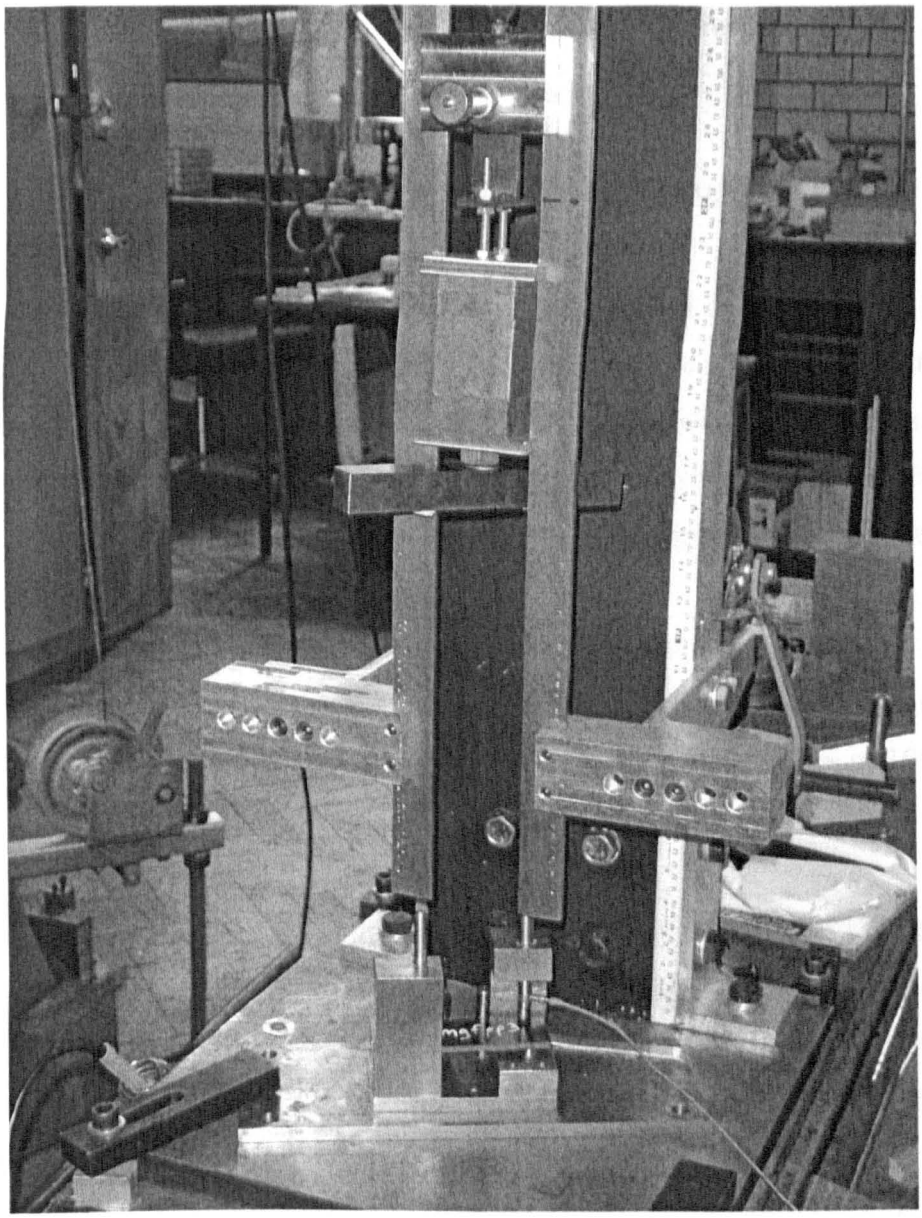

Figure 4.2: Photograph of the rig used for Mode III impact testing.

4.2.2. Woven Glass Fibre Reinforced Epoxy

The woven glass fibre reinforced epoxy ECT specimens were based on the stacking sequence:

$$[90° / 0° (+45°/-45°)_2 / (-45°/+45°)_2 / 0° / 90°]_s$$

During manufacturing, the prepregs were layed up by hand in a 200 mm x 240 mm frame mould and then placed in a heated press and heated to a temperature of 130 °C under a pressure of 1 bar for 1 hr. The temperature was monitored by thermocouples placed between the prepreg layers. The starter defect was prepared by introducing a layer of folded aluminium foil at the laminate mid-thickness during the lamination process.

The nominal final thickness of the woven glass fibre/epoxy laminates was 6.5 mm. After manufacture, specimens with length 'L' and width 'b' dimensions of 108 and 38 mm respectively were removed from the laminates.

Specimens with normalised insert lengths from 0.2 to 0.7 were tested on the Instron 4505 test machine at a crosshead displacement rate of 2 mm/min. Additionally, rates of 0.2, 20, 200 mm/min were used for specimens with a normalised insert length of 0.5. Impact tests were carried out on specimens with a normalised insert length of 0.5 at an impact speed of 3 m/sec.

4.2.3. Adhesively-Bonded Woven Glass Fibre Reinforced Epoxy

For the manufacture of the adhesively-bonded system, a two part epoxy resin adhesive (Araldite 2015, Ciba-Geigy Ltd) was used to bond the two laminates based on a stacking sequence of:

$$[90°/0°(+45°/-45°)_2/(-45°/+45°)_20°/90°]$$

During lamination, the pre-pregs for the lower half of the laminates were laid up by hand in a 200 mm x 240 mm frame mould. The two part epoxy adhesive was then added, ensuring that a widthwise and lengthwise bond thickness uniformity was achieved. A folded layer of aluminium foil was introduced at the adhesive mid-thickness to act as a starter defect and the top half of the laminates was then laid up. The nominal thickness of the adhesively-bonded woven glass fibre/epoxy laminates was 7.9 mm, giving an approximate thickness of 1.4 mm for the epoxy adhesive.

The picture frame mould was placed in a heated press at a temperature of 130 °C and a pressure of 1 bar for 1 hour. The temperature was monitored by thermocouples placed in the pre-preg layers. As before, specimens with length 'L' and width 'b' dimensions of 108 and 38 mm respectively were removed from the laminates.

Specimens with normalised insert lengths ranging from 0.2 to 0.7 were tested at a crosshead displacement rate of 2 mm/min on the Instron universal test machine. Furthermore, specimens with the aforementioned normalised insert lengths were tested at the drop-weight impact tower under an impact speed of 4.2 m/sec. In addition, specimens with normalised insert lengths of 0.5 were tested at crosshead displacement rates of 0.2, 20 and 200 mm/min.

4.2.4. Bi-material Samples with Interface Cracks

ECT testing was conducted on specimens based on two materials, one isotropic and the other orthotropic. The orthotropic material was the woven glass fibre reinforced epoxy, used previously, and the isotropic material was spring steel, chosen in order to avoid large plastic deformations during the testing.

Each specimen consisted of a 2.05 mm thick spring steel sheet bonded to eight layers of woven glass fibre reinforced epoxy material with the stacking sequence:

$$[90° / 0° (+45°/-45°) / (-45°/+45°) / 0° / 90°]_s$$

During lamination, the prepregs were laid up by hand in a 200 mm x 240 mm picture frame mould. The sheet of spring steel which had been previously cut to fit into the mould was then placed on top of the woven glass/epoxy plies. The starter defect was made by introducing a layer of folded aluminium foil (0.02 mm thick) at the interface of the two materials. The nominal thickness of the bi-material specimens was 4.2 mm.

The picture frame mould was placed in a heated press at a temperature of 130 °C and a pressure of 1 bar for 1 hr. The temperature was monitored by using thermocouples placed in the prepreg layers. Finally, specimens with length 'L' and width 'b' dimensions of 108 and 38 mm respectively were removed from the laminates.

Specimens with normalised insert lengths from 0.2 to 0.7 were tested at a crosshead displacement rate of 2 mm/min. Additionally, rates of 0.2, 20, 200 mm/min were used for specimens with a normalised insert length of 0.5. For the impact tests carried out on specimens with a normalised insert length of 0.5, an impact speed of 3.2 m/sec was used.

4.3. ECT Test Fixture

Mode III interlaminar fracture in composites has received limited attention in the research literature. Several test techniques have been proposed for characterising Mode III delamination fracture, including the split cantilever beam [3] and the cracked rail shear specimen [4]. The most commonly investigated Mode III fracture test method is the Edge Crack Torsion (ECT) test [5], the modified version of which has been used in this research programme. An ECT specimen is a rectangular laminate of tape composite material, containing an edge delamination at the mid-plane of the specimen. Equal and opposite moment arms are applied to the specimen ends.

These moment arms generate a torsion load in the specimen, resulting in relative shear sliding of the delaminated faces.

The original ECT test fixture consisted of a load frame in which the specimen was positioned between three support pins, and load was applied via a fourth pin [5]. A number of studies concluded that this specimen produced Mode III-dominated loading at the delamination front in the centre of the specimen, away from the loading points [6, 7].

A round-robin exercise was organised by the ASTM D30 committee to characterise the test method [8]. The ECT tests were undertaken in five independent laboratories on specimens manufactured from the toughened carbon/epoxy system, HTA/6376. Large scatter in calculated fracture toughness values were reported and some laboratories reported significant nonlinearity in load-displacement response of the specimens. The test frame was then modified, resulting in a symmetrical load application via two pins. A loading beam is used to allow uniform load transfer from test machine to the loading pins. Another finding of the studies was that a significant Mode II component of strain energy release rate, G_{II}, was generated near to the location of the loading pins [9]. It was argued that increasing the specimen length, L, would reduce the Mode II component and therefore promote Mode III delamination in the centre portion of the specimen. Consequently, the specimen length was increased from 82.5 mm to 108 mm.

The test rig used for ECT testing was a symmetric two-point test fixture. In this fixture, two supports are located at diagonally opposite corners of the test fixture. Two columns are located at the opposite corners to the support points. These columns contain vertical holes. Specimens are placed on the support pins. Loading pins are placed through the holes in the columns, in order to make contact with the specimen. A loading beam is placed onto the loading pins, as illustrated in Figure 4.3.

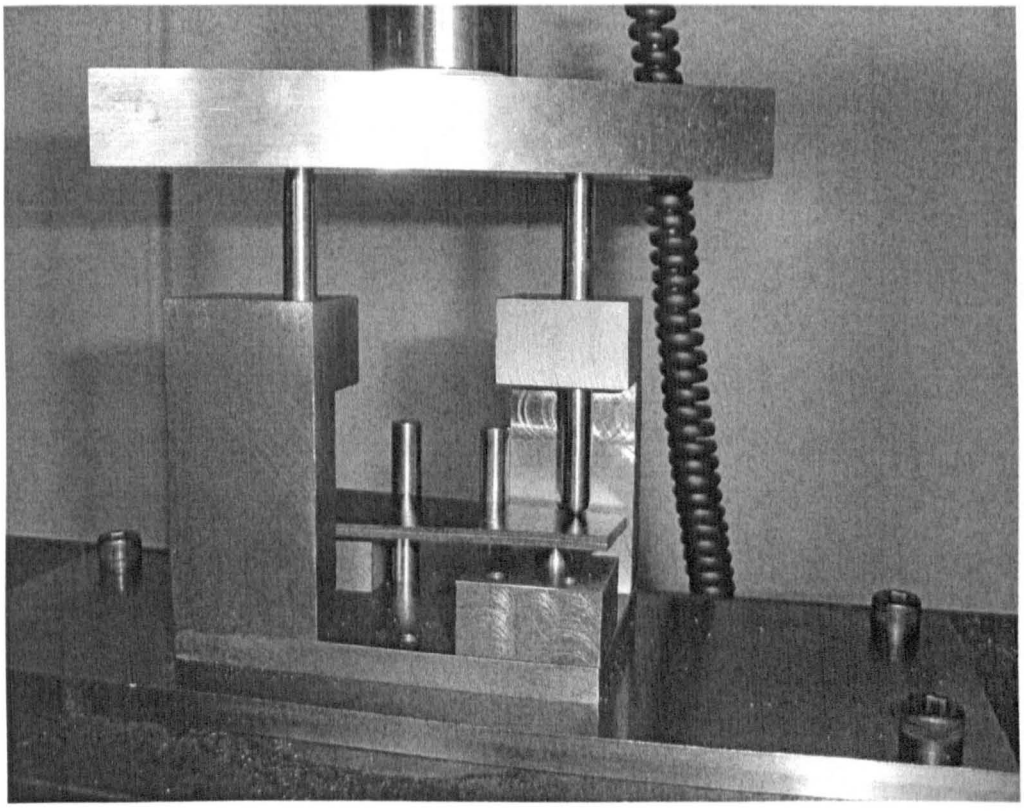

Figure 4.3: Photograph of an ECT test fixture with a specimen in position.

During an ECT test, load is applied to the centre of the loading beam positioned above the specimen. The load is equally distributed on the ECT specimen via the two load pins. Three guide pins are positioned on the fixture to enable precise alignment of the specimen.

Dassault Systemes CATIA v5 was used to design the ECT test fixture prior to its manufacture. A mechanical drawing, as well as a CAD drawing of this is shown in Figures 4.4 and 4.5 respectively. Figure 4.6 shows the resulting test rig with the guide, support and load pins in place.

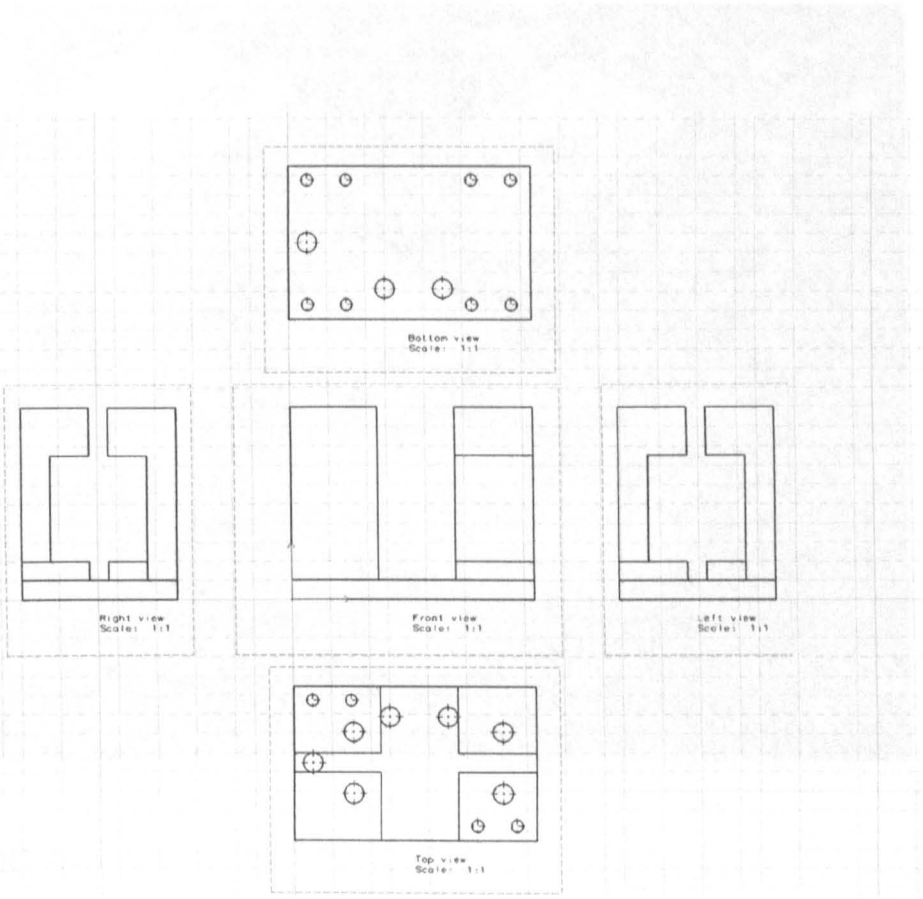

Figure 4.4: Mechanical drawing with side, top and bottom views of the ECT test fixture, produced in CATIA.

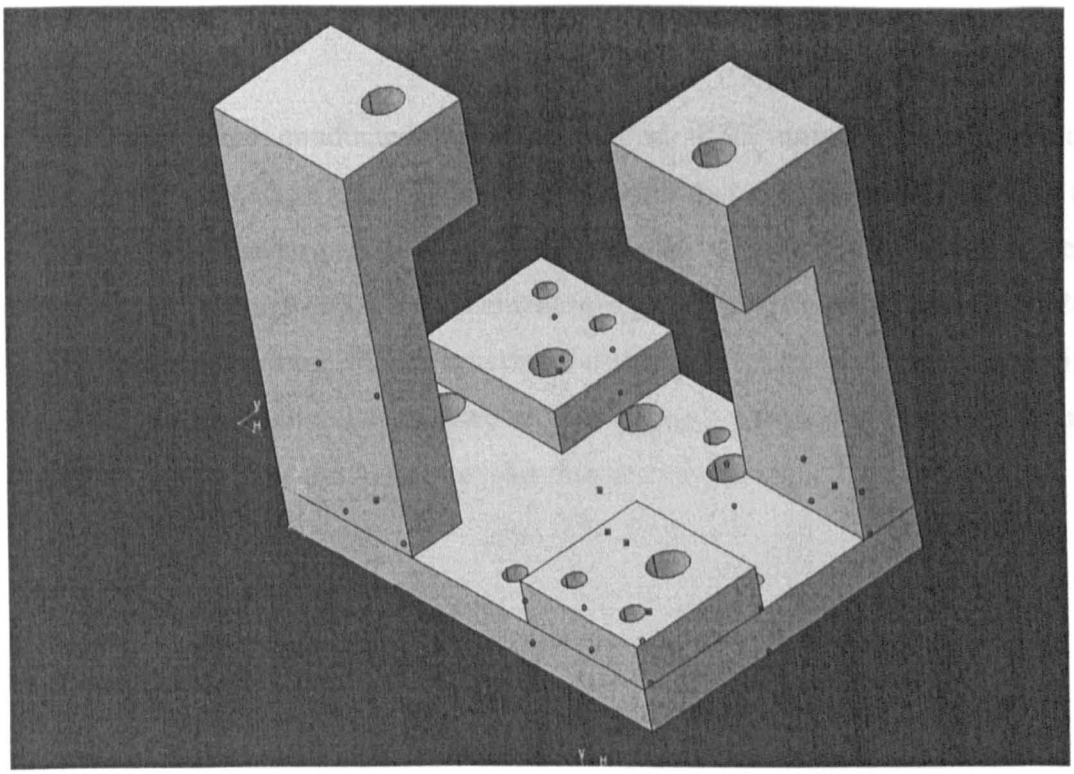

Figure 4.5: CAD drawing of the ECT test fixture.

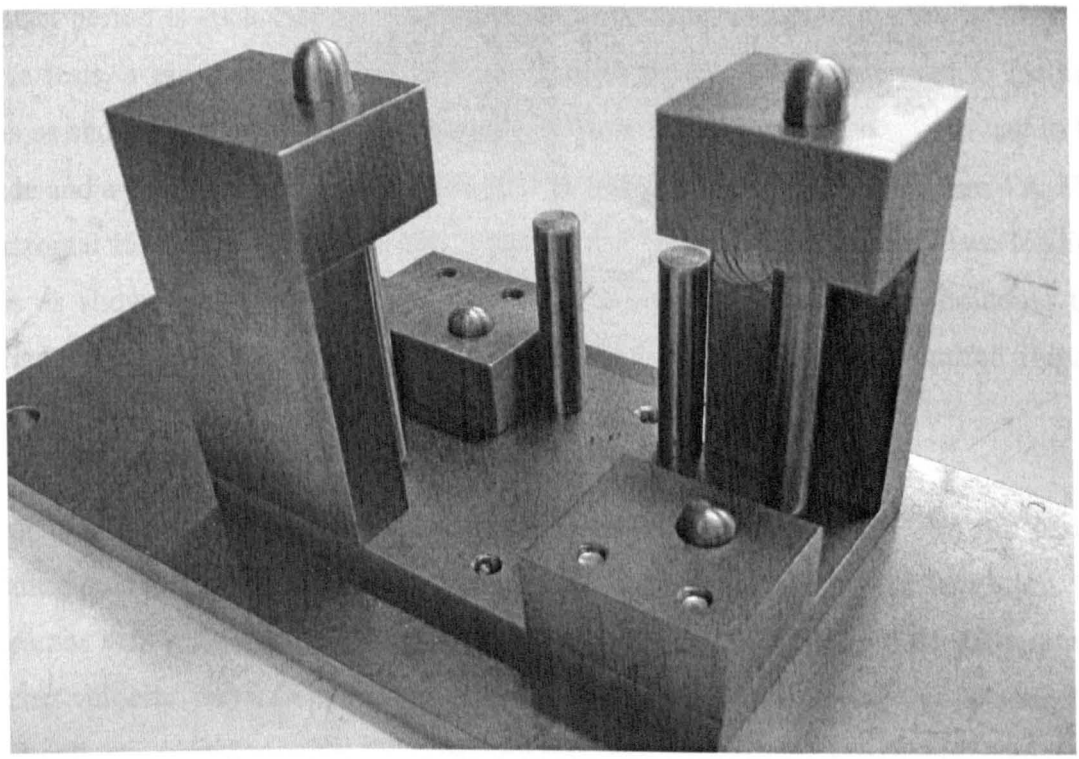

Figure 4.6: Photograph of the ECT test fixture.

4.4. ECT Tests

The ECT tests were conducted using an Instron 4505 universal test machine. Specimens were placed in the ECT test fixture, such that contact was made with all three guide pins, ensuring precise specimen alignment. After levelling, the specimens were loaded until failure under displacement control at rates ranging from 0.2 to 200 mm/min. The applied load, P, and crosshead displacement, δ, were recorded during each test using data acquisition software on a computer connected to the test machine. This data were plotted in the form of a load-displacement trace.

4.5. Impact Tests

Impact tests on the ECT samples were undertaken using an instrumented drop-weight impact tower. Due to the fact that the impact was in the range of 1 to 10 m/sec, the tests could be characterized as 'low velocity impact' [10, 11], on the grounds that the contact period is such that the whole structure has time to respond to the loading. In these tests, a piezo-electric load-cell was located in one of the two vertical loading pins as shown in Figure 4.7. For this purpose, a new two-piece loading pin had to be made and a detailed view of this load pin with the load cell is given in Figure 4.8. The horizontal loading bar was attached to the falling carriage to impact the two loading pins as shown in Figure 4.7. The total mass of the falling carriage, including the horizontal loading bar ranged from 3 to 4 kg, depending on the required impact velocity.

Prior to testing, a small amount of visco-elastic material was placed on top of the loading pins to cushion the impact with the horizontal loading bar. During testing, the impactor was released from heights ranging from 30 to 90 cm to give the required impact velocity, depending on the material tested. The voltage from the piezo-electric load-cell was recorded using the Dataflow software package on a dedicated computer. The resulting voltage-time traces were converted to force-time traces using the force-voltage calibration factor for the load cell.

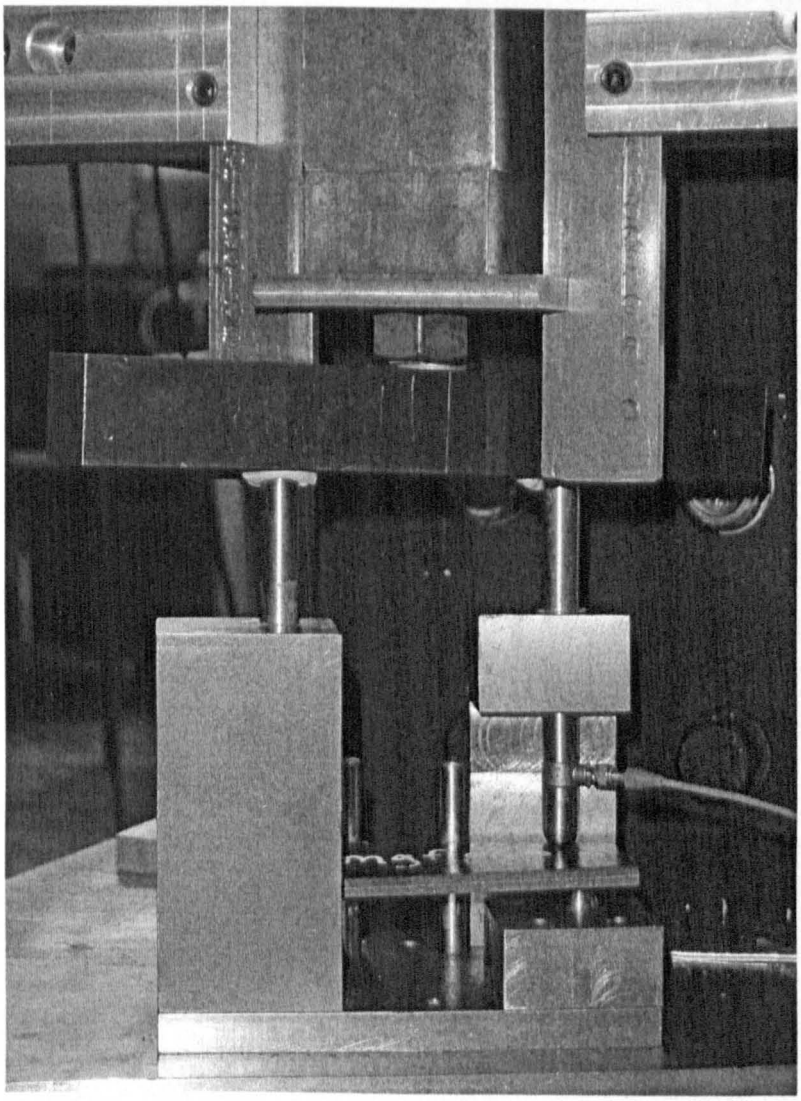

Figure 4.7: The modified ECT test fixture for impact testing.

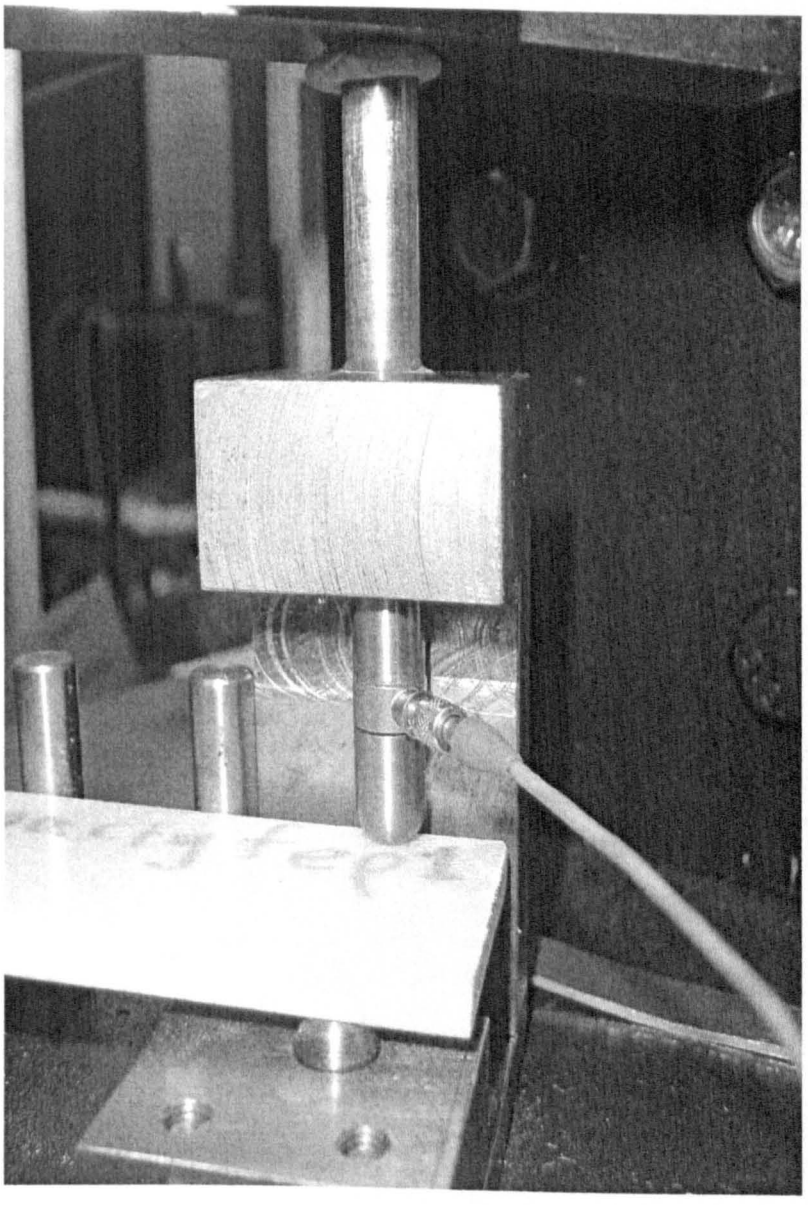

Figure 4.8: Magnified region of the load pin with the integrated load cell for ECT impact testing.

4.6. Post-processing of Results

The compliance calibration method, to be outlined in the next chapter, was used to determine the Mode III interlaminar fracture properties of the composite materials examined in this research study. Initially, the fracture toughness of the composites was determined at a crosshead displacement rate of 2 mm/min. During each test, load-displacement plots were obtained from which the specimen compliance was determined. The inverse of the specimen compliance, 1/C, was then plotted as a function of the normalised insert length, a/b and a straight line was then applied to the data, according to:

$$1/C = A\,[1\text{-}m(a/b)] \tag{4.1}$$

The Mode III fracture toughness of each ECT specimen at maximum load, G_{IIIc}^{Max} was calculated using the maximum force, P_{max}, according to [12]:

$$G_{IIIc}^{Max} = \frac{mC}{2lb[1-m(a/b)]} P_{max}^2 \tag{4.2}$$

where l is the distance between the supports and b is the specimen width, as shown in Figure 4.9.

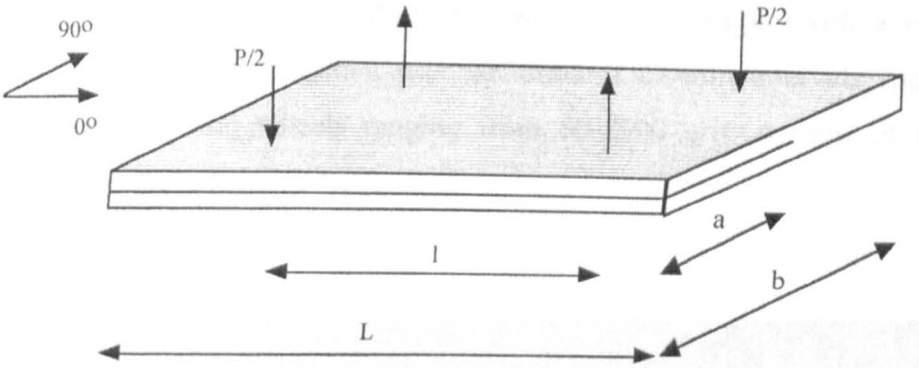

Figure 4.9: Schematic of the ECT test specimen.

As a result of a material shortage, it was not possible to conduct tests on specimens with the full range of crack lengths at each crosshead displacement rate. Instead, the value of 'm' determined at 2 mm/min was used to calculate G_{IIIc} at all crosshead displacement rates. This was considered acceptable since it is generally accepted that the elastic modulus properties of glass fibre reinforced composites are insensitive to strain rate [13].

4.7. Scanning Electron and Optical Microscopy

A Cambridge S360 scanning electron microscope was used to examine the Mode III fracture surfaces of the glass fibre reinforced polypropylene and woven glass fibre reinforced epoxy samples. Sections were taken from the centre of the test samples and examined within 2 mm of the starter crack tip. The samples were coated with a thin layer of gold prior to examination. Specimens that had been tested at a crosshead displacement rate of 2 mm/min and under impact conditions were examined.

A Wild optical microscope was used to examine the crack propagation of the adhesively-bonded woven glass fibre reinforced epoxy sample with a normalised insert length of 0.5. The specimen was sectioned at 27 mm intervals and polished using Metaserv grinding wheels ranging from 60-2500 grit. A view of the stereo microscope is given in Figures 4.10.

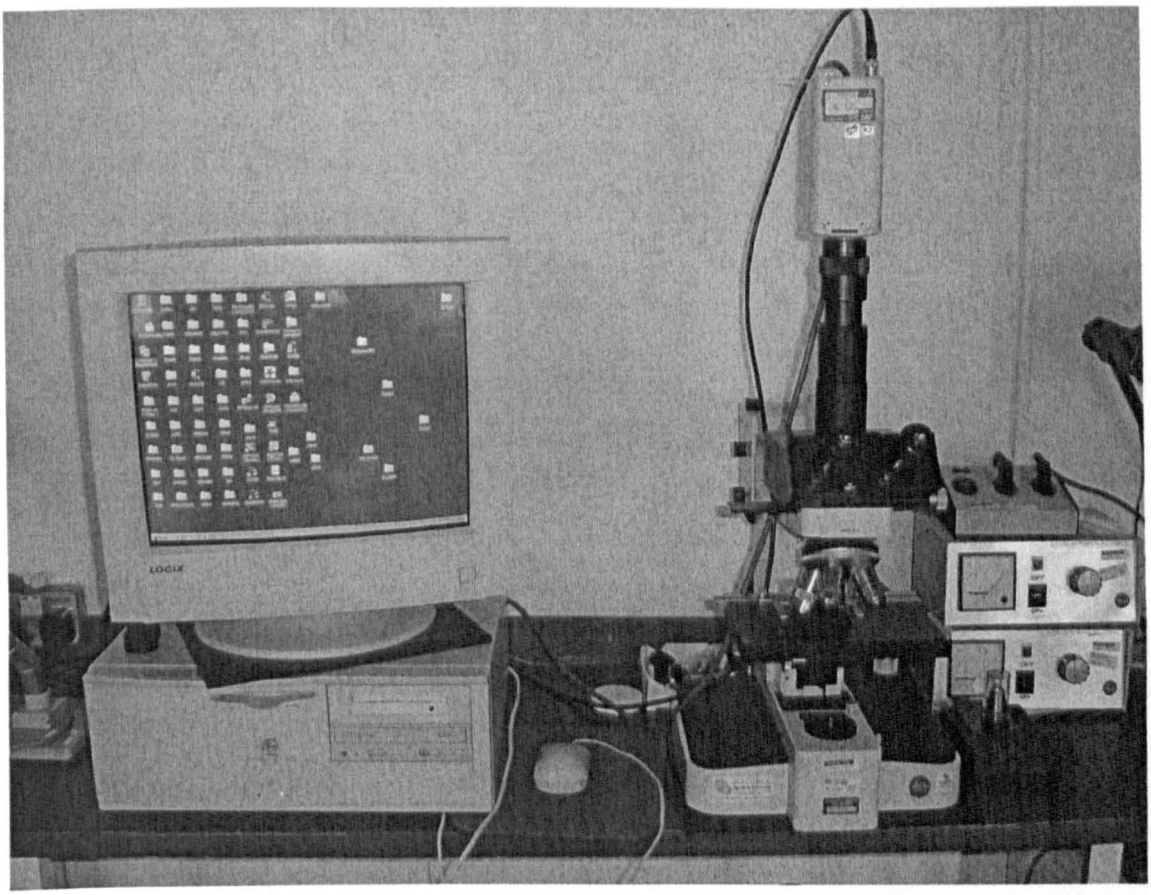

Figure 4.10: The Wild optical microscope with the dedicated computer.

4.8. References

1. Davies P., Cantwell W.J., Fracture of glass/polypropylene laminates: influence of cooling rate after moulding, Journal of Composites, Vol.25, 1994, p.869.

2. Ismail Y.S., Richardson M.O.W., Olley R.H., Optimizing impact properties of PP composites by control of spherulitic morphology, Journal of Applied Polymer Science, Vol.79, 2001, p.1704.

3. Donaldson S.L., Mall S., Ling C., The split cantilever beam test for characterising Mode III Fracture Toughness, Journal of Composites Technology and Research, JCTRER, Vol.13, 1991, p.41.

4. Becht G., Gillespie J.W. Jr, Design and analysis of the crack rail shear specimen for Mode III interlaminar fracture, Composites Science and Technology, Vol.31, 1988, p.143.

5. Lee S.M., An Edge Crack Torsion Method for Mode III Delamination Fracture Testing, Journal of Composites Technology and Research, JCTRER, Vol.15, 1993, p.193.

6. Li J., O' Brien T.K., Analytical Investigation of the Hydrothermal Effects and Parametric Study of the Edge Crack Torsion (ECT) Mode III test lay-ups, Composite Materials: Fatigue and Fracture, Sixth Volume, ASTM STP 1285, E.A. Armanios Ed., ASTM 1997, p.411.

7. Li J., O' Brien T.K., Simplified Data Reduction methods for the ECT test for Mode III Interlaminar Fracture Toughness, Journal of Composites Technology and Research, JCTRER, Vol.18, 1996, p.96.

8. Minutes of Sub-Committee D30.06 on Interlaminar Properties. Report from the Second Round-Robin on the Edge Crack Torsion Test, May 1997

9. Minutes of Sub-Committee D30.06 on Interlaminar Properties. Report from the Second Round-Robin on the Edge Crack Torsion Test, May 1999.

10. Cantwell W.J., Morton J., The impact resistance of composite materials-a review, Composites, Vol.22, 1991, p.347.

11. Richardson M.O.W., Wisheart M.J., Review of low-velocity impact properties of composite materials, Composites, Vol.27A, 1996, p.1123.

12. Ratcliffe J.G., Characterization of the edge crack torsion (ECT) test for Mode III fracture toughness measurement of laminated composites, National Research Council, NASA Langley Research Centre, Hampton, Virginia, NASA/TM-2004-213269, 2004.

13. Cantwell W.J., Büsser M., Kausch H.H., An analysis of the impact response of a composite beam, Composites Engineering, 1, 1991, p.293.

5. Numerical Results and Discussion

5.1. Introduction

This chapter presents the findings from the finite element analyses conducted to determine the crack-tip loading conditions in the ECT specimens, according to the procedures described in Chapter 3.

Verification of the analyses was performed by comparing the predicted responses of the ECT specimens with those determined experimentally during the actual ECT tests. The FEA focused on determining the distribution of the Mode II and Mode III strain energy release rates along the crack front and investigating the influence of a number of factors, such as the crack length, the applied displacement and specimen thickness on the crack-tip loading conditions in these specimens. The results of a study on the isotropic and orthotropic materials are presented.

5.2. Finite Element Model Verification

5.2.1. Optimisation of the Finite Element Mesh Density

For the virtual crack closure technique, the energy release rates are defined as the virtual crack closure integral over a finite crack closure length. This crack closure length corresponds to the length of the elements adjacent to the crack front. The element length should therefore be chosen small enough to ensure a converged FE solution but large enough to avoid oscillating results. According to previous researchers [1], upper and lower bounds must be assumed for practical applications. As a result, the element length should not be less than one tenth of a ply thickness. For smaller element sizes the assumption of modelling each ply as an orthotropic continuum is no longer valid. Furthermore, the ply thickness should be the upper limit for the element height.

In order to verify that the mesh density chosen to model the ECT specimen was of an appropriate size, three models with different element edge lengths in the region around the crack tip (element length in the y direction, Figure 3.6) were examined. The numerical simulations were conducted on a glass fibre reinforced polypropylene sample, having a normalised insert length of 0.5. A displacement of 2 mm was applied in order to ensure an elastic response from the specimens. The values chosen for the crack-tip element edge lengths were 0.1, 0.2 and 0.5 mm respectively. After analysing the results, the value of the Mode III strain energy release rate at the mid-width of the specimen was calculated, using Equation 3.2. A plot of the resulting G_{III} values versus the element edge length in the y axis is shown in Figure 5.1:

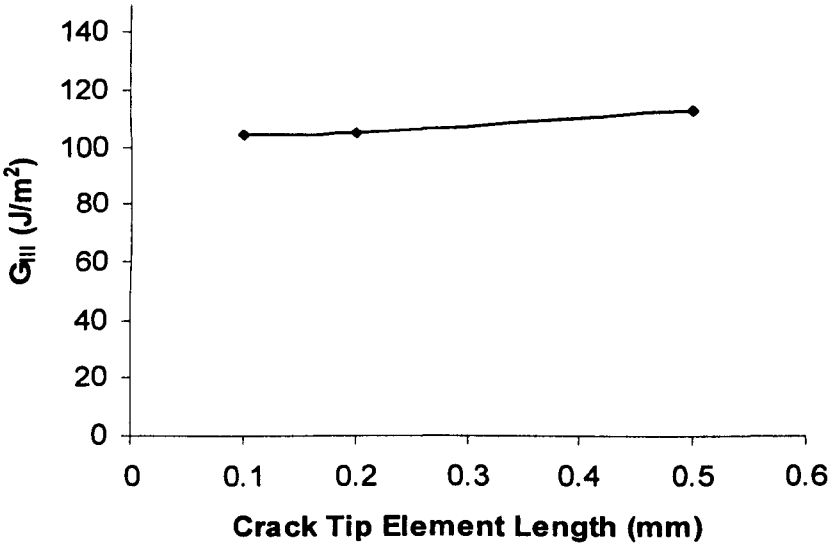

Figure 5.1: The effect of crack-tip element length on the Mode III strain energy release rate at the specimen mid-width.

In Figure 5.1 it is clear that G_{III} converges to a value of approximately 104 J/m^2. However, due to computer limitations and time constraints, an element size of 0.5 mm was selected for the crack-tip element length. The error compared to the value of convergence is only 8% which is acceptable considering that the finite element models were mainly used to observe the trends in varying crack length on G_{III} in the various materials examined in this study.

5.2.2. Comparison of Finite Element Models with Experiments

The accuracy of the finite element models was evaluated by comparing the predicted elastic responses of the ECT specimens with those determined experimentally during the actual ECT tests. This was done by calculating and plotting the variation of the inverse of specimen compliance with normalised insert length, a/b, for both the FEA and experimental data. As will be shown in Chapter 5, there is reasonable agreement

between experiments and the analyses which suggests the finite element analysis procedures used herein accurately model the response of the specimens.

5.3. Isotropic Models

5.3.1. Variation of Inverse of Specimen Compliance

Three-dimensional finite element models of isotropic ECT specimens were constructed and analysed using ANSYS, following the procedure described in Section 3.5.1. The models simulated specimens with normalised insert lengths ranging from 0.3 to 0.7, as well as an uncracked ECT specimen.

The compliance calibration method, similar to that employed elsewhere [2] was used to determine the Mode III interlaminar fracture properties of the isotropic material investigated in this part of the study. The inverse of the specimen compliance, 1/C, was then plotted as a function of the normalised insert length, a/b and a straight line was then applied to the data according to:

$$1/C = A\,[1-m(a/b)] \tag{5.1}$$

Figure 5.2 shows the variation of the inverse of specimen compliance with normalised insert length, a/b, for isotropic specimens. The predictions of the FE analysis indicated that the plot of the inverse of specimen compliance with crack length was slightly non-linear at the highest normalised crack lengths. It should be noted that the value of m in Equation 5.1 was equal to 0.74.

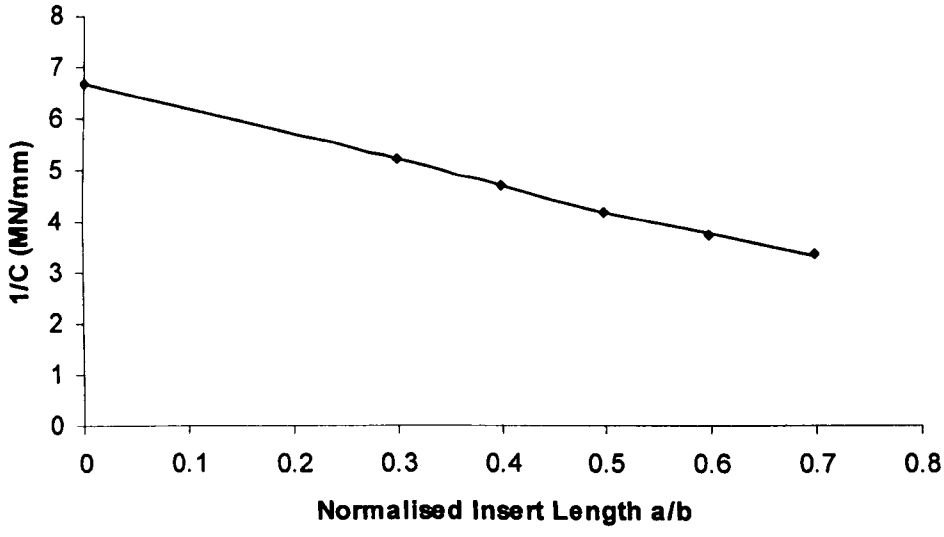

Figure 5.2: The variation of the inverse of specimen compliance with normalised crack length for the isotropic ECT specimens.

5.3.2. Mode II and Mode III Strain Energy Release Rate Distributions

The virtual crack closure technique (VCCT), as presented in Section 2.8, was used to calculate the Mode II and Mode III components of strain energy release rate (G_{II} and G_{III} respectively) along the delamination front in the finite element models. Figure 5.3 presents plots of the Mode II and Mode III strain energy release rate distributions across the delamination front, for the isotropic ECT specimen with a normalised insert length of 0.5:

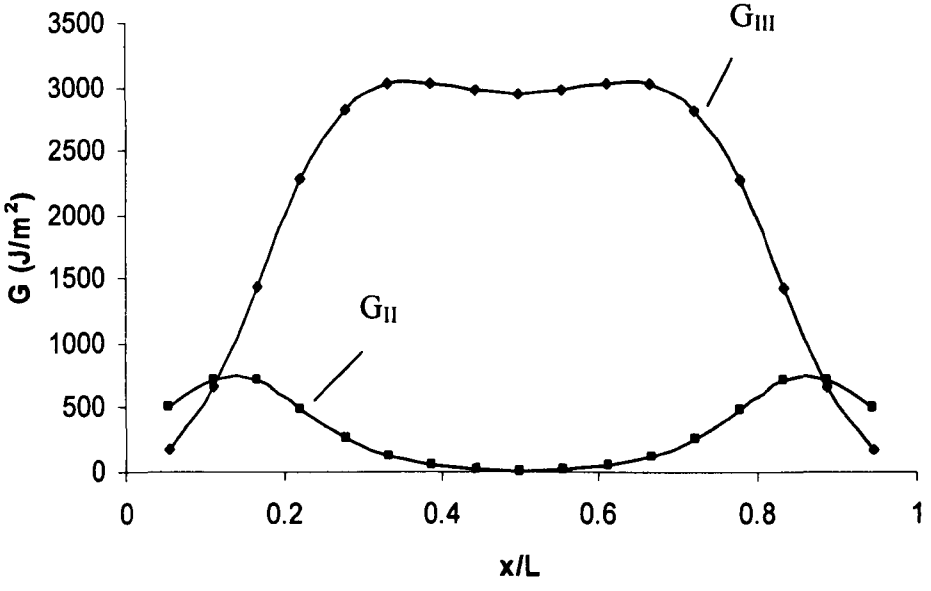

Figure 5.3: Computed strain energy release rate distribution across the delamination front for an isotropic ECT specimen with a normalised insert length of 0.5.

In the previous figure, the Mode I component of strain energy release rate was not included as this was found to be negligible relative to the values of G_{II} and G_{III} in all of the specimens. The parameter G_{II} was found to peak at the locations of the load and support pins and G_{III} peaks in the central region of the specimen. Due to the load and support pins, a moment arm is generated which causes relative sliding of the two delaminated sections of the specimen, parallel to the direction in which the delamination tends to grow. As a result, G_{II} peaks at the location of the load pins. The finding that G_I in the ECT specimen was negligible is supported by the fact that the relative opening of the delaminated sections of the specimen was also negligible. From the plot of G_{III}, it can be seen that the value of the Mode III strain energy release rate is several times higher than the corresponding Mode II strain energy release rates. This indicates that Mode III is the dominant loading condition type, resulting in delamination initiating from the centre of the specimen insert front.

Figure 5.4 shows the variation of G_{III} along the delamination front for the isotropic ECT specimens investigated. Here, the Mode III strain energy release rate is plotted for normalised insert lengths between 0.3 and 0.7. G_{III} was found to increase rapidly at the edges before reaching a maximum value closer to the centre of the specimen. An examination of the plots indicates that G_{III} is roughly constant over the central region of the test specimen in samples with intermediate crack lengths whereas two maxima are observed in specimens with shorter and longer insert lengths. The evidence suggests that normalised crack lengths between 0.4 and 0.6 yield relatively flat G_{III} profiles across the central region of the test specimen, representing the most suitable crack configurations when undertaking tests.

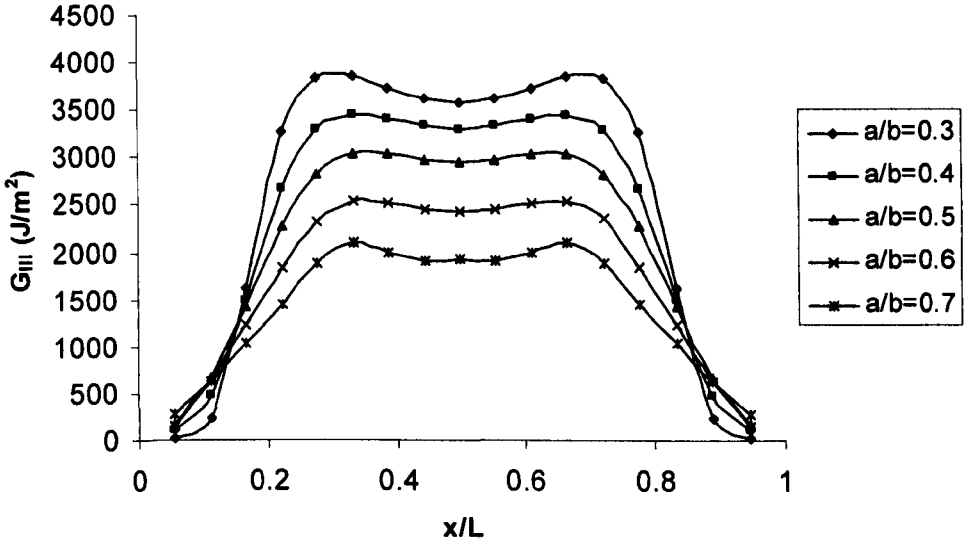

Figure 5.4: Mode III strain energy distribution for the isotropic material as a function of position along the crack front. The numbers in the legend correspond to the normalised crack length 'a/b'.

Figure 5.5 shows plots of the variation of G_{II} along the delamination front for the isotropic ECT specimens. From the plots of G_{II}, it can be seen that, as anticipated, the

values of the Mode II strain energy release rate are significantly smaller than the corresponding Mode III values. Given the relatively small contribution of Mode II loading in these specimens, it is assumed that the ECT test essentially generates a pure Mode III loading condition.

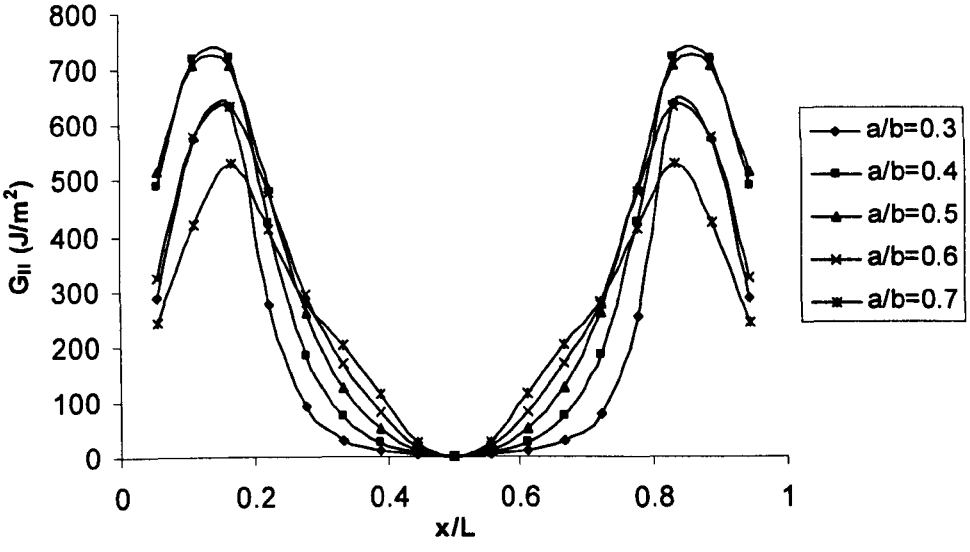

Figure 5.5: Mode II strain energy distribution for the isotropic material as a function of position along the crack front. The numbers in the legend correspond to the normalised crack length 'a/b'.

5.4. Orthotropic Models

5.4.1. Glass Fibre Reinforced Polypropylene

Three-dimensional finite element models of glass fibre reinforced polypropylene ECT specimens were constructed and analysed using ANSYS, following the procedure described in Section 3.5.2.1. The vast majority of specimens that were modelled had sixteen plies, and were based on the stacking sequence:

$$[90° / 0° (+45° / -45°) / (-45° / +45°) 0° / 90°]_s$$

Initially, the compliance calibration method was used to determine the Mode III interlaminar fracture properties of the material investigated in this part of the study. The predictions of the FE analysis on sixteen-ply specimens were compared to the calculated results from the experiments. Models simulating specimens with normalised insert lengths ranging from 0.2 to 0.7 were examined for this purpose.

The virtual crack closure technique (VCCT) was used to calculate the Mode II and Mode III components of strain energy release rate (G_{II} and G_{III} respectively) along the delamination front in the finite element models.

The effect of applied displacement on the Mode III strain energy release rate was investigated by running a series of analyses on sixteen ply glass fibre/PP ECT specimens with a normalised insert length of 0.5 and applied displacements ranging from 1 to 7 mm. In addition, the effect of the total number of plies on the Mode III strain energy release rate was investigated by constructing and analysing three-dimensional finite element models of glass fibre reinforced polypropylene ECT specimens with 24 and 32 plies, based on the stacking sequences:

$$[90° / 0° (+45°/-45°)_2 / (-45°/+45°)_2 / 0° / 90°]_s$$

$$[90° / 0° (+45°/-45°)_3 / (-45°/+45°)_3 / 0° / 90°]_s$$

respectively.

5.4.1.1. Finite Element Model Verification

The accuracy of the finite element model was evaluated by comparing the predicted elastic responses of the ECT specimens with those determined experimentally during the ECT tests. Figure 5.6 shows the variation of the inverse of specimen compliance with normalised insert length, a/b, for the glass fibre/PP composite specimens. The points in the figures correspond to the experimental data and the solid lines represent

the predictions offered by the finite element analysis. Included on the y-axis of the figure are data points corresponding to the elastic response of an uncracked plate with the same dimensions as those of the ECT specimen. From the figure, it is evident that the FE predictions are in reasonably good agreement with the experimental data over the range of crack lengths investigated. Closer inspection of the figure indicates that the trends in the experimental data are not completely linear with the gradient tending to reduce with increasing values of a/b. The predictions of the FE analysis also indicated that the plot of the inverse of specimen compliance with crack length was slightly non-linear at the highest normalised crack lengths, supporting the observations from the experimental data. In spite of the small degree of non-linearity in the inverse compliance curves, Equation 5.1 was applied to both the experimental and numerical data to yield the associated values of 'm', these being equal to 0.97 and 0.96 for the experiment and FEA data respectively.

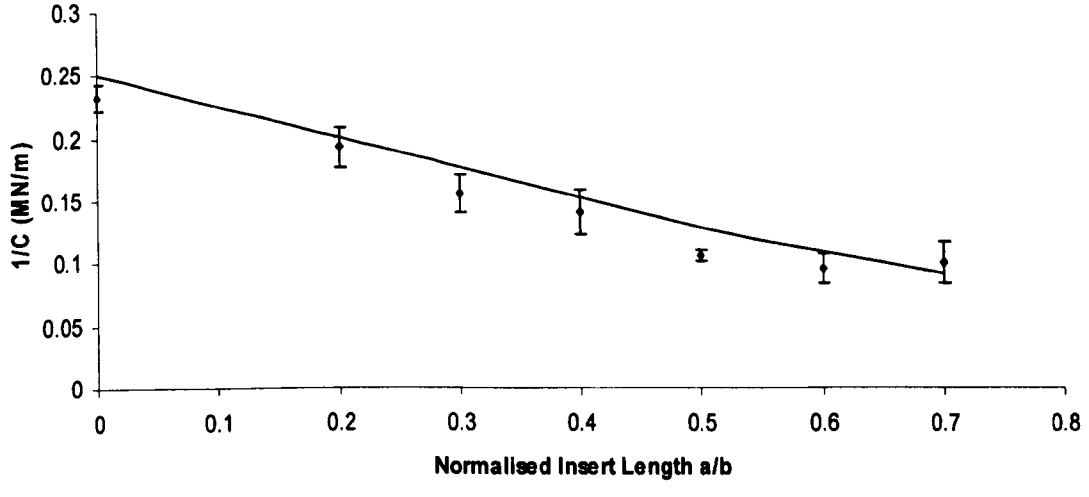

Figure 5.6: The variation of the inverse of specimen compliance with normalized crack length for the glass fibre/PP composite.

5.4.1.2. Mode II and Mode III Strain Energy Release Rate Distributions for the 16 Ply Specimens

Using the virtual crack closure technique (VCCT), the Mode II and Mode III components of strain energy release rate (G_{II} and G_{III} respectively) along the delamination front in the finite element models were calculated. Figure 5.7 includes plots of the Mode II and Mode III strain energy release rate distributions across the delamination front, for the glass fibre reinforced polypropylene ECT specimen with a normalised insert length of 0.5:

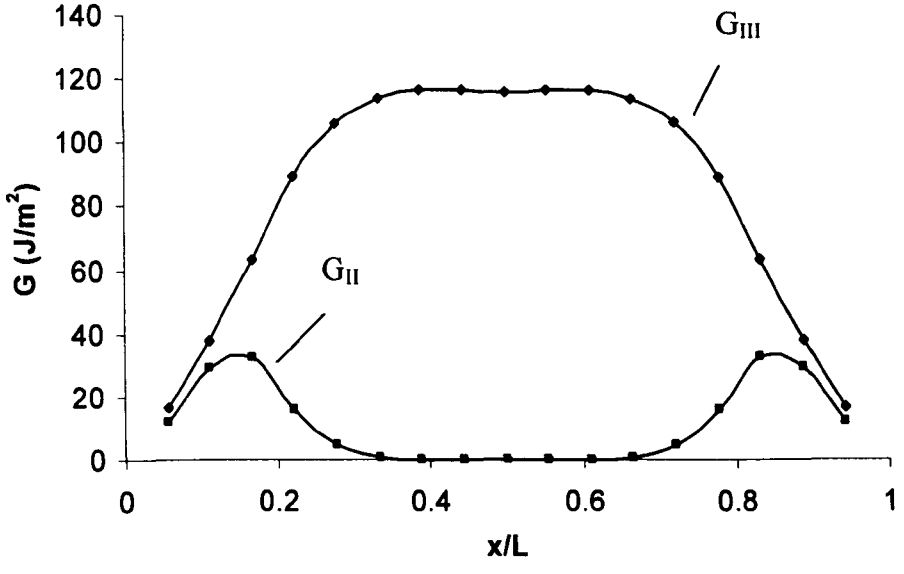

Figure 5.7: Computed strain energy release rate distribution across the delamination front for the glass fibre/PP ECT specimen with a normalised insert length of 0.5.

As was the case of the isotropic ECT specimens, the Mode I component of strain energy release rate is not included as this was found to be negligible relative to the values of G_{II} and G_{III} in all of the specimens. As before, the Mode II strain energy release rate distribution reaching its maximum value at the locations of the load and support pins. G_{III} was found to peak in the central region of the specimen. The value

of the Mode III strain energy release rate is several times higher than the corresponding Mode II strain energy release rates. This indicates that Mode III is the dominant loading condition type, resulting in delamination initiating from the centre of the specimen insert front.

Figure 5.8 shows the variation of G_{III} along the delamination front for the glass fibre reinforced polypropylene ECT specimens analysed in this study. Here, the Mode III strain energy release rate is plotted for normalised insert lengths between 0.2 and 0.7. As expected, the values of G_{III} are higher for the smaller normalised insert lengths. Moreover, the values of the Mode III strain energy release rate increased rapidly at the edges before reaching a maximum value closer to the centre of the specimen. It is clear from the plots that G_{III} is roughly constant over the central region of the test specimen in samples with intermediate crack lengths whereas two maxima are observed in specimens with shorter and longer insert lengths. The evidence suggests that normalised crack lengths between 0.3 and 0.5 yield relatively flat G_{III} profiles across the central region of the test specimen, representing the most suitable crack configurations when undertaking tests on this material.

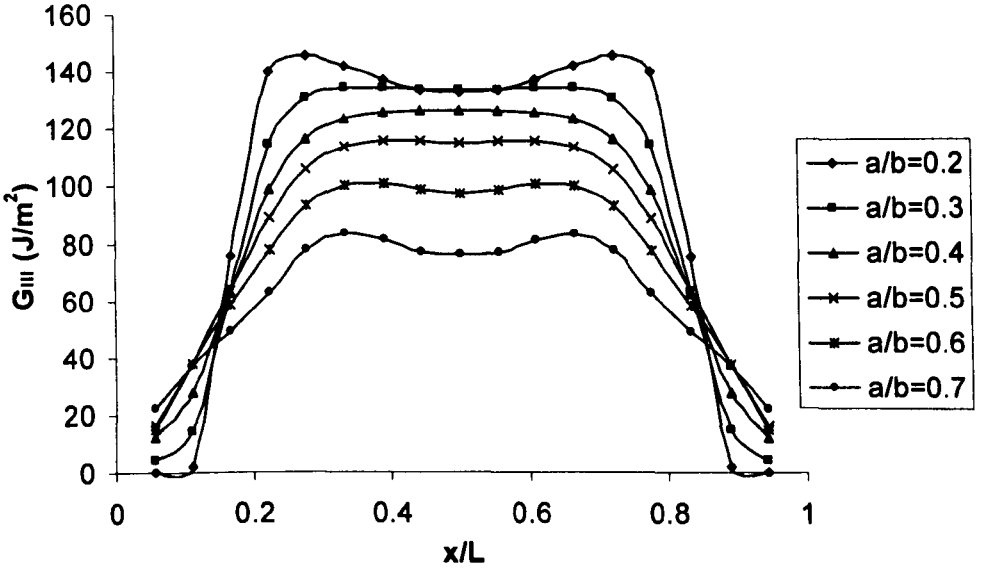

Figure 5.8: Mode III strain energy distribution for the glass fibre/PP material as a function of position along the crack front. The numbers in the legend correspond to the normalised crack length 'a/b'.

Figure 5.9 shows plots of the variation of Mode II strain energy release rate along the delamination front for the glass fibre/PP ECT specimens. The values of G_{II} are significantly smaller than the corresponding G_{III} values. For a given applied displacement, the values of G_{II} are higher for smaller crack lengths. As a result of the small contribution of Mode II loading in these specimens, it can be assumed that the ECT test essentially generates a pure Mode III loading condition.

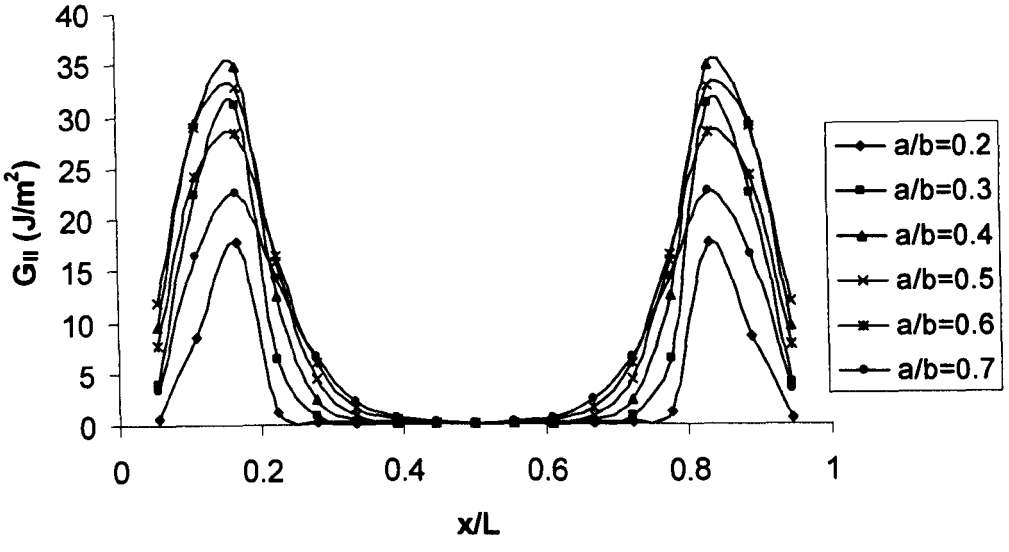

Figure 5.9: Mode II strain energy distribution for the glass fibre/PP material as a function of position along the crack front. The numbers in the legend correspond to the normalised crack length 'a/b'.

5.4.1.3. Effect of Applied Displacement

A series of finite element models of the glass fibre reinforced polypropylene ECT specimen were analysed, where the applied displacement ranged from 1 to 7 mm. These analyses were undertaken in order to investigate the effect of applied displacement on the strain energy release rate profile and to see if the profile will change during testing. All the ECT specimens simulated had a normalised insert length of 0.5. Using the VCCT, the Mode III component of the strain energy release

rate was calculated for each model across the delamination front and the results are shown in Figure 5.10. As expected, the calculated values of G_{III} are higher as the applied displacement is increased and is attributed to the higher force experienced by the material at higher displacements. The results indicate that the width of the region over which the value of G_{III} is roughly uniform for all initial displacements and should not, therefore, change during testing.

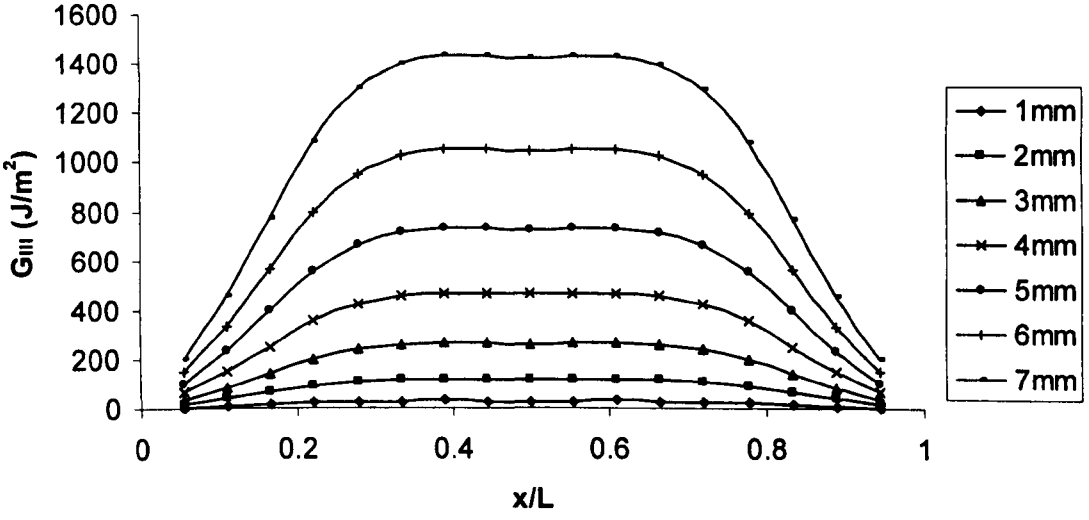

Figure 5.10: Mode III strain energy distribution for the glass fibre/PP material as a function of position along the crack front. The numbers in the legend correspond to the applied displacement.

5.4.1.4. Effect of Total Ply Number

The effect of varying the thickness of the ECT specimens on the profile of the Mode III and Mode II strain energy release rate was investigated by increasing the number of grouped +/-45° plies in the glass fibre/PP specimens. Here, finite element models with stacking sequences of $[90°/0°(+45°/-45°)_n/(-45°/+45°)_n0°/90°]_s$ where n = 1, 2 and 3 were constructed and analysed. In each analysis, the normalised insert length in these 16, 24 and 32 ply laminates was maintained at 0.5 and a prescribed displacement of 2 mm was applied.

It is clear that the calculated values of G_{III} and G_{II} are higher in the thicker samples and is attributed to the higher rigidity of these laminates. However, the curves show that the region over which the value of G_{III} is constant is the same in all three samples, suggesting that, from the point of view of the G_{III} profile, there is no perceived benefit from increasing the thicknesses of the +/-45 plies. It should be noted at this point that the research work by Zhao and Wang [3] on the Mode III fracture behaviour of ECT specimens showed similar trends with increasing thickness.

The value of the Mode III strain energy release rate is several times higher than the corresponding Mode II strain energy release rates, indicating that Mode III is the dominant loading condition type. It is clear from the plots that G_{III} is roughly constant over the central region of the 16 ply test specimen, whereas two maxima are observed in specimens with 24 and 32 plies. The evidence suggests that the 16 ply stacking sequence used with the glass fibre reinforced polypropylene material yields relatively flat G_{III} profiles across the central region of the test specimen, representing the most suitable stacking sequence configuration when undertaking tests on this material.

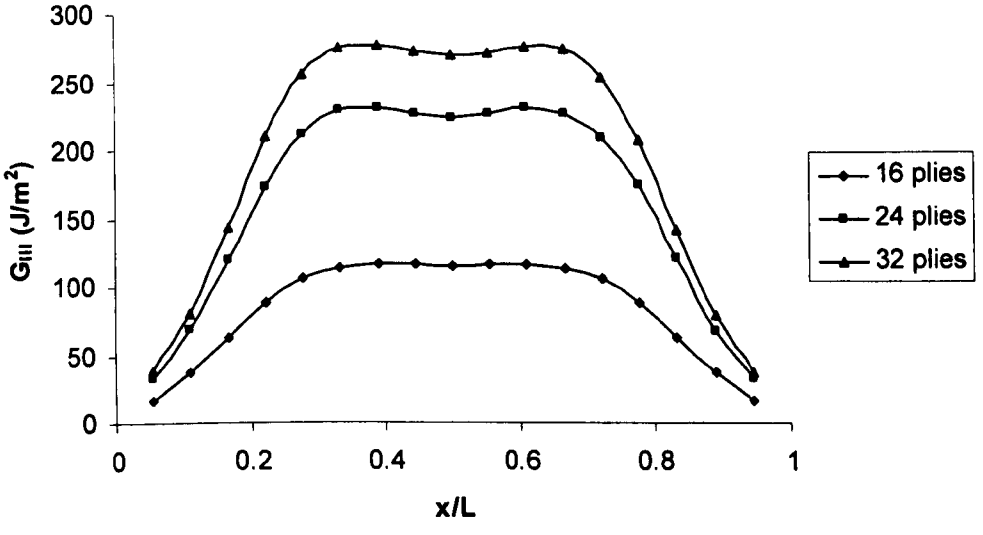

Figure 5.11: Mode III strain energy distribution for the glass fibre/PP material as a function of position along the crack front. The numbers in the legend correspond to the total number of plies of the laminates.

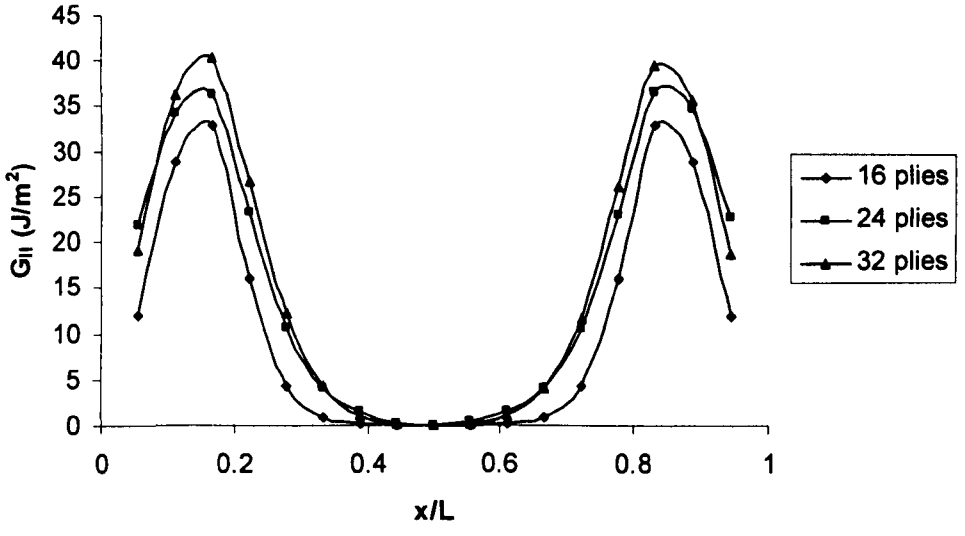

Figure 5.12: Mode II strain energy distribution for the glass fibre/PP material as a function of position along the crack front. The numbers of the legend correspond to the total number of plies of the laminates.

5.4.1.5. Effect of Insert Length on Average Total Strain Energy Release Rate

The total strain energy release rate at any location along the delamination front, G_T, was calculated as the sum of the individual strain energy release rate components:

$$G_T = G_I + G_{II} + G_{III} \tag{5.2}$$

The total average strain energy release rate across the entire delamination length, G_{Ta}, was computed as the integral of the total strain energy rate divided by the delamination length.

Figure 5.13 contains a plot of the average total strain energy release, G_{Ta}, versus normalised insert length, calculated from analyses of the glass fibre reinforced polypropylene ECT specimens. The values of G_{Ta} were found to decrease with insert length. According to Williams [4] who investigated specimen compliance and

stability criteria for fixed load and fixed displacement conditions, if the ratio dG/d(a/b) is positive then crack growth will be unstable. The opposite happens when dG/d(a/b) is negative or equal to zero. Considering that the same displacement was prescribed in each analysis, the decrease in G_{Ta} with insert length implies the delamination growth will be stable if testing is performed under displacement control.

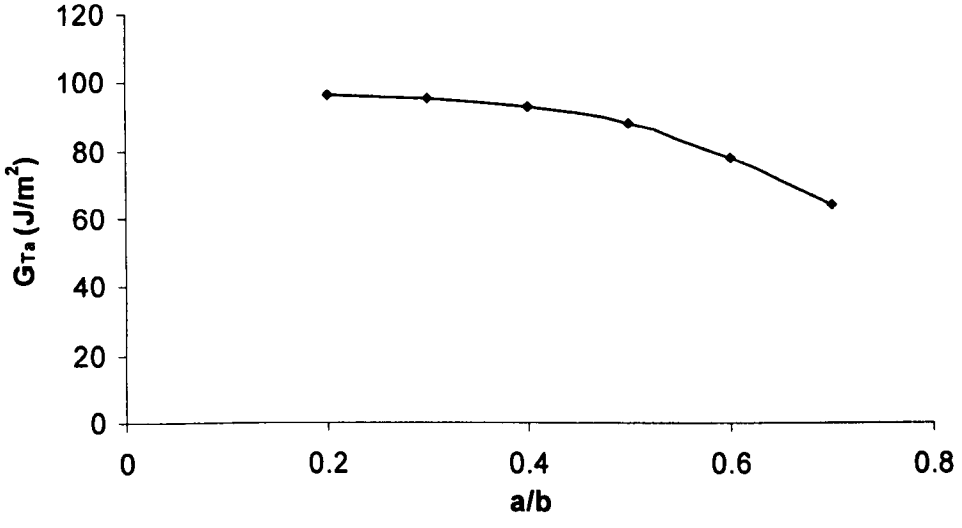

Figure 5.13: Computed average total strain energy release rate versus a/b for the glass fibre/PP ECT specimens.

5.4.2. Woven Glass Fibre Reinforced Epoxy

Twenty-four ply three-dimensional finite element models of the woven glass fibre reinforced epoxy specimens were constructed and analysed, following the procedures described in Section 3.5.2.2. The following stacking sequence was used:

$$[90° / 0° (+45° / -45°)_2 / (-45° / +45°)_2 0° / 90°]_s$$

As with the glass fibre/PP specimens, the compliance calibration method was used to determine the Mode III interlaminar fracture properties of the material. The

predictions of the FE analysis on 24 ply specimens were compared to the calculated results from the experiments. Models simulating specimens with normalised insert lengths ranging from 0.2 to 0.7 were examined for this purpose. The Mode II and Mode III components of strain energy release rate (G_{II} and G_{III} respectively) along the delamination front in the finite element models were calculated and the results were plotted. Analyses were also performed on specimens with a normalised insert length of 0.5 and the crack positioned at different locations through the thickness (at 4, 8, 16 and 20 plies from the top surface). Furthermore, a number of cases were examined, in which specimens with insert lengths ranging from 0.2 to 0.7 had the crack positioned at 4 plies from the top surface.

5.4.2.1. Finite Element Model Verification

The accuracy of the finite element model was evaluated by comparing the predicted elastic responses of the woven glass fibre reinforced epoxy ECT specimens with those determined experimentally during the ECT tests. The variation of the inverse of specimen compliance with normalised insert length, a/b, for the aforementioned composite specimens are shown in Figure 5.14. Once again, the points in the figures correspond to the experimental data and the solid lines represent the predictions offered by the finite element analysis. Data points corresponding to the elastic response of an un-cracked plate with the same dimensions as those of the ECT specimen have also been included on the y-axis. Here, the analysis models the elastic response less accurately for the two extremes of crack length with errors of up to fifteen percent being recorded for values of a/b of 0.2 and 0.7. It is likely that these differences are associated with different fibre volume fractions in some of the laminates. A number of panels suffered resin bleed during processing, an effect that will clearly lead to a lower volume fraction of fibres in the resulting laminate. Once again the predictions of the FE analyses suggested that the plot of 1/C versus a/b was slightly non-linear with the slope decreasing slightly at higher crack lengths. In spite of the small degree of non-linearity in the inverse compliance curves, Equation 5.1 was applied to the numerical data to yield an associated value of 'm' of 0.79 for the

FEA data. This compares favourably with the value of 0.73 determined experimentally.

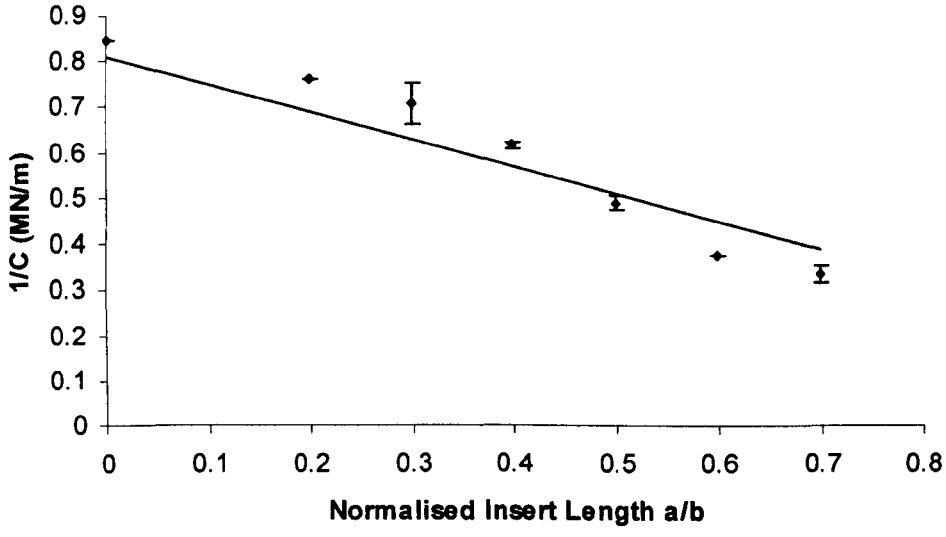

Figure 5.14: The variation of the inverse of specimen compliance with normalised crack length for the woven glass fibre/epoxy composite.

5.4.2.2. Mode II and Mode III Strain Energy Release Rate Distributions

Using the virtual crack closure technique (VCCT), the Mode II and Mode III components of strain energy release rate (G_{II} and G_{III} respectively) along the delamination front in the finite element models were calculated. Figure 5.15 includes plots of the Mode II and Mode III strain energy release rate distributions across the delamination front, for the woven glass fibre reinforced epoxy ECT specimen with a normalised insert length of 0.5:

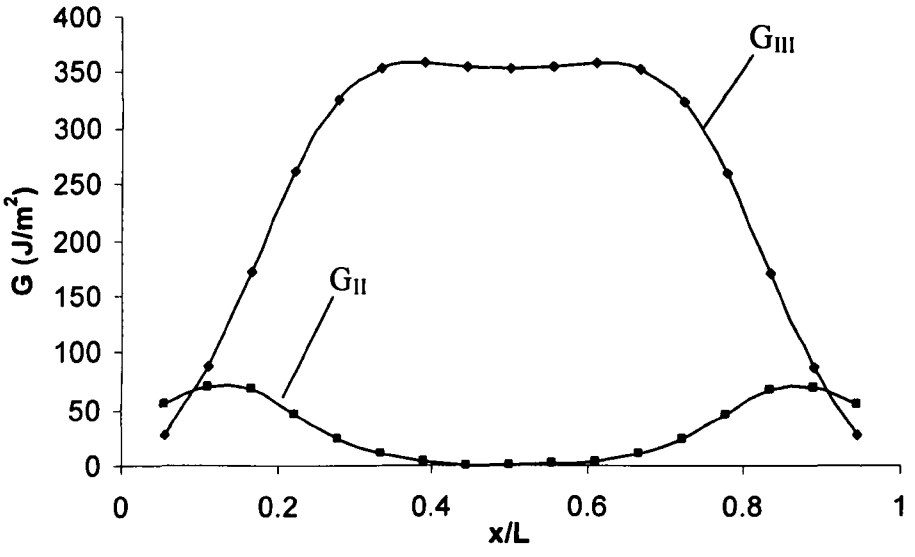

Figure 5.15: Computed strain energy release rate distribution across the delamination front for the woven glass fibre/epoxy ECT specimen with a normalised insert length of 0.5.

As with the previously examined materials, the Mode I component of strain energy release rate has not been included as this was found to be negligible relative to the values of G_{II} and G_{III} in all of the specimens. As before, the Mode II strain energy release rate distribution reaches its maximum value at the locations of the load and support pins. The G_{III} component of strain energy release rate reached its maximum value across the central region of the specimen, being several times higher than the corresponding Mode II strain energy release rates. As a result, Mode III is the dominant loading condition type and the delamination is initiated from the centre of the specimen insert front.

Figure 5.16 shows the variation of G_{III} along the delamination front for the woven glass fibre reinforced epoxy ECT specimens. Here, the Mode III strain energy release rate is plotted for normalised insert lengths between 0.2 and 0.7. This figure shows similar trends to those observed in Figure 5.7 for the glass/PP ECT specimens, with

the values of the Mode III strain energy release rate increasing rapidly at the edges before reaching a maximum value closer to the centre of the specimen. As was the case in the glass fibre reinforced polypropylene, the value of G_{III} is roughly constant over the central region of the test specimen in samples with intermediate crack lengths whereas two maxima are observed in specimens with shorter and longer insert lengths. The evidence from this figure suggests that normalised crack lengths between 0.4 and 0.5 yield relatively flat G_{III} profiles across the central region of the test specimen, representing the most suitable crack configurations when undertaking tests on this material.

A comparison of the two sets of traces in Figures 5.8 and 5.16 indicates that the calculated vales of G_{III} are higher in the woven glass fibre/epoxy, reflecting the greater rigidity of these laminates. A contributing factor to that is the greater thickness of the glass fibre/epoxy ECT specimens as opposed to the glass/PP ones, resulting in higher flexural stiffness. It is also interesting to note that the region over which the value of G_{III} is relatively constant, is similar in both sets of materials.

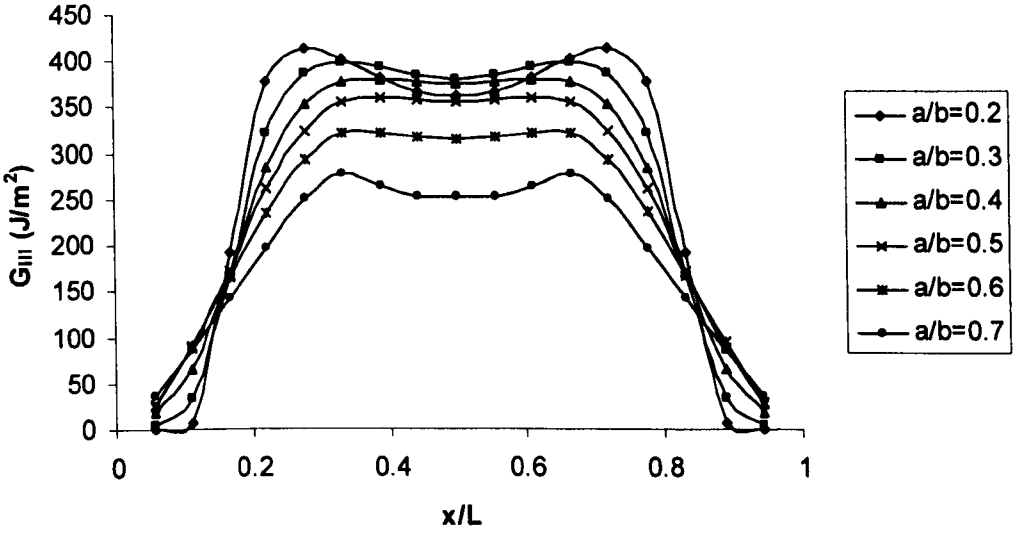

Figure 5.16: Mode III strain energy distribution for the woven glass fibre/epoxy material as a function of position along the crack front. The numbers in the legend correspond to the normalised crack length 'a/b'.

Figure 5.17 shows plots of the variation of Mode II strain energy release rate along the delamination front for the woven glass fibre/epoxy ECT specimens. The values of G_{II} are significantly smaller than the corresponding G_{III} values in Figure 5.16. A comparison of the two sets of traces in Figures 5.9 and 5.17 indicates that the calculated vales of G_{II} are higher in the woven glass fibre/epoxy, following the same trend observed from the values of G_{III} which reflects again the greater rigidity of these laminates.

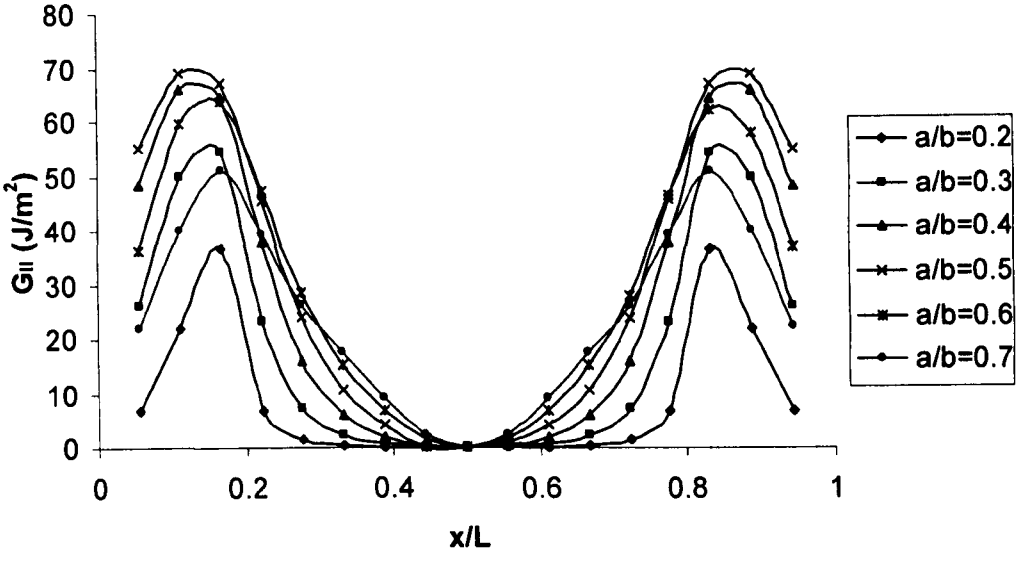

Figure 5.17: Mode II strain energy distribution for the woven glass fibre/epoxy material as a function of position along the crack front. The numbers in the legend correspond to the normalised crack length 'a/b'.

5.4.2.3. Effect of Insert Length on Average Total Strain Energy Release Rate

Following the procedure described in Section 5.3.1.5, the total strain energy release rate at any location along the delamination front, G_T, was calculated as the sum of the individual strain energy release rate components.

A plot of the average total strain energy release, G_{Ta}, versus normalised insert length, calculated from analyses of the woven glass fibre reinforced epoxy ECT specimens can be viewed in Figure 5.18. The plot of total strain energy release rate versus normalised insert length was found to be quite linear for values of a/b ranging from 0.2 to 0.5, although some non-linearity was observed at higher crack lengths. The fact that the ratio dG/d(a/b) is negative or zero [4] for all the normalised insert lengths examined leads to the conclusion that the crack growth will be stable when testing this material.

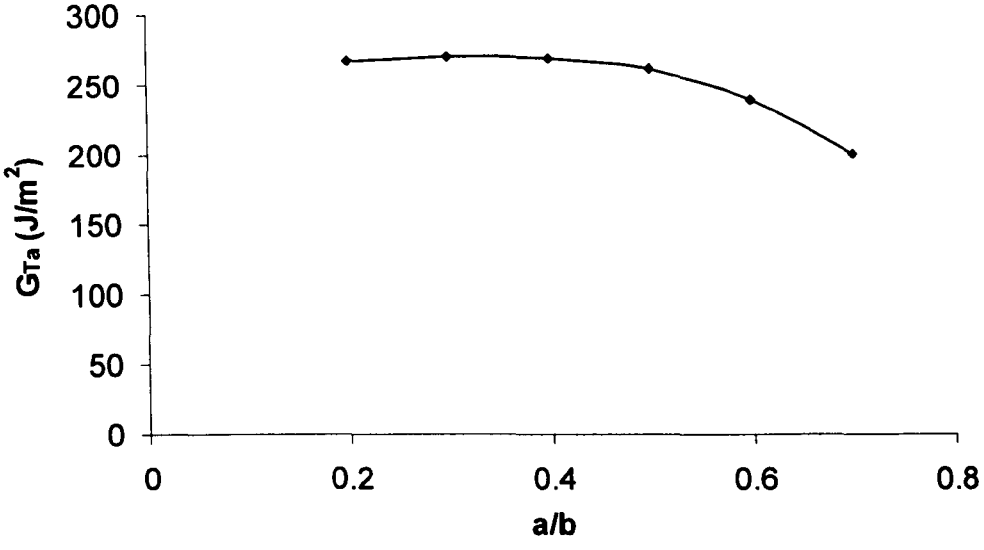

Figure 5.18: Computed average total strain energy release rate versus a/b for the woven glass fibre/epoxy ECT specimens.

5.4.2.4. Mode II and Mode III Strain Energy Release Rate Distributions for Specimens with Pre-Cracks at Off-Centre Locations

The effect of varying the crack positioning through the thickness of the ECT specimen on the Mode II and Mode III strain energy release rates was examined by constructing and analysing a series of three dimensional 24 ply finite element models,

as described previously in Section 3.5.2.2. The main aim of this series of FEA models was to examine whether a mixed mode G_{II}/G_{III} geometry could be developed. For this purpose, the crack was positioned at 4, 8, 16 and 20 plies from the top surface. The normalised insert length was 0.5 in all cases. Another series of models was examined in which the delamination was positioned at 4 plies from the top surface and the normalised insert length ranged from 0.2 to 0.7. The results were analysed and G_{III} was plotted versus the position along the delamination front.

Figure 5.19 shows the variation of G_{III} along the delamination front for the woven glass fibre reinforced epoxy ECT specimens. Here, the Mode III strain energy release rate is plotted for specimens with the crack positioned at 4, 8, 16, 20 and 12 plies from the top surface. This figure shows similar trends to those observed previously, with the values of the Mode III strain energy release rate increasing rapidly at the edges before reaching a maximum value closer to the centre of the specimen. It is clear from this figure that the original ECT geometry gives the maximum value of Mode III strain energy release rate along the crack front. The G_{III} component of strain energy release rate is higher the closer the crack is positioned to the mid-thickness of the specimen. As expected, due to symmetry, the variation of G_{III} along the delamination front is very similar between the specimens with the cracks positioned at 4 and 20 plies, as well as 8 and 16 plies from the top. Moreover, the value of G_{III} is roughly constant over the central region of the test specimen in all the models analysed. The evidence from this figure suggests that varying the position of the delamination through the thickness does not have an effect on the G_{III} profiles across the central region of the test specimen, which seems to be affected only by the normalised insert length.

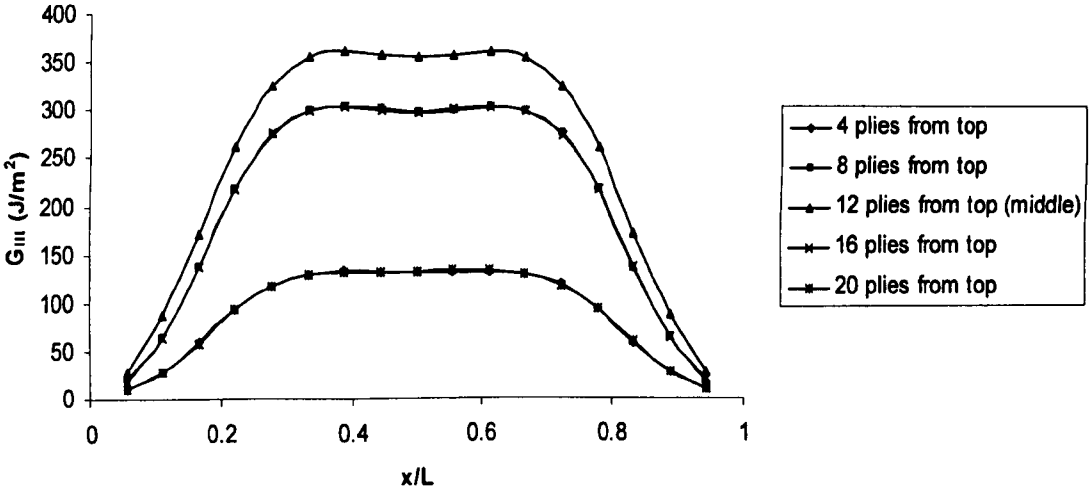

Figure 5.19: Mode III strain energy distribution for the woven glass fibre/epoxy material as a function of position along the crack front. The details in the legend describe the position of the delamination through the thickness of the specimen.

Figure 5.20 shows plots of the variation of Mode II strain energy release rate along the delamination front for the woven glass fibre/epoxy ECT specimens with the variable location of the crack through the thickness. As expected, the values of G_{II} are significantly smaller than the corresponding G_{III} values in Figure 5.19. The variation of G_{III} along the delamination front is very similar between the specimens with the cracks positioned at 4 and 20 plies, as well as 8 and 16 plies from the top, following the same trend observed by the glass/PP and glass fibre/epoxy ECT specimens.

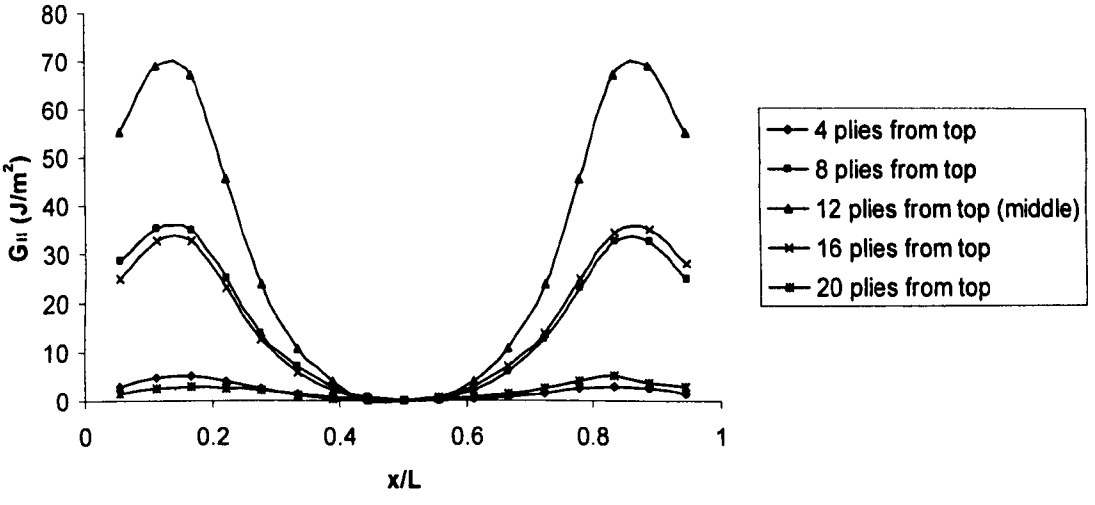

Figure 5.20: Mode II strain energy distribution for the woven glass fibre/epoxy material as a function of position along the crack front. The numbers of the legend correspond to the position of the delamination through the thickness of the specimen.

Figure 5.21 shows the plots of the Mode III strain energy release rate for the woven glass fibre reinforced epoxy specimens with the delamination positioned at 4 plies from the top surface and normalised insert lengths between 0.2 and 0.7. The findings were similar to those derived from the FEA on the original ECT geometry of previously examined materials, with the values of G_{III} being higher for smaller insert lengths, due to the higher rigidity of these laminates.

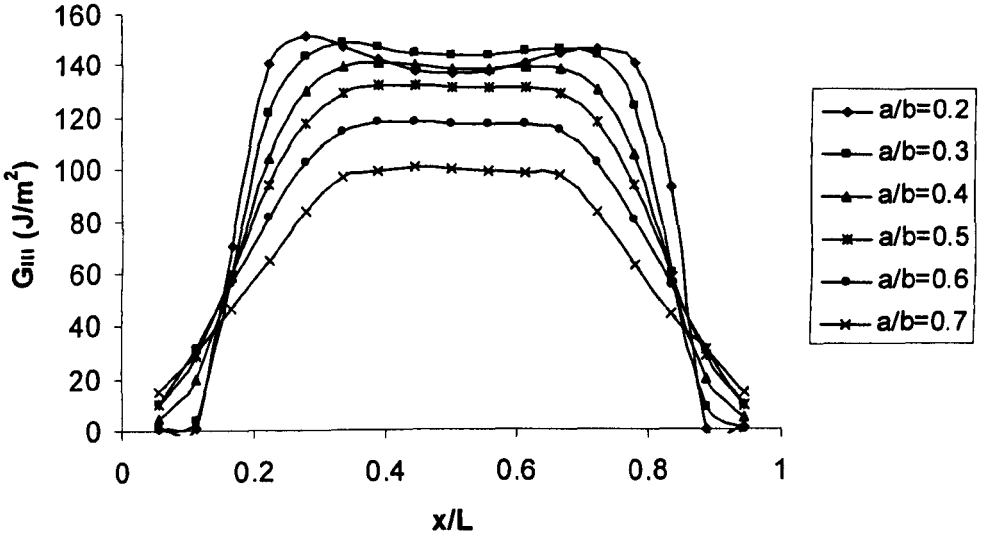

Figure 5.21: Mode III strain energy distribution for the woven glass fibre/epoxy material with the crack positioned at 4 plies from the top as a function of position along the crack front. The numbers of the legend correspond to the normalised crack length 'a/b'.

5.4.2.5. Modified ECT Geometry

Three finite element models of modified ECT geometries based on the woven glass fibre reinforced epoxy material were constructed and analysed in order to investigate the possibility of developing a mixed mode G_{II}/G_{III} geometry. The modification comprised the variation of the position of applied loads and the effect on the Mode III strain energy release rate across the delamination front was examined. Further details on each particular model can be found in Section 3.5.2.2.1.

Figure 5.22 shows the variation of G_{III} along the delamination front for the three modified woven glass fibre reinforced epoxy specimens examined, as well as the original ECT geometry. It should be noted that all models simulated specimens with a normalised insert length of 0.5. It is clear from the plots that the distribution of G_{III} in

the three modified geometries exhibits two maxima, being roughly constant only in the original ECT geometry.

Furthermore, it appears that the position of the applied load in the x direction (i.e. across the specimen width) affects the Mode III strain energy release rate values. According to the plots, the values of G_{III} along the delamination front are higher for the original ECT geometry, reaching their lowest values in Model 1, where the load is applied very close to the specimen edges. It is also worth noticing that the region where the values of G_{III} are higher seems to be affected by the positioning of the loading pins in the x direction. This becomes clearer when comparing the plots of the original ECT geometry and Model 2. Here, the load pins are located at the same point in the y axis and the only difference lies in the position of the applied load along the x axis. In Model 1 and Model 2, the width of the central region where the Mode III strain energy release rate is roughly constant, is identical. It should be noted that in both models, the load is applied at the same position along the x axis. This can be attributed to the fact that, by moving the load pins towards the edges of the specimen in the x direction, a greater part of the specimen lies between the loading points. However, from the point of view of the G_{III} profile, there is no perceived benefit to be achieved by relocating the loading points, as the original ECT geometry appears to provide the most uniform Mode III strain energy release rate distribution. These results are in good agreement with the work by Suamesu [5] who showed that, having the end portion outside the gauge section as small as possible, results in higher G_{III} values over a greater region across the specimen width.

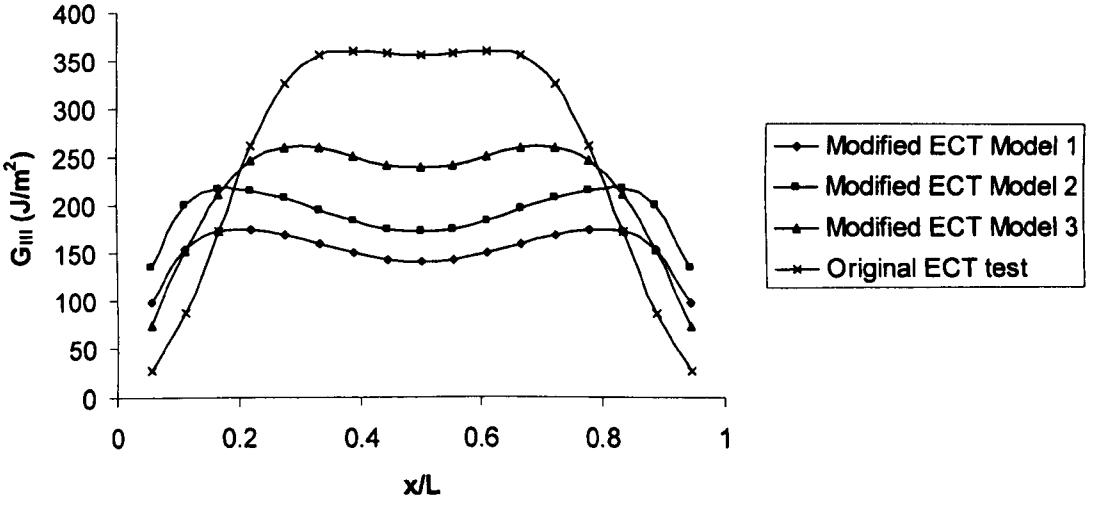

Figure 5.22: Mode III strain energy distribution for the woven glass fibre/epoxy material with the loading points at different locations. The numbers in the legend correspond to the different finite element models.

5.4.3. Adhesively-bonded Woven Glass Fibre Reinforced Epoxy

In this section, the Mode III interlaminar fracture properties, G_{IIIc}, of an adhesively-bonded glass fibre/epoxy composite are investigated using the edge crack torsion (ECT) test geometry over a wide range of normalised insert lengths ranging from 0.2 to 0.7.

Two different thicknesses of adhesive were considered in the analysis, as described in Section 3.5.2.3., these being 100 μm and 1.42 mm. This was undertaken in order to examine the effect of adhesive thickness on the Mode III strain energy release rate distribution, with the latter being the nominal thickness used in the actual experiments. It should be noted that the same ranges of normalised insert lengths were examined in both adhesively-bonded systems analysed.

For a given crack length, it was shown that the experimentally determined interlaminar fracture toughness of the adhesively-bonded system was superior to that offered by the plain composite. This was attributed to the presence of significant crack-tip blunting within the adhesive layer as well as the higher rigidity of the adhesively-bonded system due to the effect of the greater thickness on the flexural stiffness of the ECT specimens.

5.4.3.1. Finite Element Model Verification

Figure 5.23 shows the variation of the inverse of specimen compliance with normalised insert length, a/b, for the adhesively-bonded glass fibre/composite. The points in the figure correspond to the experimental data and the solid line represents the predictions of the finite element analysis of the ECT specimens with a 1.42 mm thick adhesive layer. From the figure, it is evident that the FE predictions are in reasonably good agreement with the experimental data over the range of normalized insert lengths investigated. It is clear that the FE analysis models the trends in the experimental data with some success, although it overestimates the values of 1/C at intermediate values of a/b. The constant 'm' in Equation 5.1 was calculated from the finite element analysis and shown to be 0.87. This agrees well with the value of 0.94 determined experimentally.

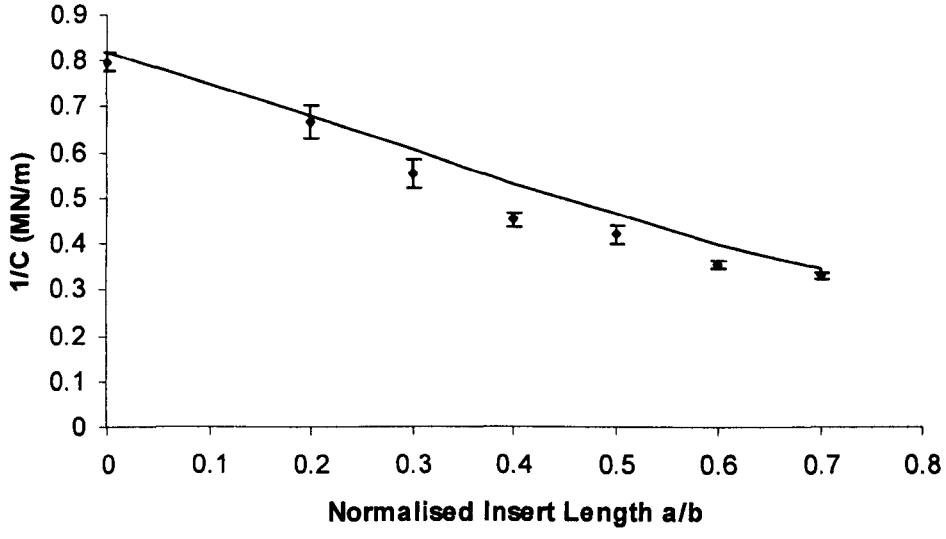

Figure 5.23: The variation of the inverse of specimen compliance with normalized crack length for the adhesively-bonded woven glass fibre/epoxy composite.

5.4.3.2. Mode II and Mode III Strain Energy Release Rate Distributions for the 1.42 mm Thick Adhesive

Using the virtual crack closure technique (VCCT), the Mode II and Mode III components of strain energy release rate (G_{II} and G_{III} respectively) along the delamination front in the finite element models were calculated. Figure 5.24 shows plots of the Mode II and Mode III strain energy release rate distributions across the delamination front, for the adhesively-bonded woven glass fibre reinforced epoxy ECT specimen with a 1.42 mm thick epoxy adhesive and a normalised insert length of 0.5:

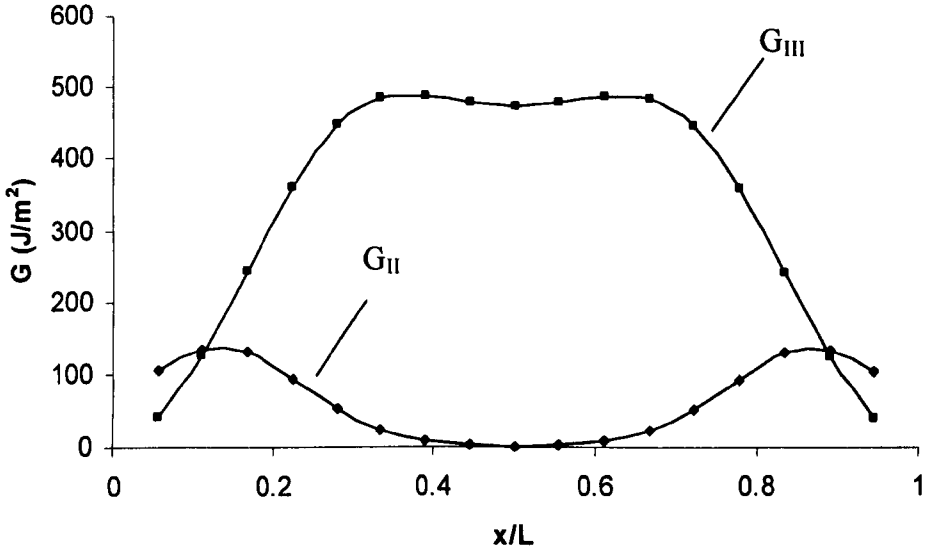

Figure 5.24: Computed strain energy release rate distribution across the delamination front for the adhesively-bonded woven glass fibre/epoxy ECT specimen with a 1.42 mm thick epoxy adhesive and a normalised insert length of 0.5.

The Mode I component of strain energy release rate has not been included since it was negligible relative to the values of G_{II} and G_{III} in all of the specimens. It is clear that the G_{II} and G_{III} components of strain energy release rate follow the same trends as in the previously examined materials. Once again, Mode III is the dominant loading condition type and the delamination is initiated from the centre of the specimen insert front.

Figure 5.25 shows the variation of G_{III} along the delamination front for woven glass fibre reinforced epoxy ECT specimens. The Mode III strain energy release rate is plotted for normalised insert lengths between 0.2 and 0.7. As expected, the plots show that the Mode III strain energy release rate increases rapidly at the edges before reaching a maximum value closer to the centre of the specimen. The value of G_{III} remains roughly constant over the central region of the test specimen in samples with intermediate crack lengths whereas two maxima are observed in specimens with shorter and longer insert lengths. The evidence from this figure suggests that

normalised crack lengths between 0.4 and 0.5 yield relatively flat G_{III} profiles across the central region of the test specimen, representing the most suitable crack configurations when undertaking tests on this material.

A comparison of the two sets of traces in Figures 5.16 and 5.25 indicates that the calculated vales of G_{III} are higher in the adhesively-bonded woven glass fibre/epoxy than in the plain composite, reflecting the greater rigidity of these laminates, due to the greater flexural stiffness resulting from the addition of the adhesive layer. It is also interesting to note that the region over which the value of G_{III} is relatively constant is the same in both sets of materials, being unaffected by the presence of the adhesive.

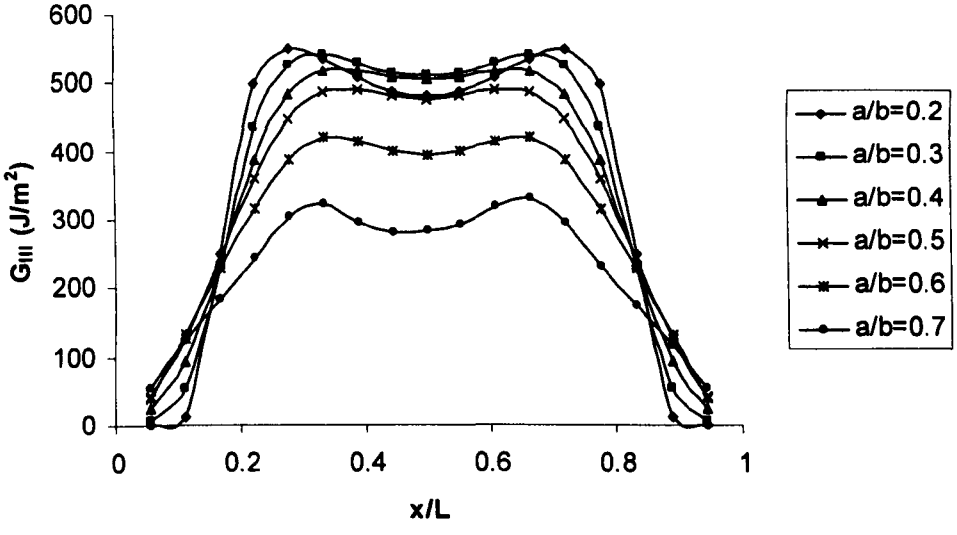

Figure 5.25: Mode III strain energy distribution for the adhesively-bonded woven glass fibre/epoxy material as a function of position along the crack front. The numbers in the legend correspond to the normalised crack length 'a/b'.

Plots of the variation of Mode II strain energy release rate along the delamination front for the adhesively-bonded woven glass fibre/epoxy ECT specimens can are shown in Figure 5.26. The values of G_{II} are significantly smaller than the corresponding G_{III} values in Figure 5.25. A comparison of the two sets of traces in

Figures 5.17 and 5.26 indicates that the calculated vales of G_{II} are higher in the adhesively-bonded woven glass fibre/epoxy than in the plain composite, following the trend observed in the values of G_{III}.

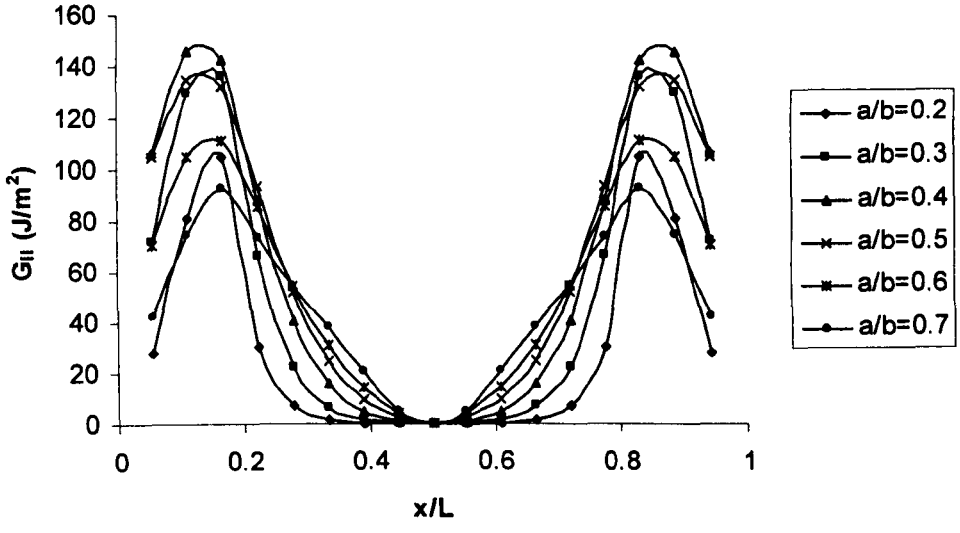

Figure 5.26: Mode II strain energy distribution for the adhesively-bonded woven glass fibre/epoxy material as a function of position along the crack front. The numbers in the legend correspond to the normalised crack length 'a/b'.

5.4.3.3. Effect of Insert Length on Average Total Strain Energy Release Rate for the 1.42 mm Thick Adhesive

A plot of the average total strain energy release, G_{Ta}, versus normalised insert length, calculated for the adhesively-bonded woven glass fibre reinforced epoxy ECT specimens is shown in Figure 5.27. The plot of total strain energy release rate versus normalised insert length was found to increase for values of a/b ranging from 0.2 to 0.4, followed by a non-linear decrease for normalised insert lengths ranging from 0.5 to 0.7. According to Williams' findings [4], crack growth will be unstable for normalised insert lengths from 0.2 to 0.4 and stable for greater values of a/b.

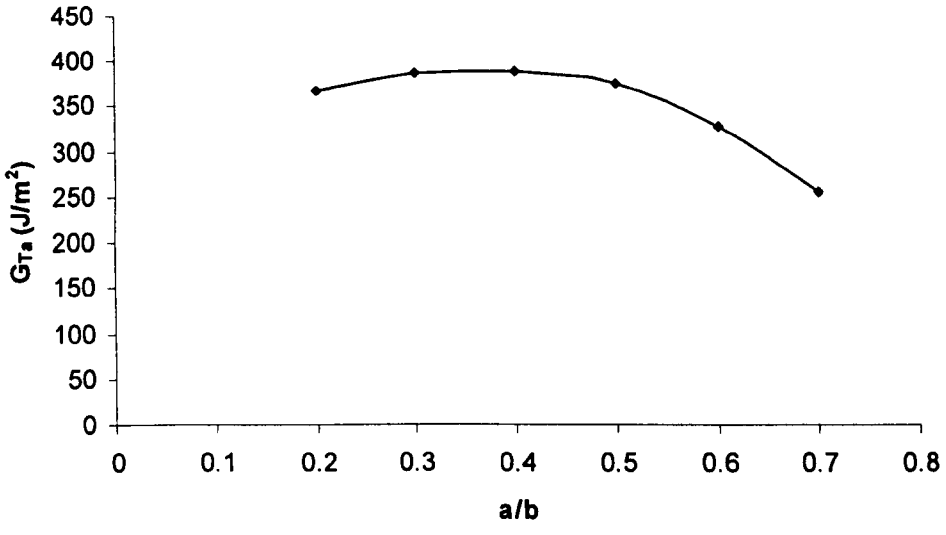

Figure 5.27: Computed average total strain energy release rate versus a/b for the adhesively-bonded woven glass fibre/epoxy ECT specimens.

5.4.3.4. Mode II and Mode III Strain Energy Release Rate Distributions for the 100 μm Thick Adhesive

Figure 5.28 shows plots of the Mode II and Mode III strain energy release rate distributions across the delamination front, for the adhesively-bonded woven glass fibre reinforced epoxy ECT specimen with a 100 μm thick epoxy adhesive and a normalised insert length of 0.5:

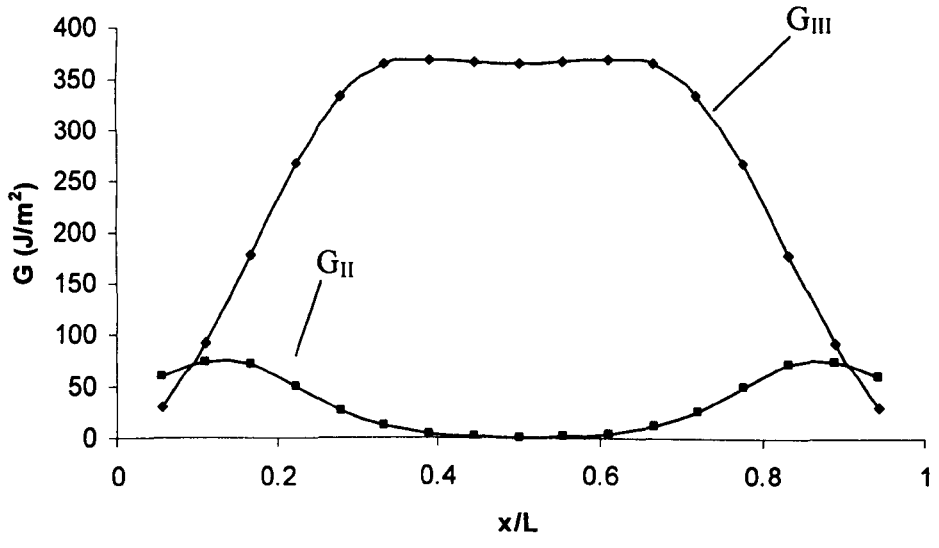

Figure 5.28: Computed strain energy release rate distribution across the delamination front for the adhesively-bonded woven glass fibre/epoxy ECT specimen with a 100 μm thick epoxy adhesive and a normalised insert length of 0.5.

Figure 5.29 shows the variation of G_{III} along the delamination front for the adhesively-bonded woven glass fibre reinforced epoxy ECT specimens. The Mode III strain energy release rate is plotted for normalised insert lengths between 0.2 and 0.7. The G_{III} distribution follows the expected trend, remaining roughly constant over the central region of the test specimen in samples with intermediate crack lengths whereas two maxima are observed in specimens with shorter and longer insert lengths. The values are slightly higher than those of the pure composite and lower than the previously examined, thicker adhesively-bonded composite, suggesting that the adhesive thickness has an effect on the Mode III strain energy release rate which follows the same trend. This is caused by the increase in the specimen's rigidity, leading to higher G_{III} values. Chai [6] showed that although the value of G_{III} increases with the adhesive thickness, G_{IIIc} exhibits a plateau followed by a phase of monotonic decline as the adhesive thickness, t, decreases.

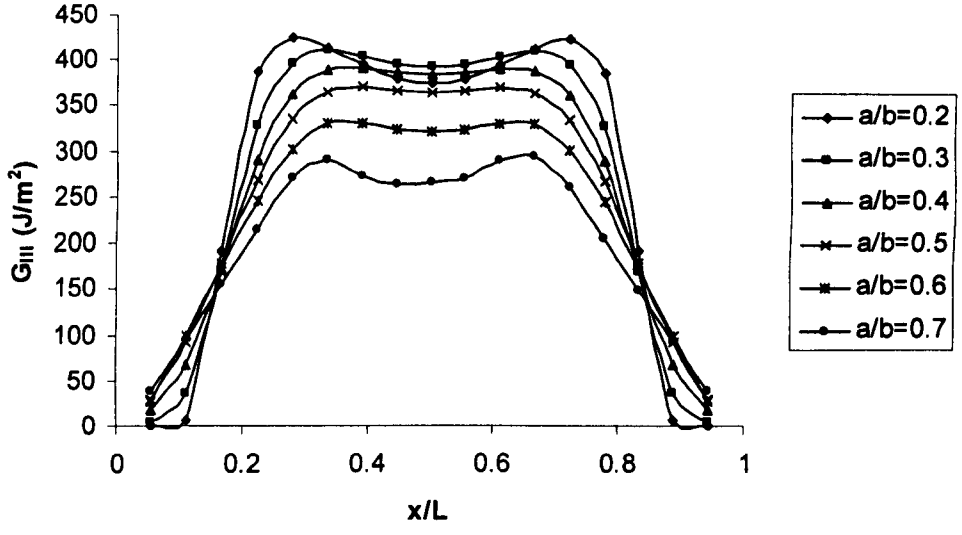

Figure 5.29: Mode III strain energy distribution for the adhesively-bonded woven glass fibre/epoxy material as a function of position along the crack front. The numbers in the legend correspond to the normalised crack length 'a/b'.

The evidence from Figure 5.30, where the variation of Mode II strain energy release rate along the delamination front is plotted, suggests that the values of the G_{II} component are several times smaller than G_{III}. Most importantly, when comparing the plots shown in this Figure to those in Figures 5.17 and 5.26, the values follow the same trend as those of G_{III}, being slightly higher than those for the pure composite and smaller than those for the adhesively-bonded glass fibre/epoxy ECT specimens with the thicker epoxy adhesive.

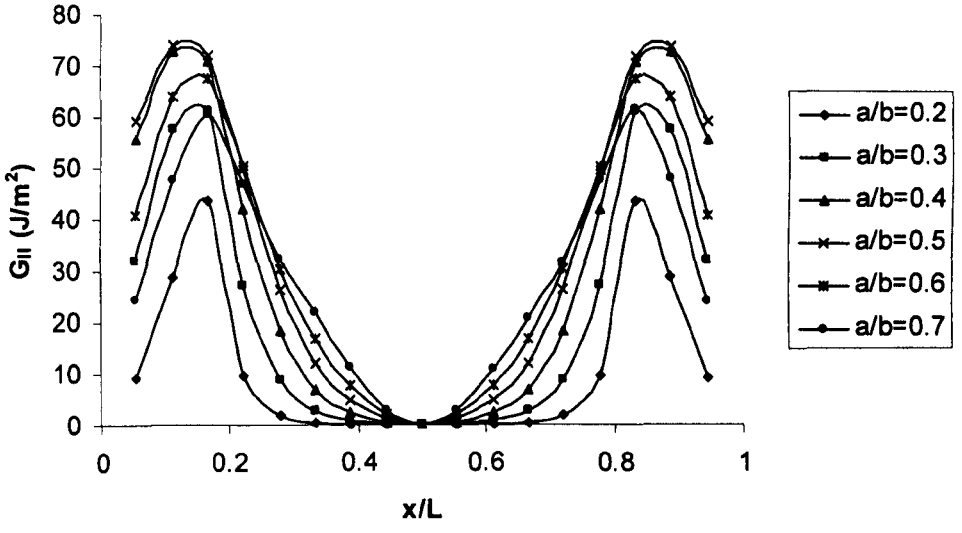

Figure 5.30: Mode II strain energy distribution for the adhesively-bonded woven glass fibre/epoxy material as a function of position along the crack front. The numbers in the legend correspond to the normalised crack length 'a/b'.

5.4.3.5. Effect of Insert Length on Average Total Strain Energy Release Rate for the 100 μm Thick Adhesive

A plot of the average total strain energy release, G_{Ta}, versus normalised insert length, calculated from analyses of the adhesively-bonded woven glass fibre reinforced epoxy ECT specimens is shown in Figure 5.31. The plot of total strain energy release rate versus normalised insert length was found to remain relatively constant for values of a/b ranging from 0.2 to 0.5, followed by a decrease for normalised insert lengths of 0.6 and 0.7. In contrast to the ECT specimens with the thicker adhesive layers, these findings suggest delamination growth will be stable under displacement control loading conditions.

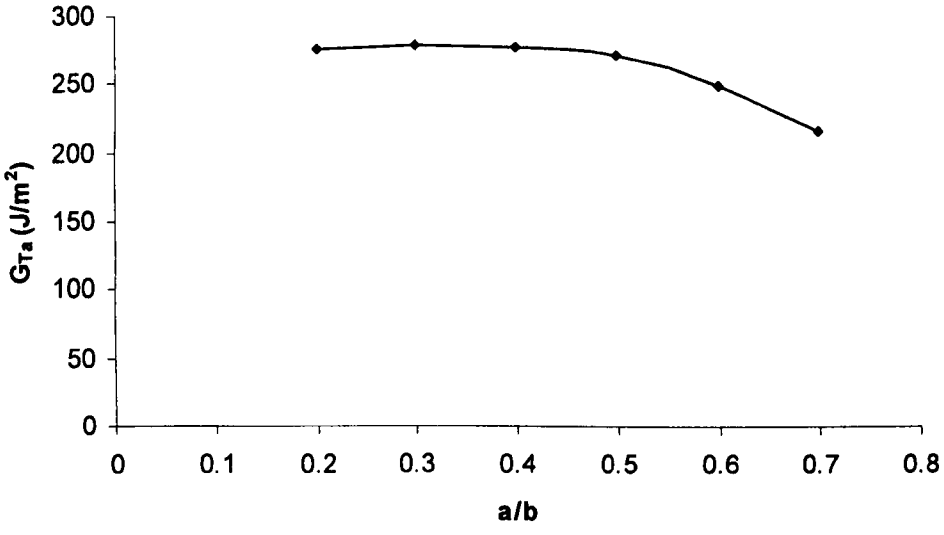

Figure 5.31: Computed average total strain energy release rate versus a/b for the adhesively-bonded woven glass fibre/epoxy ECT specimens.

5.4.4. Bi-material Samples with an Interface Crack

The Mode III interlaminar fracture properties, G_{IIIc}, of ECT specimens based on an isotropic and an orthotropic material with the delamination positioned at the interface were examined and the results are presented in this section. The FEA was conducted on models simulating specimens with normalised insert lengths ranging from 0.2 to 0.7. Further details about the modelling process and the procedures followed can be found in Section 3.5.2.4.

For a given crack length, it has been shown that the interlaminar fracture properties of the bi-material sample were lower to that offered by the plain glass fibre reinforced epoxy composite This effect is attributed the higher rigidity of the glass fibre/epoxy system due to its greater thickness. This affects the flexural stiffness which is much lower in the bi-material compared to the pure composite.

5.4.4.1. Finite Element Model Verification

Figure 5.32 shows the variation of the inverse of specimen compliance with normalised insert length, a/b, for the adhesively-bonded glass fibre/composite. The points in the figure correspond to the experimental data and the solid line represents the predictions of the finite element analysis of the ECT bi-material specimens. It is clear that the FE predictions are in good agreement with the experimental data over the range of normalised insert lengths investigated. The FE analysis models the trends in the experimental data successfully. The constant 'm' in Equation 5.1 was calculated from both the predictions of the finite element analysis as well as the experimental data, giving values of 0.41 and 0.46 respectively.

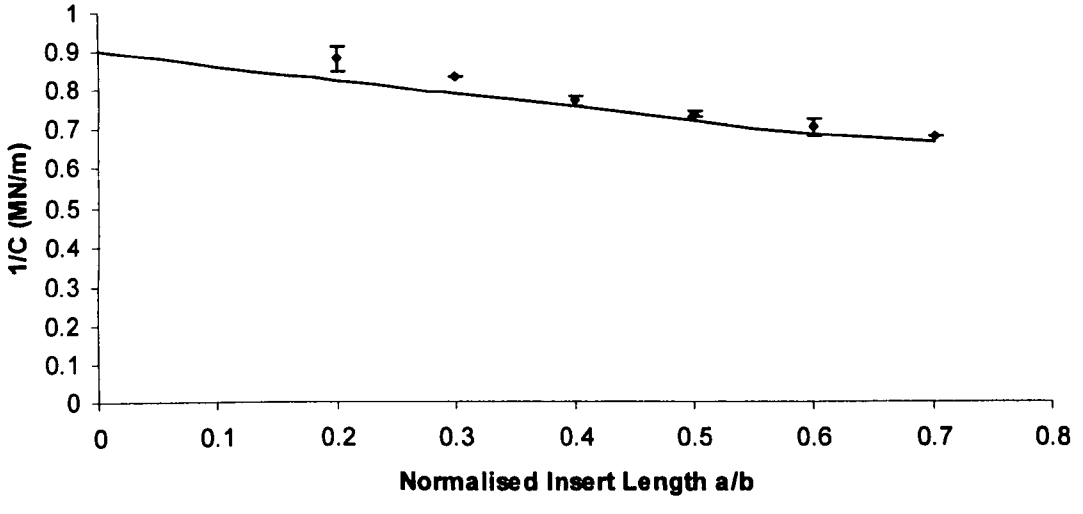

Figure 5.32: The variation of the inverse of specimen compliance with normalised crack length for the bi-material specimens.

5.4.4.2. Mode II and Mode III Strain Energy Release Rate Distributions

The Mode II and Mode III components of strain energy release rate (G_{II} and G_{III} respectively) along the delamination front in the finite element models were

calculated using the VCCT. Plots of the Mode II and Mode III strain energy release rate distributions across the delamination front, for the bi-material ECT specimen with a normalised insert length of 0.5 are shown in Figure 5.33:

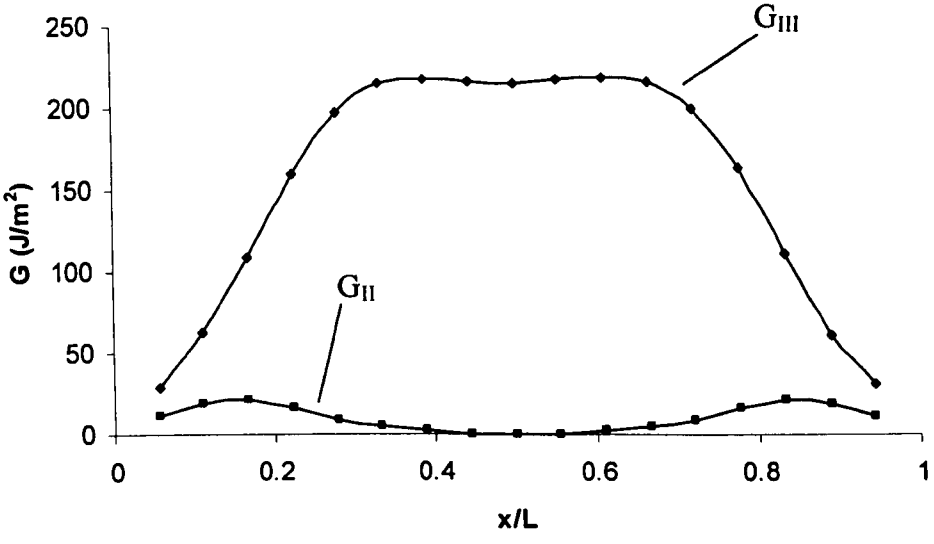

Figure 5.33: Computed strain energy release rate distribution across the delamination front for the ECT bi-material specimen with a normalised insert length of 0.5.

The Mode I component of strain energy release rate was found to be negligible relative to the values of G_{II} and G_{III} in all of the specimens and has not been included in the plots. As in the case of the plain composites, the Mode II strain energy release rate distribution reaches its maximum value at the locations of the load and support pins. The G_{III} component of strain energy release rate reaches its maximum value at the central region of the specimen, being several times higher than the corresponding Mode II strain energy release rates. As a result, Mode III is the dominant loading condition type and the delamination is initiated from the centre of the specimen insert front, at the bi-material interface.

Figure 5.34 shows the variation of G_{III} along the delamination front for ECT bi-material specimens. The Mode III strain energy release rate has been plotted for normalised insert lengths between 0.2 and 0.7. Once more, the shape of the Mode III strain energy release rate versus the position along the crack front is similar to those of the previously examined materials. The values of G_{III} increase rapidly at the edges before reaching a maximum value closer to the centre of the specimen. Furthermore, the value of G_{III} is roughly constant over the central region of the test specimen in samples with intermediate crack lengths whereas two maxima are observed in specimens with shorter and longer insert lengths. The evidence in this figure suggests that normalised crack lengths between 0.3 and 0.5 yield relatively flat G_{III} profiles across the central region of the test specimen, representing the most suitable crack configurations when undertaking tests on these hybrid materials

Comparing the two sets of traces in Figures 5.16 and 5.34 indicates that the calculated vales of G_{III} are higher in the woven glass fibre/epoxy than in the ECT bi-material specimens based on woven glass fibre/epoxy and spring steel. This is due to the greater flexural stiffness of the plain composites as they are much thicker than their bi-material counterparts. Finally, the region over which the value of G_{III} is relatively constant is similar in both sets of materials.

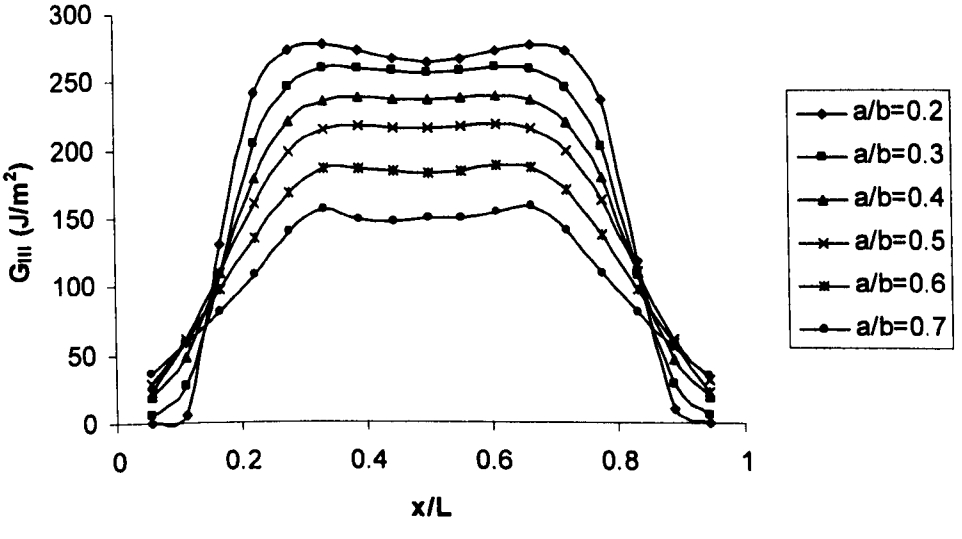

Figure 5.34: Mode III strain energy distribution for the bi-material specimen as a function of position along the crack front. The numbers in the legend correspond to the normalised crack length 'a/b'.

Figure 5.35 shows plots of the variation of Mode II strain energy release rate along the delamination front for the ECT bi-material specimens. The values of G_{II} are significantly smaller than the corresponding G_{III} values shown in Figure 5.34. The same is the case when comparing the two sets of traces in Figures 5.17 and 5.35, indicating that the calculated vales of G_{II} are higher in the woven glass fibre reinforced epoxy.

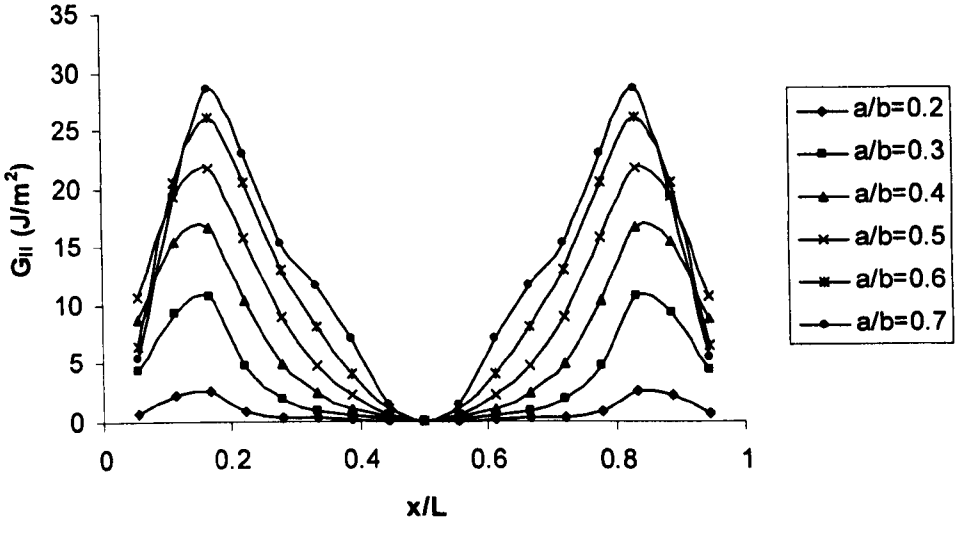

Figure 5.35: Mode II strain energy distribution for the bi-material as a function of position along the crack front. The numbers in the legend correspond to the normalised crack length 'a/b'.

5.4.4.3. Effect of Insert Length on Average Total Strain Energy Release Rate

A plot of the average total strain energy release, G_{Ta}, versus normalised insert length, calculated from analyses of the ECT bi-material specimens is shown in Figure 5.36. The plot of total strain energy release rate versus normalised insert length was found to decrease for all the normalised insert lengths examined, thus the ratio dG/d(a/b) is

negative. This finding means that the delamination growth will be stable if the testing is performed under displacement control.

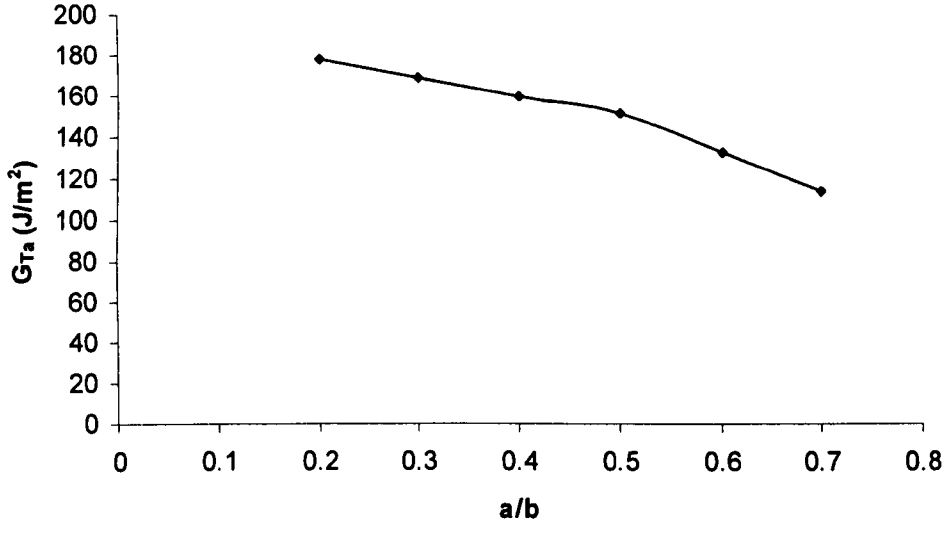

Figure 5.36: Computed average total strain energy release rate versus a/b for the ECT bi-material specimens.

5.5. Summary of Finite Element Analysis

Table 5.1 summarises the analyses conducted during the course of this research programme as well as the results/trends that were observed:

Material	a/b	Adhesive Thickness	Parameter varied	Comments
Isotropic	0.3 – 0.7	-	Insert length	G_{III} was found to peak along the central region of the specimen, G_{II} peaks at location of load and support pins. Mode III is the dominant loading condition type-common finding in all ECT models examined.
G.F.-Polypropylene	0.2, 0.3, 0.4, 0.6, 0.7	-	Insert length	Similar trends to the isotropic material were observed. Delamination growth was found to be stable.
G.F.-Polypropylene	0.5	-	Applied displacement (1-7 mm)	Value of G_{III} increases with applied displacement due to the higher forces experienced by material at higher displacements.
G.F.-Polypropylene	0.5	-	Total number of plies (24, 32)	Value of G_{III} increases with total ply number due to the higher thickness and thus rigidity of the samples.
Woven G.F.-Epoxy	0.2, 0.3, 0.4, 0.6, 0.7	-	Insert length	Similar trends to the isotropic material were observed with regards to G_{II} and G_{III} distributions. The values were higher compared to the GF/PP reflecting the higher rigidity of these specimens, due to greater thickness. Stable crack propagation under displacement control.
Woven G.F.-Epoxy	0.5	-	Crack positioning (4, 8, 12, 16, 20 plies from top surface)	Values of G_{II} and G_{III} were found to increase when delamination is placed closer to specimen mid-thickness. G_{III} profile is unaffected by re-locating the delamination.
Woven G.F.-Epoxy – Modified ECT geometry	0.5	-	Locations of applied displacements	The region where values of G_{III} are higher is greater, the closer the load and support pins are positioned to the specimen edges. However, original ECT geometry seems to provide the most uniform G_{III} distribution.
Adhesively-bonded G.F.-Epoxy	0.2 - 0.7	100 μm	Insert length	Values of G_{II} and G_{III} higher than in plain composite, reflecting the greater rigidity of the adhesively-bonded samples. Stable crack growth was observed.
Adhesively-bonded G.F.-Epoxy	0.2 - 0.7	1.42 mm	Insert length	Values of G_{II} and G_{III} dependent on adhesive thickness, thus higher than thinly-bonded samples, due to the greater flexural stiffness. Unstable crack growth for a/b=0.2, stable crack growth for a/b=0.3-0.7.
Bi-material	0.2 - 0.7	-	Insert length	Values of G_{II} and G_{III} much lower than in plain composite, reflecting the smaller rigidity of the bi-material samples with interface cracks, due to their thickness. Stable crack growth was observed for all normalised insert lengths.

Table 5.1: Summary of finite element analyses conducted in the duration of the research programme.

5.6. References

1. Krueger R., Virtual crack closure technique: history, approach and applications, Applied Mechanics Rev., Vol.57, March 2004, p.109.

2. Ratcliffe J.G., Characterization of the edge crack torsion (ECT) test for Mode III fracture toughness measurement of laminated composites, National Research Council, NASA Langley Research Centre, Hampton, Virginia, September 2004.

3. Zhao D., Wang, Y., Mode III fracture behaviour of laminated composite with edge crack in torsion , Theoretical and Applied Fracture Mechanics, Vol.29, 1998, p.109.

4. Williams J.G., On the calculation of energy release rates for cracked specimens, International Journal of Fracture, Vol.36, 1988, p.101.

5. Suamesu H., An experimental method to measure the mode-III interlaminar fracture toughness of composite laminates, Composites Science and Technology, Vol.59, 1999, p.1015.

6. Chai H., Shear Fracture, International Journal of Fracture, Vol.37, 1988, p.137.

6. Experimental Results and Discussion

6.1. Summary

This chapter presents the findings from the experiments conducted to determine the fracture properties of the ECT composites, the adhesively-bonded and the bi-material samples according to the procedures described in Chapter 4. A universal test machine was used for testing at low and intermediate crosshead displacement rates. After the tests, the data were analysed and the effect of varying crack length on G_{IIIc} was investigated by testing specimens with different normalised crack lengths, a/b.

The rate-sensitivity of the Mode III interlaminar fracture properties was initially investigated by conducting tests at crosshead displacement rates of 0.2, 2, 20 and 200 mm/minute. A number of impact tests were also undertaken on the ECT samples using an instrumented drop-weight impact tower, following the procedures described in Chapter 4. The results of the impact tests on the ECT samples are presented in this chapter.

Finally, a scanning electron and an optical microscope were used to examine the Mode III fracture surface morphology of the test samples. The micrographs are used to explain the behaviour of the materials under Mode III loading conditions at different crosshead displacement rates.

6.2. ECT Tests on the Glass Fibre Reinforced Polypropylene

Sixteen ply glass fibre/PP specimens were manufactured following the procedures described in Section 4.2.1. The stacking sequence adopted in the manufacture of these unidirectional glass fibre/PP laminates was:

$$[90° / 0° (+45° / -45°) / (-45° / +45°) 0° / 90°]_s$$

Glass fibre/PP specimens with a thickness of 4.7 mm and normalised insert lengths ranging from 0.2 to 0.7 were initially tested at a crosshead displacement rate of 2 mm/min. Furthermore, specimens with a normalised insert length of 0.5 were subjected to additional testing at higher crosshead displacement rates of 0.2, 20 and 200 mm/min. Finally, an instrumented drop-weight impact tower was used for testing the ECT specimens under impact conditions at a crosshead displacement rate of 3 m/sec.

Clearly, the material in this composite is based on the semi-crystalline thermoplastic polymer polypropylene. It is worth noting that the cooling conditions used to manufacture the panels here were similar to those used by Davies and Cantwell [1] when manufacturing Mode I and Mode II samples. The cooling rate adopted during the manufacture of the panels in this study was approximately 2 °C/min. It is well recognised that the degree of crystallinity in a semi-crystalline polymer depends on the rate of cooling from the melt as well as on the chain configuration [4-6]. In addition, it is well documented that the physical properties of polymeric materials are influenced by the degree of crystallinity. Previous research [1, 3] has shown that slow cooling results in the formation of larger spherulites within the polymer and a higher degree of crystallinity. The interspherullitic defects that are frequently observed following slow cooling, provide a path for crack propagation and water ingress, leading to a lower interlaminar fracture toughness of the material [1]. Another consequence of a higher degree of crystallinity within a polymer is that crack propagation is easier and thus the impact resistance of the composite is often lower [1]. Given that a cooling rate of 2 °C/min was adopted here, the findings of Davies

and Cantwell [1] suggest that the degree of crystallinity within the PP matrix should be approximately 60% by weight.

6.2.1. Load-Displacement Responses

Figure 6.1 shows a typical load-displacement trace following an ECT test on a glass fibre reinforced polypropylene specimen with a normalised crack length of 0.5. As can be seen, the load increases linearly, reaching a maximum before dropping rapidly after the onset of macroscopic crack propagation.

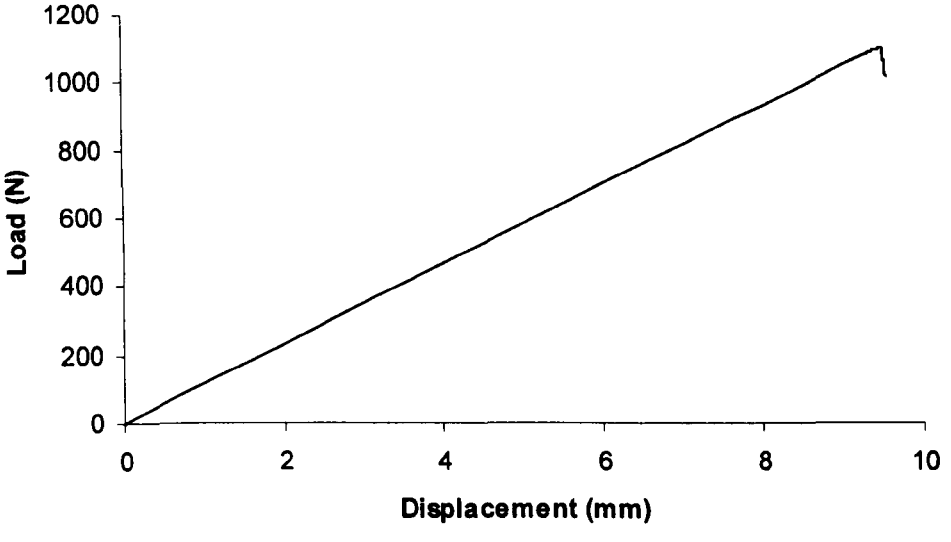

Figure 6.1: Typical load displacement trace following an ECT test on a glass fibre/PP composite specimen with a normalised insert length of 0.5.

Figure 6.2 shows typical load-displacement traces following ECT tests on glass fibre/PP samples with normalised insert lengths ranging from 0.2 to 0.7. It is clear from the graphs that the load increases in a linear fashion, becoming slightly non-linear and reaching a maximum before dropping after the onset of macroscopic crack

propagation. The figure also shows that the slope of the graphs decreases with increasing crack length, indicating that the specimen compliance increases with a/b.

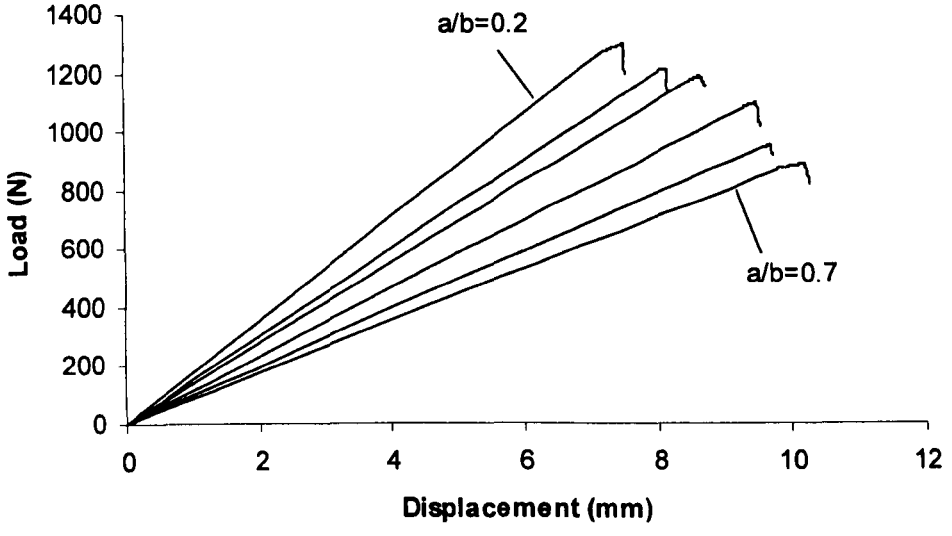

Figure 6.2: Load displacement traces following ECT tests on the glass fibre/PP composite specimens with normalised insert lengths ranging from 0.2 to 0.7.

6.2.2. The Influence of Crack Length on Specimen Stiffness

The specimen compliance was determined using the load-displacement plots recorded during the tests. This was done by taking a reading of displacement from the linear part of the load-displacement trace and dividing it by the corresponding load. The inverse of the specimen compliance, 1/C, was then plotted as a function of the normalised insert length, a/b, and a straight line was then applied to the data, according to the following equation:

$$1/C = A\,[1-m(a/b)] \qquad (6.1)$$

This approach was adopted since it is not possible to generate a compliance curve from a single ECT specimen, due to the difficulties in measuring the crack length as the crack propagates [7, 8], as discussed in Chapter 5.

A plot of the inverse of specimen compliance, 1/C, versus normalised crack length, a/b, for the glass fibre/PP composite is shown in Figure 6.3.

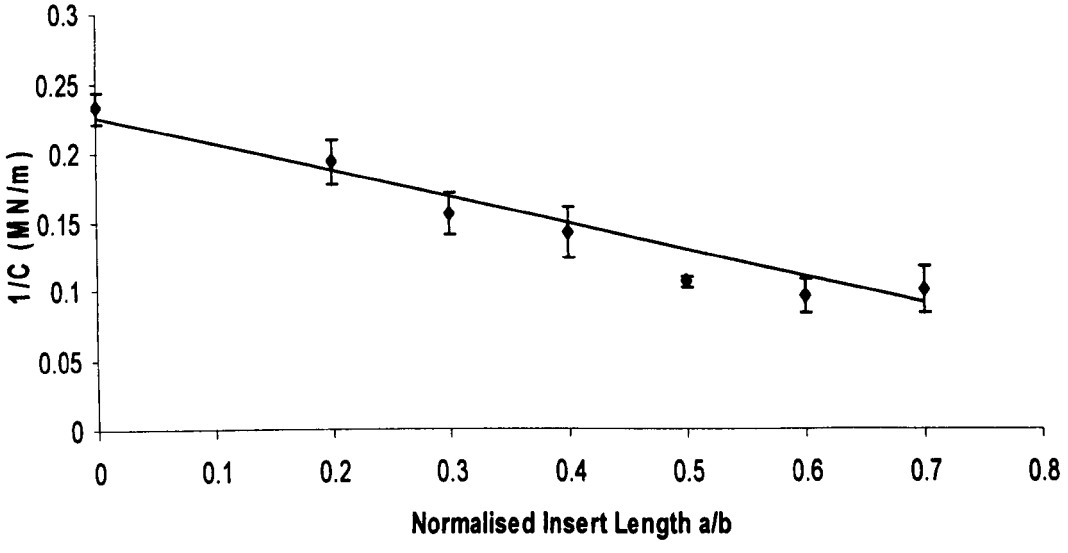

Figure 6.3: The variation of the inverse of specimen compliance, 1/C, with normalised crack length, a/b, following ECT tests on the glass fibre/PP composite.

According to Figure 6.3, the plot of 1/C versus a/b for these glass fibre reinforced polypropylene specimens exhibits a reasonably linear trend suggesting that Equation 6.1 can be used to characterise the elastic response of the ECT samples. It should be noted, however, that the values at a/b=0.5 fall below the linear fit. Equation 6.1 was applied to the experimental data, yielding a value of 'm' of 0.97. This is very close to the value of 0.96 determined numerically in Chapter 5, suggesting that the FE accurately predicts the response of these samples. Previously published results from Mode III tests on glass and carbon fibre/epoxy composites, using the ECT geometry

highlighted a linear relationship between these two parameters over a similar range of crack lengths [9].

6.2.3. Influence of Crack Length on G_{IIIc} under Quasi-Static Loading Conditions

As outlined previously, the Mode III fracture toughness of the glass fibre/PP composite was initially determined at a crosshead displacement rate of 2 mm/min. Using Equation 6.2, the Mode III fracture toughness of each ECT specimen at maximum load, G_{IIIc} was calculated by introducing the corresponding force, P_{max}:

$$G_{IIIc} = \frac{mC}{2lb[1-m(a/b)]} P_{max}^2 \qquad (6.2)$$

It should be noted that the non-linear values of force were not used to determine the corresponding value of G_{IIIc} due to difficulties in determining this force at higher crosshead displacement rates.

It should also be noted that the value of 'm' determined at 2 mm/min was used to calculate G_{IIIc} at all crosshead displacement rates. This was necessary since it was not possible to obtain plots such as that shown in Figure 6.3 at each crosshead displacement rate. As explained in Section 4.6, it is generally accepted that the elastic modulus properties of glass fibre reinforced composites are insensitive to strain rate [10] and it is therefore assumed here that the value of 'm' remains constant with increasing crosshead displacement rate.

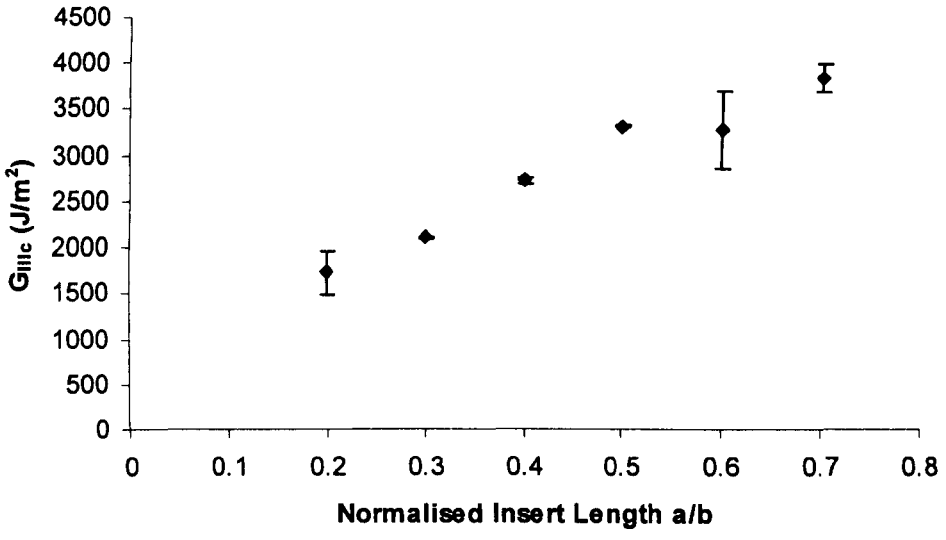

Figure 6.4: The variation of G_{IIIc} with normalised crack length for the glass fibre/PP laminates.

An examination of the data for the glass fibre/PP, Figure 6.4, indicates that the Mode III fracture toughness values increase rapidly with normalised insert length, an effect that has been observed elsewhere [9]. In principle, the Mode III fracture toughness is an intrinsic material property and therefore the measured value of G_{IIIc} should be constant with insert length. According to Figure 6.4, the value of G_{IIIc} for a normalised crack length of 0.7 is roughly double that measured on specimens with an 'a/b' of 0.2. The causes for this crack length dependency are not clear. It is possible that increased friction in samples with longer cracks may result in greater energy absorption. This is not believed to account for the trends in this figure. This pronounced variation of G_{IIIc} with crack length will be investigated in further detail in the following sections.

6.2.4. Influence of Crack Length on G_{IIIc} – Further Investigation

Although this chapter deals primarily with the experimental results generated in this research project, it is considered appropriate that the trends in the experimental data are investigated using numerical procedures. For purposes of clarity and continuity, details of these investigations are given here.

6.2.4.1. Finite Element Analysis Based on the Maximum Displacement

The influence of crack length on G_{IIIc} was investigated by conducting a series of finite element analyses in which the displacement at maximum load measured in the experimental tests, δ_{max} (Figure 6.1), was used as the imposed displacement in the FE analysis. The VCCT was then used to determine the values of G_{III} across the crack front for normalised insert lengths ranging from 0.2 to 0.7.

The resulting values of G_{III} determined using this technique for crack lengths between 0.5 and 0.7, Figure 6.5, exhibit an increase with increasing crack length. Similar trends are apparent when all of the traces between 0.2 and 0.7 are compared. This evidence supports the conclusion that the measured values of G_{IIIc} are indeed dependent on the crack length.

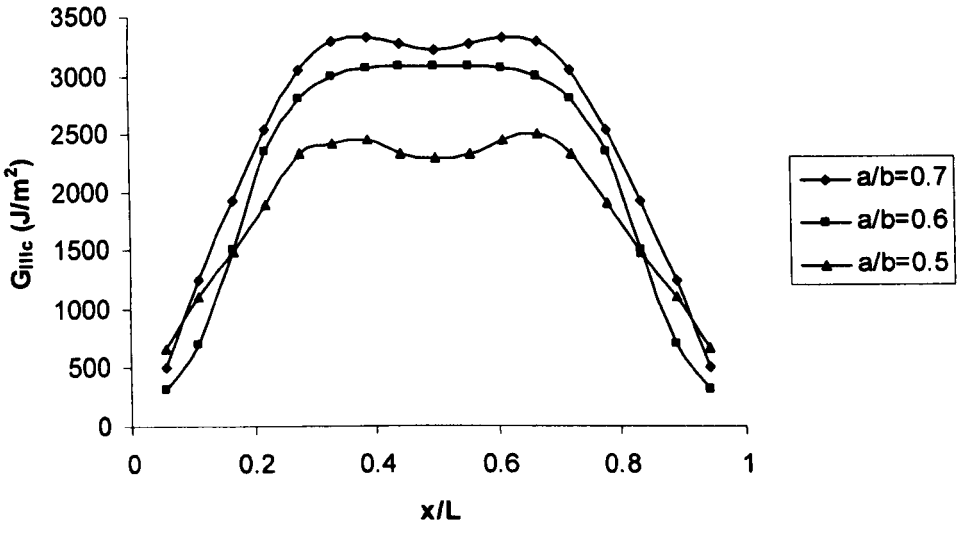

Figure 6.5: Mode III strain energy distribution for the glass fibre/PP composite as a function of position along the crack front. The displacements at maximum load measured during the experiments were used as the imposed displacements in the FE analyses.

It is evident from the plots that G_{IIIc} is roughly constant over the central region of the test specimen in samples with intermediate crack lengths, whereas two maxima are observed in specimens with shorter and longer insert lengths. There is also a considerable step between the distributions for the specimens with normalised insert lengths of 0.5 and 0.6. This is attributed to the use of experimentally-determined values of the applied displacement, which will clearly exhibit some degree of scatter.

This procedure was then extended by introducing the maximum displacement from the experiments, δ_{max}, into the FE model to calculate the maximum load, P_{max}^{FEA}. Using Equation 6.2 and inputting the values of P_{max}^{FEA} and the previously determined values for m_{FEA} and C_{FEA}, the value of G_{IIIc} was calculated for each normalised insert length examined. A plot of the G_{IIIc} values versus the normalised insert length a/b, calculated using this procedure is shown in Figure 6.6:

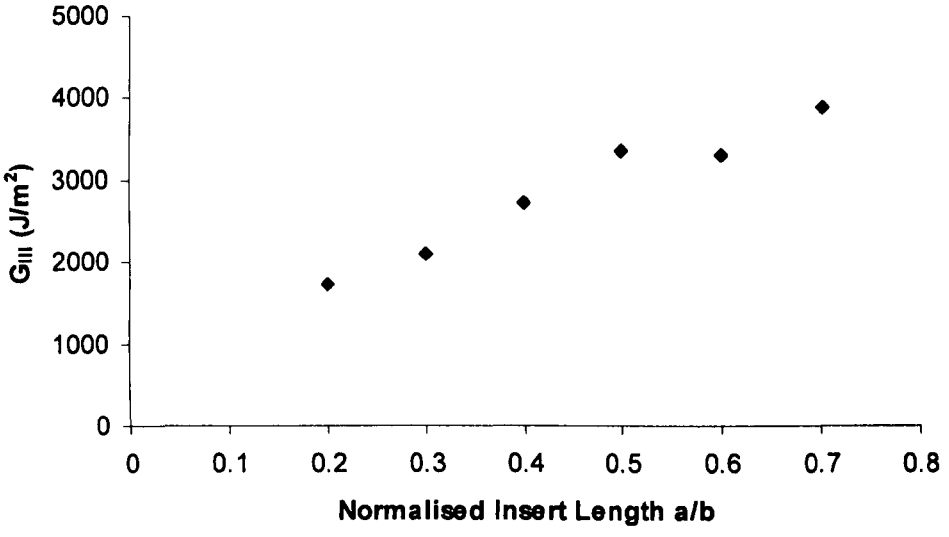

Figure 6.6: Predicted values of the maximum values of G_{IIIc} versus the normalised insert length a/b for the glass fibre/PP composite.

Clearly, these values are similar to those shown in Figure 6.4 and support the observation that the measured value of G_{IIIc} are crack length dependent. The reasons for this crack length dependency are not clear. Frictional effects are considered to be small and do not account for such variations. This effect will be investigated further in a subsequent where the Areas method is used to calculated an associated fracture energy.

6.2.5. The Influence of Loading Rate on the Load-Displacement Responses

Figure 6.7 shows typical load-displacement traces following ECT tests on the glass fibre/PP samples with a normalised insert length of 0.5, tested at crosshead displacement rates of 0.2, 2, 20 and 200 mm/min. It is clear from the graphs that the load increases in a linear fashion, reaching a maximum before dropping rapidly after the onset of macroscopic crack propagation.

The evidence indicates that the slope of the P-δ curve depends slightly on the loading rate, the variations observed here are due to slight differences in specimen thickness.

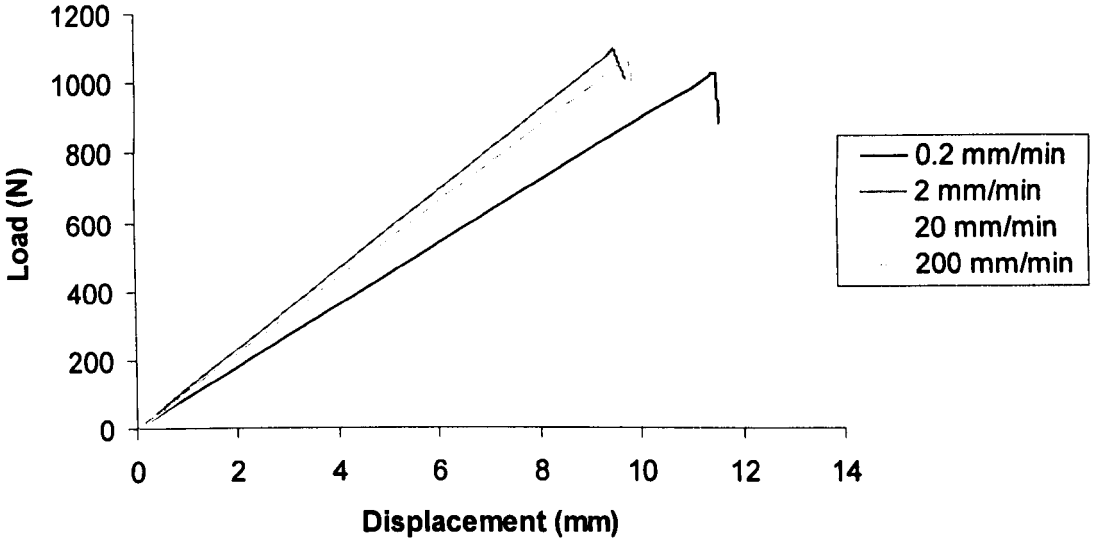

Figure 6.7: Load versus displacement traces following ECT tests on the glass fibre/PP composite specimens with a normalised insert length of 0.5, tested at crosshead displacement rates of 0.2, 2, 20 and 200 mm/min.

6.2.6. Influence of Loading Rate on Specimen Stiffness

The load-displacement curves were used to calculate the specimen compliance, C, taken as the reciprocal of the slope of the load-displacement curve. Figure 6.9 presents plots of the variation of the inverse of specimen compliance with crosshead displacement rate for the glass fibre reinforced polypropylene specimens, examined in this part of the study. The normalised insert length, a/b, for all samples shown in the figure, was 0.5. The evidence suggests that there is a slight rate dependency in the specimen stiffness. It should be noted that the specimen compliance could not be determined at impact rates. This is because during the impact test only a force-time

trace is available, since it was not possible to measure the specimen displacement. As a result, the specimen compliance at impact rates could not be determined and this is not included in the graph. The trends in Figure 6.8 are in contrast with the findings of Cantwell and co-workers [10], who showed that the elastic modulus of a glass fibre reinforced epoxy composite is insensitive to strain rate. Clearly, the material under investigation here is above its glass transition temperature at room temperature conditions. It is possible, therefore, that the polypropylene matrix exhibits a more pronounced viscoelastic response than the epoxy matrix used in other parts of this research programme.

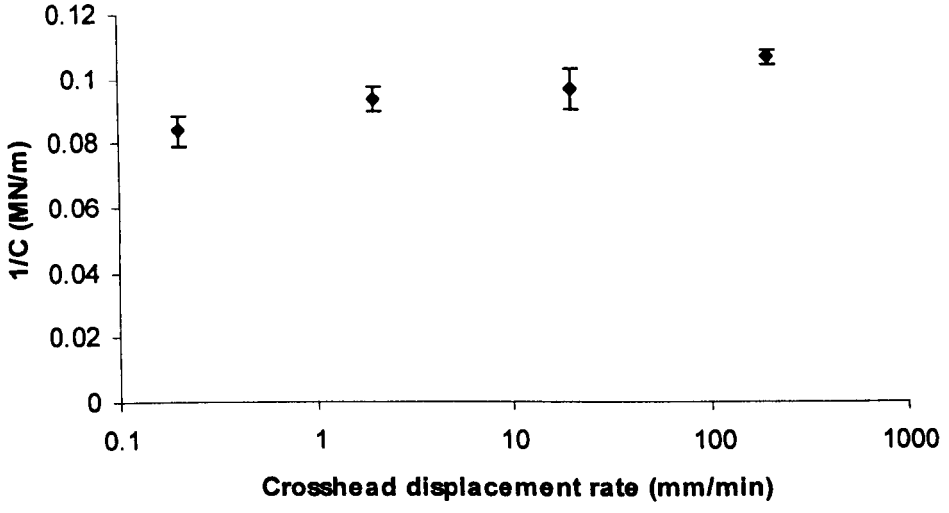

Figure 6.8: The influence of crosshead displacement rate on the stiffness of the glass fibre/PP composite specimens.

6.2.7. The Influence of Loading Rate on the Mode III Fracture Toughness of the Glass Fibre/PP Composite

The influence of loading rate on G_{IIIc} was initially investigated by conducting tests at crosshead displacement rates between 0.2 and 200 mm/min. The load-displacement traces were similar in all cases to those measured under quasi-static conditions, as shown in Figure 6.7. The dynamic fracture properties of the ECT specimens were

evaluated through a series of falling-weight impact tests on an instrumented drop-weight impact tower. Figure 6.9 shows the variation of the measured Mode III fracture toughness for the glass fibre/PP specimens at crosshead displacement rates between 0.2 and 200 mm/min, as well as under impact conditions (3 m/sec).

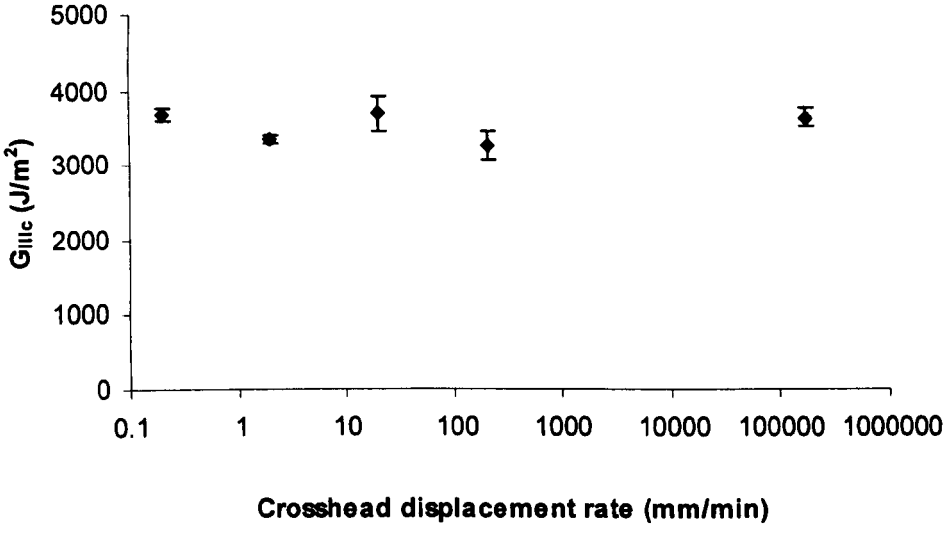

Figure 6.9: The influence of crosshead displacement rate on the Mode III interlaminar fracture toughness properties of the glass fibre/PP composite.

An examination of the data shown in Figure 6.9 indicates that the values of G_{IIIc} remain roughly constant over the range of crosshead displacement rates considered. This is encouraging and suggests that engineers can use the static values of G_{IIIc} when designing composite structures. At first, this is a little surprising as the polypropylene matrix in this composite is above its glass transition temperature (-12 °C) at room temperature which suggests that the viscoelastic effects could be significant, as noted above. At this point, it should be noted that the viscoelastic behaviour of polymeric materials is dependent on time [11]. In contrast, previous work investigating the influence of loading rate on the Mode II fracture properties of this material has shown that the interlaminar fracture properties of these composites exhibit very little

sensitivity to loading rate [12]. Further work by Blackman and co-workers [13] on the Mode II fracture toughness of composites with both thermosetting and thermoplastic matrices did not highlight any significant effect of test rate on the values of G_{IIc}. The research by Maikuma [14] on composites with thermoplastic matrices showed a decrease of about 28% in the value of G_{IIc} upon going from a low strain rate test to an impact test. However, similar work by Smiley and Pipes [15] reported far greater decreases, of the order of 80%.

6.2.8. Investigation of the Fracture Surface Morphology

Scanning electron micrographs from the fracture surface of the glass fibre reinforced polypropylene specimens tested at two different loading rates, 2 mm/min and 3 m/sec, are shown in Figure 6.10. The crack growth direction was from left to right and no significant out-of-plane fracture was observed.

Micrographs from the glass fibre/PP samples tested at 2 mm/min and under low velocity impact conditions are shown in Figures 6.10 (a) and (b). The polypropylene matrix exhibits ductile deformation, which is consistent with observations made on polypropylene-based composites tested under Mode I and Mode II loading [1,2]. It should also be noted that the deformation features are similar in each sample, despite the significant difference in loading rate. The higher magnification micrographs shown in Figures 6.10 (c) and (d) indicate a similarity in deformation features. For both loading rates, the cracks between the highly crystalline areas of polypropylene that developed due to the slow cooling during manufacture, are connected with highly deformed strands of polypropylene matrix. Once again this evidence suggests that the loading rate does not have a significant effect on the Mode III fracture morphology of the glass fibre/PP composite.

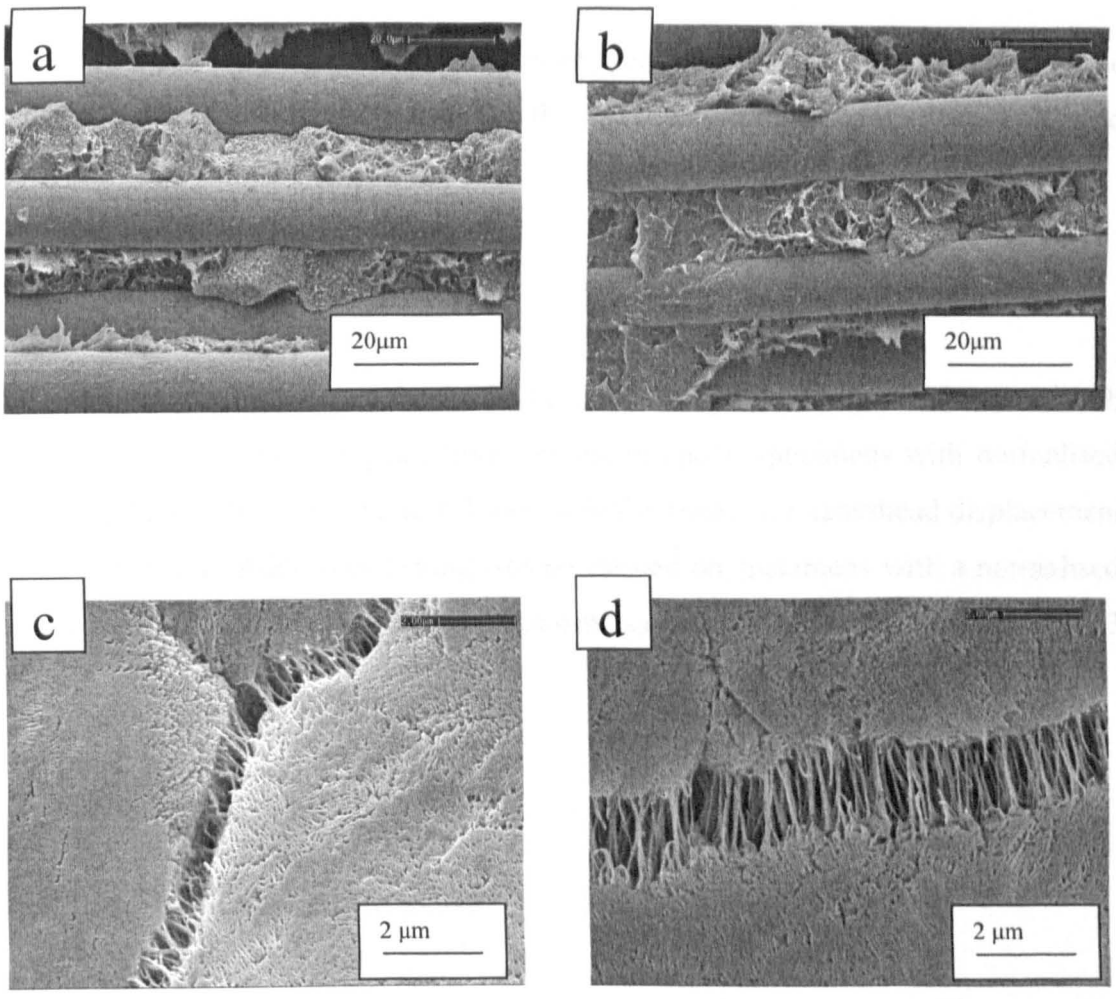

Figure 6.10: Electron micrographs of glass fibre/PP Mode III samples at (a) 2 mm/min, (b) 3 m/s, and (c) 2 mm/min, high magnification, (d) 3 m/s, high magnification.

6.3. Woven Glass Fibre Reinforced Epoxy

Twenty-four ply woven glass fibre reinforced specimens were tested in this part of the study. The stacking sequence adopted in the manufacture of the glass fibre reinforced epoxy ECT specimens was:

$$[90° / 0° (+45°/-45°)_2 / (-45°/+45°)_2 / 0° / 90°]_s$$

The nominal thickness of all the ECT specimens tested in this part of the research study was 6.5 mm. Woven glass fibre reinforced epoxy specimens with normalised insert lengths ranging from 0.2 to 0.7 were initially tested at a crosshead displacement rate of 2 mm/min. Additional testing was performed on specimens with a normalised insert length of 0.5 at crosshead displacement rates of 0.2, 20, 200 mm/min and 3 m/sec.

6.3.1. Load-Displacement Responses

Figure 6.11 shows a typical load-displacement trace following an ECT test on a woven glass fibre reinforced epoxy specimen with a normalised crack length of 0.5. The response is similar to that observed in the glass fibre/PP composite with the load increasing linearly, reaching a maximum before reducing following the onset of macroscopic crack propagation. Clearly, the force measured here is considerably higher than that measured on the glass fibre/PP sample shown in Figure 6.1.

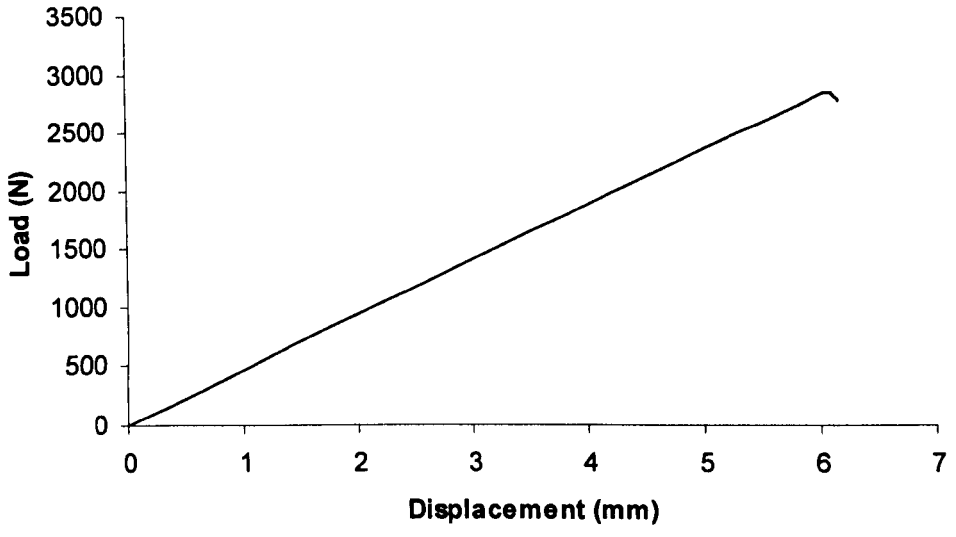

Figure 6.11: Typical load displacement trace following an ECT test on a woven glass fibre reinforced epoxy ECT specimen with a normalised insert length of 0.5.

Figure 6.12 shows typical load-displacement traces following ECT tests on the woven glass fibre/epoxy samples with normalised insert lengths ranging from 0.2 to 0.7. As in the case of the glass fibre/PP specimens, the load increases linearly before becoming slightly non-linear and reaching a maximum before dropping, indicating macroscopic crack propagation. Clearly the slope of each trace decreases with increasing crack length, this being due to the increase in specimen compliance as the crack length increases.

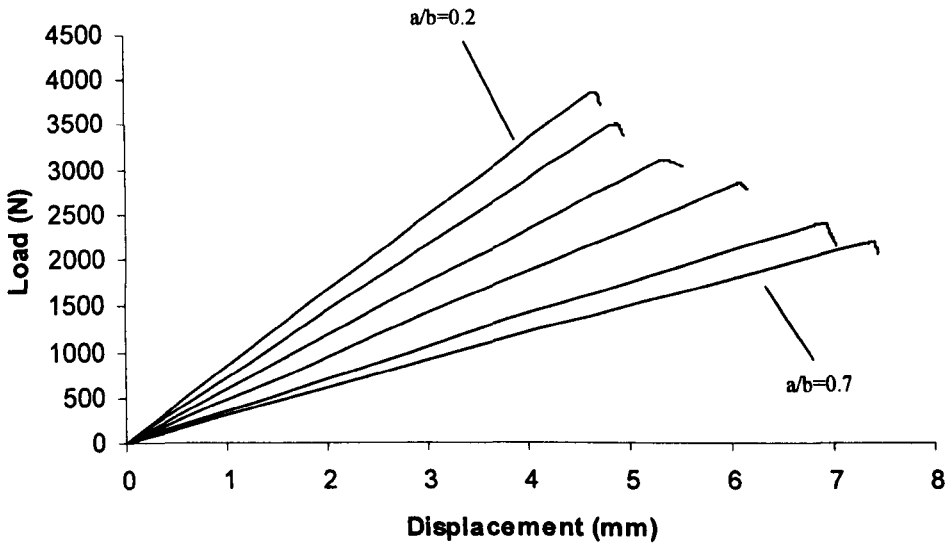

Figure 6.12: Load displacement traces following ECT tests on the woven glass fibre reinforced epoxy ECT specimens with normalised insert lengths ranging from 0.2 to 0.7.

6.3.2. The Influence of Crack Length on Specimen Stiffness

Following the procedure described in Section 6.2.2, the specimen compliance was determined from the load-displacement plots obtained during the tests. The inverse of the specimen compliance, 1/C, was then plotted as a function of the normalised insert length, a/b, and a straight line was then applied to the data, Figure 6.13.

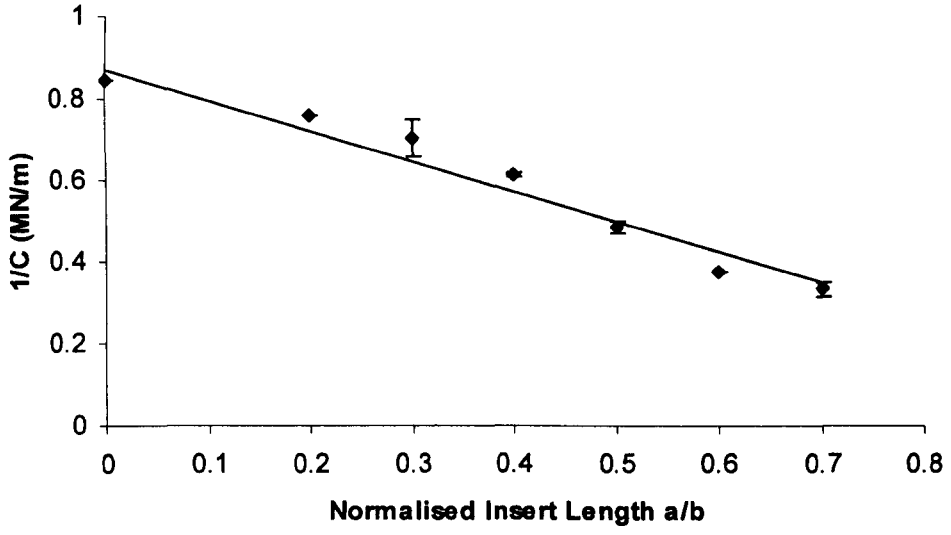

Figure 6.13: The variation of the inverse of specimen compliance with normalised crack length following tests on the woven glass fibre/epoxy composite.

It is clear from the figure that the graph of 1/C versus a/b exhibits a similar trend to that exhibited by the glass fibre/PP composite. Equation 6.1 was then applied tothe experimental data yielding a value for 'm' of 0.73. This is in good agreement with the value of 0.79 calculated in the FE analysis.

6.3.3. Influence of Crack Length on G_{IIIc} at Quasi-Static Rates of Loading

As described earlier, the fracture toughness of the composite was determined at a crosshead displacement rate of 2 mm/min. The maximum force, P_{max} was recorded following each test and introduced into Equation 6.2, to determine the Mode III fracture toughness of each ECT specimen, G_{IIIc}. As before, the value of 'm' determined at 2 mm/min was used to calculate G_{IIIc} for all of the crosshead displacement rates investigated here.

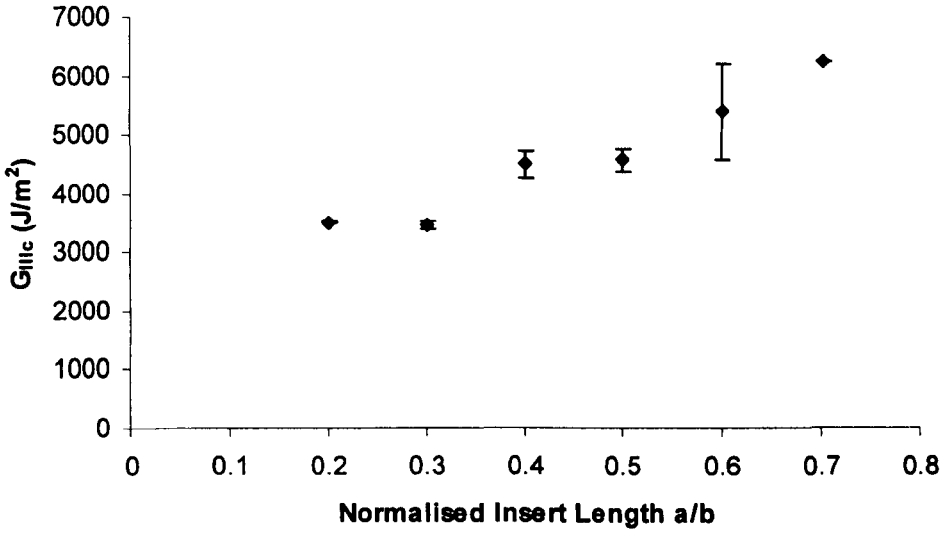

Figure 6.14: The variation of G_{IIIc} with normalised crack length for the woven glass fibre/epoxy ECT specimens.

An examination of the woven glass fibre reinforced epoxy data, Figure 6.14, indicates that the Mode III fracture toughness increases rapidly with normalised insert length. Indeed, the values of G_{IIIc} at maximum load increase by approximately eighty-five percent over the range of crack lengths considered here. The findings are in good agreement with those for the glass fibre/PP specimens and those reported by Ratcliffe [9]. Once again, this crack-length dependency of G_{IIIc} renders it virtually impossible to determine an intrinsic value of the Mode III interlaminar fracture toughness for this material. This dependency was further examined using an 'areas method' as will be outlined below.

6.3.4. Investigation of Crack Length Effects using the Areas Method

The crack length dependency of the Mode III interlaminar fracture properties of the composites was further investigated using the Areas method. Here, the specimens were sectioned at 5 mm intervals and the crack length was measured using an optical

microscope. The crack length profiles were then used to estimate the total area of fracture and this was used, along with the area under the load-displacement trace, to determine the fracture energy.

Figure 6.15 shows the data for the woven glass fibre reinforced epoxy composite, where the data calculated using the areas method are compared with the fracture energies calculated using Equation 6.2. As can be seen from the figure, the data calculated using the areas method follow a similar trend to the experimental compliance data, increasing rapidly with normalised insert length a/b. This evidence suggests that the crack length dependency of G_{IIIc} is genuine and needs to be taken into consideration when conducting Mode III tests of this nature. Furthermore, from the data in Figure 6.15 it is also clear that the values yielded by the areas method are similar to those calculated using Equation 6.2.

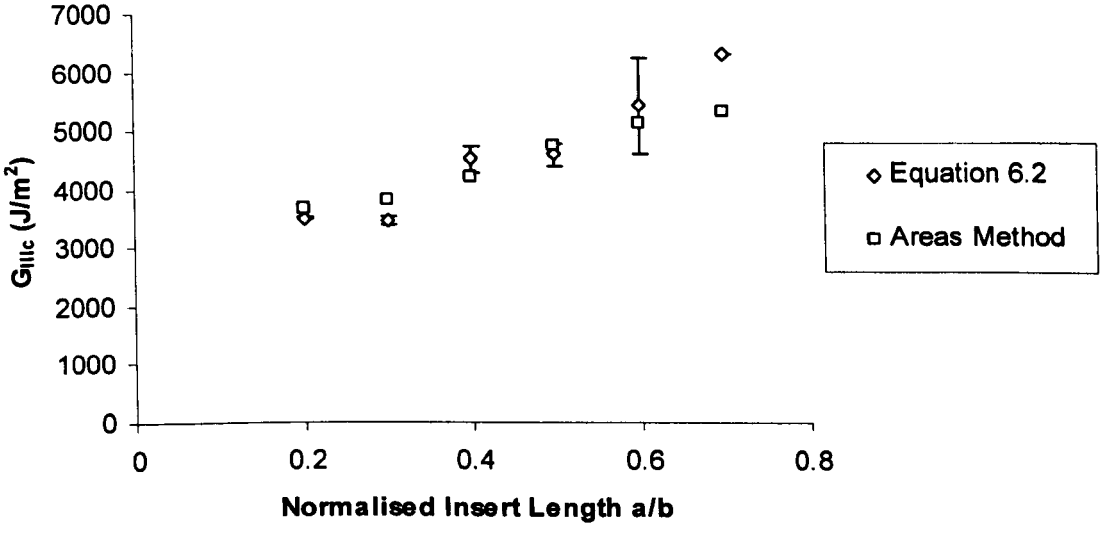

Figure 6.15: The Mode III fracture energies of the woven glass fibre/epoxy calculated using an areas method. The values of G_{IIIc} calculated using Equation 6.2 are also included for comparison.

6.3.5. Influence of Loading Rate on Load-Displacement Responses

Figure 6.16 shows typical load-displacement traces following ECT tests on the woven glass fibre/epoxy samples with a normalised insert length of 0.5, tested at crosshead displacement rates of 0.2, 2, 20 and 200 mm/min. It is clear from the graphs that the load increases in a linear fashion, reaching a maximum before dropping rapidly after the onset of macroscopic crack propagation.

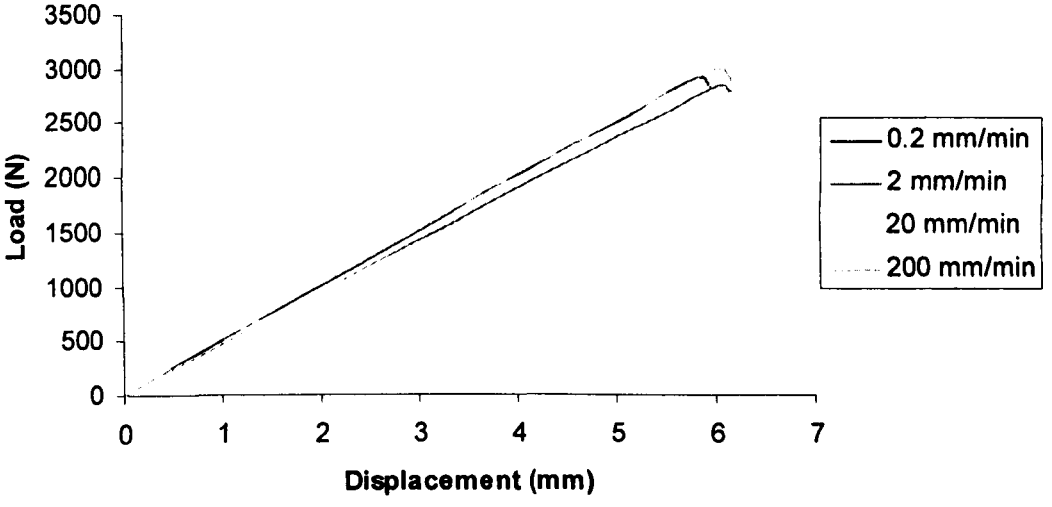

Figure 6.16: Load displacement traces following ECT tests on the woven glass fibre/epoxy composite specimens with a normalised insert length of 0.5, tested at crosshead displacement rates of 0.2, 2, 20 and 200 mm/min.

6.3.6. Influence of Loading Rate on Specimen Stiffness

Figure 6.17 shows the variation of the inverse of specimen compliance with crosshead displacement rate for the woven glass fibre reinforced epoxy specimens. The plots correspond to samples with a normalised insert length, a/b, of 0.5. As before, due to difficulties in measuring the compliance at high crosshead displacement rates, it was only determined at crosshead displacement rates ranging from 0.2 to 200 mm/min.

The evidence indicates that there is no rate dependency for the specimen stiffness with crosshead displacement rate, as the values are relatively constant across the range of loading conditions examined. This is in contrast to the data for the glass fibre/PP composites in Figure 6.8 where an increase in the value of 1/C was observed.

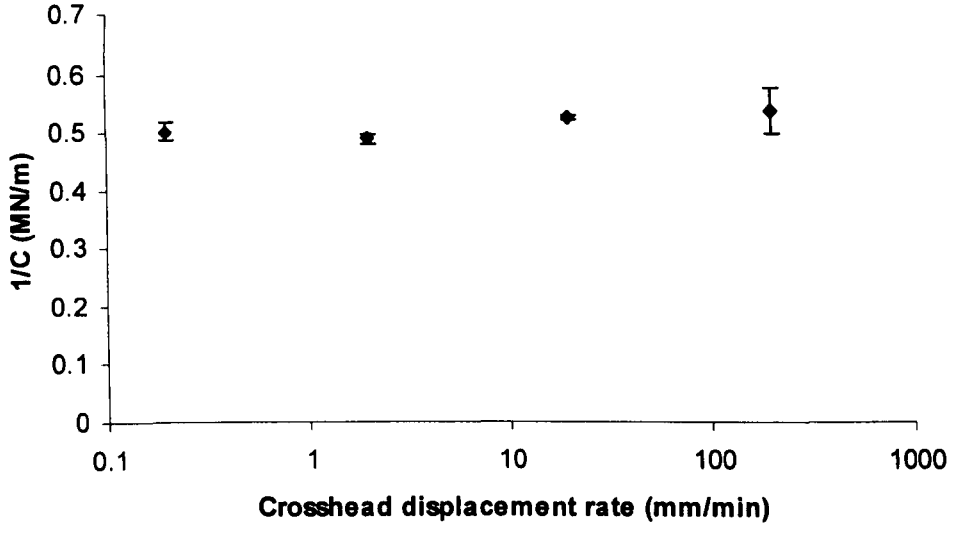

Figure 6.17: The influence of crosshead displacement rate on the stiffness of the woven glass fibre/epoxy composite ECT specimens.

6.3.7. Influence of Loading Rate on Fracture Toughness

The influence of loading rate on the G_{IIIc} of the woven glass fibre/epoxy composite was initially investigated by conducting tests at crosshead displacement rates between 0.2 and 200 mm/min. Once again, the load-displacement traces were similar in all cases to those measured under quasi-static conditions, Figure 6.16. As in the case of the glass fibre/PP, the dynamic fracture properties of the woven glass fibre reinforced epoxy ECT specimens were evaluated through a series of falling weight impact tests on an instrumented drop-weight impact tower. Figure 6.18 shows the variation of the

measured Mode III fracture toughness for this material between crosshead displacement rates of 0.2 mm/min and 3 m/sec.

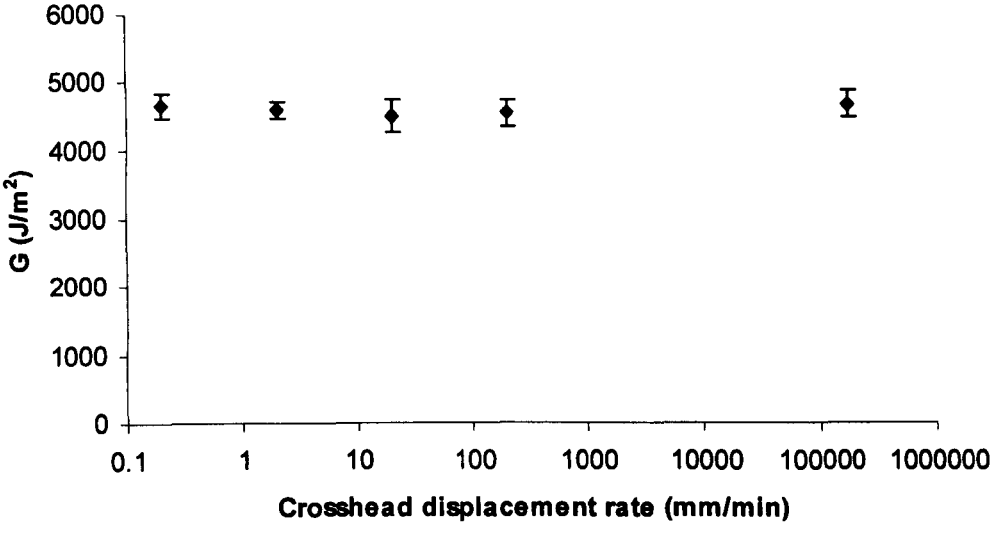

Figure 6.18: The influence of crosshead displacement rate on the interlaminar fracture toughness values for the woven glass fibre reinforced epoxy composite specimens.

An examination of Figure 6.18 highlights a similar trend to that exhibited by the glass fibre/PP specimens, with the values of G_{IIIc} remaining roughly constant over the range of crosshead displacement rates considered. It is clear that the Mode III interlaminar fracture properties of the glass fibre reinforced epoxy remain superior to those of its polypropylene counterpart across the spectrum of crosshead displacement rates. Moreover, the dynamic value of G_{IIIc} for the epoxy-based sample is similar to that determined at much lower rates of loading. This evidence suggests that the Mode III interlaminar fracture properties of this system are not sensitive to loading rate. Blackman and co-workers [13] conducted Mode II fracture toughness tests on a carbon fibre reinforced epoxy composite and showed that G_{IIc} remains roughly constant over a wide range of loading rates.

6.3.8. Investigation of the Fracture Surface Morphology

Fracture surface electron micrographs from woven glass fibre reinforced epoxy specimens tested at loading rates of 2 mm/min and 3 m/sec are shown in Figure 6.19. As in the case of the glass fibre/PP specimens, crack growth direction was from left to right and no significant out-of-plane fracture was observed.

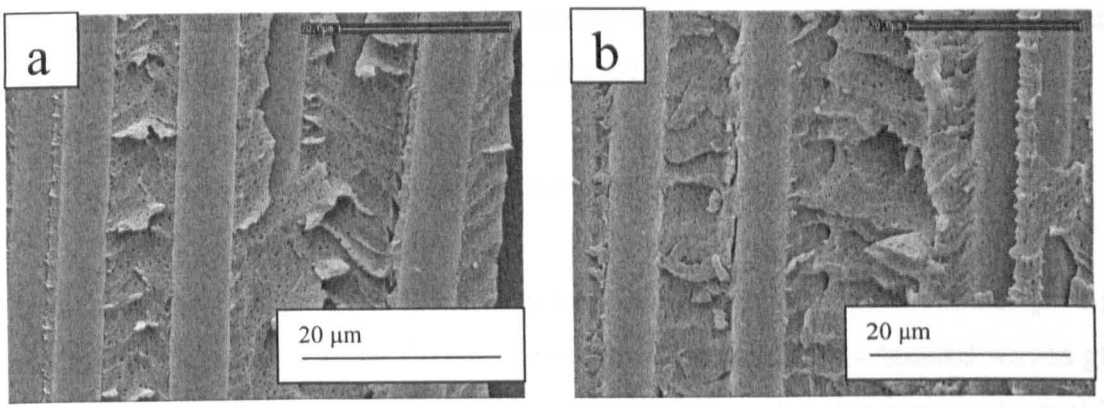

Figure 6.19: Electron micrographs of woven glass fibre/epoxy Mode III samples tested at (a) 2 mm/min and (b) 3 m/s.

It is clear from the above figures that, for the woven glass fibre/epoxy composite, the specimens tested at 2 mm/min and under impact conditions exhibit hackle mark deformation in the matrix. This type of deformation is common for thermoset-based matrices under Mode II loading and is a significant energy-absorbing mechanism [16-21]. In addition, under Mode II loading, the hackle marks typically lie normal to the fibre direction. In the material examined in this part of the research study, under Mode III loading, the hackle marks are oriented at an angle to the fibres; up to 45° in the case of the sample tested at a crosshead displacement rate of 2 mm/min. The matrix in the impacted woven glass reinforced epoxy specimen shows slightly less well defined hackle marks and smoother fracture features. This may be attributed to the higher loading rate. However, the features in both micrographs shown in Figure 6.19 are similar enough to support the results presented for the woven glass fibre/epoxy in

Figure 6.18, and the conclusion that there is no significant loading rate effect for this composite.

6.4. Adhesively-Bonded Woven Glass Fibre Reinforced Epoxy

Adhesively-bonded woven glass fibre reinforced epoxy specimens were manufactured following the procedures outlined in Section 4.2.3. A two-part epoxy resin system was used to bond two laminates based on the following stacking sequence:

$$[90° / 0° (+45°/-45°)_2 / (-45°/+45°)_2 / 0° / 90°]_s$$

The thickness of the ECT adhesively-bonded specimens was 7.9 mm, giving a nominal thickness of 1.4 mm for the epoxy adhesive. Adhesively-bonded woven glass fibre reinforced epoxy specimens with normalised insert lengths ranging from 0.2 to 0.7 were initially tested at a crosshead displacement rate of 2 mm/min. Testing was subsequently performed on specimens with a normalised insert length of 0.5 at crosshead displacement rates of 0.2, 20 and 200 mm/min. Additional specimens with normalised insert lengths ranging from 0.2 to 0.7 were tested on the instrumented drop-weight impact tower shown in Figure 4.2 at an impact velocity of 4.2 m/sec.

6.4.1. Load-Displacement Responses

Figure 6.20 shows a typical load-displacement trace following an ECT test on an adhesively-bonded woven glass fibre reinforced epoxy specimen with a normalised crack length of 0.5. Once again, the load increases in a linear fashion, reaching a maximum before dropping after the onset of macroscopic crack propagation. Clearly, the forces involved here are much greater than those in the plain ECT samples, due to the increased thickness of these specimens.

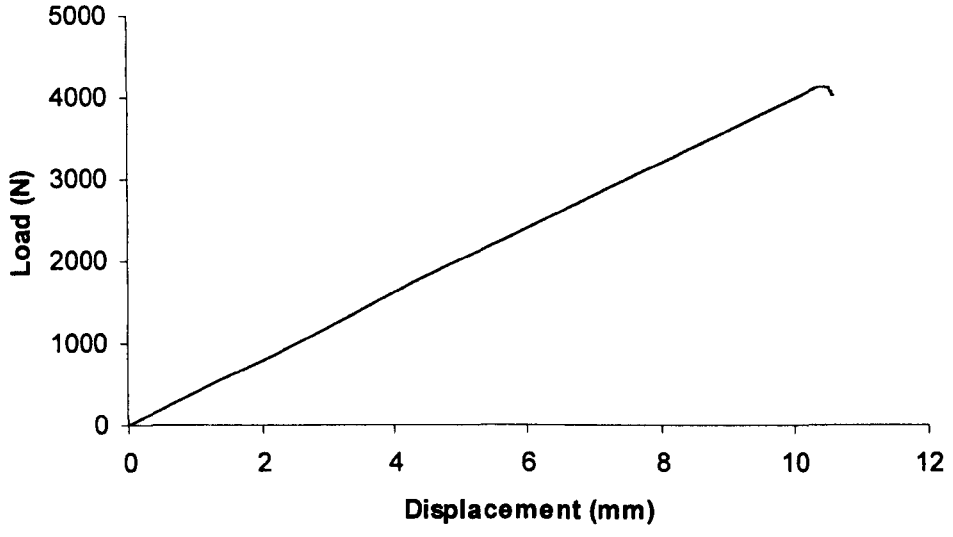

Figure 6.20: Typical load displacement trace following an ECT test on the adhesively-bonded woven glass fibre reinforced epoxy composite specimen with a normalised insert length of 0.5.

Figure 6.21 shows typical load-displacement traces following ECT tests on the adhesively-bonded woven glass fibre/epoxy samples with normalised insert lengths ranging from 0.2 to 0.7. As before, the load increases in a relatively linear fashion, reaching a maximum before dropping following the onset of macroscopic crack propagation. Once again, the slope of the traces decreases with increasing compliance of the samples with longer crack lengths.

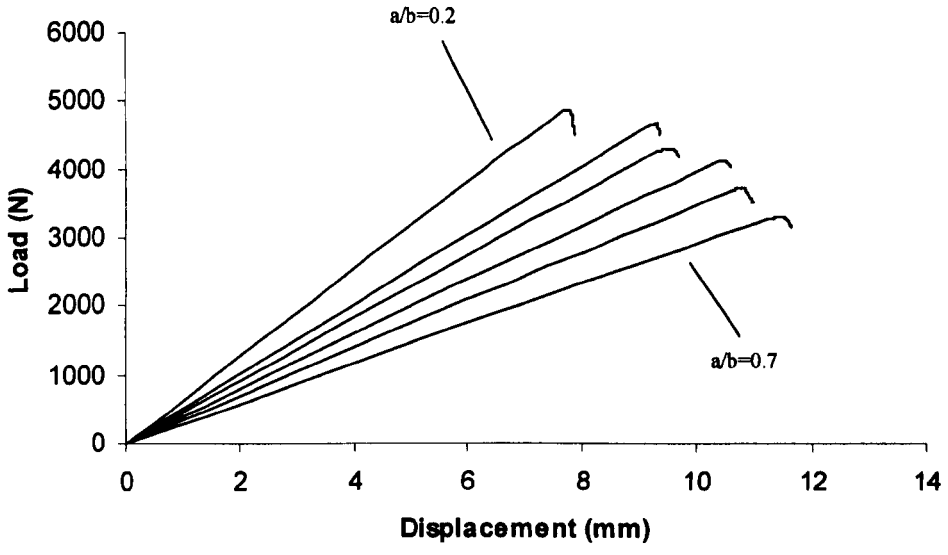

Figure 6.21: Typical load-displacement responses following ECT tests on the adhesively-bonded woven glass fibre/epoxy specimens.

6.4.2. The Influence of Crack Length on Specimen Stiffness

The specimen compliance was determined from the load-displacement plots obtained during the tests. The inverse of the specimen compliance, 1/C, was plotted as a function of the normalised insert length, a/b, and a straight line was then applied to the data, according to Equation 6.1. Using this equation, the value of 'm' was calculated from the experimental data.

A plot of the inverse of specimen compliance, 1/C, with the normalised insert length, a/b, for the adhesively-bonded woven glass fibre/epoxy specimens is shown in Figure 6.22.

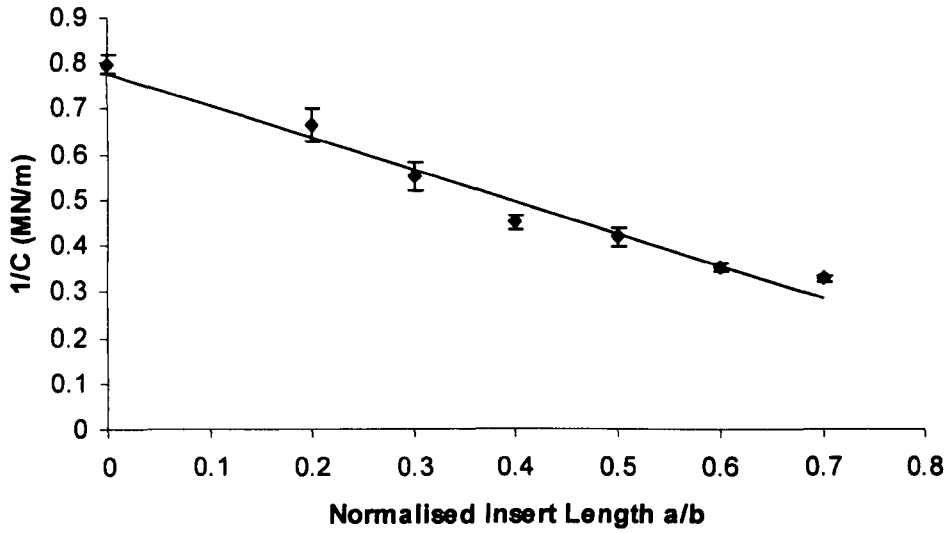

Figure 6.22: The variation of the inverse of specimen compliance with normalised crack length for the adhesively-bonded woven glass fibre/epoxy composite.

According to Figure 6.22, the values of 1/C decrease with increasing normalised insert length, as expected from Equation 6.1. This behaviour is similar to the response of the previously examined composite materials. The constant 'm' in this equation was calculated and found to be 0.94. This agrees reasonably well with the value of 0.87 determined in the FE study.

6.4.3. Influence of Crack Length on G_{IIIc} at Quasi-Static Rates of Loading

The fracture toughness of the adhesively-bonded woven glass fibre/epoxy composite was determined at a crosshead displacement rate of 2 mm/min. The value of the Mode III interlaminar fracture toughness of the composite, G_{IIIc}, was calculated using the maximum force, P_{max}, according to Equation 6.2.

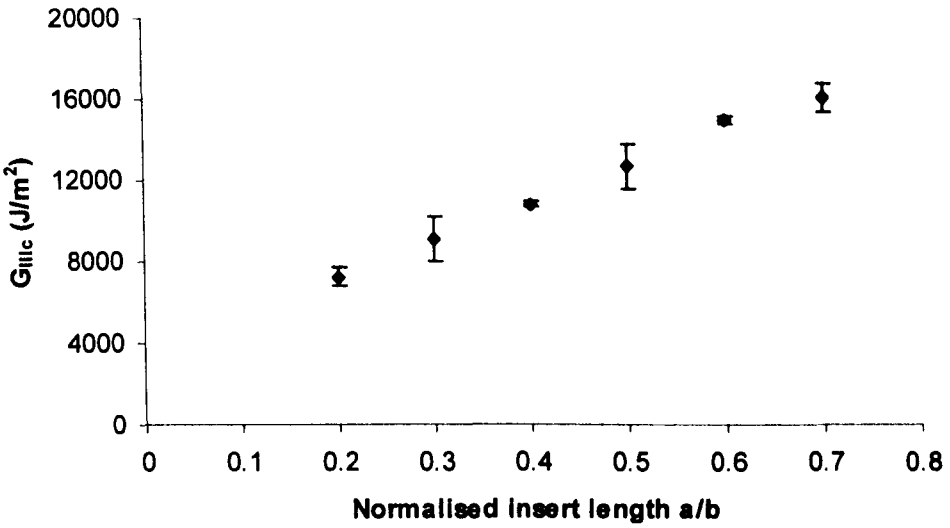

Figure 6.23: Critical Mode III strain energy release rate versus insert length for the adhesively-bonded woven glass fibre/epoxy specimens tested at a crosshead displacement rate of 2 mm/min.

Figure 6.23 shows a plot of G_{IIIc} versus a/b for the adhesively-bonded composite system tested at 2 mm/min. Clearly, the Mode III fracture toughness increases with normalised insert length. A comparison of Figures 6.23 and 6.15, shows that, for a given crack length, the interlaminar fracture toughness of the adhesively-bonded system is considerably higher than that offered by the plain composite. This effect is attributed to the presence of significant crack-tip blunting within the adhesive epoxy layer [22-25, 27-29]. Furthermore, the adhesive fracture energy increases with bond thickness, a phenomenon attributed to the increase in the volume of resin undergoing plastic deformation. As a result, more energy is absorbed, making crack propagation more difficult. This effectively increases the amount of blunting at the crack tip.

Chai [27-29] undertook a detailed investigation of the fracture properties of adhesively-bonded joints. Here, the interlaminar fracture toughness in Mode II and Mode III fracture were elucidated for a range of adhesives. The thickness of the

adhesive was varied from as little as a small fraction of the natural crack tip damage zone to a value large enough to expose the bulk fracture behaviour. Chai's work highlighted a dependency of G_{IIIc} on the adhesive thickness and was found to exhibit a plateau followed by a phase of steady decrease as the adhesive thickness, t, was decreased. This is a parameter that should be taken into consideration when employing adhesively-bonded joints in the design of a structure.

Clearly, the values of joint thickness are very large here and it could be argued that these values are approaching those for the plain composite. Finally, it should be noted that the trends in the experimental data were verified by conducting an FEA analysis of the ECT specimen and have been presented in Chapter 5.

6.4.4. Influence of Loading Rate on the Load-Displacement Responses

Figure 6.24 shows typical load-displacement traces following ECT tests on the adhesively-bonded woven glass fibre/epoxy samples with a normalised insert length of 0.5, tested at crosshead displacement rates of 0.2, 2, 20 and 200 mm/min. Once again, the load increases in a linear fashion, reaching a maximum before dropping rapidly after macroscopic crack propagation.

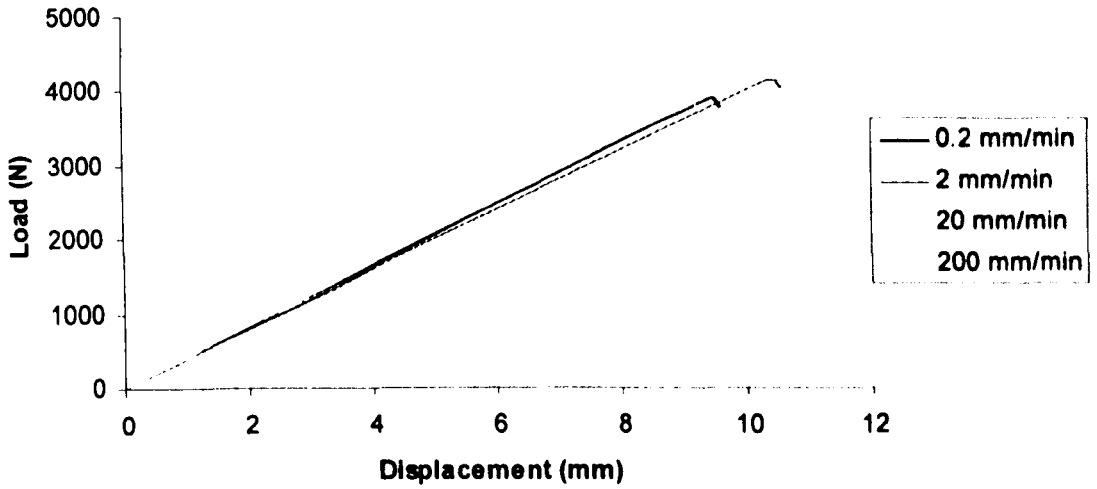

Figure 6.24: Load displacement traces following ECT tests on the adhesively-bonded woven glass fibre/epoxy composite specimens with a normalised insert length of 0.5, tested at crosshead displacement rates of 0.2, 2, 20 and 200 mm/min.

6.4.5. Influence of Loading Rate on Specimen Stiffness

Figure 6.25 presents a plot of the variation of the inverse of specimen compliance with crosshead displacement rate for the adhesively-bonded woven glass fibre reinforced epoxy specimens. The data were obtained from samples with a normalised insert length, a/b, of 0.5, tested at crosshead displacement rates ranging from 0.2 to 200 mm/min. The trends are similar to those observed in its plain composite counterpart, Figure 6.17, suggesting that the specimen stiffness remains constant with crosshead displacement rate. It is a little surprising that the measured values of 1/C are a little lower than in the plain composite samples in spite of the fact that the bonded samples are thicker and therefore stiffer. The reasons for this are not clear.

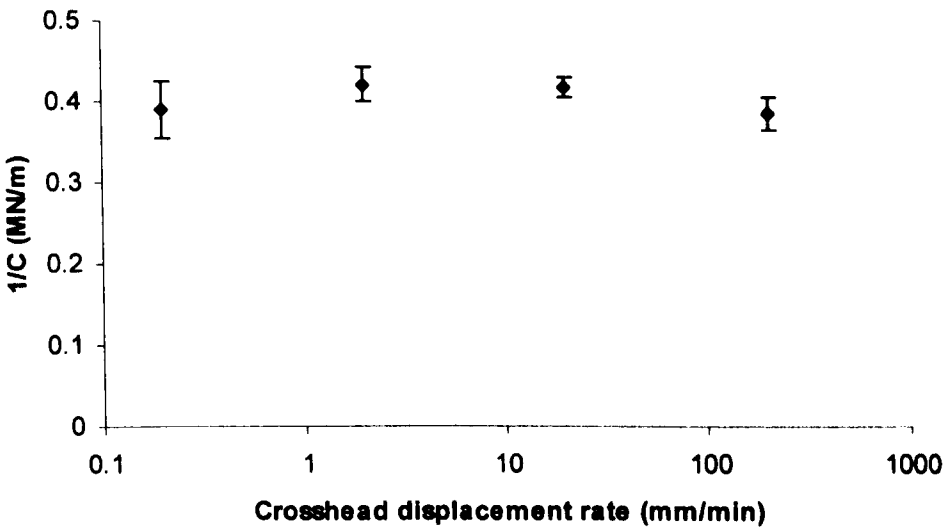

Figure 6.25: The influence of crosshead displacement rate on the stiffness of the adhesively-bonded woven glass fibre/epoxy composite ECT specimens.

6.4.6. Influence of Loading Rate on Mode III Fracture Toughness

The dynamic Mode III fracture toughness of the adhesively-bonded woven glass fibre reinforced epoxy specimens was determined at a crosshead displacement rate of 4.2 m/sec. As before, the G_{IIIc} values of the ECT specimen were calculated based on the maximum critical load for crack propagation, P_c^{max} and Equation 6.2.

Figure 6.26 shows the critical Mode III strain energy release rate as a function of the normalized insert length, a/b, for tests performed under impact conditions. The Mode III fracture toughness was found to increase with normalised insert length, as was the case at a crosshead displacement rate of 2 mm/min. A comparison of the plots in Figures 6.23 and 6.26 shows very similar values of G_{IIIc} for a given crack length, suggesting that the crosshead displacement rate does not influence the fracture toughness.

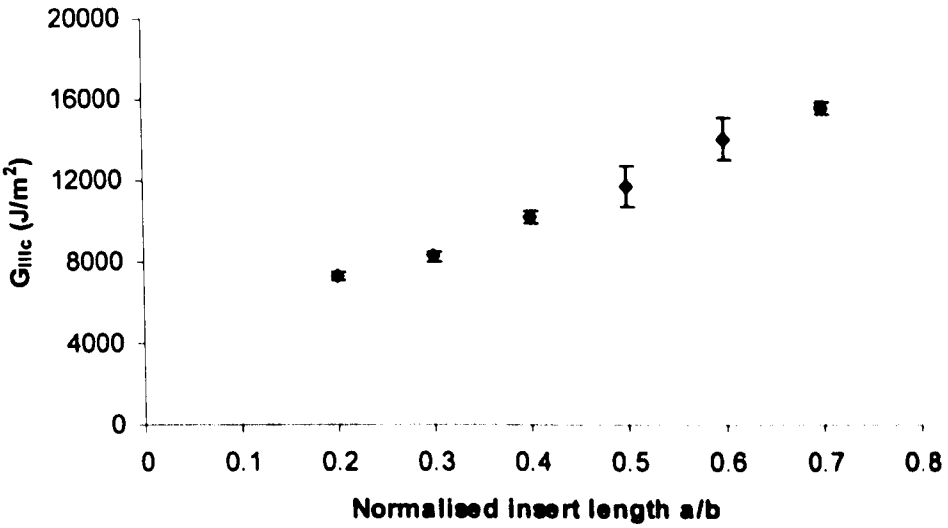

Figure 6.26: Critical Mode III strain energy release rate versus insert length of adhesively-bonded woven glass fibre/epoxy specimens loaded at 4.2 m/sec.

Figure 6.27 shows the variation of the Mode III fracture toughness of the adhesively-bonded woven glass fibre/epoxy composite as a function of crosshead displacement rate. All specimens in this figure had a normalised insert length of 0.5. It is clear from the graph that the values of G_{IIIc} for the adhesively-bonded woven glass fibre/epoxy composite specimens remain roughly constant with increasing crosshead displacement rate. This evidence suggests that the Mode III interlaminar fracture properties of the adhesively-bonded system follow similar trends to its plain composite counterpart, that is, it is not sensitive to loading rate.

According to Bell and Kinloch [26], the value of the adhesive fracture energy, G_c, may be dependent on the type of substrates employed, even when cohesive fracture through the adhesive layer is observed. At this point, it is worth noting that previous work investigating the influence of loading rate on the Mode II fracture properties of glass fibre reinforced composites has shown that there is very little sensitivity to loading rate [12]. This finding agrees with the experimental results of the present

research programme regarding the Mode III fracture toughness of the glass fibre reinforced polypropylene and woven glass fibre reinforced epoxy ECT specimens. Furthermore, the work by Blackman and co-workers on the effect of the strain rate on the Mode II interlaminar fracture toughness of adhesively-bonded fibre composites [13] has shown a very small dependency of about 5%.

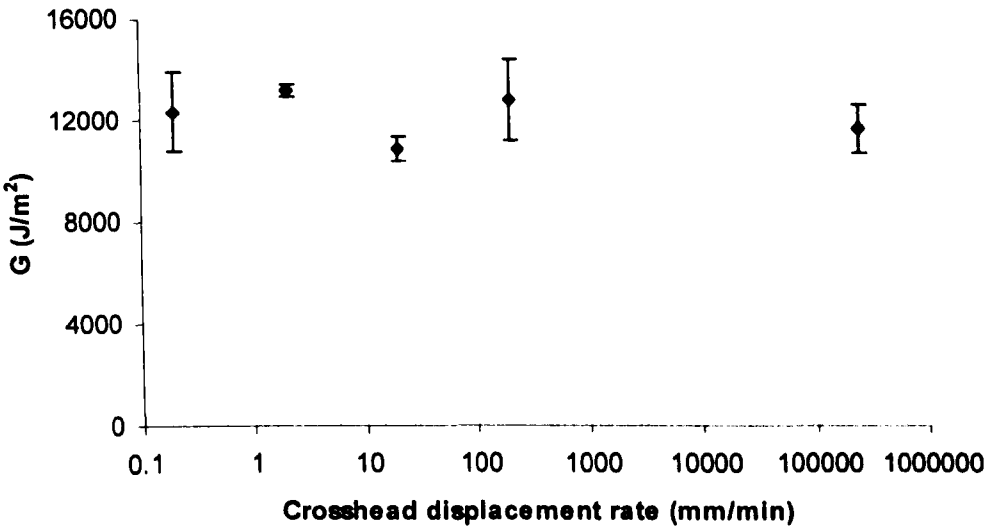

Figure 6.27: The variation of critical Mode III strain energy release rate with crosshead displacement rate for the adhesively-bonded woven glass fibre/epoxy.

6.4.7. Failure of the Adhesive Joints

There are two main fracture types of fracture observed in adhesive joints, depending on the location where fracture occurs. These are referred to as cohesive and interfacial fracture. Cohesive fracture occurs when the crack propagates in the bulk polymer, i.e. within the adhesive. Here, the surfaces of both adherands will be covered by fractured adhesive after debonding. On the other hand, fracture is said to be adhesive or interfacial when debonding occurs between the adhesive and the adherand. In most cases, the occurrence of interfacial fracture for a given adhesive is associated with a

lower adherand fracture toughness. Figure 6.28 gives a schematic of these two types of failure in adhesive joints.

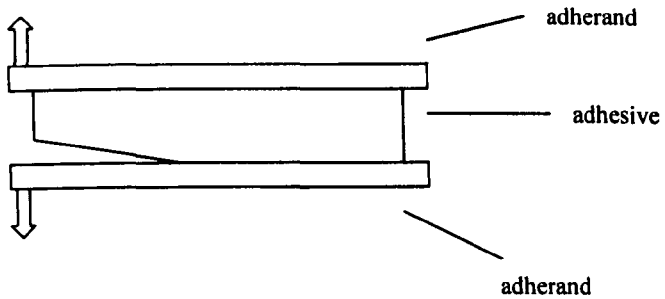

(a) Adhesive Failure

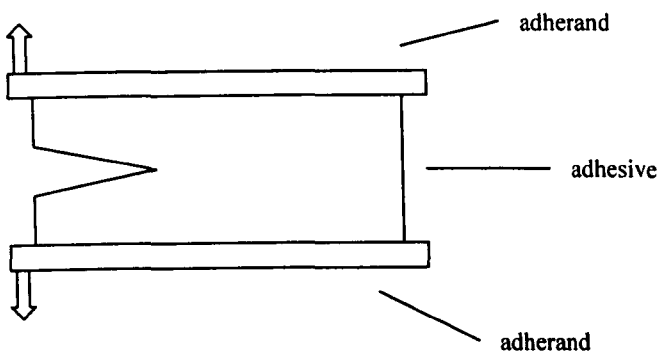

(b) Cohesive Failure

Figure 6.28: Schematic of the different locations of failure in an adhesive joint.

Optical microscopy was used to examine the crack tip regions in the adhesively-bonded woven glass fibre reinforced specimens. A specimen with a normalised insert length of 0.5 was sectioned at 27 mm intervals and examined in the optical microscope. The regions around the crack tip at the specimen edge and mid-span are shown in Figures 6.29 and 6.30 respectively.

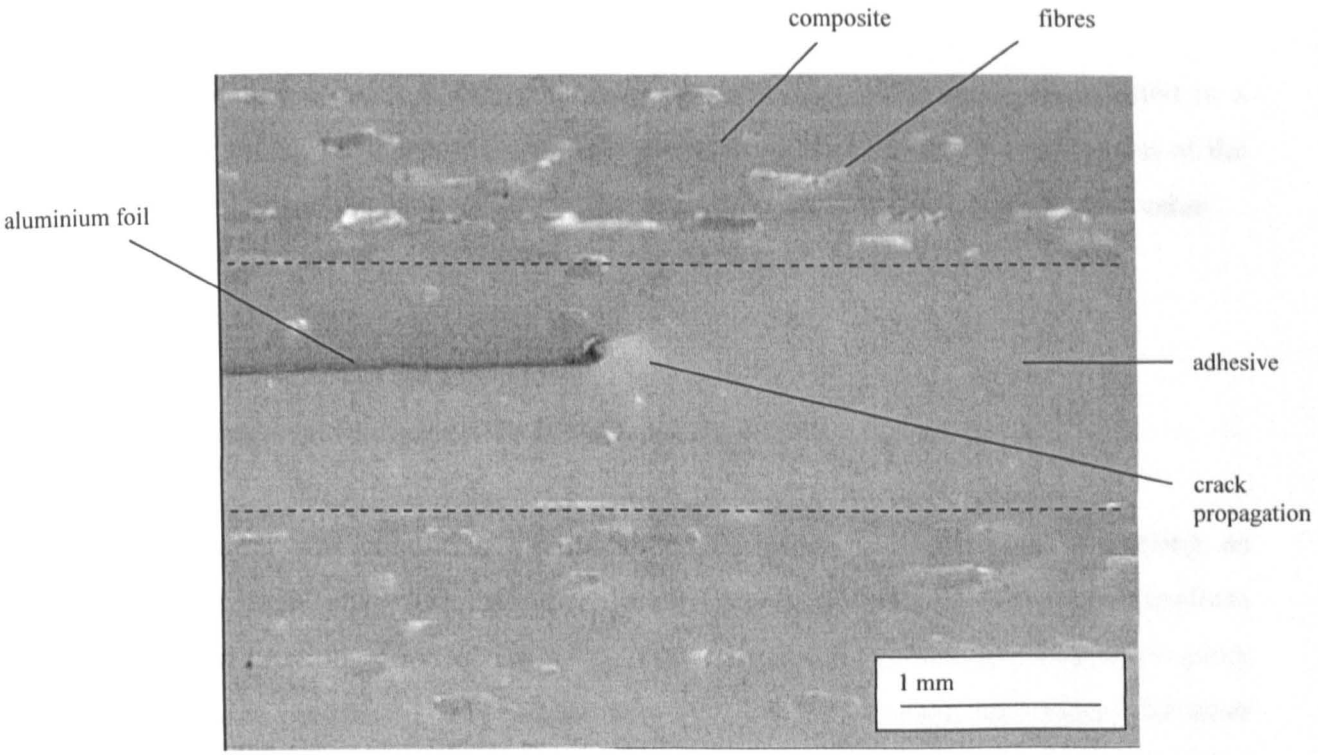

Figure 6.29: Optical micrograph of the crack tip region at the specimen edge in an adhesively-bonded glass fibre reinforced epoxy specimen.

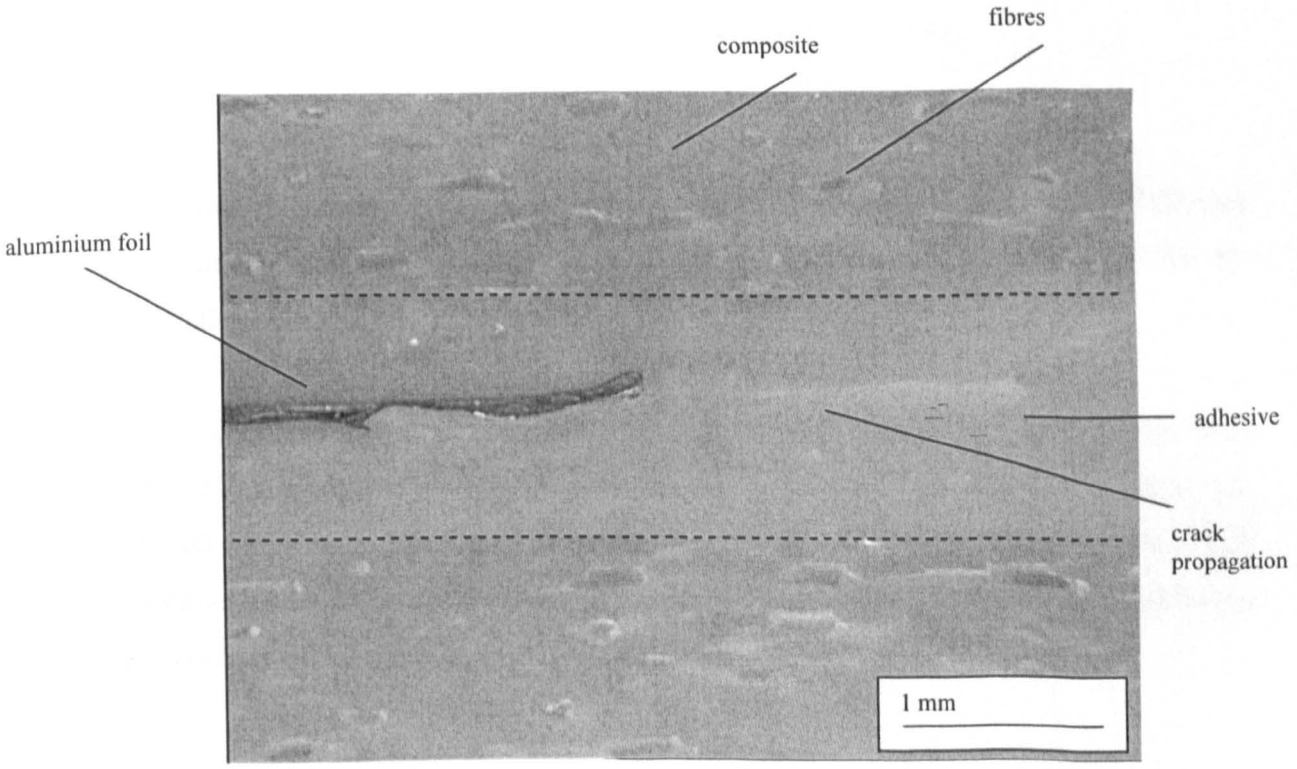

Figure 6.30: Optical micrograph of the crack tip in an adhesively-bonded glass fibre reinforced epoxy specimen near the mid-width.

By examining Figures 6.29 and 6.30 it is evident that the specimen has failed in a cohesive mode. Furthermore, crack propagation is greater in the central region of the specimen, where the Mode III strain energy release rate reaches its maximum value.

6.5. Bi-material Samples with Interfacial Cracks

ECT testing was conducted on specimens based on two materials, one being an isotropic metal alloy and the other a composite material, following the procedures described previously in Section 4.2.4. The same woven glass fibre reinforced epoxy as that used previously, was bonded to a 2.05 mm thick spring steel plate. The latter was chosen in order to avoid large plastic deformations during testing. The spring steel was bonded to an eight ply woven glass fibre reinforced epoxy material based on the following stacking sequence:

$$[90^\circ / 0^\circ (+45^\circ/-45^\circ) / (-45^\circ/+45^\circ) / 0^\circ / 90^\circ]_s$$

The starter defect was made by introducing a layer of folded aluminium foil (0.02 mm thick) at the interface between the two materials. The nominal thickness of the bi-material specimens following manufacture was 4.2 mm.

Mechanical testing was conducted on specimens with normalised insert lengths from 0.2 to 0.7, at a crosshead displacement rate of 2 mm/minute. Furthermore, rates of 0.2, 20, 200 mm/minute were used for specimens with a normalised insert length of 0.5. Specimens with a normalised insert length of 0.5, were tested under impact conditions at a velocity of 3.2 m/sec.

6.5.1. Load-Displacement Responses of the Bi-material Samples

Figure 6.31 shows a typical load-displacement trace following an ECT test on a bi-material sample containing an interface crack with a normalised length of 0.5. As can be seen, the response exhibited by this sample is very similar to that associated with the different materials examined in this research programme. As a result, the load was found to increase linearly, becoming slightly non-linear and reaching a maximum before dropping after the onset of macroscopic crack propagation.

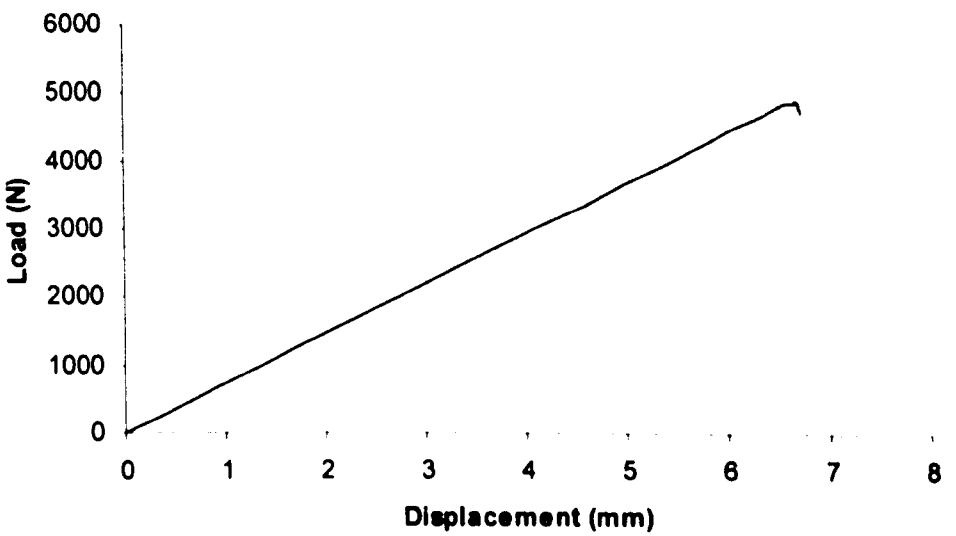

Figure 6.31: Load displacement trace following the ECT test on a bi-material ECT specimen containing interface crack with a normalised insert length of 0.5.

Figure 6.32 shows typical load-displacement traces following ECT tests on bi-material samples with normalised insert lengths ranging from 0.2 to 0.7 tested at a crosshead displacement rate of 2 mm/min. As before, the load increases in a relatively linear fashion, reaching a maximum before dropping following the onset of macroscopic crack propagation. Here again, the forces measured during these tests are

significantly higher than these measured on the plain ECT samples. This is due to the fact that the samples contained a steel layer that greatly increased the stiffness of the specimens.

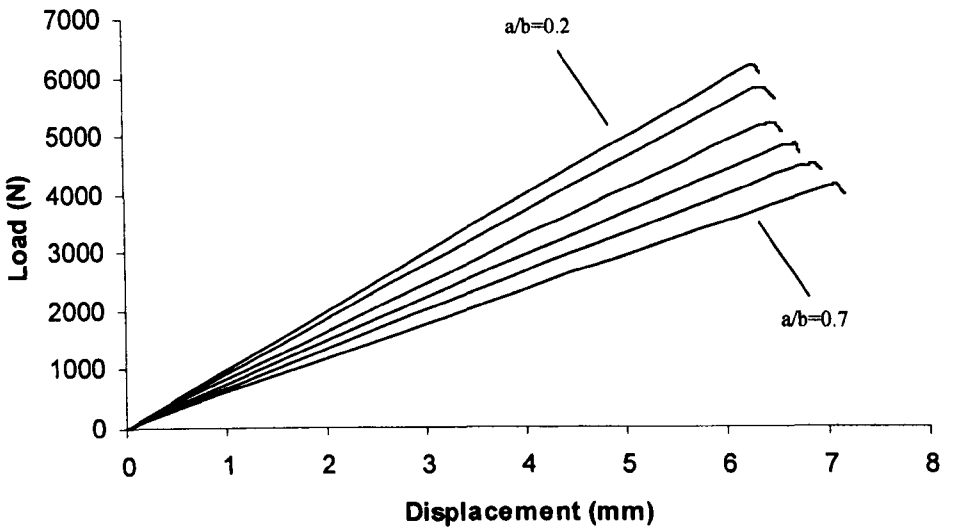

Figure 6.32: Load-displacement responses following ECT tests on bi-material ECT samples.

6.5.2. Influence of Crack Length on Specimen Stiffness

Similar procedures to those outlined previously were followed in order to determine the specimen compliance from the load-displacement plots obtained from the ECT tests. A plot of the inverse of specimen compliance, 1/C, with a/b for the bi-material ECT specimens is shown in Figure 6.33.

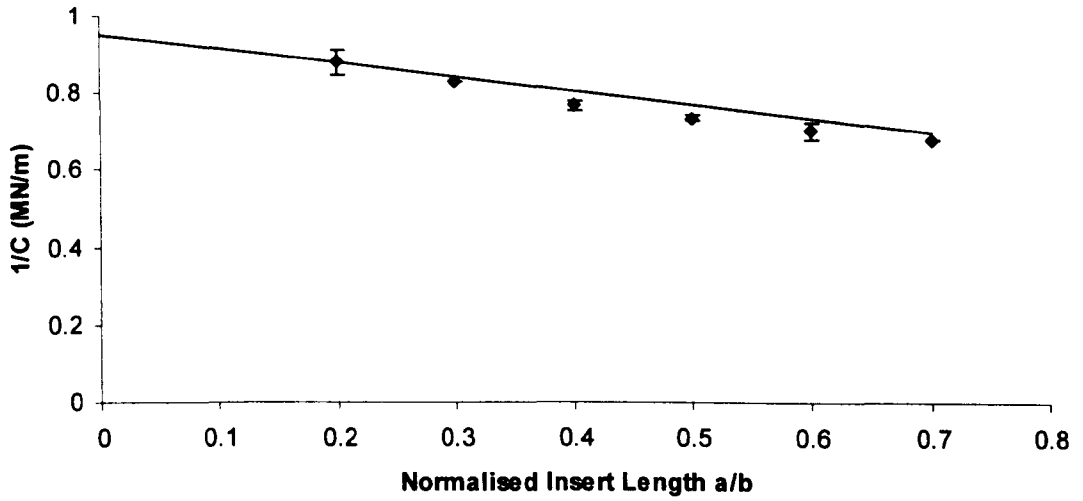

Figure 6.33: The experimentally determined variation of the inverse of specimen compliance with normalised crack length for the bi-material samples.

According to Figure 6.33, the plot of 1/C versus a/b from the bi-material specimens exhibits a reasonably linear response as has also been verified by the results of the finite element analysis. The constant 'm' in Equation 6.1 was calculated from the experimental data, giving values of 0.46. This value compares favourably with the value of 0.41 calculated by the FE analysis in the previous chapter.

6.5.3. Influence of Crack Length on G_{IIIc} at Quasi-Static Loading Rates

Repeating the procedure described earlier in this chapter and using Equation 6.2, the Mode III fracture toughness of each ECT specimen at maximum load, G_{IIIc}, was calculated using the maximum force, P_{max}.

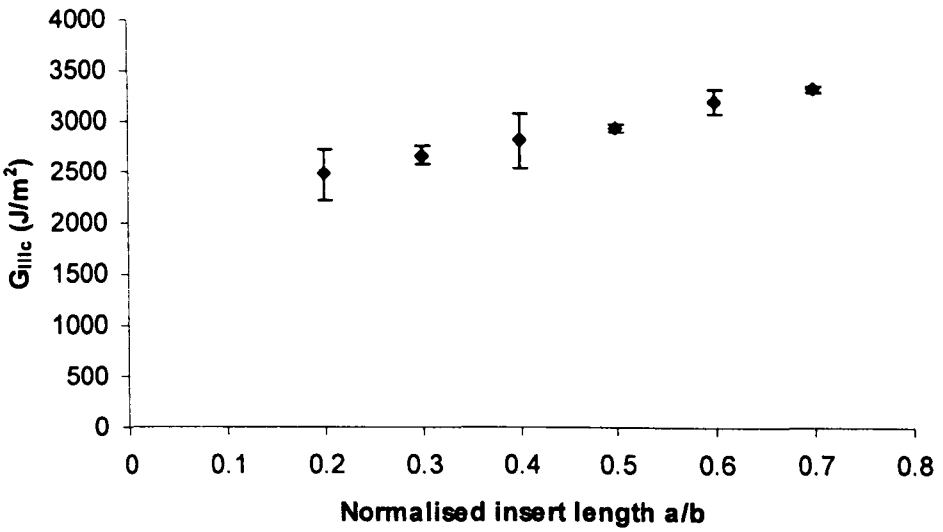

Figure 6.34: The variation of G_{IIIc} with normalised crack length for the bi-material samples with interface cracks.

An examination of the data presented in Figure 6.34, indicates that the Mode III fracture toughness values increase with normalised insert length, an effect that was observed in both the epoxy and polypropylene based systems examined earlier, as well as by other researchers [1]. It is worth noting that the increase in the values of G_{IIIc} with a/b is less rapid than that exhibited by the glass fibre/PP, woven glass fibre/epoxy and adhesively woven glass fibre/epoxy materials.

A comparison of Figures 6.34 and 6.14 indicates that the values of Mode III fracture toughness measured on the woven glass fibre reinforced epoxy composite are higher than the bi-material samples. Work by Bell and Kinloch [26] has shown that the nature of the substrate material has a significant effect on the value of the fracture energy, G_c. Although their work was on adhesively bonded joints, it showed that the degree of interfacial adhesion does not directly affect the value of G_c. However, this was found to be affected by the type of substrate employed. CFRP, steel and aluminium alloy joints were investigated with the use of FEA and it was found that the distortion and elevation of the stress field in the adhesive layer were far more

pronounced in the case of the steel joints, compared to the CFRP joints. This greater distortion and elevation of the stress field in the case of the steel joints would be expected to lead to a larger plastic zone [30, 31], compared to the case of the CFRP joints. According to Bell [26], the highest values of G_c are associated with those joints where the material surrounding the crack is subjected to the highest degree of constraint.

6.5.4. Influence of Loading Rate on the Load-Displacement Responses of the Bi-material Samples

Figure 6.35 shows typical load-displacement traces following ECT tests on the bi-material specimens with a normalised insert length of 0.5, tested at crosshead displacement rates of 0.2, 2, 20 and 200 mm/min. The load increases in a linear fashion, reaching a maximum before dropping rapidly after macroscopic crack propagation.

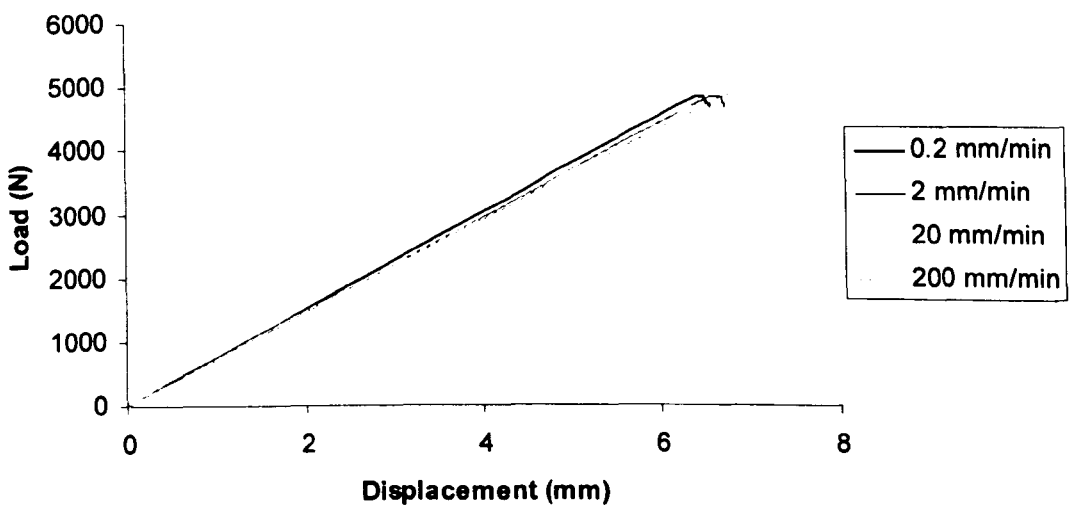

Figure 6.35: Load displacement traces following ECT tests on the bimaterial specimens with a normalised insert length of 0.5, tested at crosshead displacement rates of 0.2, 2, 20 and 200 mm/min.

6.5.5. Influence of Loading Rate on Specimen Stiffness

Figure 6.36 presents plots of the variation of the inverse of specimen compliance with crosshead displacement rate for the bi-material ECT specimens. As before, the plots correspond to samples with a normalised insert length, a/b, equal to 0.5. The crosshead displacement rate values range from 0.2 to 200 mm/min, excluding the impact case. As explained in Section 6.2.6, this is because the specimen compliance could not be determined at impact rates, since only a force-time trace is recorded during the impact test. The evidence in the graph shows that specimen stiffness remains constant for the crosshead displacement rates examined. This is in agreement with the observations on the plain glass fibre/epoxy where no rate sensitivity was observed.

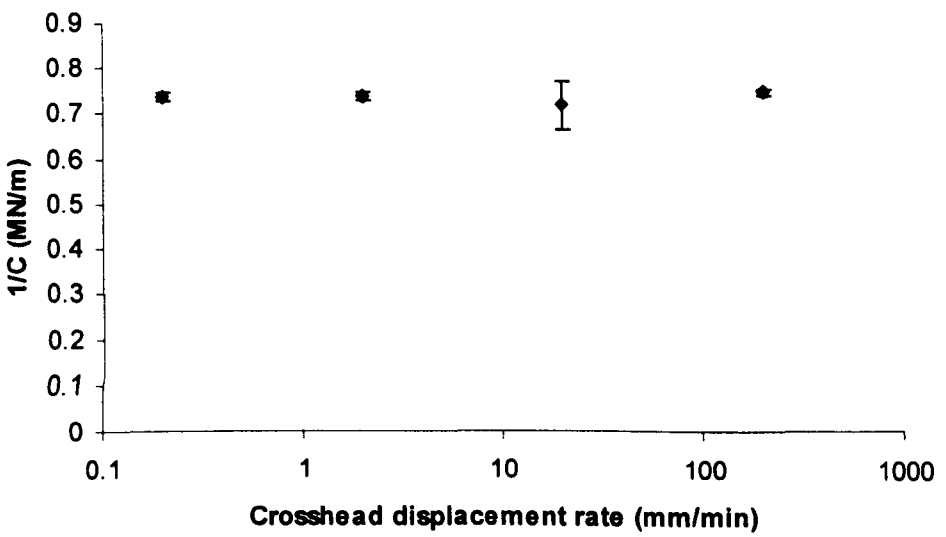

Figure 6.36: The influence of crosshead displacement rate on the stiffness of the bi-material ECT samples with interfacial cracks.

6.5.6. Influence of Loading Rate on the Mode III Fracture Toughness

The influence of loading rate on G_{IIIc} was investigated by conducting tests at crosshead displacement rates between 0.2 and 200 mm/min. The load-displacement traces were similar in all cases to those measured under quasi-static conditions. The dynamic fracture properties of the ECT specimens were evaluated through a series of falling weight impact tests on the previously-discussed instrumented drop-weight impact tower. Figure 6.37 shows the variation of the measured Mode III fracture toughness for the bi-material specimens with interface cracks between crosshead displacement rates of 0.2 and 200 mm/min, as well under impact conditions (3.2 m/sec).

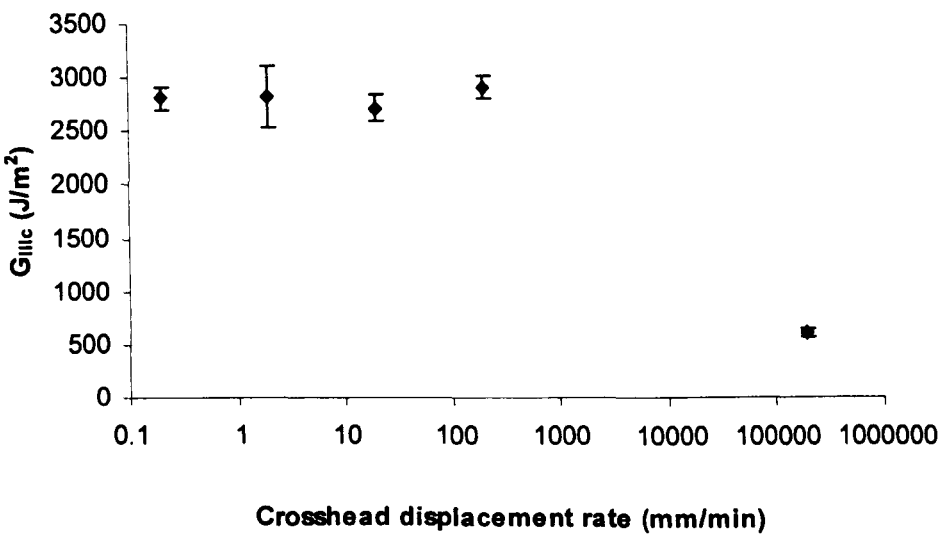

Figure 6.37: The influence of crosshead displacement rate on the interlaminar fracture toughness values of the bi-material ECT samples with interface cracks.

An examination of the data shown in Figure 6.37 indicates that the values of G_{IIIc} remain roughly constant for crosshead displacement rates ranging from 0.2 to 200

mm/min. Interestingly, at impact rates, the material exhibits very low values of Mode III fracture toughness these being 80% lower than at quasi-static rates. This significant reduction in G_{IIIc} is attributed to the debonding of the two halves of the impacted ECT specimens. Clearly, the bi-material samples with interface cracks proved to be good under quasi-static conditions but very brittle at impact rates of loading, due to the debonding of the isotropic material from the composite material.

During the bonding of two different materials, residual stresses may arise as a result of differential contraction between the materials when they are cooled from the joining temperature. This is due to different coefficients of thermal expansion of the materials and from a volume contraction which often accompanies curing or cross-linking of the epoxy material [32, 33]. Kinloch and co-workers [32] investigated the effect of residual stresses on the failure of epoxy joints using symmetrical bi-material specimens (SBM) and concluded that they can significantly influence the fracture behaviour. Furthermore, the extent of overall residual stresses in the adhesive layer increased with increasing post-cure temperature, as expected.

These results suggest that care should be taken when employing bi-material systems such as these under impact conditions.

6.6. Summary of Experimental Results

Table 6.1 gives an overview of the ECT tests conducted during the course of this research programme as well as the results/trends that were observed:

Material	a/b	Adhesive Thickness	Parameter varied	Comments
G.F.-Polypropylene	0.2-0.7	-	Insert length	G_{IIIc} was found to increase with a/b. This dependency was further examined using a numerical method. Similar trends and good agreement in the values of G_{IIIc} were observed.
G.F.-Polypropylene	0.5	-	Strain Rate	Specimen stiffness increases slightly with strain rate as the polypropylene matrix exhibits a more pronounced viscoelastic response than the epoxy matrix. G_{IIIc} appears unaffected by strain rate. SEM showed no significant loading rate effect on fracture morphology.
Woven G.F.-Epoxy	0.2-0.7	-	Insert length	G_{IIIc} was found to increase with a/b. This dependency was further examined using an areas method. Similar trends and good agreement in the values of G_{IIIc} were observed. Values of G_{IIIc} higher than GF/PP as it exhibited a high degree of crystallinity due to slow cooling.
Woven G.F.-Epoxy	0.5	-	Strain Rate	Specimen stiffness appears to be unaffected by strain rate. Similar trends observed for the G_{IIIc} , suggesting the interlaminar fracture properties of the system are insensitive to loading rate. SEM showed slightly smoother fracture surfaces for the impacted specimen.
Adhesively-bonded G.F.-Epoxy	0.2-0.7	1.42 mm	Insert length	G_{IIIc} was found to increase with a/b. Values of G_{IIIc} higher than plain composite due to the presence of significant crack-tip blunting within the adhesive epoxy layer. Crack propagated cohesively in all specimens.
Adhesively-bonded G.F.-Epoxy	0.2 - 0.7	1.42 mm	Insert length, Strain rate	Specimen stiffness was found to be constant with crosshead displacement rate. Mode III fracture toughness was found to increase with a/b under impact loading conditions, like in the quasi-static case. G_{IIIc} was unaffected by strain rate, similarly to observations by other researchers. Crack propagated cohesively in all specimens.
Bi-material samples with interface cracks	0.2 - 0.7		Insert length	G_{IIIc} was found to increase with a/b. Values of G_{IIIc} lower than plain composite due to the presence of residual stresses generated by the difference in coefficients of thermal expansion between spring steel and composite material during cooling. These have already exposed the crack tip to a stress field and the observed values of G_{IIIc} are therefore low. This is more pronounced under impact.
Bi-material	0.5	-	Strain rate	Specimen stiffness appears to be unaffected by strain rate. Similar trends observed for the G_{IIIc} , although in the impacted specimen the value was 80% lower due to residual stresses.

Table 6.1: Summary of ECT tests and findings of this research programme.

6.7. References

1. Davies P, Cantwell W.J., Fracture of glass/polypropylene laminates: Influence of cooling rate after moulding, Composites, Vol.25, 1994, p.866.

2. Friedrich K., Advances in Polymer Science, edited by H.H. Kausch, Springer-Verlag, Berlin, Vol.52-53, 1983, p.225.

3. Ismail Y.S., Richardson M.O.W., Olley R.H., Optimizing impact properties of PP composites by control of spherulitic morphology, Journal of Applied Polymer Science, Vol.79, 2001, p.1704.

4. Padden F.J., Keith H.D., Spherulitic crystallization in polypropylene, Journal of Applied Physics, Vol.30, Oct. 1959, p.1479.

5. Khoury F., Spherulitic crystallization of isotactic polypropylene from solution – on evolution of monoclinic spherulites from dendrinic chain-folded crystal precursors, Journal of the National Bureau of Standards Section A-Physics and Chemistry, Vol.70A, Jan.-Feb. 1966, p.29.

6. Wunderlich B., Macromolecular Physics, Vol. 2, Academic Press, New York, Ch.5, 1976, p.210.

7. Li J., Lee S.M., Lee E.W., O'Brien T.K., Evaluation of the edge crack torsion (ECT) test for Mode III interlaminar fracture toughness of laminated composites, Journal of Composites Technology & Research, Vol. 19, 1997, p.174.

8. Lee S.M., An edge crack torsion method for Mode III delamination fracture testing, Journal of Composites Technology & Research, Vol.15, 1993, p.193.

9. Ratcliffe J.G., Characterization of the Edge Crack Torsion (ECT) test for Mode III fracture toughness measurement of laminated composites, National Research Council, NASA Langley Research Centre, Hampton, Virginia, September 2004.

10. Cantwell W,J., Büsser M. and Kausch H.H., An evaluation of the interlaminar fracture toughness of a thermoplastic composite with offset centre plies, Composites Engineering, Vol.1, 1991, p.293.

11. Callister W.D., Materials Science and Engineering an Introduction, 7th Edition, Ch.15, 1996, p.523.

12. Cantwell W.J., unpublished work.

13. Blackman B.R.K., Dear J.P., Kinloch A.J., MacGillivray H., Wang Y., Williams J.G., Yayla P., The failure of fibre composites and adhesively-bonded fibre composites under high rates of test. Mixed-Mode I/II and Mode II loadings, Journal of Materials Science Vol.31, 1996, p.4467.

14. Maikuma H., Gillespie J.W., Wilkins D.J., Mode II interlaminar fracture of the centre notch flexural specimen under impact loading, Journal of Composite Materials, Vol.24, 1990, p.124.

15. Smiley A.J., Pipes R.B., Rate effects on Mode I fracture toughness in composite materials, Composites Science and Technology, Vol.29, 1987, p.1.

16. Hibbs M.F., Bradley W.L., Mode II delamination failure mechanisms of polymer matrix composites, ASTP-948, (American Society for Testing and Materials, Philadelphia PA), 1987, p.68.

17. Acran L., Acran M., Daniel I.M., ASTM STP-948, (American Society for Testing and Materials, Philadelphia PA), 1987, p.41.

18. Smith B.W., Grove R.A., ASTM STP-948, (American Society for Testing and Materials, Philadelphia PA), 1987, p.154.

19. Russel A.J., Theory of multiple fracture of fibrous composites, Polymer Composites, Vol.8, 1987, p.342.

20. Davies P., de Charentenay F.X., Proceedings of 6th International Conference on Composite Materials (ICCM-VI), London, July 20-24, 1987, (Elsevier, London, 1987), p.3284.

21. Lee S.M., Mode II delamination failure mechanisms of polymer matrix composites, Journal of Materials Science, Vol.32, 1997, p.1287.

22. Low M., Mai Y.W., Rate and temperature effects on crack blunting mechanisms in pure and modified epoxies, Journal of Materials Science, Vol.24, May 1989, p.1320.

23. Williams J.G., Hodgkinson J.M., Crack-blunting mechanisms in impact tests on polymers, Proceedings of the Royal Society of London, Series A, Mathematical and Physical Sciences, Vol.375, March 1981, p.231.

24. D'almeida J.R.M., Cella N., Analysis of the fracture behaviour of epoxy resins under impact conditions, Journal of Applied Polymers Science, Vol.77, 2000, p.2486.

25.Kinloch A.J., Williams J.G., Crack blunting mechanisms in polymers, Journal of Materials Science, Vol.15, 1980, p.987.

26. Bell A.J., Kinloch A.J., The effect of the substrate material on the value of the adhesive fracture energy Gc, Journal of Materials Science Letters, Vol.16, 1997, p.1450.

27. Chai H., Shear fracture, International Journal of Fracture, Vol.37, 1988, p.137.

28. Chai H., Interlaminar shear fracture of laminated composites, International Journal of Fracture, Vol.43, 1990, p.117.

29. Chai H., Micromechanics of shear deformations in cracked bonded joints International Journal of Fracture, Vol.58, 1992, p.223.

30. Kinloch A.J., Shaw S.J., The fracture resistance of a toughened epoxy adhesive, Adhesion, Vol.12, 1981, p.59.

31. Hunston D.L., Kinloch A.J., Wang S.S., Micromechanics of fracture in structural adhesive bonds, Journal of Adhesion, Vol.28, 1989, p.103.

32. Kinloch A.J., Thrusabanjong, Williams J.G., Fracture at biomaterial interfaces-the role of residual stresses, Journal of Materials Science, Vol.26, 1991, p.6260.

33. Williams J.G., Fracture Mechanics of Polymers, Ellis Horwood, Chichester, 1984, p.55.

7. Conclusions

7.1. General Summary

A numerical and experimental study has been carried out to investigate the Mode III interlaminar fracture properties of composite materials, adhesive joints and bi-material samples. For this purpose, the Edge Crack Torsion (ECT) test geometry was employed.

Samples with isotropic as well as orthotropic properties were modelled and their response under Mode III loading conditions simulated. More specifically, glass fibre reinforced polypropylene, woven glass fibre reinforced epoxy, adhesively-bonded woven glass fibre reinforced epoxy and a bi-material sample based on the same material were the materials examined using FEA. The specimens had normalised insert lengths ranging from 0.2-0.7 and a displacement of 2 mm was applied to ensure an elastic response.

A major finding of the finite element analysis on all the materials examined was the fact that a state of pure Mode III shear exists at the centre of the specimen, whereas Mode II components exist near the locations of the load and support pins. An explanation for this can be offered by the positioning of the load and support pins

which generates a moment arm that causes relative sliding of the two delaminated sections of the specimen, parallel to the direction in which the delamination tends to grow. It should also be noted that the Mode III component of strain energy release rate was found to be several times higher (approx. 600%) than the Mode II component, indicating that Mode III is the dominant loading condition type, resulting in delamination initiating from the centre of the specimen insert front. This proves the suitability of the ECT specimen geometry for Mode III testing, eliminating any disadvantages experienced by the Crack Rail Shear and Split Cantilever Beam tests. To add to this, the value of the total strain energy release rate across the delamination front, G_{Ta}, was calculated and plotted versus normalised insert length to characterize the mode of crack propagation. An important finding for the ECT geometry was that the delamination growth for all the materials investigated would be stable, if testing is performed under displacement control.

The effect of a number of factors on the Mode III strain energy release rate distribution was investigated by a series of additional numerical analyses. The response of glass fibre reinforced polypropylene when applying a displacement ranging between 1-7 mm showed that the Mode III component of strain energy release rate increases with applied displacement by up to 900%. This was due to the higher forces experienced by the material at higher displacements. Similar results were obtained when the total ply number was increased from 16 to 24 and finally 32. Once more, the values of G_{III} increased with ply number by 300% for the thickest sample. This was attributed to the greater thickness and thus the higher forces exhibited due to the greater rigidity of these specimens.

In the case of the woven glass fibre reinforced epoxy, the values of Mode III strain energy release rate were found to be 300% higher than those observed for the glass fibre polypropylene. This was attributed to the greater thickness of these specimens, resulting in higher flexural stiffness.

The possibility of developing a mixed Mode II/III test geometry was also investigated in this research programme. For this purpose, numerical analysis was performed on woven glass fibre reinforced samples with the delamination positioned at variable locations through the thickness. However, according to the findings, the values of

Mode II and Mode III strain energy release rates were higher (up to 300%), the closer the crack was positioned relative to the mid-thickness. Another part of the analysis focused on the effect of re-positioning the load and support pins on the ECT geometry. The findings were very interesting as they revealed the possibility of having a uniform Mode III strain energy release rate distribution over a 40% greater region along the specimen width, by locating the load and support pins towards the specimen edges. However the obtained values of G_{III} were considerably lower (50%) compared to the original ECT.

The effect of adhesive thickness on the Mode II and Mode III strain energy release rates was investigated in the case of the adhesively-bonded woven glass fibre reinforced epoxy material. Two different thicknesses, 100 μm and 1.42 mm were examined with noticable results, as the adhesively-bonded specimens showed superior properties compared to the plain composite. The values of G_{III} were increased by nearly 25% for the thickest adhesive, reflecting the greater rigidity offered.

Bi-material samples with interface cracks based on spring steel and a woven glass fibre reinforced composite were modelled and analysed using FEA. These specimens were of lower thickness compared to the plain composite and as a result the values of Mode II and Mode III strain energy release rate were considerably lower (35%).

A great part of this research programme focused on mechanical testing of the aforementioned materials to study their interlaminar fracture properties and response under Mode III loading conditions.

Glass fibre reinforced polypropylene specimens with normalised insert lengths ranging from 0.2-0.7 were tested at a crosshead displacement rate of 2 mm/min. Furthermore, specimens with an a/b = 0.5 were tested at 0.2, 20, 200 mm/min and under impact to investigate their rate sensitivity. A high degree of crystallinity of 60% by weight was observed in the specimens, owing to the relatively slow cooling rate adopted during manufacture. This affected the Mode III interlaminar fracture properties which were lower than for the woven glass fibre reinforced epoxy. The effect of cooling rate and crystallinity on the Mode III interlaminar fracture properties of thermoplastic matrices should be taken into consideration when using such

materials as it can significantly alter their response to delamination. Another important finding was the increasing values of G_{IIIc} with a/b. This was a little surprising as the Mode III fracture toughness is an intrinsic property and should be constant with insert length. Similar results can be found in the literature, although no explanation has been given. In order to find a reasonable explanation, a numerical method was used in which the response of glass fibre reinforced polypropylene specimens was modelled, applying a displacement equal to those obtained from the actual experiments, when crack propagation occured. The results were in very good agreement and showed that this increase in the values of Mode III fracture toughness is genuine.

The specimen stiffness was found to be slightly dependent on strain rate, with the values of 1/C increasing by 15% between 0.2 and 200 mm/min. This was attributed to the pronounced viscoelastic response of the polypropylene matrix. No rate sensitivity was observed regarding the values of the Mode III interlaminar fracture toughness, a finding which is of significant importance, since it means that the engineers could potentially use the value determined at quasi-static conditions when designing a composite component. The SEM conducted on the fractured surface further verified the results, as there was no obvious strain rate effect on the Mode III fracture morphology of the glass fibre reinforced polypropylene material.

The experimental work on the woven glass fibre reinforced epoxy material revealed 40% higher values of G_{IIIc}, owing to the high crystallinity in the polypropylene matrix. Additionally, the values of Mode III interlaminar fracture toughness were found to increase with normalised insert length a/b. Here, an areas method was employed, only to obtain similar findings. This evidence, together with the numerical method used in the glass fibre polypropylene material, showed that the crack length dependency of G_{IIIc} is genuine and needs to be taken into consideration when conducting Mode III tests of this nature.

No strain rate effects were observed with regards to specimen stiffness and Mode III interlaminar fracture toughness of the woven glass fibre reinforced epoxy material, with the values remaining roughly constant over a wide range of loading rates.

The ECT testing of adhesively-bonded woven glass fibre reinforced epoxy specimens focused on the effects of adhesion and adhesive thickness on Mode III interlaminar fracture properties. This work revealed considerable high values of G_{IIIc} (nearly 50%) compared to the plain composite. The increase in the volume of resin undergoing plastic deformation led to significant crack-tip blunting within the epoxy adhesive layer. As a result, more energy was absorbed, making crack propagation more difficult, revealing another toughening mechanism that could be taken into consideration in the design phase. Finally, it should be noted that the crack propagated cohesively and did not jump out of plane.

No obvious strain rate effects were observed with regards to specimen stiffness and Mode III interlaminar fracture toughness. Additionally, a range of adhesively-bonded specimens with normalised insert lengths ranging from 0.2-0.7 were tested under impact. Once more, the values of G_{IIIc} increased with a/b and were similar to those observed at quasi-static testing.

Bi-material samples with interface cracks were manufactured and tested at crosshead displacement rates ranging from 0.2-200 mm/min and under impact, in order to evaluate their response under Mode III loading conditions. The values of G_{IIIc} appeared to increase with normalised insert length, like in the previously examined materials. However, the obtained values were considerably lower, reduced by approximately 30% when compared to the plain woven glass fibre reinforced epoxy composite. This was attributed to the presence of residual stresses and the stress field in which they exposed the crack tip. This was more pronounced when testing the bi-material samples under high rates of strain. For the range between 0.2- 200 mm/min, the values of Mode III interlaminar fracture toughness remained roughly constant, with a high drop of nearly 82% observed for the impacted specimens. It appears that the effect of residual stresses was more pronounced under impact due to the ductile-brittle transition experienced by the material. As a result, residual stresses can greatly affect the obtained values of Mode III fracture toughness and should therefore be taken into consideration when using similar materials.

In conclusion, this project investigated the Mode III fracture properties of high-performance composites similar to those used in the aerospace industry. The project

involved a detailed finite element analysis of the current ECT geometry in order to characterise the response of the ECT geometry for evaluating the Mode III response of composites. The Mode III geometry was then modified to look at mixed-mode failure involving Mode III contributions. The project used the Virtual Crack Closure Integral to characterise the loading conditions at the crack tip in these samples. Once the quasi-static response of the composites were analysed, dynamic tests were undertaken using a newly-developed modified ECT test geometry in order to investigate the rate-sensitive behaviour of these high-performance materials, leading to a greater understanding of the behaviour of composites under in-service conditions.

7.2. Future Work

As a direct consequence of the research detailed here, there are a number of considerations, which may be of interest for future workers in this field. The investigation of the Mode III interlaminar fracture properties of high-performance composites, such as carbon fibre epoxies, would be of great interest. Furthermore, it would be useful to conduct ECT tests at higher strain rates, both experimentally and numerically. The effect of varying temperature on the Mode III fracture properties of composite materials could provide useful information, leading to the establishment of fracture maps that will offer a greater understanding of the behaviour of composites under in-service conditions.